Magnetic Interface Effects in Thin Film Heterostructures

Von der Fakultät für Mathematik, Informatik und Naturwissenschaften der RWTH Aachen University zur Erlangung des akademischen Grades eines Doktors der Naturwissenschaften genehmigte Dissertation

vorgelegt von

Diplom-Physiker

Paul Jan Zakalek

aus Heydebreck-Cosel

Berichter: Univ.-Prof. Dr. rer. nat. Thomas Brückel
Univ.-Prof. Dr. rer. nat. Larissa Juschkin

Tag der mündlichen Prüfung: 17.11.2015

“God made the bulk;
surfaces were invented
by the devil.”

- Wolfgang E. Pauli -

Abstract

Magnetic interface effects in thin film heterostructures, especially the possibility of an induced magnetic moment in a non-magnetic film or the enhancement of the magnetism at an interface, are very promising for new spintronic devices. Three different kinds of interfaces were investigated in this thesis, namely metal/metal, metal/oxide, and oxide/oxide interfaces. With the complementary investigation methods of SQUID magnetometry, polarized neutron reflectometry and X-ray magnetic circular dichroism, a possible magnetic interface effect could be addressed.

In addition to the investigation of these interface effects, this work covers the sample preparation and characterization of the transition metal oxide thin films grown on $SrTiO_3$ substrates. All samples were grown with either molecular beam epitaxy or high oxygen pressure sputtering.

The first metal/metal interface system is a Pd/Fe multilayer. It is known, that Pd can be magnetically polarized in contact with ferromagnetic Fe due to the large Stoner parameter. The mechanism for the induced magnetism is a hybridization of the Pd 4d orbitals with the Fe 3d orbitals. The investigation showed that Pd is magnetically polarized at the interface to Fe. With polarized neutron reflectometry, the exact magnetism profile in the Pd layer could be determined.

The second metal/oxide system are the $La_{0.7}Sr_{0.3}MnO_3$/Pd and $La_{0.7}Ca_{0.3}MnO_3$/Pd thin films. The large Stoner parameter of Pd could also enable the possibility of an induced magnetic moment in this system class. With the mentioned investigation methods, a possible interface effect could be excluded. Even more, the polarized neutron reflectometry measurements showed an extended “dead” magnetic layer in $La_{0.7}Sr_{0.3}MnO_3$ and $La_{0.7}Ca_{0.3}MnO_3$ at the interface to Pd.

The last oxide/oxide system is a $La_{0.7}Sr_{0.3}MnO_3/La_{0.7}Ca_{0.3}MnO_3$ multilayer, where the Curie temperatures are $T_C = 380$ K and $T_C = 260$ K. Due to the similar structure of both layers, a magnetic interface effect could be present, which could be shown with polarized neutron reflectometry measurements. Due to the contact to the $La_{0.7}Sr_{0.3}MnO_3$ layer, the magnetism at the $La_{0.7}Ca_{0.3}MnO_3$ interface is increased and the width of the interface effect increases with decreasing temperature.

The effects here are limited to the interface, a region of only a few atom layers. Thus, they are tiny in respect to the signal of the whole sample and hard to detect. But with the development of the data treatment and analysis of polarized neutron reflectometry experiments, they could be determined. Special attention was put to the handling of alignment inaccuracies, off-specular scattering, detector insensitivities and resolution considerations. For the modeling of these heterostructures in polarized neutron reflectometry, the magnetic and nuclear scattering length densities were separated, allowing the concentration on the magnetism depth profile.

Zusammenfassung

Magnetische Grenzflächeneffekte in Dünnschicht-Heterostrukturen sind vielversprechende Phänomene für neue Spintronik. Das Induzieren von magnetischen Momenten in nichtmagnetischen Filmen oder die Verstärkung des Grenzflächenmagnetismus sind hierbei von herausragender Bedeutung. Drei verschiedene Arten von Grenzflächeneffekten wurden in dieser Arbeit untersucht, die Metall/Metall-, Metall/Oxid- und Oxid/Oxid-Grenzflächen. Mögliche magnetische Grenzflächeneffekte konnten mit sich ergänzenden Messmethoden, insbesondere der SQUID Magnetometrie, der polarisierten Neutronenreflektometrie und des Röntgendichroismus, untersucht werden.

Zusätzlich zur Analyse der Grenzflächeneffekte behandelt diese Arbeit die Präparation und Charakterisierung von Dünnschicht-Übergangsmetalloxiden, die auf $SrTiO_3$ gewachsen wurden. In diesem Zusammenhang wurden alle Proben mithilfe der Molekularstrahlepitaxie oder des Hochdruck-Sauerstoff-Sputterns gewachsen.

Das erste Metall/Metall-Grenzflächensystem ist ein Pd/Fe-Vielfachschichtsystem. In diesem System wird das Palladium durch Kontakt zum ferromagnetischem Eisen magnetisch polarisiert, wobei die Polarisation wegen des großen Stoner-Parameters von Palladium ermöglicht wird. Eine Hybridisierung der Palladium 4d-Orbitale mit den Eisen 3d-Orbitalen induziert dabei den Magnetismus im Palladium. Die Auswertung ergab, dass Palladium an der Grenzfläche zu Eisen eine magnetische Polarisation aufweist, wobei das genaue magnetische Profil mithilfe der polarisierten Neutronenreflektometrie bestimmt werden konnte.

$La_{0.7}Sr_{0.3}MnO_3$/Pd and $La_{0.7}Ca_{0.3}MnO_3$/Pd sind Dünnschichtsysteme des zweiten Metall/Oxid-Systems. Der große Stoner-Parameter von Palladium könnte auch einen magnetischen Grenzflächeneffekt in diesen Systemen ermöglichen. Mit den genannten Untersuchungsmethoden konnte aber ein magnetischer Grenzflächeneffekt ausgeschlossen werden. Zusätzlich konnte mithilfe der polarisierten Neutronenreflektometrie gezeigt werden, dass eine ausgedehnte magnetisch “tote” Schicht in $La_{0.7}Sr_{0.3}MnO_3$ und $La_{0.7}Ca_{0.3}MnO_3$ an der Grenzfläche zu Palladium existiert.

Das letzte Oxid/Oxid-Grenzflächensystem ist ein $La_{0.7}Sr_{0.3}MnO_3$/$La_{0.7}Ca_{0.3}MnO_3$-Vielfachschichtsystem, das Curie-Temperaturen von $T_C = 380$ K und $T_C = 260$ K aufweist. Aufgrund der ähnlichen Struktur beider Schichten könnte ein magnetischer Grenzflächeneffekt vorhanden sein. Der Grenzflächeneffekt wurde mithilfe der polarisierten Neutronenreflektometrie gezeigt. Die $La_{0.7}Ca_{0.3}MnO_3$-Grenzfläche weist aufgrund des Kontakts zur $La_{0.7}Sr_{0.3}MnO_3$-Schicht einen erhöhten Magnetismus auf, wobei die Dicke des Grenzflächeneffektes mit sinkender Temperatur zunimmt.

Die beschriebenen Grenzflächeneffekte sind auf die Grenzschicht beschränkt, die nur ein paar Atomlagen dick ist. Aus diesem Grund sind die Signale dieser Grenzflächeneffekte im Vergleich zu den Signalen der ganzen Probe winzig und somit schwer zu messen. Mit

der Weiterentwicklung der Datenverarbeitung und Analyse der polarisierten Neutronenreflektometrie-Experimente, konnten aber diese Grenzflächeneffekte bestimmt werden. Besonderes Augenmerk wurde auf die Handhabung von Kalibrierungsungenauigkeiten, diffuser Streuung, Detektorungenauigkeiten und Auflösungsbetrachtungen gelegt. In den Modellen der Heterostrukturen in polarisierter Neutronenreflektometrie wurde die magnetische und nukleare Streulängendichte separiert, was eine Konzentration auf das magnetische Profil ermöglichte.

Contents

1. Introduction

Over the last 2000 years magnetism is known to mankind in the form of magnetite, which is a strong ferrimagnet at room temperature. It was only over the last few centuries that the understanding of magnetism improved and many magnetic phenomena could be explained. Theories were developed, which could explain the intrinsic magnetism of elemental Fe, Co and Ni and the reason why only these elements exhibit ferromagnetism. More complex materials, which show ferromagnetism through strongly correlated electrons, like $\mathrm{La}_x\mathrm{Sr}_{1-x}\mathrm{MnO}_3$, were the next hurdle for which a basic understanding has been developed. Simple models exist for bulk ferromagnetism, which reproduce some of its main features, but electronic correlations are far from being understood.

The next hurdle is the influence on these magnetic phenomena through e.g. interface effects. Modern sample preparation methods enable the creation of artificial systems, where theories of magnetism are put to a test. Enormous progress was made in thin film preparation, which allows the creation of heterogeneous multilayer samples with atomically flat interfaces [1]. Using different magnetic layers, the magnetism of the individual layers will be altered at the interface just by the presence of the interface [2]. At the interface two antiferromagnetic materials can show ferromagnetic behavior [3], the Curie temperature at the interface might be higher than in bulk material [4, 5] or superconductivity and ferromagnetism can coexist [6]. One well known interface effect is the induced polarization in otherwise paramagnetic palladium [7, 8, 9] in contact to ferromagnetic iron. Pd is on the edge of becoming a ferromagnet, whereby nearly fulfilling the Stoner criterion for ferromagnetism [10]. The first evidence of Pd polarization was shown in FePd alloys [11, 12], where the ferromagnetic Pd could be explained by hybridization of the 3d Fe orbitals with the 4d Pd orbitals increasing the density of states at the Fermi level and inducing a polarization into Pd. In theory [7] and experiment [9] it was shown that this hybridization also takes place at the interface of Pd/Fe layered samples. Pd becomes ferromagnetic with a magnetic moment of around $m = 0.37\ \mu_\mathrm{B}$ directly at the interface and decays after two unit cells inside the Pd layer. Before magnetic interface effects in strongly correlated electron systems were investigated, the Pd/Fe system was analyzed in this PhD thesis as a reference sample.

Strongly correlated electron systems, like $\mathrm{La}_x\mathrm{Sr}_{1-x}\mathrm{MnO}_3$ (LSMO) [13] or $\mathrm{La}_x\mathrm{Ca}_{1-x}\mathrm{MnO}_3$ (LCMO) [14], where the anti- or ferromagnetism is explained through the superexchange and double exchange interactions [15, 16, 17] between the $\mathrm{Mn}^{3+/4+}$ ions mediated through the oxygen, should also exhibit a magnetic interface effect in LSMO/LCMO heterostructures. These interface effects are based on another physical mechanism as in the case of Pd/Fe layered samples. At the interface of LSMO and LCMO, the superexchange and double exchange will be altered through different bonding lengths and bonding angles due to strain [18] or the different ionic radii of Sr and Ca. Another possibility is the intermixing of the LSMO and LCMO thin films [19]. The main difference is that, in the case of LSMO and LCMO, the ferromagnetism is attributed to the localized 3d $\mathrm{Mn}^{3+/4+}$ electrons, whereas the magnetism on the Pd/Fe layered samples is attributed to the delocalized band electrons.

Considering the different models used to describe ferromagnetism in Pd (itinerant electron approach) and LSMO/LCMO (modeled by overlapping orbitals leading to superexchange and double exchange interaction), a Pd/LSMO or Pd/LCMO heterostructure appears to be particularly interesting. Will such a layered sample also show induced ferromagnetism in the Pd layer? Kim *et al.* [20] showed that in a $\mathrm{La}_{0.7}\mathrm{Ca}_{0.3-x}\mathrm{Sr}_x\mathrm{MnO}_3$ framework, with $x = 0.1$, Pd can be magnetically polarized with a magnetic moment of about 0.6 μ_B. This was attributed to finite size effects, resulting in ferromagnetic Pd [21], although a contact to the $\mathrm{La}_{0.7}\mathrm{Ca}_{0.3-x}\mathrm{Sr}_x\mathrm{MnO}_3$ oxide was necessary. In a different system, it was theoretically shown that a contact with semiconductors, like ZnS [22] or CdS [23], should result in ferromagnetic Pd, due to a strong coupling chain allowing the double exchange mechanism. The needed interaction between the Pd and the $\mathrm{La}_{0.7}\mathrm{Ca}_{0.3-x}\mathrm{Sr}_x\mathrm{MnO}_3$ oxide might be a similar double exchange chain, coupling the Pd atoms through the Mn atoms in the perovskite structure. LSMO/Pd and LCMO/Pd layered samples were investigated in this thesis, because understanding the interface effects of complex transition metal oxides is a true challenge in condensed matter research.

The outline of this thesis is as follows:

Chapter 1: This chapter gives a short introduction into the topic of magnetic interface effects and the motivation for this work.

Chapter 2: Theoretical background of the underlying physics is presented. Beginning with the perovskite structure of LSMO and LCMO, the magnetism is described by means of superexchange and double exchange interactions for the localized magnetic moments of the Mn ions. Additionally, the ferromagnetism of metals is presented using the Stoner model. Possible interface effects are explained with regard to both magnetism mechanics.

Chapter 3: This chapter gives an overview of the scattering theory, which was used to analyze the samples.

Chapter 4: The experimental methods for sample preparation are described, as well as the instruments used for sample characterization.

Chapter 5: The sample preparation with oxide molecular beam epitaxy and high oxygen pressure sputtering is described with the optimization of the growth parameter.

Chapter 6: The data reduction of the scattering experiments is described, as well as the problems encountered with the analysis and subsequent solutions thereof.

Chapter 7: The results of all experiments are presented for the Pd/Fe, the LSMO/Pd, the LCMO/Pd and the LSMO/LCMO thin films. A special focus is set on the results of the scattering experiments.

Chapter 8: The conclusion and the reunification of all analyzed systems is presented and discussed. The results shown in **chapter 7** are discussed with special attention to the underlying physical mechanism of ferromagnetism.

Appendix: In the appendix an overview of all measurements on prepared and analyzed samples, relevant for this thesis, is presented. Additionally, the band structure and the density of states is shown for all involved materials. The recipes used for the film growth are presented, as well as all growth parameters.

2. Basics of Perovskites, Bulk and Interface Magnetism and Thin Film Growth

In this chapter the theoretical background on interface effects in transition metal oxide (TMO) and metals is given. It starts with a short introduction to TMOs with a perovskite structure and their magnetism, followed by the theory of band magnetization inside metals. The third and fourth section gives a short overview of possible growth modes and interface effects in layered oxide/oxide, metal/metal and metal/oxide structures.

2.1. Transition Metal Oxide Perovskites

Transition metal oxide perovskites are a fascinating material class, which is well known and shows a huge variety of different effects, like ferromagnetism at room temperature [13], colossal magnetoresistance [24, 25], multiferroic behavior [26, 27] magnetocaloric effects [28, 29] and many more. These effects are due to the complex interplay between structure, orbital ordering, exchange interactions and strain inside these materials. Due to the simple structure and the possibility of altering these effects through e.g. substitution, these materials attract a lot of attention.

Structure

The TMO perovskites, investigated in this PhD thesis, have the chemical composition ABO_3, where La, Sr or Ca are on the A site and a transition metal cation, like Mn is on the B site. The cation on the B site is in an octahedral environment formed by oxygen. The investigated LSMO and LCMO materials crystallize in a distorted perovskite structure. Substituting La on the A site with Sr or Ca disturbs the perovskite structure, due to different ionic radii of Ca (1 Å) and Sr (1.16 Å) [30]. Due to the distortion and the resulting lower symmetry, the LSMO crystallize in a rhombohedric symmetry [31] and the LCMO crystallizes in a orthorhombic symmetry [32]. Considering the strain induced distortions of TMO thin films (**section 2.4**), it is convenient to express these structures in the (pseudo) cubic perovskite structure shown in **figure 2.1** and analyze the deviations from the (pseudo) cubic structure. The lattice parameters in the pseudo cubic structure are 3.88 Å for LSMO [31] and 3.87 Å for LCMO [32]. The substrate $SrTiO_3$ (STO) has a lattice parameter of 3.901 Å [33] and, thus, the LSMO and LCMO have a lattice mismatch of 1.00% and 1.01%, respectively. The small lattice mismatch and the similar

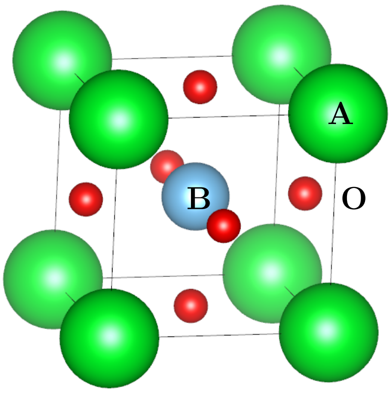

Figure 2.1.: Perovskite structure, with the different A and B sites. La, Sr and Ca are located on the A site and Mn is located on the B site. The B site is surrounded by an oxygen octahedron.

structure allows the growth of high crystalline quality LSMO/LCMO heterostructure on STO substrates.

Electronic Structure of Perovskites

Many phenomena of TMO perovskites can be explained by means of the crystal field splitting, changing the energetic ground state (compared to free TMO ions) in this material class and, therefore, altering the electronic interactions. Due to the crystal field of the oxygen octahedron, the degeneracy of the d orbitals is lifted, resulting in a splitting into two sub-levels separated by an energy gap of Δ. The sub-levels are the t_{2g} orbitals, with three fold degeneracy, and the e_g orbitals, with a two fold degeneracy. In an octahedral symmetry, the t_{2g} orbitals are lower in energy than the e_g orbitals (see **figure 2.2**).

In a distorted perovskite structure or with a strain induced lattice parameter change (see **section 2.4**), the degeneracy of the t_{2g} and e_g orbitals is further lifted. The t_{2g} orbitals are separated into degenerated d_{xz}, d_{yz} orbitals and a d_{xy} orbital. The e_g orbital is separated into one $d_{3z^2-r^2}$ orbital and one $d_{x^2-r^2}$ orbital. Depending on the symmetry of the distortion and the ratio of the out-of-plane lattice parameter a and the in-plane lattice parameter b, either the d_{xy} orbital or the d_{xz}, d_{yz} orbitals are lower in energy. For example, a ratio of $a/b < 1$ leads to a lowest d_{xy} orbital and the splitting presented in **figure 2.2**. Depending on the symmetry of the environment and the valance state of the B site cation, different orbitals are occupied, which has direct influence on the magnetic properties, described below.

In LSMO and LCMO the Mn atom is on the B site. It has an electronic configuration of $[\mathrm{Ar}]3d^5 4s^2$ and two possible valence states Mn^{3+} and Mn^{4+}, resulting in $[\mathrm{Ar}]3d^4$ or $[\mathrm{Ar}]3d^3$, respectively. In the tetragonal environment, one electron of Mn^{3+} has to be

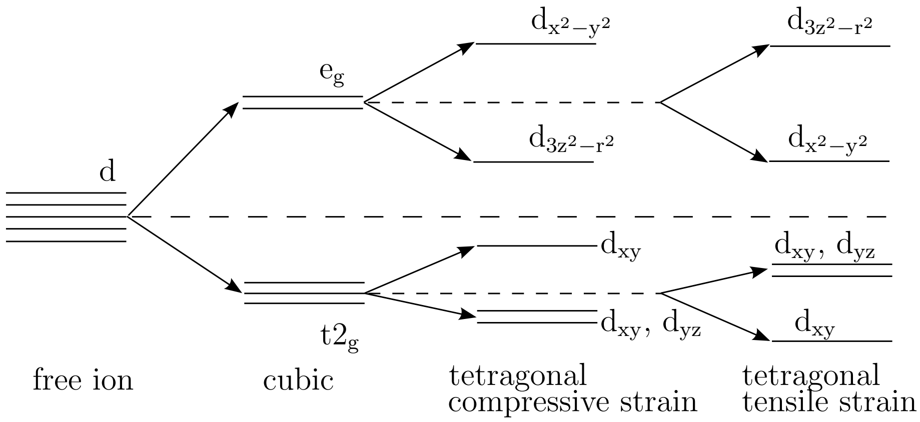

Figure 2.2.: Change of the energy levels of electrons in the *d* orbital due to different environments.

either in the d$_{3z^2-r^2}$ or in the d$_{x^2-r^2}$ orbital, depending on the ratio between out-of-plane and in-plane lattice parameter. This directly influences the possible bonds with adjacent atoms, which might play an important role for interface effects. Nevertheless, the possible orbital ordering and magnetic interactions are also directly influenced.

Magnetism in Strongly Correlated Electron Systems

The magnetism in TMO perovskites cannot be explained through the direct exchange between the magnetic ions, due to relatively localized 3d electrons and therefore negligible overlap of the involved orbitals. In these systems the magnetic ordering has to be explained through the superexchange and the double exchange interactions, which couple the magnetic manganese cations indirectly through the orbitals of the oxygen anions. Hopping processes, between the 3d orbitals of the manganese cations and the 2p orbitals of the oxygen anions, will lower the overall energy either for a ferromagnetic or an antiferromagnetic alignment [34, 15, 16, 17]. The derivation of the involved energies and the resulting magnetism can be described within the single band Hubbard model, provided that the hopping integral t and the Coulomb interaction U are known:

$$\hat{H}_{\text{Hubbard}} = -t \sum_{<i,j>,\sigma} \left(c^{\dagger}_{i,\sigma} c_{j,\sigma} + c^{\dagger}_{j,\sigma} c_{i,\sigma} \right) + U \sum_{i} n_{i,\uparrow} n_{i,\downarrow}, \tag{2.1}$$

where $\sigma = \downarrow, \uparrow$ is the spin orientation of the electron, $c_{i,\sigma}$,$c^{\dagger}_{i,\sigma}$ are annihilation and creation operators, respectively, for an electron at site i with spin σ and $n_{i,\sigma}$ is the number operator. Considering the ferromagnetic and antiferromagnetic cases separately, the resulting ground state energies can be calculated.

Superexchange

The superexchange is a “virtual” hopping process derived from second-order perturbation theory in the Hubbard model [35, 36]. The sign of the interaction strongly depends on

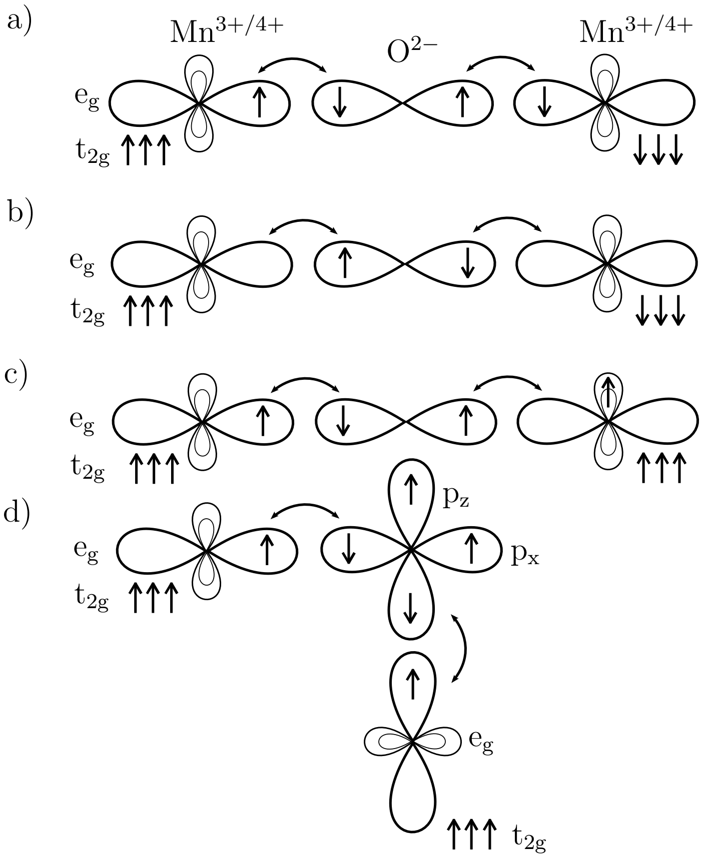

Figure 2.3.: Explanation for antiferromagnetic or ferromagnetic alignment of the Mn cations following the superexchange interaction, which is depending on the orbital occupation and the angle between the Mn orbitals (inspired by [37]).

the angle between involved orbitals and the occupancy thereof. This dependence can be summarized with the semi-empirical Goodenough-Kanamori rules [15, 16, 17]:

- 180° exchange between filled or empty cation orbitals is antiferromagnetic
- 180° exchange between filled and empty cation orbitals is ferromagnetic
- 90° exchange between filled cation orbitals is ferromagnetic

The superexchange depends on the exact alignment of the involved orbitals. For LSMO and LCMO perovskites four different alignments of the involving orbitals can be distinguished, which are presented in **figure 2.3**. The electrons inside the p orbitals of the oxygen atom are aligned antiparallel, but different orbital occupations for the Mn orbitals are possible. The occupation of the Mn orbitals depends on the oxidization state and the crystal structure. Three electrons occupy the t_{2g} orbitals for Mn^{3+}/Mn^{4+} and an octahedral symmetry. Mn^{3+} has one additional electron either in the $d_{3z^2-r^2}$ or the $d_{x^2-y^2}$ orbital. All electrons inside the t_{2g} and e_g orbitals are aligned parallel due to Hund's rule. The electrons from the p orbitals can jump to the e_g orbitals of the Mn atoms, but must fulfill Pauli's exclusion principle and Hund's rule for spin maximization. This leads to

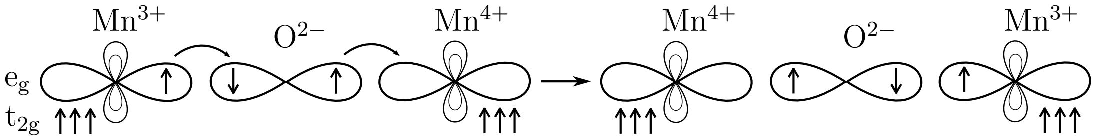

Figure 2.4.: Schematic explanation for ferromagnetic alignment of the Mn^{3+} and Mn^{4+} cations due to double exchange interaction (inspired by [37]).

the ferromagnetic and antiferromagnetic alignment presented in **figure 2.3** a-c) for an 180° angle between the Mn orbitals. The difference for an angle of 90° between the Mn atoms, presented in **figure 2.3** d), is the state of the oxygen p orbital. In the virtual state, where two electrons from different oxygen p orbitals (like p_x and p_z) jump to the e_g orbitals of different Mn atoms, the oxygen has two vacancies. In this virtual state, the energy minimum of the oxygen atom is for a parallel alignment of the left oxygen electrons following Hund's rule. This leads to the ferromagnetic alignment presented in **figure 2.3** d).

A simple hand-wavy argument for the ferromagnetic or antiferromagnetic alignment of Mn cations, is the increase of space, where the oxygen electrons can be located. Following the uncertainty principle $\Delta x \Delta p \geq \hbar/2$ and by delocalizing the oxygen electrons, the momentum can be lowered. This has direct influence on the possible lowest energy.

Double Exchange

The double exchange, in contrast to the superexchange, is a real hopping process of electrons from cations with different valence states. In the case of manganese perovskites Mn^{3+} and Mn^{4+} valence states are involved. An electron on either the first or the second Mn ion will have the same energy, resulting in real hopping processes and metallic behavior. Because of Hund's rule, a hopping of electrons between manganese ions comes together with a ferromagnetic alignment of these [38].

In the first step, one oxygen electron is transferred to the e_g orbital of the Mn^{4+} ion. Based on Hund's rule, the electron has to be aligned parallel to the spins of the electrons inside the t_{2g} orbital. In the second step, the electron in the e_g orbital of the Mn^{3+} ion can hop to the half filled oxygen orbital. This hopping process can only take place, when the Mn moments align ferromagnetically, as can be seen in **figure 2.4**, resulting in a lowering of the overall energy.

Magnetism in LSMO and LCMO

In strongly correlated electron systems, like LSMO and LCMO, both exchange interactions are present and compete with each other. Therefore, these compounds exhibit ferromagnetic or antiferromagnetic behavior depending on the stoichiometry (see **figure 2.5**). Following the explanation for superexchange and double exchange, the end members of LSMO and LCMO have to be aligned antiferromagnetic, because of same valence states of the Mn ions. As can be seen in **figure 2.5**, it's the case for the $SrMnO_3$ and $CaMnO_3$ end members on the right-hand-side of both phase diagrams. The other member is in both cases $LaMnO_3$, which should also be antiferromagnetic, but exhibits

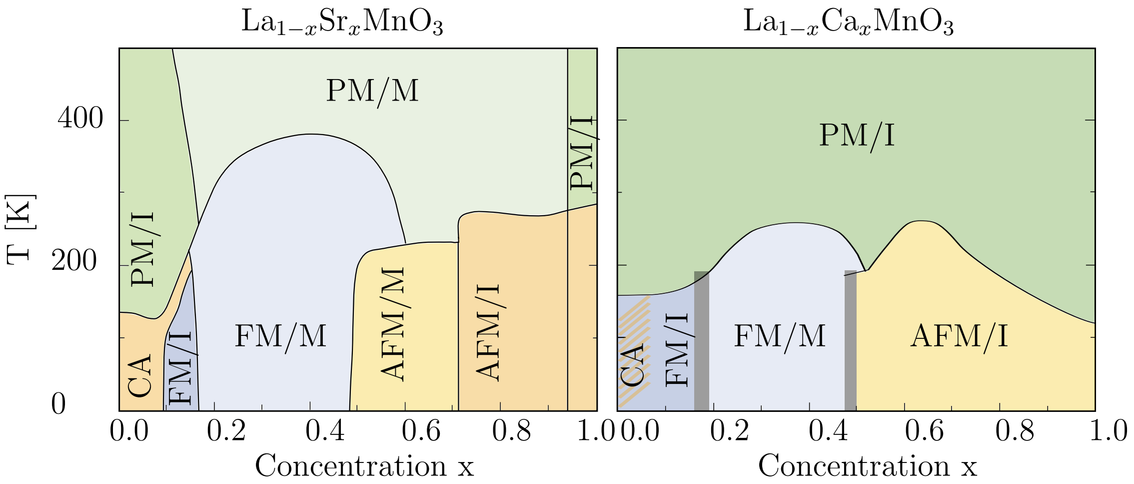

Figure 2.5.: LSMO and LCMO phase diagram inspired by [13, 14]. The magnetic phases are indicated as: paramagnetic (PM), canted antiferromagnetic (CA), antiferromagnetic (AFM) and ferromagnetic (FM). The electronic phases are given as: metallic (M) and insulating (I).

a weak ferromagnetism. The magnetism in $LaMnO_3$ cannot be explained alone through superexchange interaction, other mechanisms, like a canting of the oxygen octahedron, due to Dzyaloshinskii-Moriya interactions, have to be taken into account [39, 40], leading to a canted antiferromagnetic structure [41]. The Goodenough-Kanamori rules are only semiempirical and the field of strongly correlated electron systems is more complex.

Nevertheless, the mixed compounds are ferromagnetic in a concentration range of $0.1 < x < 0.5$, due to the double exchange interaction [38, 13, 14, 42]. In this ferromagnetic region, the LSMO and LCMO also exhibit metallic behavior, because of the double exchange, allowing real hopping processes. For a desired stoichiometry of $La_{0.7}Sr_{0.3}MnO_3$ and $La_{0.7}Ca_{0.3}MnO_3$, both materials show a Curie temperature of 380 K and 260 K, respectively. The band structure of LSMO is presented in the appendix. Based on the nearly same structure and lattice parameters, but different Curie temperatures, these systems are most suitable to investigate magnetic interface effects with polarized neutron reflectometry (**section 3.3**).

2.2. Ferromagnetism of Metals

The theory presented in this section is based on the textbook [43]. Information, which is not summarized in this chapter, can be read in more detail in the textbook mentioned above. The ferromagnetism in metals occurs due to the exchange interaction of free electrons and the consideration of the kinetic and potential energy. Due to the exchange interaction, electrons prefer to align parallel, resulting in a shift of electrons from the ↓-spin state to the ↑-spin state (see **figure 2.6**). Pauli's exclusion principle prohibits that two electrons with the same spin state occupy the same place, leading to the shift of electrons.

The reallocation of the density of states (DOS) will lead to an increase in kinetic energy

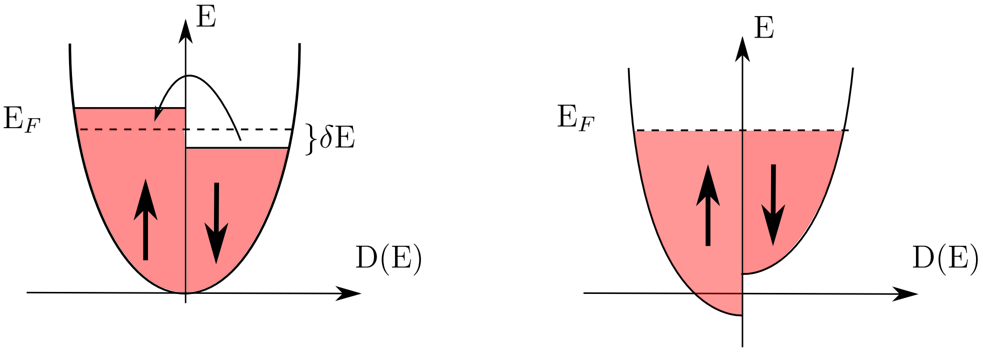

Figure 2.6.: Density of state in metals with reallocation of ↓-spin and ↑-spin states [44]
.

and a decrease in potential energy. Moving D(E)δE/2 spin-down electrons to the spin-up states, a gain in energy δE can be observed, which results in a kinetic energy change of:

$$\Delta E_{\mathrm{kin}} = \frac{1}{2} D(E_{\mathrm{F}})(\delta E)^2, \tag{2.2}$$

where $D(E_{\mathrm{F}})$ is the DOS at the Fermi energy E_{F}, δE is the change of the electron kinetic energy. In contrast to the increase in kinetic energy, the potential energy is reduced. With λM, as the molecular field, and the magnetization $M = \mu_{\mathrm{B}}(n_\uparrow - n_\downarrow)$, the energy gain is:

$$\Delta E_{\mathrm{pot}} = -\frac{1}{2}\mu_0 \lambda M^2 = -\frac{1}{2}\mu_0 \mu_{\mathrm{B}}^2 \lambda (n_\uparrow - n_\downarrow)^2, \tag{2.3}$$

with μ_0 as the magnetic permeability. Using $n_\uparrow = 1/2(n + D(E_{\mathrm{F}})\delta(E))$ and $n_\downarrow = 1/2(n - D(E_{\mathrm{F}})\delta(E))$, as the density of spin-up and spin-down states and $U = \mu_0 \mu_{\mathrm{B}}^2 \lambda$ as the Coulomb energy, will lead to:

$$\Delta E_{\mathrm{pot}} = -\frac{1}{2} U D(E_{\mathrm{F}})^2 \delta E^2. \tag{2.4}$$

Therefore, the total energy change is given by:

$$\Delta E = \Delta E_{\mathrm{kin}} + \Delta E_{\mathrm{pot}} = \frac{1}{2} D(E_{\mathrm{F}})(\delta E)^2 \left(1 - U D(E_{\mathrm{F}})\right). \tag{2.5}$$

Ferromagnetism requires a lowering of the ground state energy compared to the non-magnetic case. Then the term in the brackets has to be negative, resulting in the Stoner criterion for ferromagnetism:

$$U D(E_F) > 1. \tag{2.6}$$

This Stoner criterion is fulfilled for ferromagnetic metals Fe, Ni, Co and nearly fulfilled for other metals, like Pd and Pt (see **table 2.1**). The density of states at the Fermi level can be calculated, using density functional theory calculations, e.g. in the local spin density approximation or can be measured with photo electron spectroscopy. The Stoner

Elements	$D(E_F)$ [eV^{-1}]	U [eV]	$UD(E_F)$
Fe	3.08	0.46	1.43
Co	3.44	0.48	1.7
Ni	4.04	0.5	2.04
Pd	2.28	0.34	0.78
Pt	1.48	0.31	0.5

Table 2.1.: Presented is the density of states at the Fermi level $D(E_F)$, Stoner parameter U and the product of both for Fe, Co, Ni, Pd [45] and Pt [46]. Only Fe, Co and Ni are fulfilling the Stoner criterion for ferromagnetism.

parameter is a measure of the Coulomb repulsion of the electrons in the same orbital and can also be determined using density functional theory calculations. The band structures and DOS are presented in **appendix C**. Increasing the density of states at the Fermi energy, for instance by hybridizing the orbitals, the Stoner criterion can be fulfilled. This will result also in ferromagnetism in Pd or Pt. The hybridization will shift the Pd states at the Fermi level to the position of the Fe *d* orbitals.

2.3. Growth Modes

Before the interface effects in heterostructures will be discussed in the next section, different growth modes of heterogeneous films on a substrate while growing with physical vapor deposition techniques, as well as the involved atomic processes need to be discussed. The field of film growth is very complex and it is difficult to unify all growth processes and the dependence of the involved parameters, like substrate temperature, growth rate and base pressure. Thus, only a simplified model will be presented, following the paper [48].

During the growth of a film, single atoms are deposited on the surface of the underlying film and create adatoms, which are either re-evaporated again or can diffuse over the surface. The adsorbtion energy E_a and the diffusion energy E_d are related to the adsorbtion and the diffusion, respectively. The adatom stays for the adsorbtion residence time τ_a on

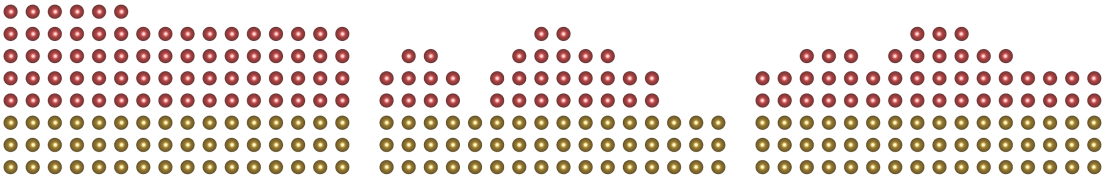

Figure 2.7.: On the left-hand side is the Frank-van der Merve growth mode, in the middle the Volmer-Weber growth mode and on the right-hand side the Stranski-Krastanow growth mode (inspired by [47]).

the surface.

$$\tau_\mathrm{a} = \nu_\mathrm{a} e^{-E_\mathrm{a}/k_\mathrm{B}T}, \tag{2.7}$$

with ν_a the atomic vibration frequency ($\nu_\mathrm{a} \sim 1 - 10$ THz), k_B the Boltzmann constant and T the temperature of the vapor source. During this time, the adatom can diffuse with the diffusion constant D:

$$D = \frac{\nu_\mathrm{d} a^2}{4} e^{-E_\mathrm{d}/k_\mathrm{B}T}, \tag{2.8}$$

where a is the jump distance and ν_d is the diffusion frequency ($\nu_\mathrm{d} < \nu_\mathrm{a}$). The average displacement of the adatom in τ_a can be therefore calculated to:

$$x = a \left(\frac{\nu_\mathrm{d}}{\nu_\mathrm{a}} \right)^{1/2} e^{\frac{E_\mathrm{a} - E_\mathrm{d}}{2k_\mathrm{B}T}}. \tag{2.9}$$

Single adatoms will diffuse over the film surface and try to reduce the surface energy by creating clusters (nucleation) or bonds at already existing edges (step capture). Depending on the surface energy, three different growth modes can be distinguished [47]:

Frank-van der Merve: This growth mode is a layer-by-layer growth mode, where adatoms preferably attach to edge sides, resulting in a smooth and homogeneous layer. During this growth mode RHEED oscillations can be seen [49]. This growth mode is the preferred growth mode, due to the resulting smooth surfaces, which is needed to investigate interface effects with X-ray reflectometry (XRR) and polarized neutron reflectometry (PNR).

Volmer-Weber: This growth mode is an island growth mode, where the adatoms preferably form clusters. The clusters grow separately from each other, resulting in a three dimensional island growth and therefore in rough surfaces.

Stranski-Krastanov: This growth mode is a combination of the Frank-van der Merve and the Volmer-Weber growth modes. At the beginning, the film grows in the Frank-van der Merve growth mode, but after a critical thickness h_c it starts to grow in the Volmer-Weber growth mode, also resulting in rough surfaces.

When depositing material A on a film of material B with involved surface energies of γ_A and γ_B, respectively, the different growth modes can be determined by comparing the related surface energies. If $\gamma_\mathrm{B} < \gamma_\mathrm{A}$, then the preferred growth mode is the Volmer-Weber growth mode, because of an increase of surface energy during the growth of material A. If $\gamma_\mathrm{A} + \gamma^* < \gamma_\mathrm{B}$, where γ^* is the effective interfacial energy, then a reduction of the surface energy can be achieved, when growing in the Frank-van der Merve growth mode. An increase in interfacial energy γ^*, due to dislocations in material A, might result in an increase of the sum of the interfacial energy and the surface energy of material A. This might lead to the case that the sum becomes larger than the surface energy of material B, $\gamma_\mathrm{A} + \gamma^* > \gamma_\mathrm{B}$. This will result in a Stranski-Krastanov growth mode, where the first atom layers are homogeneous, but continues to grow in an island-like manner after the critical thickness h_c.

These different growth modes play a crucial role in the growth of different materials, like a metal on an oxide surface. The different surface energies might prefer either the Frank-van der Merve or the Volmer-Weber growth mode. It could be shown [50] that Au grows on a TiO_2 surface in the Stranski-Krastanov growth mode, but with a critical thickness of one monolayer $h_c = 1$ monolayer. While growing Pd on a MgO substrate [51], the Pd grows over a wide temperature range 200-800 K in the Volmer-Weber growth mode. Depending on the growth mode, the substrate temperature, during Pd growth, has to be maximized or minimized to yield smooth surfaces (see **section 5.4**), but also to increase the crystalline quality.

2.4. Interface Effects

Interface effects unite all effects that occur directly at the interface between two different materials. Therefore, interface effects are very complex and the underlying physical behaviors might be very different [52]. Due to e.g. strain, charge transfer, interdiffusion, orbital ordering and symmetry breaking at the interface, many different effects can take place. The most commonly known interface effect is a p-n diode, where an n-doped semiconductor is in contact with a p-doped semiconductor. Depending on the applied voltage, the diode is either conductive or insulating. However, at interfaces many other effects are present: two insulating materials might form a conducting layer [53]; two antiferromagnets can be ferromagnetic at the interface [54]; a paramagnetic material can become ferromagnetic due to the interface with a ferromagnet [9] or an electric polarization can be induced [55]. Utilizing these effects one can say in the words of Herbert Kroemer: “The interface is the device”.

This thesis will focus on the magnetic interface effects occurring mostly due to strain and charge effects, like hybridization, though, other mechanism’s might be possible. These effects will be discussed in the following, but with a mean focus on the systems used in this thesis.

Strain

The most obvious interface effect in thin films is strain at the interface. Due to different lattice parameters of films with a common interface, the film becomes strained or relaxed. In first approximation the unit cell keeps the same volume resulting in a change of the out-of-plane lattice parameter. This will distort the e.g. pseudo cubic perovskite structure to a tetragonal structure with changed bonding lengths and angles of the $Mn - O - Mn$ chain [56, 57], as well as the occupation of the orbitals (see **figure 2.2** in **section 2.1**). With compressive in-plane strain the out-off-plane lattice parameter will increase leading to an energy lowering of the $\mathrm{d}_{3z^2-r^2}$, d_{xz}, d_{yz} orbitals and an energy increase of the $\mathrm{d}_{x^2-r^2}$, d_{xy} orbitals. For tensile strain this behavior is inversed. With these induced distortions, the superexchange and double exchange interaction will be altered, changing the magnetic ground state and e.g. the Curie temperature [58, 59].

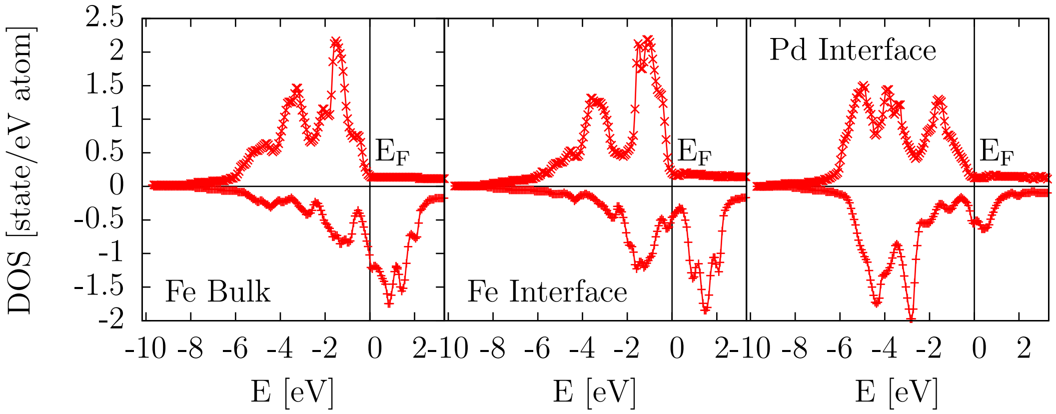

Figure 2.8.: The density of states for bulk Fe (left), Fe at interface to Pd (middle) and magnetically polarized Pd due to an interface with Fe (right) (inspired by [62]).

$La_{0.5}Sr_{0.5}MnO_3$, which is at the edge between ferromagnetism and antiferromagnetism can be tuned to one side or the other by changing slightly the stoichiometry [13]. This change of the magnetic ground state can also be induced through strain, caused by an interface [18]. In contrast to the LSMO film, the $La_{0.5}Ca_{0.5}MnO_3$ shows, over a wide strain range, antiferromagnetic behavior [60]. The difference between LSMO and LCMO was attributed to a narrower-bandwidth in LCMO, resulting in a different ground state.

In LSMO/LCMO multilayers, the strain should have some effect, because of the slightly different lattice parameters, additionally to the induced strain from the substrate. Normally, strain reduces the magnetic moment inside these films and relaxes after a critical thickness [58, 59].

Another strain effect might be induced ferroelectric behavior in perovskites. A strained STO film, already at the edge of ferroelectric behavior, can exhibit ferroelectricity [61, 55]. Depending on the type of strain, tensile or compressive, STO can have a net polarization in out-of-plain or in in-plain direction, respectively.

Charge effects

Another aspect, important at interfaces, are charge effects, like charge transfer or hybridization. Due to the interface alone, the symmetry at the interface is broken, and the atoms at the interface will have different bonds compared to bulk atoms.

At the interface of $La_{0.5}Sr_{0.5}MnO_3/BaTiO_3$, the ferroelectric polarization of BTO leads to a change of the Mn valance state in the LSMO layer. This changes the magnetization in the first unit cell depending on the ferroelectric polarization inside the BTO layer between ferromagnetism and antiferromagnetism. At the interface of $La_{0.67}Sr_{0.33}MnO_3/BaTiO_3$, the magnitude of the LSMO magnetization depends on the electric polarization of the BTO layer due to electrostatic doping [63].

In contrast to the charge effects in perovskite related heterostructures, charge effects are also important at the metal/metal interface. In **section 2.2**, the magnetism in metals was explained with the Stoner model for ferromagnetism. In this model, metals are ferromagnetic, when they fulfill the Stoner criterion for ferromagnetism $UD(E_F) \geq 1$, with U the exchange interaction and $D(E_\mathrm{F})$ the density of states at the Fermi energy. As already mentioned, only Fe, Ni and Co fulfill the Stoner criterion for ferromagnetism, but Pd has a high Stoner parameter of $U = 0.78$ and is at the edge to become ferromagnetic. Increasing the density of states at the Fermi level for Pd will lead to ferromagnetism. This can be accomplished by a charge transfer and a hybridization of the Fe 3d orbitals with the Pd 4d orbitals in Pd/Fe alloys [11, 12] or at interfaces of Pd/Fe heterostructures [9]. By hybridization, the spin-up states of Pd are shifted to lower energy and the spin-down states of Pd are shifted to higher energy. In this way, the maxima in the Fe DOS and Pd DOS overlap in energy, resulting in a ferromagnetic Pd interface (see **figure 2.8**). Additionally, the Fe DOS at the interface are modified by the hybridization increasing the magnetic moment of Fe.

The hybridization of the Pd 4d orbitals might also occur at the LSMO interface with the 3d orbitals of Mn. This might lead to ferromagnetism in Pd at the Pd/LSMO interface, as it was shown in a $\mathrm{La_{0.7}Ca_{0.3-\mathit{x}}Sr_\mathit{x}MnO_3}$ framework in contact to Pd [20] with a magnetic moment of about 0.6 μ_B per Pd atom. The magnetically polarized Pd was deduced from an increase of the magnetic moment in field cooled measurements. The double exchange and superexchange might also play a crucial role for this interface effect. It was shown theoretically that in contact with semiconductors like ZnS [22] or CdS [23], Pd should become ferromagnetic due to a strong coupling chain allowing the double exchange interaction.

Contradicting results are being reported for a charge transfer into a nonmagnetic Pt layer, which behaves similar to Pd, with interfaces to an insulating $\mathrm{Y_3Fe_5O_{12}}$ layer, resulting in ferromagnetism. Lu et al. [64] suggested that a 1.5 nm Pt layer becomes ferromagnetic at the interface to a $\mathrm{Y_3Fe_5O_{12}}$ layer with an average magnetic moment of 0.054 μ_B at 300°C, but this phenomenon is still under investigation. Geprägs et al. [65] showed that the upper limit of the Pt magnetization at the interface to a $\mathrm{Y_3Fe_5O_{12}}$ layer is around 0.003 μ_B. The differences could be explained through an intermixing of the $\mathrm{Y_3Fe_5O_{12}}$ and the Pt layer, resulting in a different oxidization state of the Pt layer [66]. A nonmagnetic Pt interface is most plausible when no intermixing occurs.

Although this is just a short overview of possible interface effects, it is evident that this field is very large and many different interface effects are present. Especially, the attribution of one effect to a specific mechanism is very difficult and additional work has to be carried out.

3. Scattering Theory

Scattering techniques are used to investigate thin film properties, because of the possibility to probe nuclear and magnetic depth profiles non-destructively. The scattering theory can be read in many good textbooks like [44, 67]. Here only the most important aspects will be presented without derivation.

3.1. Basic Scattering

Scattering experiments are carried out to investigate the scattering potential $V(\vec{r'})$, describing the interaction of the sample with the probing particle. The derivation of the scattering theory is done in the wave frame and mostly in the Fraunhofer approximation, where the incoming waves can be described as plane waves $\Psi(\vec{r}) = \Psi_0 e^{i\vec{k_i}\vec{r}}$, with wave vector $\vec{k_i}$. These plane waves interact with the scattering potential $V(\vec{r'})$ of the sample and create spherical waves $\Psi(\vec{r'}) = \Psi_0' e^{i\vec{k_f}\vec{r}} V(\vec{r'})/(4\pi|\vec{r} - \vec{r'}|)$ at all sample positions. The amplitude and phase of the spherical waves depends on the complex scattering potential $V(\vec{r'})$ and the interference of all spherical waves will create the scattered wave.

The exact interaction of the scattering potential and the probing particle is described through the stationary Schrödinger equation for elastic scattering, as a starting point for neutrons and electrons, and the Maxwell equations, for photons. In the case of single

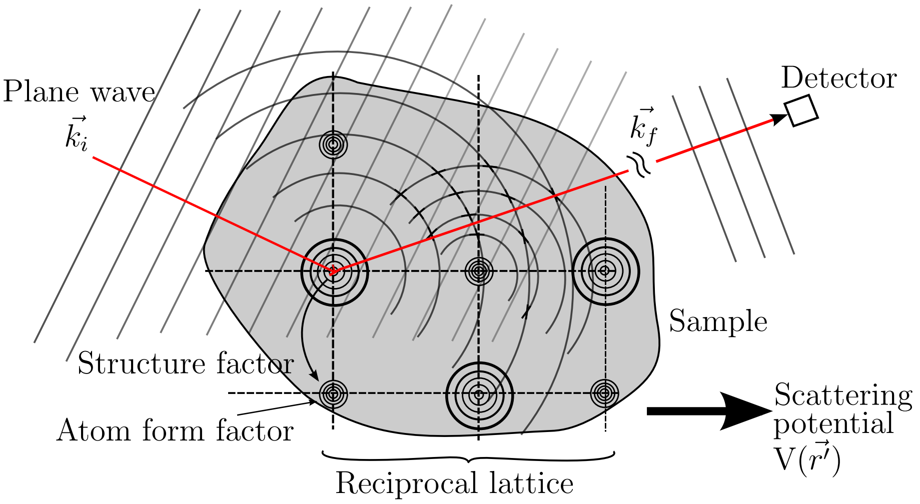

Figure 3.1.: Scattering geometry with scattering potential $V(\vec{r'})$, incident wave vector $\vec{k_i}$ and scattered wave vector $\vec{k_f}$.

.

scattering, which is valid for a weak interaction potential, the resulting wave function after scattering, in the Born approximation, can be described by:

$$\Psi^1(\vec{r}) = e^{i\vec{k_i}\cdot\vec{r}} + \Psi_0 \int \frac{e^{ik_i\left|\vec{r}-\vec{r'}\right|}}{4\pi\left|\vec{r}-\vec{r'}\right|} V(\vec{r'}) e^{i\vec{k_i}\cdot\vec{r'}} \mathrm{d}^3r', \tag{3.1}$$

where the scaling constant is either $\Psi_0 = 2m_n/\hbar^2$ for neutrons or $\Psi_0 = 1$ for X-rays. In the Fraunhofer approximation, where $|\vec{r}-\vec{r'}| \gg |\vec{r'}|$, this equation can be further simplified, using $\vec{R} = \vec{r} - \vec{r'}$ and $\vec{Q} = \vec{k_f} - \vec{k_i}$, as the scattering vector, to yield:

$$\Psi^1(\vec{R}) = e^{i\vec{k_i}\cdot\vec{R}} + \Psi_0 \frac{e^{ik_iR}}{4\pi R} \int V(\vec{r'}) e^{i\vec{Q}\cdot\vec{r'}} \mathrm{d}^3r' = e^{i\vec{k_i}\cdot\vec{R}} + A(\vec{Q})\frac{e^{ik_i|R|}}{R}, \tag{3.2}$$

$$\text{with} \quad A(\vec{Q}) = \frac{\Psi_0}{4\pi} \int V(\vec{r'}) e^{i\vec{Q}\vec{r'}} \mathrm{d}^3r', \tag{3.3}$$

From this scattering function, the differential cross section $\frac{d\sigma}{d\Omega}$ can be determined as

$$\frac{d\sigma}{d\Omega} \sim \left|A(\vec{Q})\right|^2, \tag{3.4}$$

which describes the scattered intensity at a given angle normalized to the incident beam intensity and the sample area covered by the beam. It is evident that the phase information of the scattered wave is lost in a scattering experiment. Because of this, a direct Fourier transformation $\mathscr{F}$, to get the scattering potential, is impossible. In order to get information about the scattering potential a comparison between measured scattering intensities and calculated intensities is necessary and is done by applying a model for the scattering potential and calculating the resulting scattering intensities.

Bragg Scattering

The scattering from a crystal structure can be described with Bragg scattering. The scattering potential used in **equation 3.1** is a convolution of the scattering potential of the periodic lattice g with the basis b (position of atoms in the unit cell) and each atom ρ_A^j. As can be seen in **equation 3.3**, the scattering amplitude is a Fourier transformation $\mathscr{F}$ of the scattering potential. With the convolution theorem, the scattering amplitude can be separated easily into the following terms:

$$A(\vec{Q}) = \mathscr{F}(V(\vec{r})) = \mathscr{F}(g \otimes \rho_B) = \mathscr{F}(g \otimes b \otimes \sum_j \rho_A^j) = \mathscr{F}(g) \cdot \mathscr{F}(b) \cdot \mathscr{F}(\sum_j \rho_A^j), \tag{3.5}$$

where g is the lattice function and ρ_B is the scattering potential of the unit cell, which can be further separated into the basis b and the atom scattering potential of the j-th atom ρ_A^j in the given basis. The Fourier transformation of these scattering potentials are the reciprocal lattice, the structure factor and the atomic form factor, respectively. The structure factor $S_{\tilde{\mathrm{G}}}$, describing the coherent interferences of the basis, with $\vec{G}$ as reciprocal lattice vector, can be expressed by:

$$S_{\tilde{\mathrm{G}}} = \mathscr{F}(\rho_B) = \sum_j e^{-i\vec{G}\cdot\vec{r}} \cdot \int_{\mathrm{Atom}} \rho_{\mathrm{A}}^j(\vec{r'}) e^{-i\vec{G}\cdot\vec{r'}} \mathrm{d}^3 r' = \sum_j f_j e^{-i\vec{G}\cdot\vec{r}} \quad \text{with} \tag{3.6}$$

$$f_j = \int_{\mathrm{Atom}} \rho_{\mathrm{A}}^j(\vec{r'}) e^{-i\vec{G}\cdot\vec{r'}} \mathrm{d}^3 r', \tag{3.7}$$

describing the amplitude of the scattered wave function and, therefore, the measured intensities in reciprocal space. For a perovskite like STO, which is described in **section 2.1**, the structure factor is given by:

$$\begin{aligned} S_G(h,k,l) &= f_{\mathrm{Sr}} + f_{\mathrm{Ti}} e^{2\pi i(h/2+k/2+l/2)} + f_{\mathrm{O}} \left(e^{2\pi i(h/2+k/2)} + e^{2\pi i(h/2+l/2)} + e^{2\pi i(k/2+l/2)} \right) \\ &= f_{\mathrm{Sr}} + f_{\mathrm{Ti}}(-1)^{h+k+l} + f_{\mathrm{O}} \left[(-1)^{h+k} + (-1)^{h+l} + (-1)^{k+l} \right]. \end{aligned} \tag{3.8}$$

As can be seen in **equation 3.8** the cubic perovskite STO has for all indexes h, k, l a non-zero structure factor. Only the intensity varies with different combinations of h, k, l. The films LSMO and LCMO have a more complex structure factor due to the mixing on the A site, which results in slightly different Bragg peak intensities. For a whole structure analysis many Bragg peaks have to be investigated with absolute intensities, which is nearly impossible for thin films. The substrate will limit the access to many Bragg peaks, because of the large absorption of the substrate.

Small Incident Angle Scattering - Reflectometry

In reflectometry measurements the scattering vector $\vec{Q} = \vec{k}_f - \vec{k}_i$ is close to zero (up to $1\ \mathrm{\AA}^{-1}$), resulting in nearly no sensitivity to the atomic structure (Bragg scattering from atom planes is not visible). Only the interfaces between homogeneous layers with different scattering potentials are visible. Parratt derived in 1954 [68] the recursive formula to calculate the reflection of N homogeneous media, by giving a formula for the ratio $R_{n-1,n}$ of the amplitude for the incoming and scattered wave function (E_n^R and E_n) in the n-th medium

$$R_{n-1,n} = a_{n-1}^2 (E_{n-1}^R / E_{n-1}) = a_{n-1}^4 \left[\frac{R_{n,n+1} + F_{n-1,n}}{R_{n,n+1} F_{n-1,n} + 1} \right], \tag{3.9}$$

$$F_{n-1,n} = \frac{k_{n-1,z} - k_{n,z}}{k_{n-1,z} + k_{n,z}} \qquad a_n = e^{-ik_{n,z}\frac{d_n}{2}}, \tag{3.10}$$

with $k_{n,z}$ as the z component of the beam wave vector. The Fresnel coefficient $F_{n-1,n}$ describes the partial reflexion at a potential barrier, which is in this case the interface between adjacent layers. The recursion starts at the bottom layer N, which is assumed to be a half infinite substrate layer, where no reflection from a lower layer is present, resulting in $R_{N,N+1} = 0$. Recursively using **equation 3.9** all quotients $R_{n,n+1}$ can be calculated up to $R_{1,2} = E_1^R / E_1$ with $E_1 = 1$ and $a_1 = 1$, leading to the measured amplitude $E_1^R = R_{1,2} E_1$.

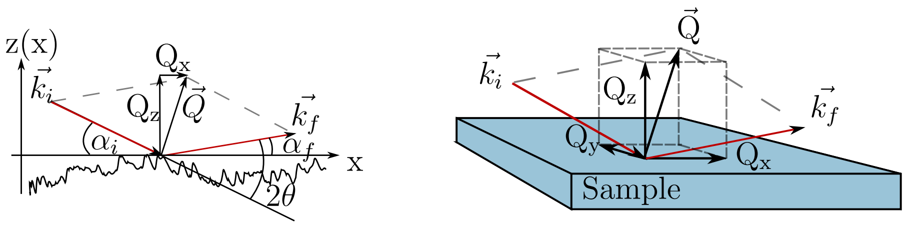

Figure 3.2.: Geometry of a reflectometry experiment with incident (outgoing) angle α_i (α_f), incident (outgoing) wave vector k_i (k_f), scattering vector $\vec{Q}$ and the x-, y- and z-component of the scattering vector $Q_{x,y,z}$.

In the formula derived by Parratt ideal layers without roughness are assumed, but can be included with the following model of fractal surfaces. For simplicity it is shown for one layer with a rough surface. It is possible to transform **equation 3.1** from the volume integral into an integral over the layer surface by using the divergence theorem for small incident angle scattering. After a lengthy calculation [69], it is possible to separate the specular scattering from the off-specular scattering:

$$\frac{d\sigma}{d\Omega} = \left(\frac{d\sigma}{d\Omega}\right)_{\text{spec}} + \left(\frac{d\sigma}{d\Omega}\right)_{\text{off-spec}}; \tag{3.11}$$

$$\left(\frac{d\sigma}{d\Omega}\right)_{\text{spec}} = \frac{4\pi^2\rho^2 b^2}{Q_\mathrm{z}^2} e^{-Q_\mathrm{z}^2\sigma'^2}\delta(Q_x)\delta(Q_y); \tag{3.12}$$

$$\left(\frac{d\sigma}{d\Omega}\right)_{\text{off-spec}} = \frac{4\pi^2\rho^2 b^2}{Q_\mathrm{z}^2} e^{-Q_\mathrm{z}^2\sigma'^2} \int R\left(e^{Q_\mathrm{z}^2\sigma'^2 e^{-(R/\xi)^{2h}}} - 1\right) J(Q_\mathrm{r}, R)\mathrm{d}R; \tag{3.13}$$

$$J(Q_\mathrm{r}, R) = e^{-i(Q_\mathrm{x}^2+Q_\mathrm{y}^2)^{1/2}R} = e^{-iQ_\mathrm{r}R}, \tag{3.14}$$

where ρ is the sample density, b is the scattering length, σ' is the surface roughness, ξ is the correlation length, h is the fractal parameter, Q_x, Q_y and Q_z are the scattering vectors in x, y and z direction, respectively, where x and y are in-plane and z is out-of-plane (**figure 3.2**).

The difference here compared to scattering without off-specular scattering is the damping factor $e^{-Q_\mathrm{z}^2\sigma'^2}$ in the specular scattering, due to the off-specular scattering and the roughness. In this model of fractal surfaces, the off-specular scattering depends on the in-plane correlation length ξ and the fractal parameter h, describing the texture of the roughness. The most important result is the overlap of the specular and off-specular scattering at $Q_\mathrm{x} = 0$ and $Q_\mathrm{y} = 0$. Because of this overlap, it is necessary to subtract the off-specular scattering from the measured reflectivity to get the right roughness parameter σ'.

To introduce roughness between layers in the recursive formula derived by Parratt, it is necessary to expand the Fresnel coefficient in **equation 3.10** with the damping factor $e^{-Q_z^2\sigma'^2}$.

3.2. X-ray Scattering

In a chemical description electromagnetic waves, which can be considered as perpendicular oscillating electric and magnetic fields, accelerate the electrons. These oscillating electrons will emit secondary radiation. The scattering can be described by Thomson scattering in the case of free electrons:

$$\frac{d\sigma}{d\Omega}_{Thomson} = \frac{r_e^2}{2}(1 - cos^2(2\theta)), \tag{3.15}$$

$$r_{\mathrm{e}} = \frac{1}{4\pi\epsilon_0}\frac{e^2}{m_{\mathrm{e}}c^2} \sim 2.82 \cdot 10^{-13}\mathrm{cm}, \tag{3.16}$$

where r_{e} is the electron radius, m_{e} is the electron mass, e is the electron charge, c is the speed of light, ϵ_0 is the vacuum permittivity and 2θ is the scattering angle. Thomson scattering depends on the atomic form factor $f_{\mathrm{a}}(\vec{Q})$, due to an extended electron cloud. The atomic form factor is proportional to the total number of electrons in forward scattering direction $f_a(Q = 0) = Z$ and decays with increasing magnitude Q of the scattering vector $\vec{Q}$.

$$f_{\mathrm{a}}(\vec{Q}) = \int \mathrm{d}^3r'\rho(\vec{r'})e^{i\vec{Q}\vec{r'}}, \tag{3.17}$$

where $\vec{r}$ is the vector from the atom center to all positions in the integration range and $\rho(\vec{r})$ is the charge density. In addition to Thomson scattering, an absorption of photons can take place, which can be described with the absorption cross section σ_x,

$$\sigma_x = \frac{\Gamma_{i\to f}}{I_{ph}}, \tag{3.18}$$

where $\Gamma_{i\to f}$ is the number of excited electrons from the initial state i to the final state f in unit time and I_{ph} is the photon flux. The absorption process of a photon beam measures the free density of states above the Fermi level. It follows the dipole selection rules:

$$\Delta j = 0, \pm, 1 \quad \Delta s = 0 \quad \Delta l = \pm 1 \quad \Delta m = 0, \pm 1, \tag{3.19}$$

with j, s, l, m as the total angular momentum, spin, orbital and magnetic quantum numbers. $\Delta m = 0$ holds for linearly polarized light, while $\Delta m = \pm 1$ holds for circular polarized light, which is important for X-ray magnetic circular dichroism (XMCD).

X-ray Magnetic Circular Dichroism (XMCD)

The absorption process of X-rays can be used to probe the element specific magnetic properties (**figure 3.4**) in an XMCD experiment, when the sample is ferromagnetic. A sketch of the XMCD experiment is shown in **figure 3.3**, where left or right circular polarized light is directed on the sample. The XMCD experiment can be done in two ways: either by measuring the absorption of the beam intensity after the sample or by

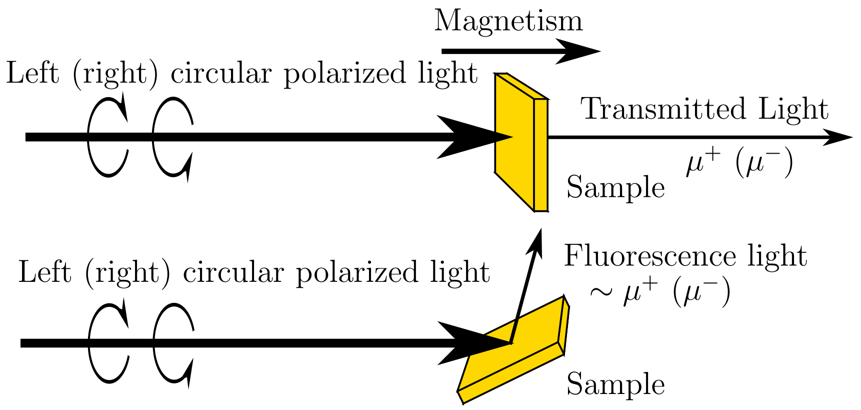

Figure 3.3.: Sketch of an XMCD experiment. Left or right circular polarized light is emitted on the sample and either the beam absorption coefficient is determined by measureing the beam intensity after the sample or the fluorescence light is measured, which is proportional to the absorption coefficient.

measuring the fluorescence signal coming from the sample. The fluorescence signal is proportional to the absorption coefficient but has to be normalized. The XMCD signal is measured at specific absorption edges for different beam energies. The absorption cross section, at specific edges, depends on the helicity of the X-rays and on the magnetism inside the sample. Therefore, the XMCD is defined as the difference in the absorption cross sections:

$$\Delta\mu(E) = \mu^+(E) - \mu^-(E), \tag{3.20}$$

with $\mu^\pm$ the absorption cross section for left and right circular polarized light. The average of the absorption cross sections for left and right circular polarized light is the isotropic XAS:

$$\mu(E) = \frac{1}{2}(\mu^+(E) + \mu^-(E)) \tag{3.21}$$

The XMCD signal can be measured at different edges, but the strongest XMCD signal is mostly present at the L-edges, like in the case of the transition metals Fe and Pd. A simple two step model [70] can be used to describe these differences in the absorption cross section. In the first step, circular polarized light excites electrons from the $L_{2,3}$ edges. These electrons are largely spin polarized [71] due to the spin-obit-coupling. At the L_3 edge the spin polarization is $P = \pm 0.25$ for left and right circular polarized light respectively, whereas at the L_2 edge the spin polarization is $P = \pm 0.5$ [70].

In the second step the empty states in the d band act as a spin sensitive "detector" following the dipole selection rules (see **figure 3.4**). Assuming an imbalance of the spin-up and spin-down states, the absorption cross section for left and right circular polarized light will be enhanced or reduced with respect to the used X-ray polarization. Thole [73] and Carra [74] have derived for these differences in absorption cross section sum rules for

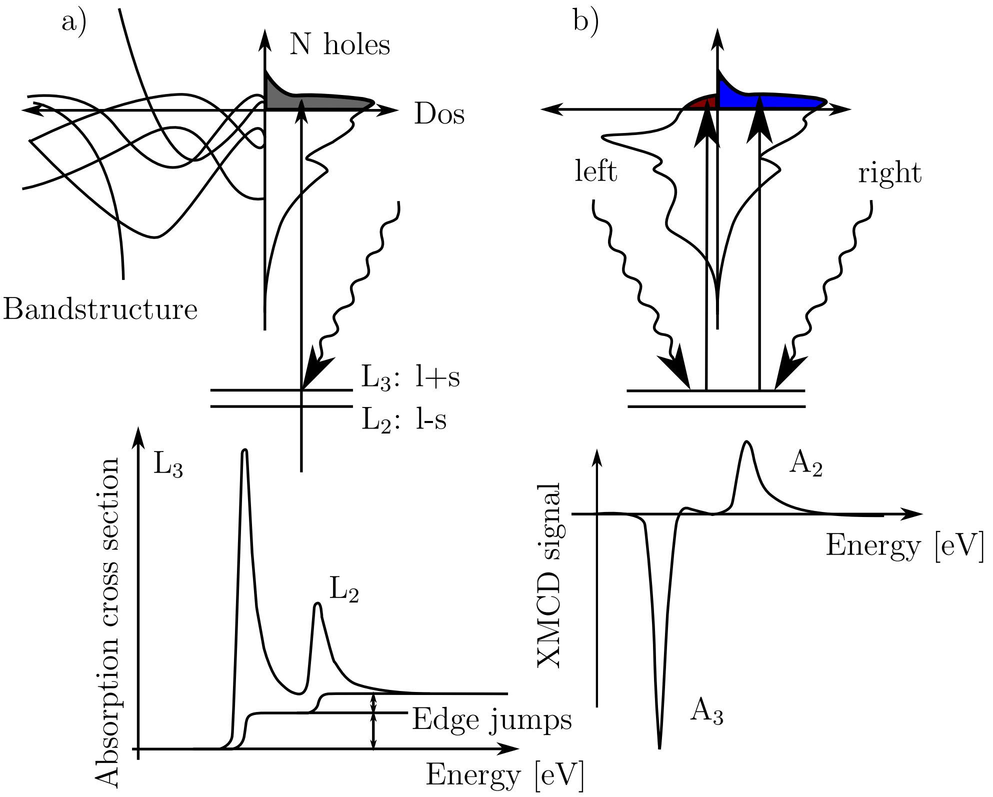

Figure 3.4.: a) The absorption cross section measures the density of states above the Fermi level. The step-like function of the absorption cross section is shown, with a ratio of 2:1, for the edge jumps at the L$_{2,3}$ edge. b) XMCD measurement with left and right polarized light probe the spin and orbital moment (inspired by [72]).

the orbital quantum number and the spin quantum number:

$$\frac{\int_{j^+ + j^-} dE(\mu^+ - \mu^-)}{\int_{j^+ + j^-} dE(\mu^+ + \mu^- + \mu^0)} = \frac{1}{2}\frac{l(l+1) + 2 - c(c+1)}{l(l+1)(4l+2-n)} \langle L_\mathrm{z} \rangle \tag{3.22}$$

$$\frac{\int_j^+ dE(\mu^+ - \mu^-) - [(c+1)/c] \int_j^- dE(\mu^+ - \mu^-)}{\int_{j^+ + j^-} dE(\mu^+ + \mu^- + \mu^0)} = \frac{l(l+1) - 2 - c(c+1)}{3c(4l+2-n)} \langle S_\mathrm{z} \rangle + \tag{3.23}$$

$$\frac{l(l+1)[l(l+1) + 2c(c+1) + 4] - 3(c-1)^2(c+2)^2}{6lc(l+1)(4l+2-n)} \langle T_\mathrm{z} \rangle \,, \tag{3.24}$$

with $\mu^{\pm,0}$ the absorption coefficient for left, right and linearly polarized light, $j^{\pm}$ the integration over the two involved edges, c the orbital quantum number of the initial state and l the orbital quantum number of the final state. $\langle L_\mathrm{z} \rangle$, $\langle S_\mathrm{z} \rangle$ and $\langle T_\mathrm{z} \rangle$ are the z-projections of the expectation values of the orbital operator, the spin operator, and the magnetic dipole operator, respectively. These formulas can be further simplified considering a specific edge, like the L$_{2,3}$ edge, with the transition $2p \rightarrow 4d$ resulting in $c = 1$, $l = 2$. Additionally, it is possible to define the number of holes to $n_h = 4l + 2 - n$ and neglecting the $\langle T_\mathrm{z} \rangle$ term, which is in metals sufficiently quenched [75, 70]. Furthermore, the μ^0 term of the linearly polarized light and the transition $p \rightarrow s$, which is additionally allowed by the dipole selection rules, can be neglected [76]. In the last process the integration over the edges can be defined with:

$$\Delta A_i = \int_{L_i} dE \Delta\mu \tag{3.25}$$

$$A_i = \int_{L_i} dE \left(\frac{1}{2}(\mu^+ + \mu^-) - \mu_\mathrm{step} \right), \tag{3.26}$$

where μ_step is the transition into the continuum, which has to be subtracted for the integration over the energy region at the edges. The formula is therefore an integral over the whole absorption spectrum at the $\mathrm{L}_{2,3}$ edges. The transition into the continuum can be simulated by two step-like functions, which are convoluted with a Voigt function for resolution considerations. With these assumptions and simplifications, **equations 3.22**, and **3.23** are as follows:

$$\langle L_\mathrm{z} \rangle = 2 \frac{\Delta A_3 + \Delta A_2}{A_3 + A_2} n_h \tag{3.27}$$

$$\langle S_\mathrm{z} \rangle = \frac{3}{2} \frac{\Delta A_3 - 2\Delta A_2}{A_3 + A_2} n_h \tag{3.28}$$

Knowing the number of holes, which are proportional to the isotropic XAS, and measuring the absorption coefficient at the $\mathrm{L}_{2,3}$ edges, a separation of the spin and orbital magnetic moment is therefore possible. Though the independent determination of the spin and orbital quantum number is very inaccurate, due to the uncertainties in the number of holes, the light polarization and the angle between the applied magnetic field and the X-ray wave vector, the quotient of the spin and orbital magnetic moment can be well determined:

$$\frac{\langle L_\mathrm{z} \rangle}{\langle S_\mathrm{z} \rangle} = \frac{4}{3} \frac{\Delta A_3 + \Delta A_2}{\Delta A_3 - 2\Delta A_2}. \tag{3.29}$$

Thus with XMCD one can easily investigate the magnetism of a sample and distinguish the origin of the magnetism.

3.3. Neutron Scattering

The difference between light scattering and the scattering of neutrons is the different scattering potential. Neutrons interact with the strong interaction of the atomic nucleus. Furthermore, the neutrons carry a nuclear spin, which interacts with other magnetic moments inside the sample.

Due to the local character of the strong interaction, which is restricted to the atomic nucleus ($\sim 10^{-15}$ m) in comparison to the wavelength of thermal neutrons ($\sim 10^{-10}$ m), the interaction can be assumed to take place in a point-like scattering center. The scattering potential of the strong interaction can be expressed with the Fermi pseudo potential:

$$V(\vec{r}) = \frac{2\pi\hbar^2}{m_\mathrm{n}} \sum_i b_i \rho_i = \frac{2\pi\hbar^2}{m_\mathrm{n}} \sum_i b_i \delta(\vec{r} - \vec{r_i}), \tag{3.30}$$

where m_n is the neutron mass, b_i is the scattering length and ρ_i is the density of the i-th element inside the sample. The strength of the scattering potential, described by the scattering length b_i, depends on the complex interactions of the neutron with the strong nuclear force. This also depends on the nucleus spin quantum number. Therefore, the scattering length varies between different isotopes and changes drastically from one element to the next.

The magnetic interaction of the neutron spin and the magnetic spins inside a sample can be described by the magnetic dipole interaction:

$$V_\mathrm{m}(\vec{r}) = -\vec{\mu}_\mathrm{n}\vec{B} = -\gamma_\mathrm{n}\mu_\mathrm{n}\vec{\sigma}\vec{B}, \tag{3.31}$$

where μ_n is the magnetic moment of the neutron, $\vec{B}$ is the magnetic induction inside the sample and $\vec{\sigma} = (\sigma_x, \sigma_y, \sigma_z)$ is the vector of Pauli matrices. After a lengthy derivation, using the interaction potential for the magnetic field of the spin and the orbital angular momentum, the magnetic scattering cross section can be expressed by:

$$\frac{\mathrm{d}\sigma}{\mathrm{d}\Omega} = (\gamma_\mathrm{n} r_e)^2 \frac{1}{2\mu_\mathrm{B}} \left| \langle \sigma_z' | \vec{\sigma} \cdot \vec{M}_\perp(\vec{Q}) | \sigma_z \rangle \right|^2, \tag{3.32}$$

where r_e is the electron radius, σ_z is the spin projection along a quantization axis given by the external magnetic field and $\vec{M}_\perp = \hat{Q} \times \vec{M} \times \hat{Q}$ is the perpendicular Fourier transformation of the magnetization with respect to the scattering vector $\vec{Q}$. As can be seen in **equation 3.32**, only the perpendicular component $\vec{M}_\perp$ to the scattering vector, can be measured with neutrons.

In contrast to particles without spin, the neutron state $|\Psi(\vec{r})\rangle$ has to be described as a linear combination of the two eigenvectors $(|+\rangle, |-\rangle)$ of the neutron spin states with respect to a quantization axis $|\Psi(\vec{r})\rangle = \Psi_+(\vec{r})\,|+\rangle + \Psi_-(\vec{r})\,|-\rangle$. Neglecting the imaginary part of the σ_z Pauli matrix, because the scattering vector in reflectometry measurements is perpendicular to the sample surface, the Schrödinger equations can be written in the following form:

$$\Psi_+''(\vec{r}) + \left[k^2 - 4\pi b\rho_n + \frac{2m\gamma_\mathrm{n}\mu_\mathrm{n}}{\hbar^2}B_\parallel\right]\Psi_+(\vec{r}) + \frac{2m\gamma_\mathrm{n}\mu_\mathrm{n}}{\hbar^2}B_\perp\Psi_-(\vec{r}) = 0, \tag{3.33}$$

$$\Psi_-''(\vec{r}) + \left[k^2 - 4\pi b\rho_n - \frac{2m\gamma_\mathrm{n}\mu_\mathrm{n}}{\hbar^2}B_\parallel\right]\Psi_-(\vec{r}) + \frac{2m\gamma_\mathrm{n}\mu_\mathrm{n}}{\hbar^2}B_\perp\Psi_+(\vec{r}) = 0, \tag{3.34}$$

where ρ_n is the nuclear sample density, $B_\parallel$ and $B_\perp$ are the parallel and perpendicular components of the magnetic induction inside the sample with respect to the quantization axis. Because of the two different components of the neutron state, four different types of reflectivity can be measured, namely two non-spinflip (NSF) and two spinflip (SF) reflectivities, respectively. As can be seen in **equations 3.33** and **3.34**, the SF reflectivity arises from a magnetic component, which is not parallel to the quantization axis, given by the external magnetic field. For polarized neutron reflectometry measurements, **equations 3.33** and **3.34** are solved for each layer as described in the case of X-ray reflectometry by the use of simulation programs with the Parratt formalism.

4. Experimental Methods and Instruments

This chapter will introduce the wide range of instruments used for sample preparation and characterization. The methods for sample preparation are described in the next two sections. The sample preparation with high oxygen pressure sputtering automaton (HOPSA) is given in **section 4.1.1**, and in **section 4.1.2**, the oxide molecular beam epitaxy (OMBE) is described, which was taken into operation and where most samples were prepared.

After this, the in-house characterization methods are described, beginning with the in-situ methods while growing with OMBE. The low-energy electron diffraction (LEED) (**section 4.2.1**) and reflection high energy electron diffraction (RHEED) (**section 4.2.2**) are used to characterize the surface quality during or directly after growth. In **section 4.2.3**, a short introduction of Auger-electron spectroscopy (AES) is given, which was used to check the chemical property at the surface. The grown films were characterized for the surface quality with atomic force microscopy (AFM) (**section 4.2.5**) and X-ray reflectometry (XRR) (**section 4.2.7**). The bulk crystalline quality was checked with X-ray diffraction (XRD) measurements (**section 4.2.7**). In order to characterize the bulk chemical properties, Rutherford backscattering (RBS) was used (**section 4.2.6**). Finally, in **section 4.2.4**, the superconducting quantum interference device (SQUID) is described as a method to investigate the macroscopic magnetic properties.

At the end, the large scale facility instruments, which are necessary to investigate the interface effects, are described. polarized neutron reflectometry (PNR) experiments (**section 4.3.1**) were used to determine the magnetic density profiles. The element specific X-ray magnetic circular dichroism (XMCD) measurement, is then described finally in **section 4.3.2**.

4.1. Sample Preparation Methods

4.1.1. High Oxygen Pressure Sputtering Automaton (HOPSA)

Sputtering techniques are, due to their relatively easy application, frequently used for thin film deposition in research and industry. Applying radio frequency on a sputter target, in a well defined sputter gas atmosphere, creates a plasma at the target position. Oxygen as a sputtering gas ensures mostly oxidized thin films. Nevertheless, other sputtering gases, like Ar, can also be used for thin film growth. The principle is as follows: The created oxygen ions are accelerated to the sputter target and emit its material, which will be deposited on the substrate lying on a heating stage below. Compared to normal sputtering, which

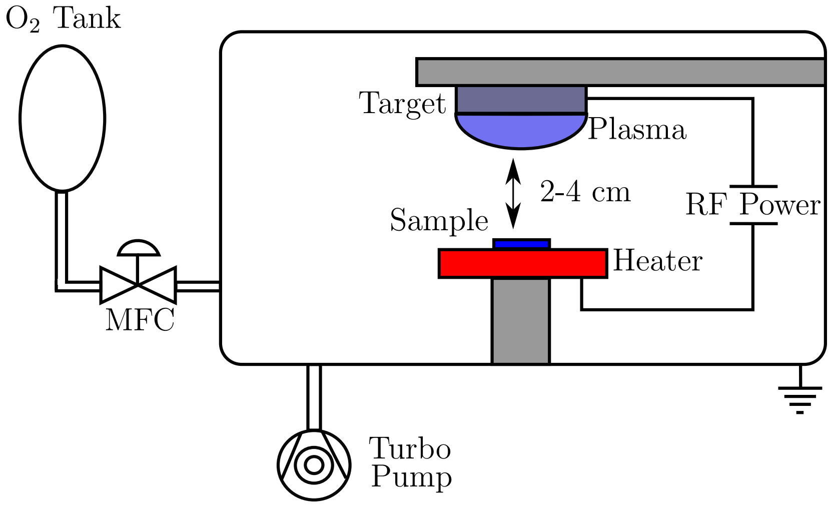

Figure 4.1.: Sketch of the high oxygen pressure sputtering.

operates at pressures around 10^{-4} mbar, high oxygen pressure sputtering (1-3 mbar) has the advantage of a short mean free path, resulting in a more localized plasma. The localization of the plasma will suppress resputtering from already deposited material in comparison to sputtering at lower pressures. This resputtering depends on the distance between target and sample.

The substrate is placed on a heater stage, which can be adjusted in height (2-4 cm) and can be heated up to 1000°C. The parameters which will influence the growth quality are the substrate temperature, the gas pressure (0.5 mbar - 3 mbar), adjustable with the mass flow controller (MFC), the distance from the substrate to the target, and the applied power (up to 200 W) between the substrate and the target.

The advantage of sputtering techniques is the fixed stoichiometry of the target, resulting in fast and easy film growth. Time consuming rate calibration to achieve the desired stoichiometry is unnecessary. But this is also a disadvantage, because with wrong stoichiometry of the growing films, no possibility of improving the stoichiometry is present. Another advantage is the fully automatized sample growth, presented in **appendix D**. Growth parameters for all films can be looked up in **appendix E**. The disadvantage of sputtering techniques is the restricted reproducibility of sample preparation. The deposition rate changes in time, resulting in different film thicknesses in multilayers.

4.1.2. Oxide Molecular Beam Epitaxy (OMBE)

A major part of this thesis was spent to bring the OMBE system into operation. Here, a short overview of the OMBE system will be given. The OMBE (**figure 4.2**) consists of three parts separated through valves, namely the load-lock, the buffer-line and the main chamber. All parts can be vented separately without breaking the vacuum in the other parts. Due to the oxygen usage inside the chamber, all pumps are dry and oil free.

The vacuum at the load-lock is created with a turbo molecular pump, allowing a fast transfer of substrates and samples. From the load-lock, the sample can be transferred to the buffer line, with a base pressure of 10^{-8} mbar, created with an ion-getter pump.

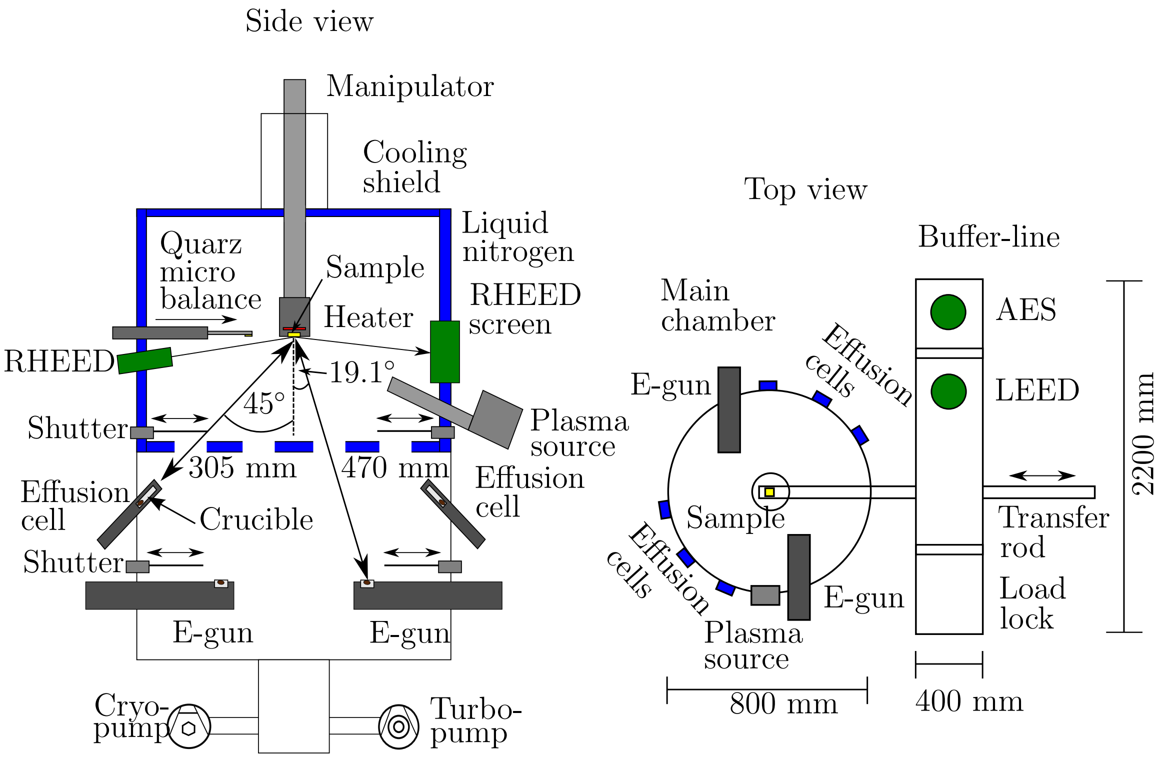

Figure 4.2.: Sketch of the OMBE main chamber: inside view (left) and top view (right). The OMBE is operated at a base pressure of 10^{-10} mbar in the main chamber and buffer line.

There the samples can be investigated with LEED and AES (see **section 4.2.3** and **4.2.1**) regarding their surface quality and stoichiometry. The latter requires a reference sample to be measured beforehand. Additionally, the substrates can be tempered up to 1000°C to remove carbon or other organic materials from the surface and for annealing reasons.

From the buffer line, the samples can be transferred into the main chamber, where the vacuum is created through a turbo molecular pump, supported by a cryopump, with a base pressure of 10^{-9} mbar. In order to further reduce the pressure, a cooling shield, surrounding the main chamber, is filled with liquid nitrogen, resulting in a base pressure of 10^{-10} mbar. The filling level of the nitrogen is kept fixed to ensure stable growth conditions.

For the growth itself, the main-chamber has six Knudsen effusion cells and two E-guns with four crucibles each for material deposition. In the effusion cells the material is heated to vapor pressure by a filament. The evaporation rate is determined by the temperature of the surrounding cell, controlled by an Eurotherm controller via a PID algorithm. In the E-guns the material is evaporated by an electron beam impinging on the material in a crucible. The growth rate is determined before growth with a quartz micro balance, which can be placed at the sample position. In order to grow oxidized films, an atomic oxygen stream is directed onto the sample by a plasma source. With a constant oxygen flow, the base pressure of the main chamber will be in the order of 10^{-6} mbar.

The sample can be rotated by the manipulator of the main chamber to reduce the thickness gradient, due to a deposition angle different from 90°. The sample holder can take 2″ wafers, but inlets are available for smaller samples. The substrates are heated through thermal radiation from a heater, which is in proximity to the back of the sample. The height of the sample position is adjustable to place the sample in the focus of the effusion cells, the E-guns and the RHEED.

The advantage of an OMBE system is the possibility of varying the stoichiometry of the films. With pulsed laser deposition (PLD) or HOPSA, the stoichiometry is given by the used target. Another advantage is the atomic growth process, resulting in a high crystalline quality with smooth film surfaces. Additionally, the sample growth can be automatized, using a receipt for sample growth, once the growth conditions are known. Only the plasma source has to be calibrated for every use. A receipt for thin film growth is presented in **appendix D** and all growth parameters are shown in **appendix E**. The disadvantage is the complexity of the OMBE system and the difficulty of adjusting the growth rates according to the desired stoichiometry (**section 5.1.2**). Additionally, the whole growth process is more time consuming compared to PLD or HOPSA (Only one sample can be grown in a day).

4.2. In-house Characterization Methods

4.2.1. Low-Energy Electron Diffraction (LEED)

Low-energy electron diffraction (LEED) is used to investigate the crystalline quality of the films in a surface sensitive manner; a sketch is shown in **figure 4.3**. It uses low energy electrons with a few electron volts ($\sim 40 - 300$ eV). Electrons in this kinetic energy band have a small penetration depth of a few Å due to the strong Coulomb interaction with

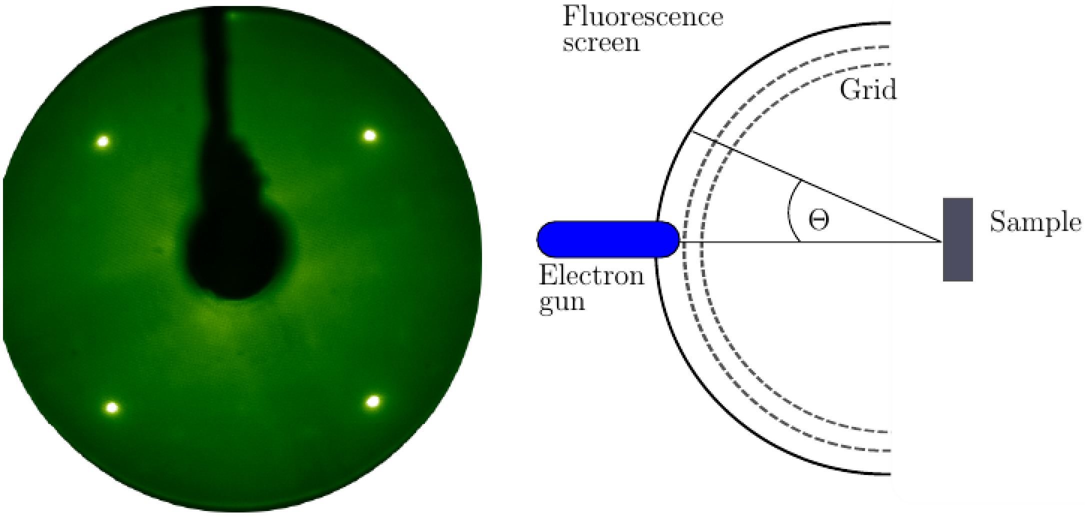

Figure 4.3.: Left: LEED image of a LSMO thin film grown on a STO substrate at an electron energy of 75 eV. Right: Schematic view of the LEED principle.

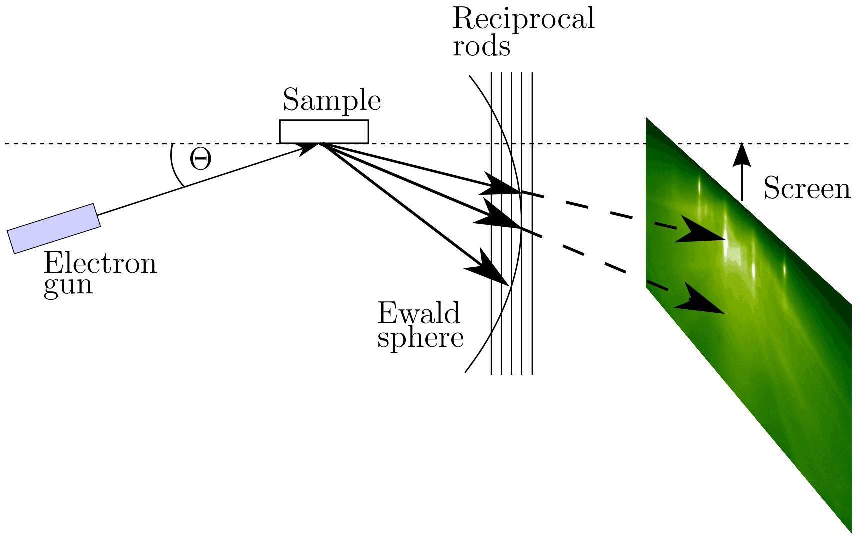

Figure 4.4.: Sketch of RHEED experiment and a resulting RHEED image from LSMO thin film.

the electron clouds of the sample's atoms [77, 78].

The primary electrons are directed perpendicular to the sample surface, where they are backscattered, mostly from the electron cloud of the surface atoms. The backscattered electrons, are accelerated by a grid on a positive potential and are detected on a fluorescent screen. This gives an image of the reciprocal space of the surface. At specific positions, in reciprocal space, Bragg peaks are present, which are due to constructive interference of scattered electron waves from surface atoms. These Bragg peaks are at positions where the Laue equation is fulfilled

$$\vec{Q} = \vec{k_f} - \vec{k_i} \mathrel{\widehat{=}} \vec{G}_{hk}, \tag{4.1}$$

where $\vec{k_i}$ and $\vec{k_f}$ are the wave vectors of the incident and scattered electrons, $\vec{Q}$ is the scattering vector and $\vec{G}_{hk}$ is the reciprocal lattice vector. Therefore, the in-plane lattice parameter can be derived from the positions of the Bragg peaks. Sharp Bragg peaks indicate a high crystalline quality of the film surface. Therefore, LEED can be used in-situ at the OMBE for a first test of the sample quality.

4.2.2. Reflection High Energy Electron Diffraction (RHEED)

Reflection high energy electron diffraction (RHEED) is used for a similar purpose as LEED: to characterize the crystalline quality of the sample surface. The difference to LEED is the higher electron kinetic energy of around 15-20 keV and a grazing incident angle $1^\circ - 3^\circ$ of the electron beam. Due to the small incident angle, RHEED has the advantage that it can be employed during growth.

Electrons scattered from the surface of a sample interfere constructively, when the Laue equation is fulfilled and when the wave vectors of the incident and diffracted electron beam are lying on the Ewald sphere (see **figure 4.4**). In a first approximation, the scattering origins from the two dimensional surface, which results in one-dimensional rods in the reciprocal space. The intersection of these one-dimensional rods with the Ewald sphere fulfills the Laue equation. Due to the small incident angle and the uncertainty of the angle and the wavelength, these intersections are extended rods visible on the screen [79].

Monitoring the RHEED pattern during growth, directly shows the crystalline quality of the sample. In case of a good crystalline quality with a low surface roughness, the RHEED pattern shows extended rods for the low indexed Bragg refections and sharp spots lying on Laue circles for high indexed Bragg refections. When the roughness of the surface becomes worse, e.g. a Volmer-Weber growth, the extended rods will transform to point like Bragg refections, as can be seen in normal diffraction experiments. Is the growing film not crystalline but amorphous, the RHEED pattern will vanish completely.

Assuming a Frank-van der Merve growth mode, RHEED oscillations are visible, when monitoring the intensity of a Bragg peak over time. The intensity of the refection is at maximum, when an atomic plane is completed, whereas it has an intensity minimum at a half grown atomic plane. These RHEED oscillations can be used to monitor the thickness of the growing films.

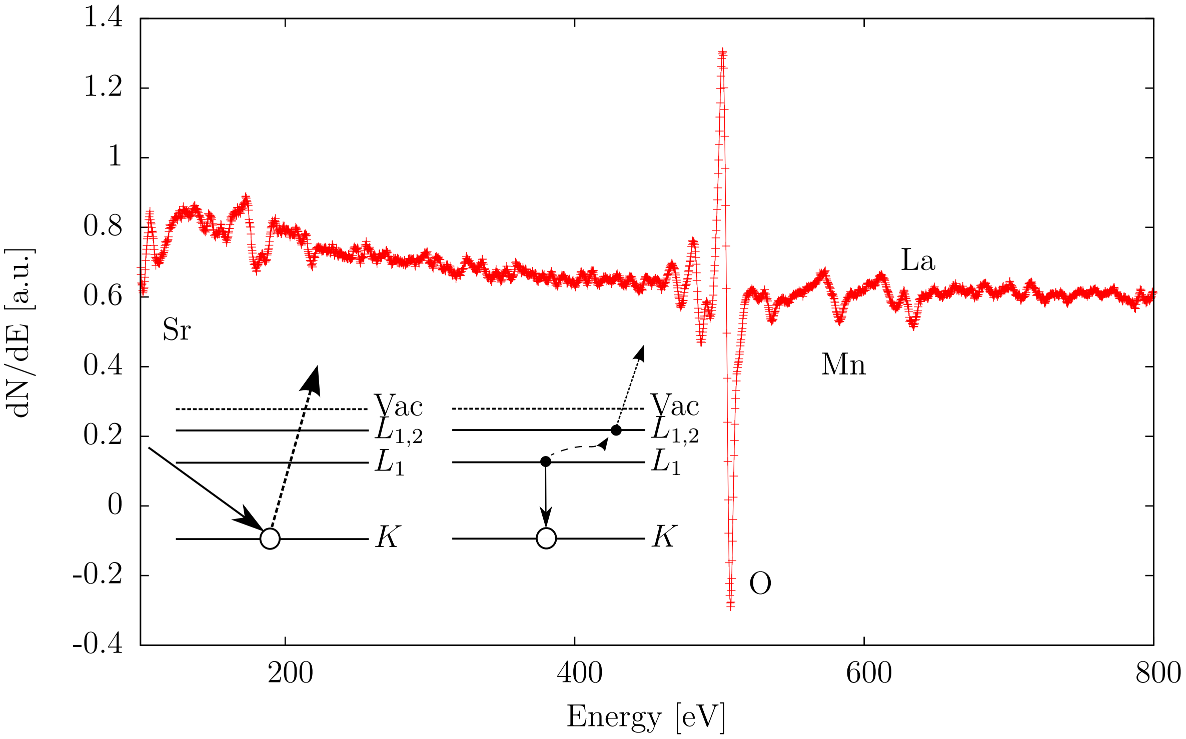

Figure 4.5.: AES spectrum of LSMO thin film grown on STO substrate, with an illustration of the Auger process, shown in the inset (inspired by [80]).

4.2.3. Auger-Electron Spectroscopy (AES)

Auger-electron spectroscopy (AES) is used to determine the chemical composition at the surface (see [81, 80]) directly after film growth. In AES, electrons, with an energy of 3 keV, are directed to the sample surface and can remove electrons from lower atomic shells. A relaxation of electrons from higher atomic shells will transfer the energy with a given probability to another electron, the Auger electron. This probability decays with increasing atomic number, due to a competition between radiative and non-radiative processes [82]. The Auger electron will be emitted, when the transmitted energy is higher than the binding energy. The kinetic energy of the Auger electrons is specific for all elements and is published in [83]. The mean free path of Auger electrons, with a typical energy of around $10 - 2000$ eV, is around $4 - 40$ Å making AES very surface sensitive.

The most convenient way to present AES spectra is to take the derivative of the number of Auger electrons with respect to the energy $dN(E)/dE$. An analysis of $dN(E)/dE$ will suppress the increasing background of detected electrons with increasing energy. In **figure 4.5** an AES spectrum of LSMO is shown, where the peak positions can be attributed to the different elements in LSMO.

4.2.4. Magnetic Property Measurement System (MPMS)

A magnetic property measurement system (MPMS), utilizing a SQUID magnetometer, is used to measure very small magnetic moments. A sketch of the used SQUID XL from Quantum Design is shown in **figure 4.6**. A sample mounted in a straw is moved through superconducting pickup coils formed as a second order gradiometer, which reduces the noise and the magnetic background from the surrounding components. The magnetic

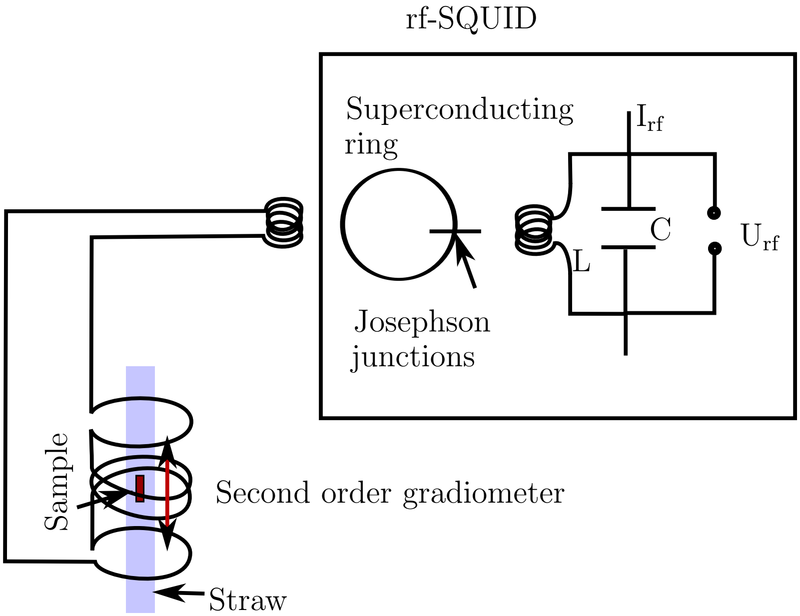

Figure 4.6.: Sketch of the MPMS with rf-SQUID.

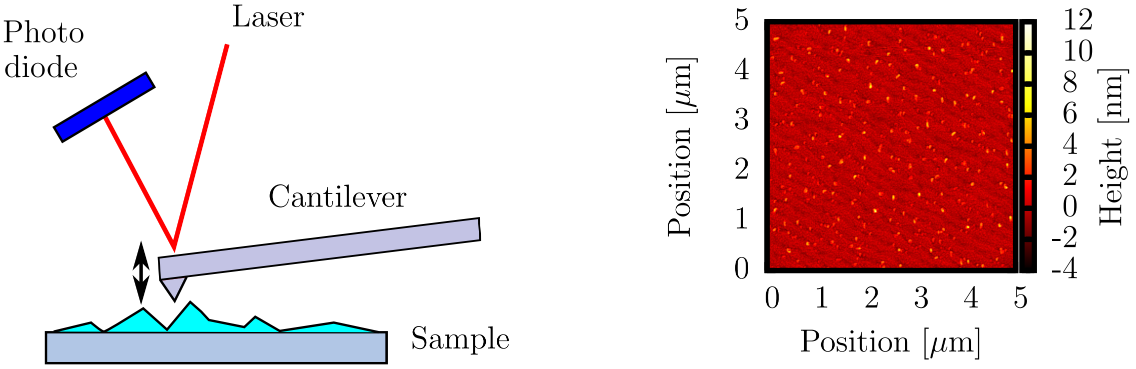

Figure 4.7.: Left: Sketch of an AFM experiment. Right: Topography of sample surface.

moment of the sample induces a current in the gradiometer, which is transferred to a rf-SQUID device, working as a flux-to-voltage transformer. The rf-SQUID consists of a superconducting ring interrupted by a Josephson junction [84, 85]. It is coupled inductively to a LC circuit. An oscillating current is applied to the LC circuit and the time-dependent voltage is measured. Due to the non-linear behavior of the Josephson junction in the rf-SQUID, the phase and the amplitude of the measured voltage depends on the magnetic moment of the sample. The amplitude of the measured voltage shows a typical shape of a second order gradiometer, when moving a dipole through the gradiometer. Fitting the output voltage with the expected behavior of a dipole, moving through the second order gradiometer, gives the measured magnetic moment.

The SQUID can be operated in two ways, in a direct current (DC) mode and a reciprocating sample option (RSO) mode. In a DC measurement, the sample moves through the superconducting loop in discrete steps. Using the sample rotation option, only DC measurements are possible. For the RSO option the sample oscillates rapidly through the superconducting loop. The RSO option is faster and more accurate ($5 \cdot 10^{-9}$ emu) than the DC option.

4.2.5. Atomic Force Microscopy (AFM)

Atomic force microscopy (AFM) is used to analyze the surface quality of a sample. The AFM measures the height profile of the surface in a specific scan area, which is in the order of 1-20 μm^2. From such a height profile the roughness can be determined and can be compared to other methods like X-ray reflectometry, which operates in reciprocal space in contrast to the direct space measurement with the AFM.

To measure the topography, the AFM scans the surface in close proximity using a cantilever with a small tip at the end. The cantilever is driven externally to oscillations. Due to atomic forces, like the Van-der-Waals force, the amplitude and the frequency of the oscillations will change with a changing distance from cantilever to the sample surface. By directing a layer at the end of the cantilever and measuring the reflexion with a photo diode, the amplitude and the frequency of the oscillations can be recorded (see **figure 4.7**).

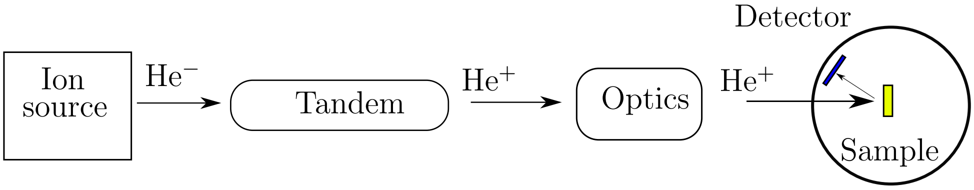

Figure 4.8.: Sketch of RBS experiment.

The AFM can be operated in different ways (contact mode, tapping mode or non-contact mode). In this thesis the AFM Agilent 5400 is operated in a non-contact mode, where the amplitude of the cantilever's oscillation is used in a feedback loop to adjust the height of the cantilever with a piezo element to keep the cantilever at a specific amplitude. The images were corrected with the *PicoView* software for sample tilt and non-linearity effects from the piezo element.

4.2.6. Rutherford Backscattering Spectroscopy (RBS)

In an RBS experiment, high energy He$^+$-ions (1.4 MeV) are used for resolving the elemental composition and the depth profile of individual elements. He$^+$-ions with high kinetic energies are backscattered from the nuclei inside the sample. Due to kinematic considerations, the energy of the backscattered ions depends on the masses of the involved particles and is therefore element specific. The energy of the backscattered particles E_1 can be calculated for single scattering with the formula

$$E_1 = K \cdot E_0 \quad \text{with} \tag{4.2}$$

$$K = \frac{M_1^2}{(M_1 + M_2)^2} \left(\cos\theta \pm \left[\left(\frac{M_2}{M_1} \right)^2 - \sin\theta^2 \right]^{1/2} \right)^2 \tag{4.3}$$

as the kinematic factor (can be derived from momentum and energy conservation) and E$_0$ as the initial energy of the He$^+$-ions. Penetrating the sample will result in an energy loss of the ions due to inelastic small angle scattering from the electron clouds of the atoms. This can be described with the stopping power $S = \mathrm{d}E/\mathrm{d}x$ [86] and the particle energy is therefore

$$E(x) = E_0 - \int_0^{x/cos\theta} \frac{dE}{dx'}(E(x'), x')\mathrm{d}x'. \tag{4.4}$$

The energy loss of the ions results in a lower energy of the backscattered particles. The RBS measurements of all samples where carried out by Dr. Bernhard Holländer from the PGI-9 institute on a Tandetron tandem accelerator (see **figure 4.8**). The RBS data was then analyzed with the RUMP software [87].

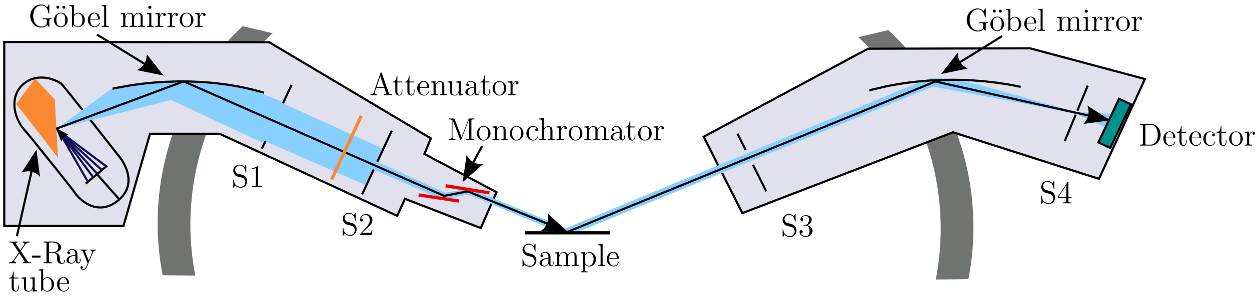

Figure 4.9.: Sketch of the Bruker D8 reflectometer (based on [88]).

4.2.7. X-ray Scattering (XRR and XRD)

In order to analyze the film properties, like thickness, roughness, density and the crystalline quality, the Bruker D8 instrument was used for X-ray reflectometry (XRR) and X-ray diffraction (XRD) measurements. The Bruker D8 uses Copper K$_\alpha$ radiation and can be used in two different setups. The first setup has only a Göbel mirror mounted on the tube side for monochromatization and collimation. This is the preferred setup for XRR measurements, because of the higher beam intensity. In the second setup a channel cut monochromator is additionally mounted on the tube side, which only permits Copper K_α radiation (1.54 Å) and as a result suppresses the Bremsberg and wavelengths other than Copper K_α. Due to the reduced background, this is the preferred setup for XRD measurements. A second Göbel mirror on the detector side focuses the beam on a scintillation detector. With a slit system, different collimations of the beam can be realized, adjusting either for high intensity or good resolution. A sketch of the beam path of the Bruker D8 is shown in **figure 4.9**.

For simulation and analysis of the reflectometry data, the GenX program [89] is used. GenX is a flexible script-based python program, which uses the Parratt Formalism described in **section 3.1**.

4.3. Large Scale Facility Instruments

4.3.1. Polarized Neutron Reflectometry (PNR)

The magnetic profiles inside the samples can be investigated with polarized neutron reflectometry (PNR) experiments. Three different neutron reflectometers (MARIA, D17 and MR) were used. A setup of a typical polarized neutron reflectometry (PNR) experiment is shown in **figure 4.10**. The wavelength and the spin state (up, down) of the neutrons has to be defined with a monochromator and a polarizer before the sample position. In order to preserve the spin state of the neutrons after the polarizer, a guide field is necessary. A slit system will define the beam size of the neutrons, which is important for resolution considerations, especially when using a variable resolution. After the scattering process, the neutron spin state is analyzed with a system consisting of a spin flipper and an analyzer. A two dimensional detector measures the intensity distribution after the scattering. The sample can be mounted in a cryostat, with the lowest temperature

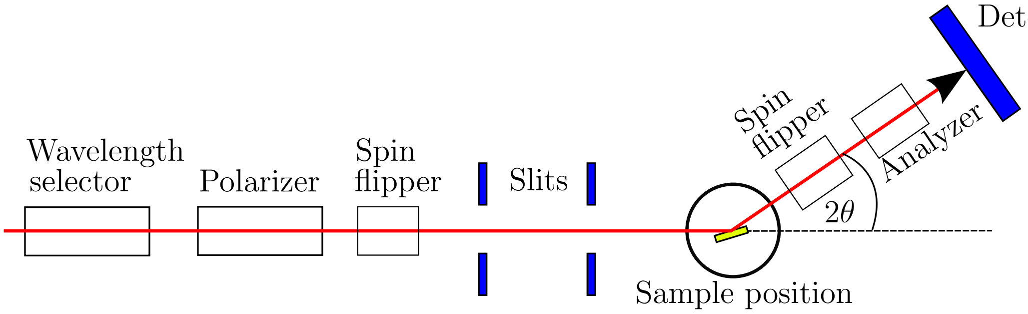

Figure 4.10.: Sketch of a PNR experiment.

of around 5 K. A magnetic field of up to 1 T can be applied in-plane of the thin films and perpendicular to the scattering vector. The relevant parameters for the analysis of the PNR experiments are listed in **table 4.1** and in the following paragraphs only the peculiarities of the different neutron reflectometers will be described.

Magnetic Reflectometer With High Incident Angle (MARIA)

The parameters for the reflectometer MARIA of the Jülich Centre for Neutron Science (JCNS) institute at the Heinz Maier-Leibnitz Zentrum (MLZ) are stated in [90]. MARIA uses a velocity selector for wavelength selection ($\Delta\lambda/\lambda \approx 10\%$) and a double reflection polarizer for spin polarization. The resulting wavelength distribution can be well described with a Gaussian function. A ^{3}He cell can be used for the spin analysis, which was removed for our experiment, as no spin-flip was expected. This results in a higher intensity of the reflected neutron beam. A multi-wire detector is used for neutron detection, which is described in more detail in **section 6.1.2**, where also the experimental shortcomings are described.

The data reduction for the MARIA reflectometer is described in **section 6.1**, with the handling of the off-specular scattering from multilayers, which was a major part of this PhD thesis.

	$\Delta\lambda/\lambda$	d$_{S_1-S_2}$ [mm]	d$_{S_2-Sam}$ [mm]	d$_{Sam-Det}$ [nm]
MARIA	0.1	4100	400	1910
D17	0.04	3300	305	3100
MR	relaxed to $\Delta\lambda = 2.74$ Å	2000	600	2500

Table 4.1.: Presented are the wavelength spread $\Delta\lambda/\lambda$, the distance between the first and the second slit d$_{S_1-S_1}$, the distances between the second slit and the sample d$_{S_2-Sam}$ and the distance between the sample and the detector d$_{Sam-Det}$.

Advantage: High flux of the neutron beam, due to the large wavelength band, which allows fast measurements, as well as measurements up to high Q values.

Disadvantage: Relaxed resolution, due to the large wavelength band.

D17

The reflectometer D17 at the Institute Laue-Langevin (ILL) is described in [91]. It can be used in two different modes: Firstly, the time-of-flight mode, where a part of the reflectivity curve can be measured without changing the sample angle. Secondly, the normal monochromatic mode, which was used for the PNR experiments. In this mode, the wavelength selection and polarization are carried out using a Fe/Si multilayer monochromator. The resulting wavelength distribution is asymmetric and has to be taken into consideration in order to simulate the resolution appropriately. A ^{3}He cell is used as an analyzer. Data reduction was accomplished using the LAMP software [92], which handles the data reduction similarly to the MARIA reflectometer described in **section 6.1**.

Advantage: High flux of the neutron beam.

Disadvantage: Complex simulation of reflectometry data, with a poorer resolution than $\Delta\lambda/\lambda \approx 4\%$, due to the asymmetric wavelength distribution.

Magnetism Reflectometer (MR)

The MR reflectometer at the Spallation Neutron Source (SNS) [93] is operated in the time-of-flight (TOF) mode with a frequency of 60 Hz. In a TOF neutron reflectometry experiment the wavelength distribution is relaxed to a broad wavelength band of around 3 Å bandwidth around 5 Å. Each neutron bunch has a time stamp and the position of the scattering in reciprocal space is determined from the detection position on the two dimensional detector and the flight time of each neutron. Due to the large wavelength band, part of the reflectivity curve is measured at one sample angle position. Therefore, only a few angle positions need to be measured. The data reduction was accomplished using the QuickNXS software [94].

Advantage: Good resolution.

Disadvantage: Complex experiment due to TOF experiment.

4.3.2. X-ray Magnetic Circular Dichroism (XMCD)

The XMCD measurements were carried out at the 4-ID-D beamline at the Advanced Photon Source (APS). The optical setup is shown in **figure 4.11**, where one important optical part is the phase retarder positioned directly after the monochromator. The phase retarder changes the linear polarization of the incoming X-ray beam to a circular one. Depending on the angular position of the phase retarder, the X-ray beam will be left or right circularly polarized. Behind the second slits the sample is mounted in a closed

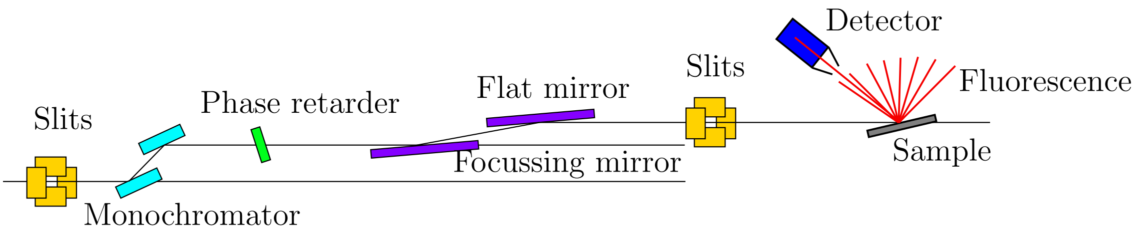

Figure 4.11.: 4-ID-D optics inspired by [95].

cycle cryostat with an electromagnet with a maximum field of 300 Oe. The beam flux at the sample position is around 10^{13} photons/s with a beam size of 2.6 mm × 1.2 mm. The polarization efficiency of the phase retarder depends on the photon energy used for the measurement. For measurements at the L_2 edge, the polarization efficiency is around 0.6% and at the L_3 edge around 0.56%.

The XMCD signal is determined by measuring the fluorescence signal of the sample with an energy sensitive Si detector. The fluorescence signal is in first approximation proportional to the absorption cross section and is measured for different photon energies around the absorption edges. In the case of Pd, the L_3 and L_2 edges are measured in an energy range of 3.16 keV to 3.2 keV and 3.315 keV to 3.355 keV, respectively. However, depending on the X-ray polarization, the measured absolute intensity varies slightly. Between left and right circular polarized light an intensity offset is visible, with an unknown origin. This intensity offset has a direct influence on the XMCD signal. In order to circumvent this and other artifacts, four measurements were performed. The fluorescence signal was measured with left and right circular polarized light and also by changing the direction of the magnetic field. A more detailed discussion is given in **section 6.3**.

5. Sample Preparation

This chapter handles the aspects of growing thin films with an oxide molecular beam epitaxy (OMBE) and an high oxygen pressure sputtering automaton (HOPSA). The important parameters, like substrate temperature and growth rates are described in more detail for the growth of perovskite thin films. The best growth parameters are determined for the growth of LSMO, LCMO and the Pd/oxide thin films. Having been largely involved in the installation of the OMBE at the beginning of my thesis, the biggest focus is on the growth of perovskite films by using OMBE.

5.1. Preliminary Work

5.1.1. Substrate Preparation

Substrate preparation is an important part of the sample growth. Only with a clean surface of the substrate, highly crystalline films can be produced. Thus, it is necessary to clean the substrate's surface from adatoms to get well defined surfaces. Depending on the substrate, different procedures have to be carried out.

The $SrTiO_3$ substrates, used for polarized neutron reflectometry measurements, are so-called epi-ready substrates from CrysTec GmbH, which can be directly used to grow thin films. Cleaning the substrates with isopropyl alcohol or acetone is not necessary, but in

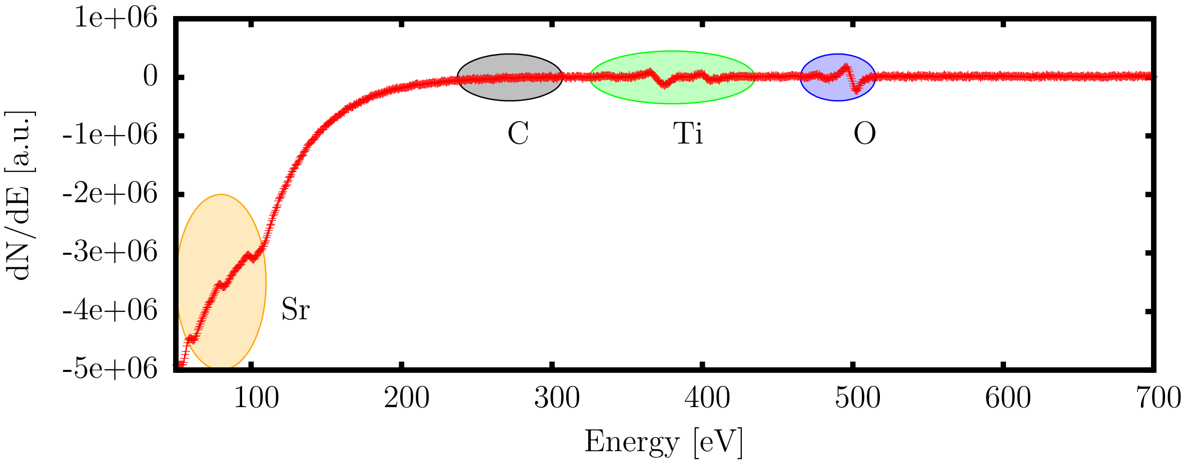

Figure 5.1.: AES measurement of STO substrate after the annealing process at 1000°C. At the element specific energy of carbon, no peaks are present indicating no carbon contamination.

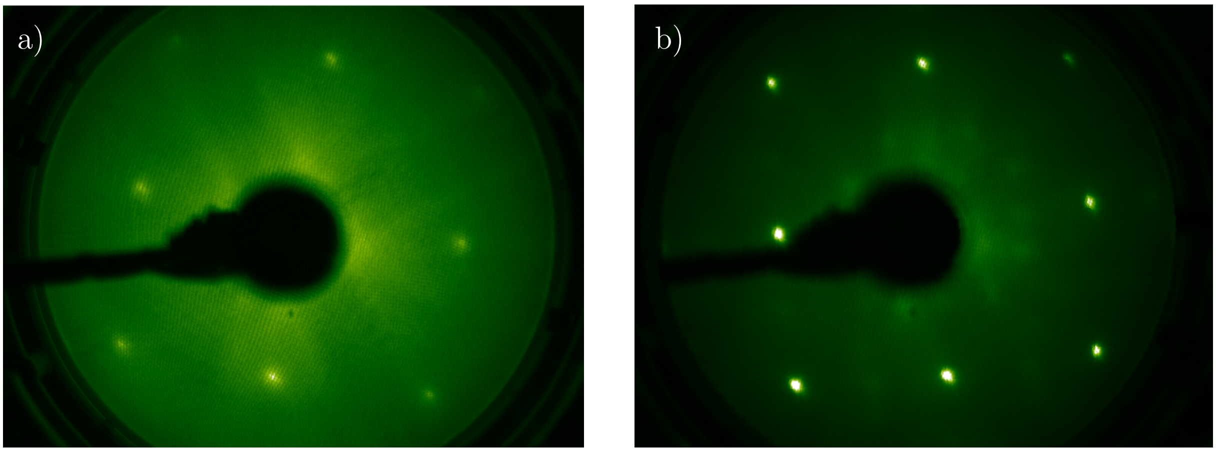

Figure 5.2.: a) STO substrate before the annealing process started. b) STO substrate after annealing at 1000°C. The peaks are much sharper after the annealing.

order to improve the growth of oxide thin films on the STO substrates, a TiO_2 termination of the STO substrate is preferred. This can be achieved with a hydrofluoric acid etching process, which was carried out by Markus Schmitz and used for the samples grown with OMBE. Additionally to the hydrofluoric acid buffering, it is important to clean the surface from adatoms, like carbon, by tempering at high temperatures. In the first step the STO substrates are tempered in the OMBE system in ultra high vacuum (UHV) at 500°C over night. After this, the substrates are tempered for one hour at 1000°C in an oxygen atmosphere at a pressure of $5 \cdot 10^{-6}$ mbar. Growing with HOPSA, the STO substrates are heated directly at 1000°C in 3 mbar oxygen pressure. Due to the poorer crystalline quality of the films, a hydrofluoric acid etching process was not necessary.

The heating procedure removes the carbon from the surfaces. This can be seen in the AES measurement presented in **figure 5.1** done on a STO substrate after heating in the OMBE system. In this measurement peaks from Sr, Ti and O are clearly visible, but there are no carbon peaks around 272 eV.

Additionally, the LEED picture improves (**figure 5.2**) after the heating process, as much sharper peaks are visible. This indicates the removal of adatoms and, thus, an improved surface quality of the STO substrate, which is a necessity in order to investigate interface effects.

5.1.2. Stoichiometry

The stoichiometry of TMO thin films depends mostly on the substrate temperature, the pressure and the adjusted growth rates. The growth of stoichiometric TMO samples is a long iterative process of sample growth and stoichiometry analysis with RBS. The growth rates of the elements are adjusted and described in the following paragraph.

Rate Calibration

The rate calibration for the growth of TMO thin films depends on the type of growth (co-deposition, shuttered growth). If the films are grown with co-deposition, the rates have to be adjusted according to the desired stoichiometry. In shuttered growth, where the elements are deposited consecutively, the deposition time of one element has to be adjusted in the way that one atomic layer is grown. In both cases the growth rates are determined with a quartz micro balance (QMB). The frequency change Δf of the QMB is proportional to the deposited mass, which is equivalent to the deposited thickness. The rate is therefore the first derivative of the frequency $\Delta f/\Delta t$. Using the proportionality of the frequency to the deposited mass, the rates can be adjusted:

$$\Delta f \sim m \cdot \Delta n, \tag{5.1}$$

where m is the atomic mass and Δn is the number of deposited atoms. To grow a complex TMO like $A_\mathrm{x}B_\mathrm{y}C_\mathrm{z}O_3$, with different elements A, B and C, the number of deposited atoms has to be equal to the concentration ratio:

$$\frac{\Delta n_i}{\Delta n_j} = \frac{k}{l}, \text{ with (i,k),(j,l) } \in \text{((A,x), (B,y), (C,z))}. \tag{5.2}$$

This leads to:

$$\Delta f_i = \frac{k}{l}\frac{m_i}{m_j} \cdot \Delta f_j, \text{ with (i,k),(j,l) } \in \text{((A,x), (B,y), (C,z))} \tag{5.3}$$

The rates determined in this way are rough estimates of the needed rates. Effects, like different sticking coefficient for the quartz balance and the substrates or a different thermodynamic equilibrium at the substrate surface for the adsorption and desorption of the elements, change the needed rates for stoichiometric growth. The rates can only be found through a time-consuming iterative process of sample preparation and determination of grown stoichiometry (see **section 5.1.2**) with RBS. Monitoring RHEED oscillations, which are very sensitive to stoichiometric changes, can improve the stoichiometry of the films additionally [96]. However, this procedure is even more time-consuming and RHEED oscillations have to be present.

Substrate Temperature

The effects of different substrate temperatures, during growth, can be well investigated in $\mathrm{La}_x\mathrm{Bi}_{1-x}\mathrm{MnO}_3$ (LBMO) with the volatile Bi. Growing LBMO with the procedure described above, the volatile Bi will desorb from the LBMO film leading to non-stoichiometric thin films. Lowering the growth temperature down to 500 °C will improve the stoichiometry of the LBMO films at the expense of the crystalline quality, which is not enough for stoichiometric films.

In **figure 5.3** it is clearly visible that by reducing the substrate temperature, the concentration of the volatile Bi increases in the LBMO thin film. Nevertheless, this is still far away from the desired $\mathrm{La}_{0.5}\mathrm{Bi}_{0.5}\mathrm{MnO}_3$, as this corresponds to $\mathrm{La}_{0.5}\mathrm{Bi}_{0.05}\mathrm{MnO}_{3-x}$

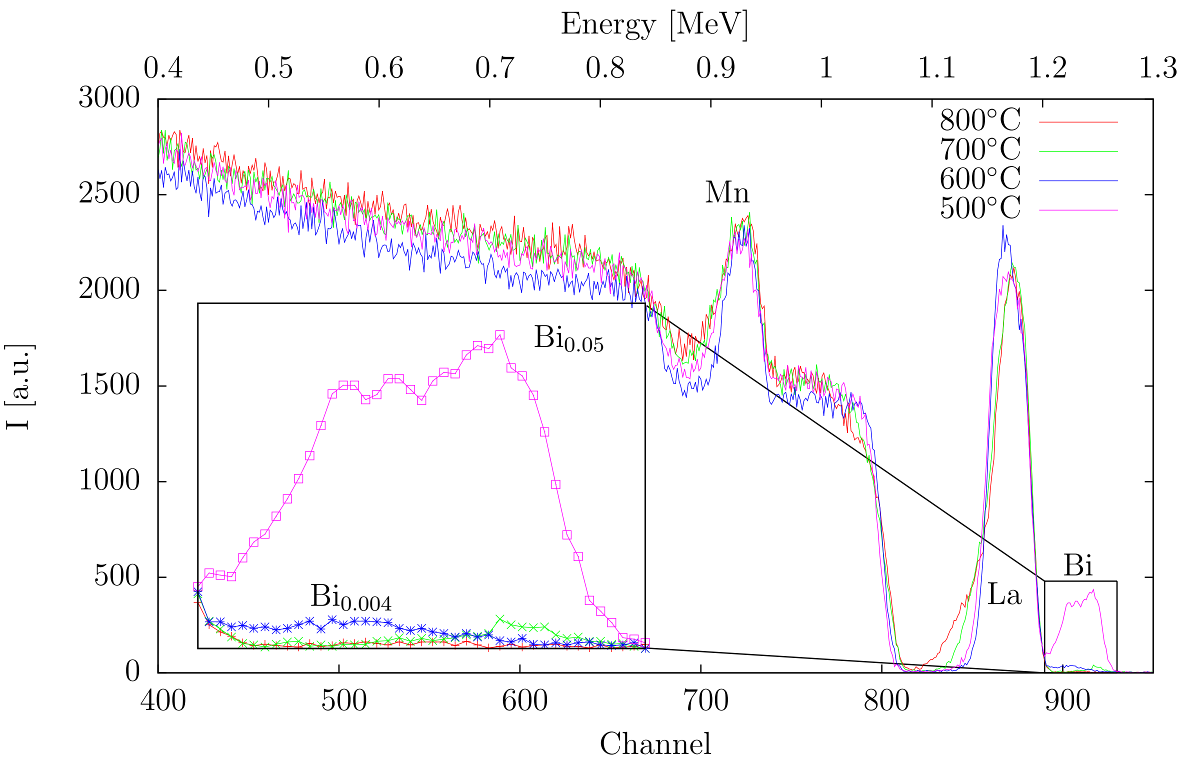

Figure 5.3.: RBS measurements of LBMO thin films grown on a STO substrate at different temperatures.

Sample	OMBE$_{0118}$	OMBE$_{0116}$	OMBE$_{0115}$	OMBE$_{0113}$
Temperature [°C]	500	600	700	800
Roughness [nm]	10.52	6.29	3.09	1.63
Bi content	0.05 ± 0.004	0.004 ± 0.002	0.004 ± 0.002 (at surface)	0

Table 5.1.: Roughness of LBMO films calculated from AFM measurements shown in **figure 5.4** for different substrate temperatures during growth, as well as the Bi content in the LBMO thin films with a normalization of the RBS measurement to a Mn concentration of one.

(**table 5.1**). The tails on the left side of all peaks can be explained through interdiffusion of different layers or through very rough surfaces of thin films. Measuring the films with AFM (**figure 5.4**, **table 5.1**), it becomes obvious that such RBS spectra originate from a high roughness. With increasing substrate temperature the surface roughness is decreasing, which is consistent with the RBS measurement.

Due to the volatile Bi and strong off-stoichiometric films, the growth mode of the LBMO films is either the Volmer-Weber or the Stranski-Kranstov growth mode. For stoichiometric LBMO films it would be necessary to reduce the growth temperature further. But by reducing the temperature further, the films will grow with rougher surfaces and with a crystalline quality, which is not good enough for correlated electron effects like ferromagnetism or ferroelectricity.

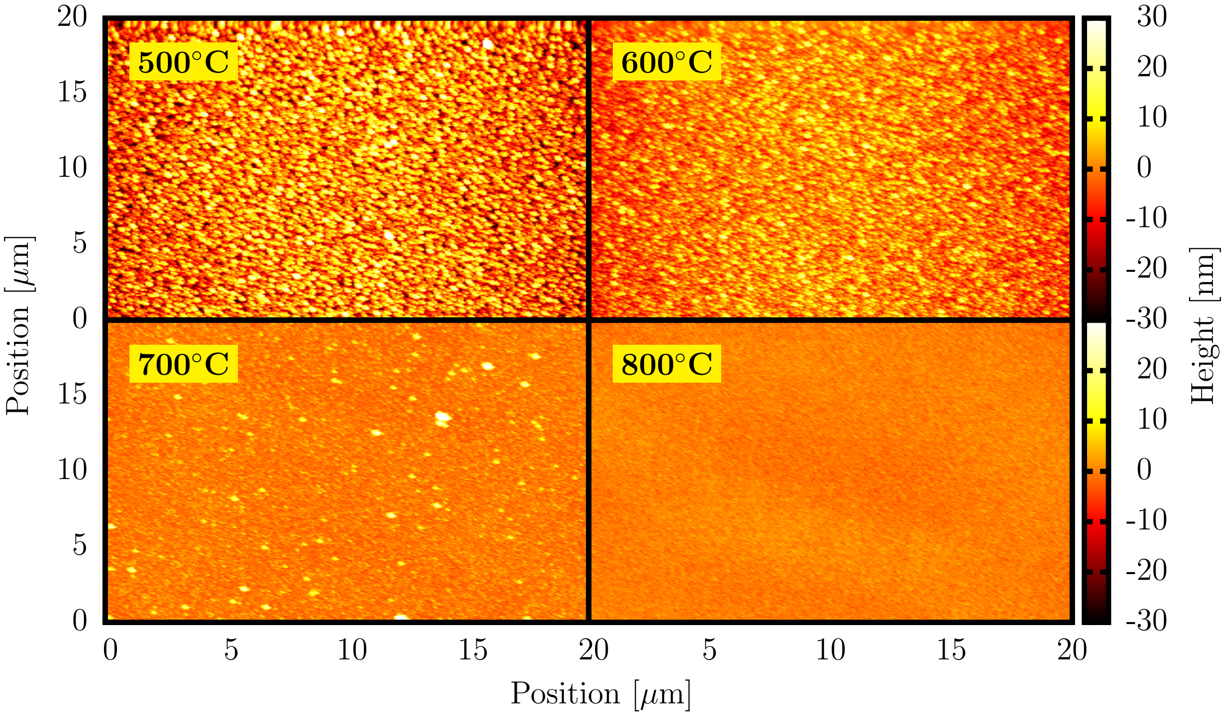

Figure 5.4.: AFM measurements of LBMO thin films grown on STO substrates. The surface roughness decreases significantly with increasing temperature from 500°C to 800°C.

A possibility to improve the stoichiometry is the growth in a shuttered deposition mode [97, 49, 79], where the different elements are deposited successively. Between the deposition of different elements, the system has time for relaxation. The problem with this growth mode is the need to stop the deposition of one element exactly when one atomic layer is grown, which has to be controlled with RHEED oscillations. But to see RHEED oscillations, the stoichiometry has to be very close to the right stoichiometry and the sample has already to grow in the Frank-van der Merve growth mode. With RHEED controlled growth, it is possible to improve the stoichiometry to less than 1% deviation, which is not possible with RBS measurements and quartz micro balance alone. Unfortunately, it was not possible to grow stoichiometric LBMO films with a shuttered deposition mode.

Oxygen Content and Lattice Parameter

Another important aspect of the growth procedure of TMO is the oxygen content of the grown films. Although the oxygen content is difficult to measure directly, (RBS error $\sim 30\%$) the oxygen content can be measured indirectly through the lattice parameter of the grown thin films. Tempering $La_{0.5}Sr_{0.5}MnO_3$ thin films grown on a STO substrate at 400°C in a vacuum of 10^{-4} mbar results in defects in the crystal structure, as the oxygen desorbs from the TMO films ($O_O^X \rightarrow \frac{1}{2}O_{2(g)} + 2e'$). These defects disturb the

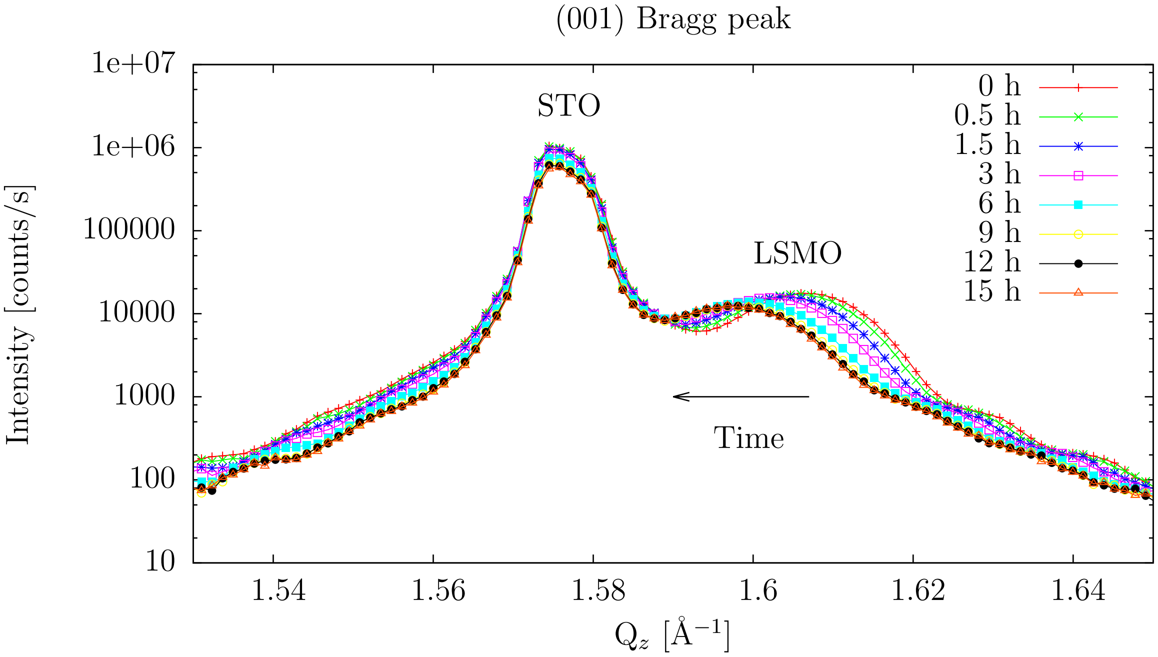

Figure 5.5.: XRD measurement of the (001) Bragg peak of $La_{0.5}Sr_{0.5}MnO_3$ film on STO (Sample: $OMBE_{0071}$) while tempering at 400 °C in 10^{-4} mbar vacuum.

surrounding crystal structure increasing the lattice parameters. This can be seen in XRD measurements in the change of the (001) Bragg peak position (**figure 5.5**). The Bragg peak of the STO substrate and the LSMO film were fitted with a Gaussian function assuming a fixed background due to the Bremsberg. The position of the LSMO peak is plotted against the heating time (**figure 5.6**), where a exponential decay can be seen. This decay is temperature-dependent and the rate of the lattice parameter change increases with increasing temperature.

Heating the same sample afterwards in 0.5 mbar oxygen at 500°C reverses this process. After heating in oxygen, the position of the (001) Bragg peak of the LSMO film is the same as before heating in vacuum. Heating in oxygen, the TMO films absorb oxygen, which conciliates the defects and the distorted structure and the oxygen content in the TMO films can be saturated in the samples. One could make a phase diagram, which depends on the temperature and the oxygen partial pressure and shows whether the oxygen is desorbed or absorbed. At the phase boundary the desorption and the absorption of oxygen are equal resulting in a constant oxygen content in the TMO films. Below or above this boundary the oxygen content in the TMO films will increase or decrease, depending on the oxygen pressure and the temperature.

An important result for growing TMO thin films is that after the growth, the oxygen partial pressure has to be high to ensure oxygen saturation of the samples or the samples have to be heated in an oxygen atmosphere after the growth process. In contrary to metallic films, which should be placed in an exicator to minimize oxidization of the surface, TMO films should be placed in oxygen atmosphere.

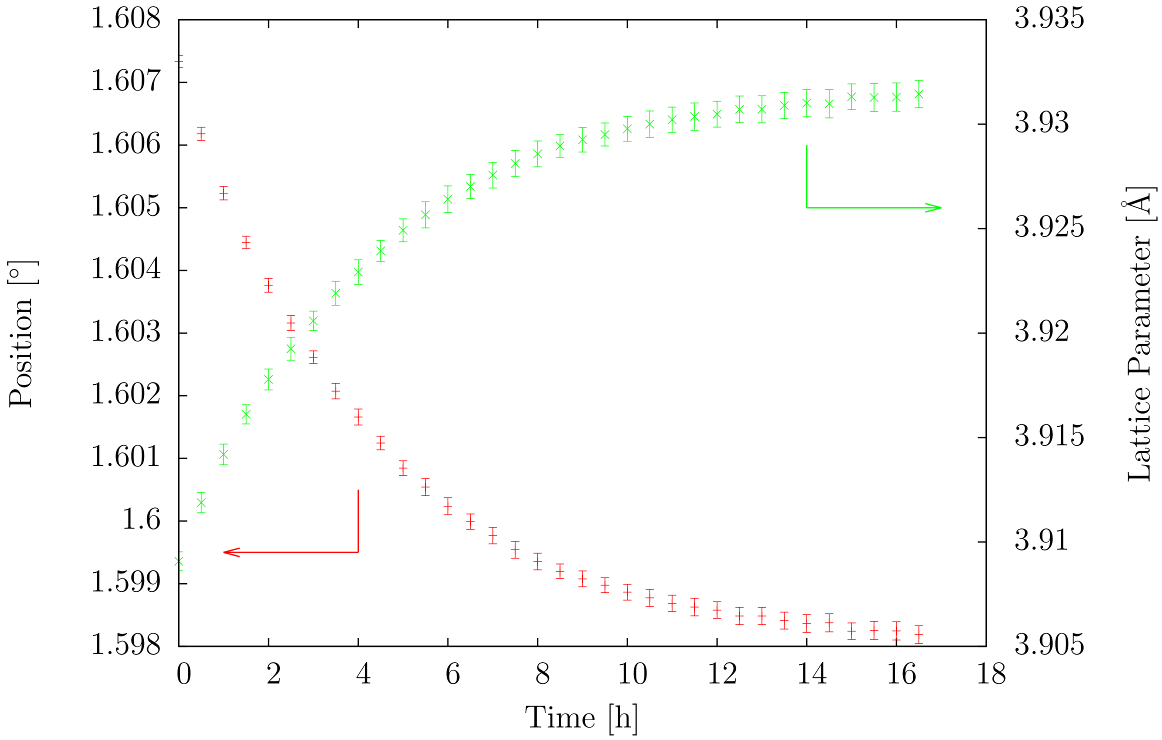

Figure 5.6.: Plotted is the peak position of the LSMO (001) Bragg peak (Sample: $OMBE_{0071}$) against the heating time at 400°C in a vacuum of 10^{-4} mbar and the resulting out-of-plane lattice parameter change.

5.2. Growth of Transition Metal Oxides

The receipts for the thin film growth with OMBE and HOPSA are given in **appendix D** and all parameters are listen in **appendix E**.

5.2.1. $La_{0.7}Ca_{0.3}MnO_3$

The LCMO thin films were grown by OMBE and HOPSA in order to compare different growth methods with a desired stoichiometry of $La_{0.7}Ca_{0.3}MnO_3$.

Oxide Molecular Beam Epitaxy (OMBE)

The rate calibration described in **section 5.1.2** was used for the growth of LCMO thin films with OMBE. The oxygen partial pressure dependence on thin film growth was investigated by Markus Waschk [98] from the JCNS-2 institute. With an oxygen flow of 0.08 sccm[1], resulting in a pressure if $2.5{\cdot}10^{-6}$ mbar, the materials in the crucibles will not oxidize during growth in an oxygen atmosphere, resulting in stable growth rates. Therefore, an oxygen flow of 0.08 sccm was used for the growth of LCMO thin films.

---

[1] The unit sccm is a standard cubic centimeter per minute. A standard cubic centimeter is a gas volume of $V = 1\ \mathrm{cm}^3$ under standard conditions for temperature and pressure ($T = 0$°C and $p = 1013.25$ hPa).

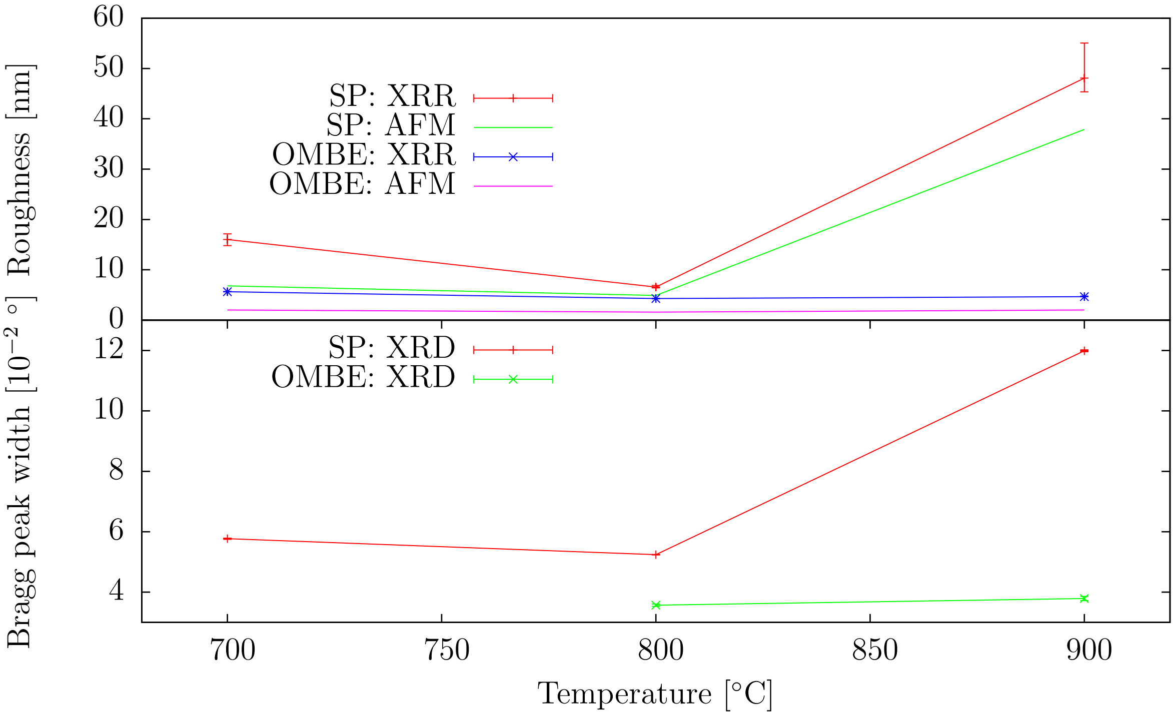

Figure 5.7.: Derived film parameters from XRR, XRD and AFM measurements of the LCMO film grown with HOPSA and OMBE. Presented are the film roughnesses from the XRR and AFM measurements, as well as (002) Bragg peak width derived from rocking scans.

Temperature [°C]	700 (OMBE$_{0242}$)	800 (OMBE$_{0240}$)	900 (OMBE$_{0239}$)
XRR roughness [Å]	$5.65\ ^{+0.05}_{-0.03}$	$4.28\ ^{+0.01}_{-0.03}$	$4.66\ ^{+0.11}_{-0.01}$
RO width [10^{-2} °]	-	3.57 ± 0.04	3.79 ± 0.07
AFM roughness [Å]	1.93	1.63	2.10

Table 5.2.: Derived LCMO film parameters from XRR, XRD and AFM measurements of LCMO films grown with OMBE. Presented are the film roughnesses from the XRR and AFM measurements, as well as the (002) Bragg peak width derived from rocking scans.

Samples of LCMO films on commercial STO (100) substrates from MaTecK GmbH [99] were grown at different substrate temperatures (700°C to 900°C) to optimize the growth quality. The quality of the grown films can be investigated with LEED, XRR, XRD and AFM measurements, which are shown in **appendix H**. In **table 5.2** all parameters concerning the film quality are summarized. The best substrate temperature, for the growth of LCMO thin films, is 800°C. At this temperature the width of the (002) Bragg peak in rocking scans is the smallest indicating small mosaicity and the thickness oscillations of the (002) Bragg peak are most pronounced (**figure 5.8**). Furthermore, the

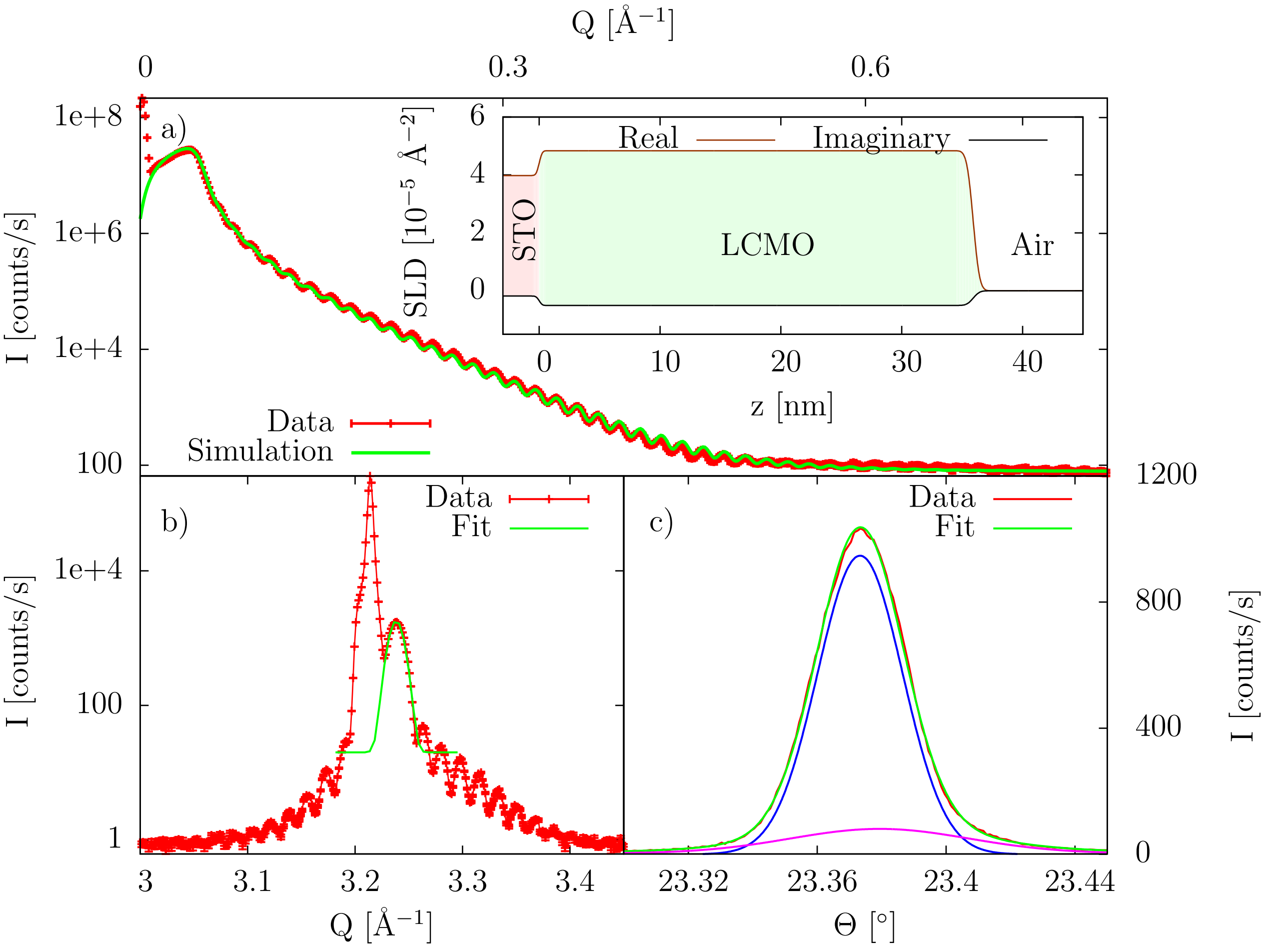

Figure 5.8.: a) X-ray reflectometry measurement with simulation thereof. SLD of simulation is shown in the inset. b) Diffraction measurement at the (002) Bragg peak in out-of-plane direction. c) Rocking scan of the (002) Bragg peak fitted with two Gaussian functions in order to get the FWHM. (Sample: OMBE_{0240})

surface roughness derived from XRR measurements is the smallest at this temperature (fitting parameters are presented in **appendix G**), which is supported by AFM measurements. All measurements are summarized in **figure 5.7**. Taking all measurements (LEED, RHEED, AFM, XRR and XRD) into account, the best growth temperatures for the growth of LCMO thin films by OMBE is 800°C, but with small differences for other temperatures.

Another important aspect is the stoichiometry of the LCMO films. RBS measurements were performed on the LCMO film prepared at 800°C grown on a STO substrate (Sample: OMBE_{0240}) and are presented in **figure 5.9**. The stoichiometry used for the simulation was $\mathrm{La}_{0.85\pm0.02}\mathrm{Ca}_{0.34\pm0.05}\mathrm{MnO}_{3.5\pm0.5}$, with a higher concentration of Ca and La atoms. The film shows a deficiency of Mn atoms in the order of 0.15%. The Mn rate has to be scaled by 1.15 during the rate calibration (Sample: OMBE_{0247}), which will result in the stoichiometry $\mathrm{La}_{0.72\pm0.02}\mathrm{Ca}_{0.3\pm0.05}\mathrm{MnO}_{2.7\pm0.5}$ shown in **figure 5.9**. This stoichiometry is

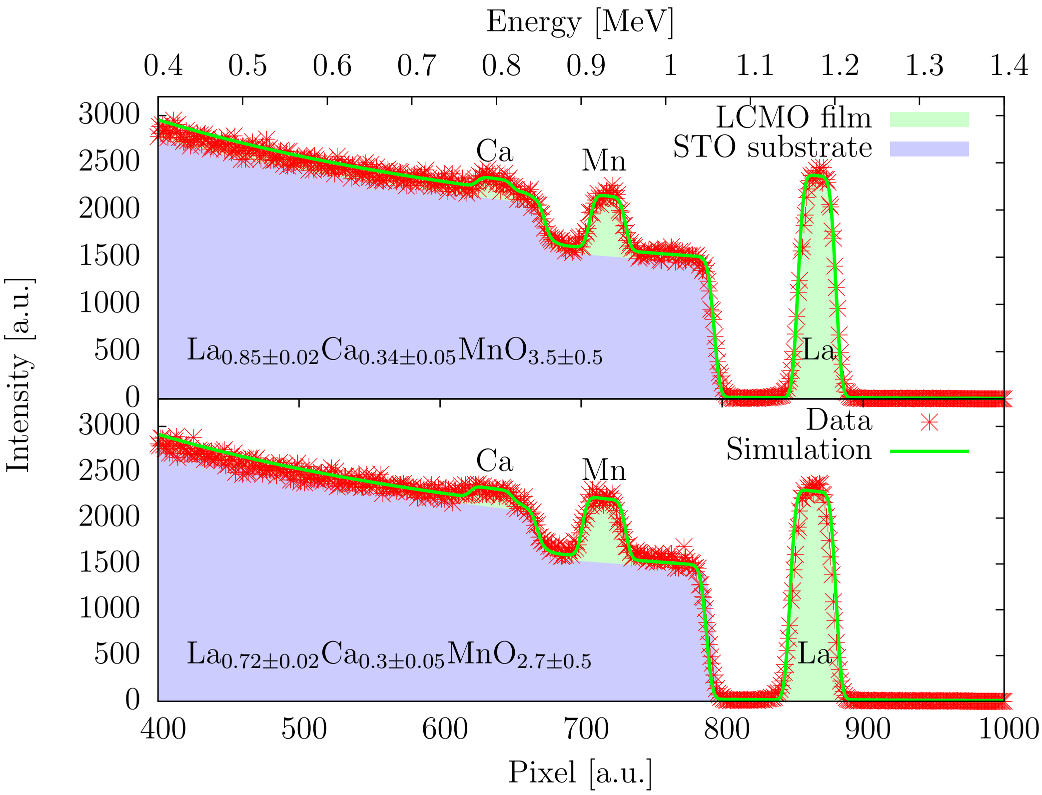

Figure 5.9.: RBS measurement carried out on a LCMO thin film grown on a STO substrate at 800°C, with a simulation of the stoichiometry with (Sample: $OMBE_{0247}$) and without (Sample: $OMBE_{0240}$) a rate calibration factor. Film at the top was grown with no calibration factor. For the sample at the bottom, the Mn rate was scaled by 1.15.

in the range of the inaccuracy of the RBS measurement method and can only be improved by calibrating the rates of the elements with the shuttered growth mode [96] and keeping the RHEED oscillations constant.

The magnetic properties of the LCMO film, grown on a STO substrate at a growth temperature of 800°C and by scaling the rate of Mn by 0.15, are presented in **figure 5.10** (Sample: $OMBE_{0251}$). The magnetism of the film is normalized to the magnetic moment of one Mn atom by calibrating with the sample surface $A = 25\ \text{mm}^2 \pm 0.1\ \text{mm}^2$, the thickness of the layer d $= 403.45\ ^{+0.32}_{-0.25}$ Å and the unit cell of the LCMO film $\rho = 1.71\ ^{+0.01}_{-0.01} \cdot 10^{-2}$ Å^{-3}. The field cooled measurement shows a reduced Curie temperature of $T_\text{C} = 180$ K ± 5 K compared to the bulk Curie temperature of LCMO $T_\text{C} = 260$ K. Additionally, the magnetic moment of the LCMO film is reduced to 2.7 μ_B from the bulk magnetic moment of 3.7 μ_B. The reduced magnetization might be due to the induced strain from the substrate or an oxygen deficiency, which cannot be detected with RBS measurements. But the LCMO film shows a typical ferromagnetic behavior (inset of **figure 5.10**).

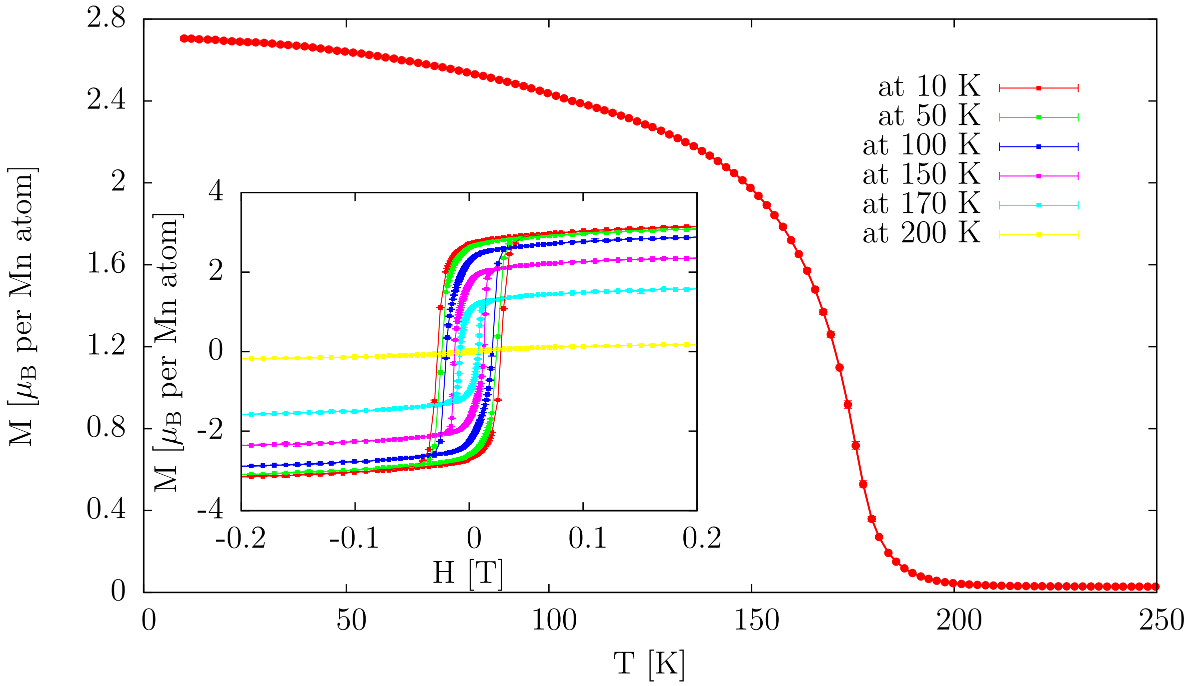

Figure 5.10.: Field cooled measurement at 100 Oe of LCMO film grown on STO substrate at a growth temperature of 800°C and adjusted growth rates. Inset: hysteresis measurements corrected for dia- and paramagnetism. (Sample: OMBE_{0251})

High Oxygen Pressure Sputtering Automation (HOPSA)

In contrast to the atomic deposition of the OMBE the growth with HOPSA (**section 4.1.1**) uses targets with the desired stoichiometry. A $La_{0.7}Ca_{0.3}MnO_3$ target, with 2″ diameter and 0.125″ thickness, from Kurt J. Lesker Company [100] was used for the growth of LCMO thin films. The target has a purity of 99.99% and the stoichiometry was checked by analyzing grown LCMO films with RBS measurements (**figure 5.12**).

The substrate and the target have to be prepared before growth, especially when the target was stored outside of the vacuum. The target is cleaned by applying a power of 100 W at the target in an oxygen partial pressure of 1.5 mbar over twelve hours. After this first cleaning of the target, it is sufficient to apply the desired power of 120 W for one hour before growth. In the same time, the substrate is heated at 1000°C in an oxygen atmosphere, with a oxygen partial pressure of 3 mbar, to remove adatoms, as described in **section 5.1.1**.

The quality of the films grown with HOPSA mainly depends on the oxygen partial pressure, the substrate temperature, the target to substrate distance and the applied power at the target. High oxygen pressures of around 3 mbar are used during growth to ensure oxygen saturated grown films [101]. The target to substrate distance and the applied power influences the growth rate. The growth rate increases with an increase in

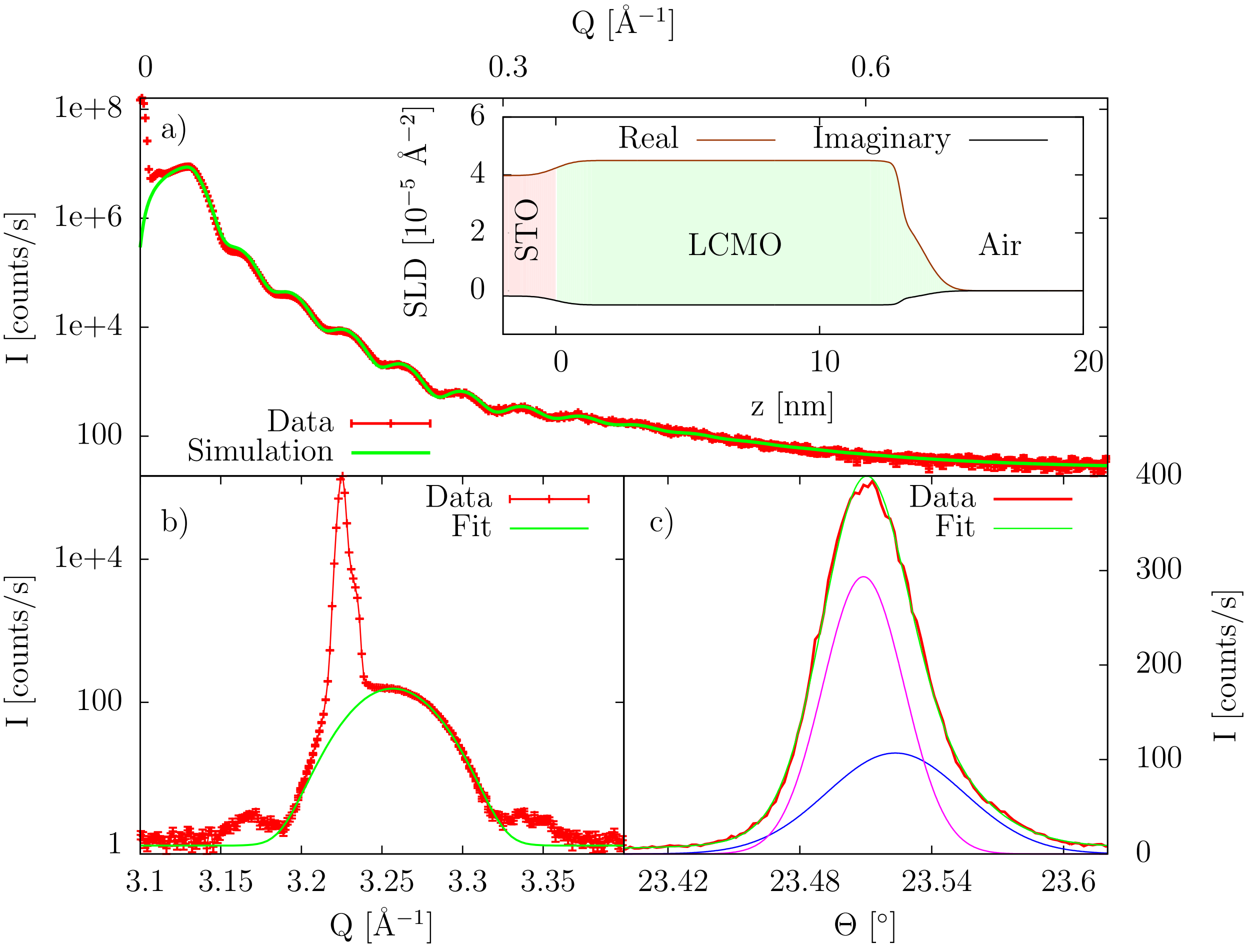

Figure 5.11.: a) X-ray reflectometry measurement with simulation thereof. SLD of simulation is shown in the inset. b) Diffraction measurement of the (002) Bragg peak in out-of-plane direction. c) Rocking scan of the (200) Bragg peak fitted with two Gaussian functions in order to get the FWHM. (Sample: SP_{193})

the applied power and a decrease of the target to substrate distance. The above mentioned parameters were adjusted for fast growth in order to minimize thickness variations, due to a non-stable growth rate. Therefore, all films were grown in 3 mbar oxygen pressure, an applied power of 120 W and a target to substrate distance of 2.5 cm and only the best growth temperature had to be determined.

Then XRR, AFM measurements and rocking scans, around the (002) Bragg peak, were performed to determine the film quality. The important parameters are presented in **table 5.3** and in **figure 5.7** and the data for the parameter determination can be looked up in **appendix H**. No LEED measurements can be carried out while growing with HOPSA.

The parameters determined from XRR and AFM measurements, as well as the width of the Bragg peak, show a similar behavior. The best growth temperature for LCMO, grown with HOPSA, is around 800°C with slightly lesser growth quality at lower temperatures

Temperature [°C]	700 (SP$_{194}$)	800 (SP$_{193}$)	900 (SP$_{195}$)
XRR roughness (Top layer) [Å]	$16.03\ ^{+1.10}_{-1.23}$	$6.56\ ^{+0.33}_{-0.14}$	$48.08\ ^{+6.98}_{-2.73}$
XRR roughness (LCMO layer) [Å]	$3.95\ ^{+0.25}_{-0.24}$	$1.59\ ^{+0.06}_{-0.03}$	$4.00\ ^{+0.23}_{-0.25}$
RO width [10^{-2} °]	5.77 ± 0.02	5.24 ± 0.01	11.99 ± 0.03
AFM roughness [Å]	6.82	4.95	37.90

Table 5.3.: The film roughness, from XRR and AFM measurements, as well as the (002) Bragg peak width derived from rocking scans, are presented for the LCMO film grown with HOPSA.

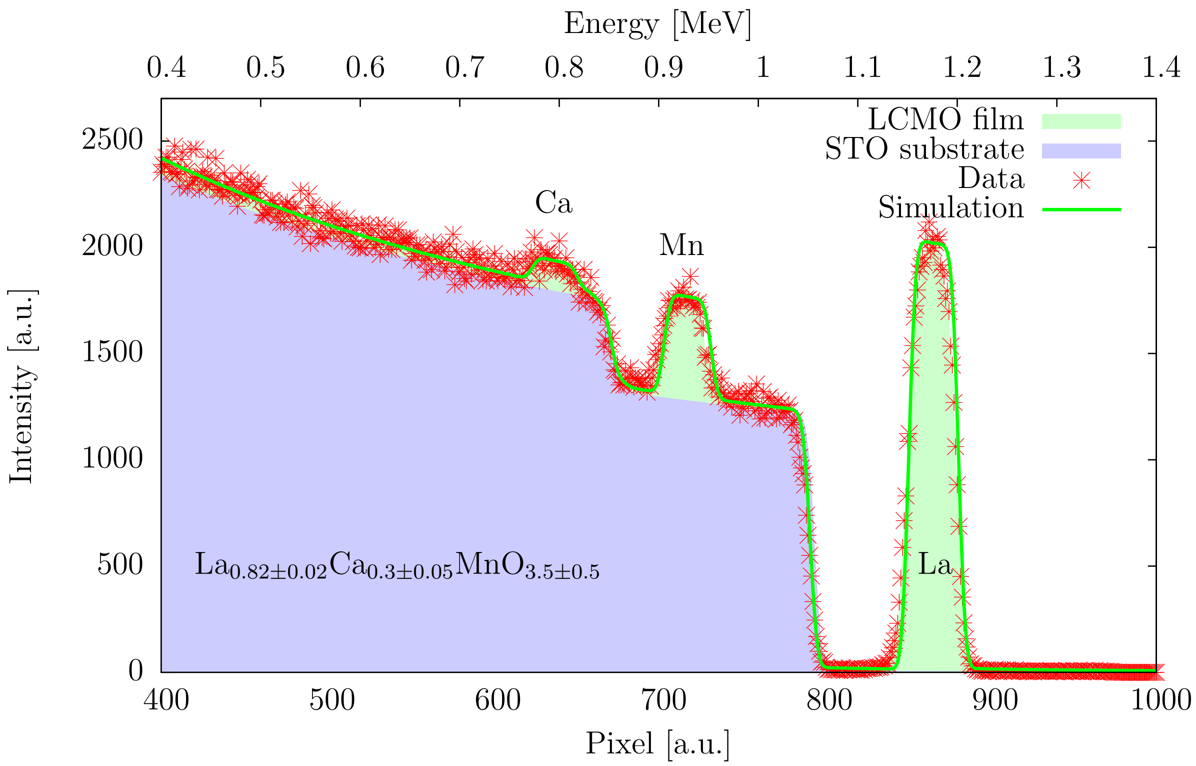

Figure 5.12.: RBS measurement done on a LCMO thin film (Sample: SP$_{208}$) grown on a STO substrate at 800°C, with a simulation in order to derive the stoichiometry.

and a much poorer growth quality at higher temperatures. As expected, the quality of the film grown with HOPSA has, in general, a significantly lower film quality than grown with OMBE. This can be especially seen in the broader (002) Bragg peak in **figure 5.11** c) and the less pronounced thickness oscillations in the diffraction measurement in out-of-plane direction in **figure 5.11** b). The lower crystalline quality leads to a higher film roughness visible in the XRR measurement (see **figure 5.11** a). However, the growth process with HOPSA is much simpler and faster.

The stoichiometry was determined with RBS measurement on a LCMO film grown at 800°C (Sample: SP$_{208}$). The measurement and the simulation thereof is shown in

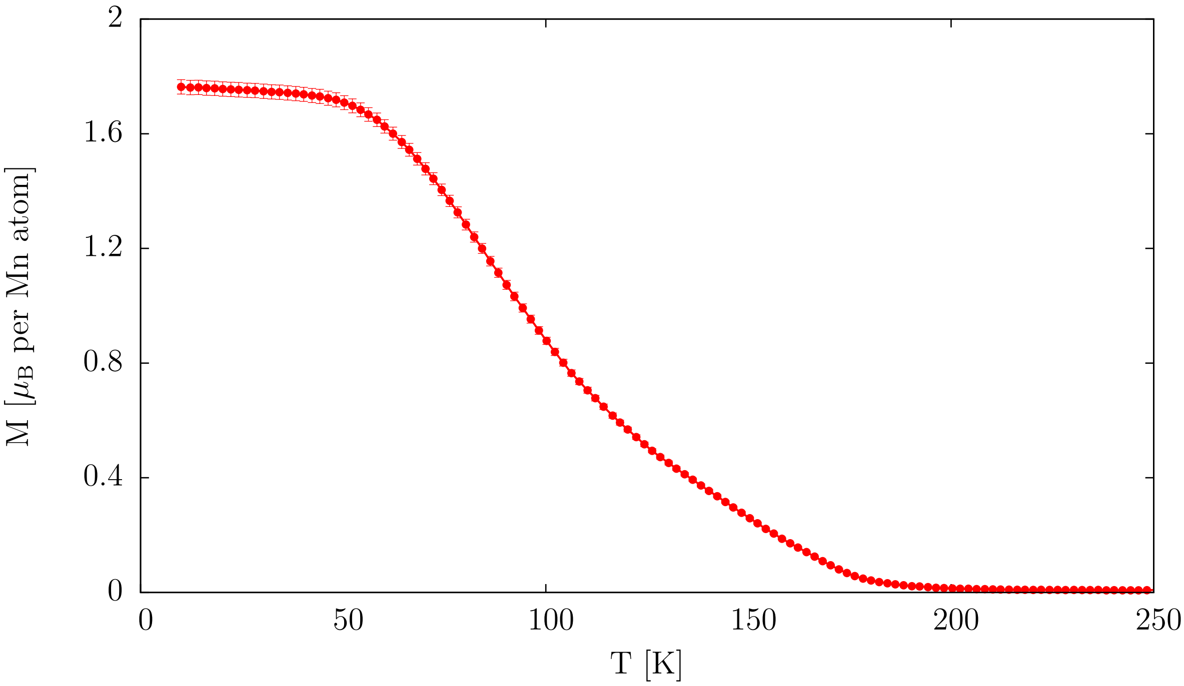

Figure 5.13.: Field cooled measurement at 100 Oe of LCMO film grown at 800°C on a STO substrate. (Sample: SP_{193})

figure 5.12, where a stoichiometry of $La_{0.82}Ca_{0.3}MnO_3$ could be determined. Therefore, the LCMO films grown by sputtering have an excess of La, which might explain the decline in structural quality.

The magnetic properties of the LCMO film grown at 800°C with HOPSA (Sample: SP_{193}) show a different behavior than the LCMO film grown with OMBE. The field cooled measurement is shown in **figure 5.13**, where the magnetic moment was assigned to the Mn atoms ($d = 130.71\ ^{+0.24}_{-0.09}$ Å, $A = 25$ mm$^2 \pm 0.1$ mm^2 and $\rho = 1.70\ ^{+0.01}_{-0.00} \cdot 10^{-2}$Å^{-3}). The magnetic moment of the LCMO film is reduced, which is similar to the LCMO film grown with OMBE, but even further down to 1.75 μ_B. The Curie temperature is difficult to determine, but the onset of the magnetization starts at 170 K ± 5 K. The shape of the field cooled measurement does not show a typical ferromagnetic behavior. Between 100 K and 170 K an additional magnetic contribution seems to be present. This might come from the off-stoichiometry of the LCMO film or due to defects in the crystalline structure caused by the growth method. These defects might alter the superexchange and double exchange interactions and lead to this behavior.

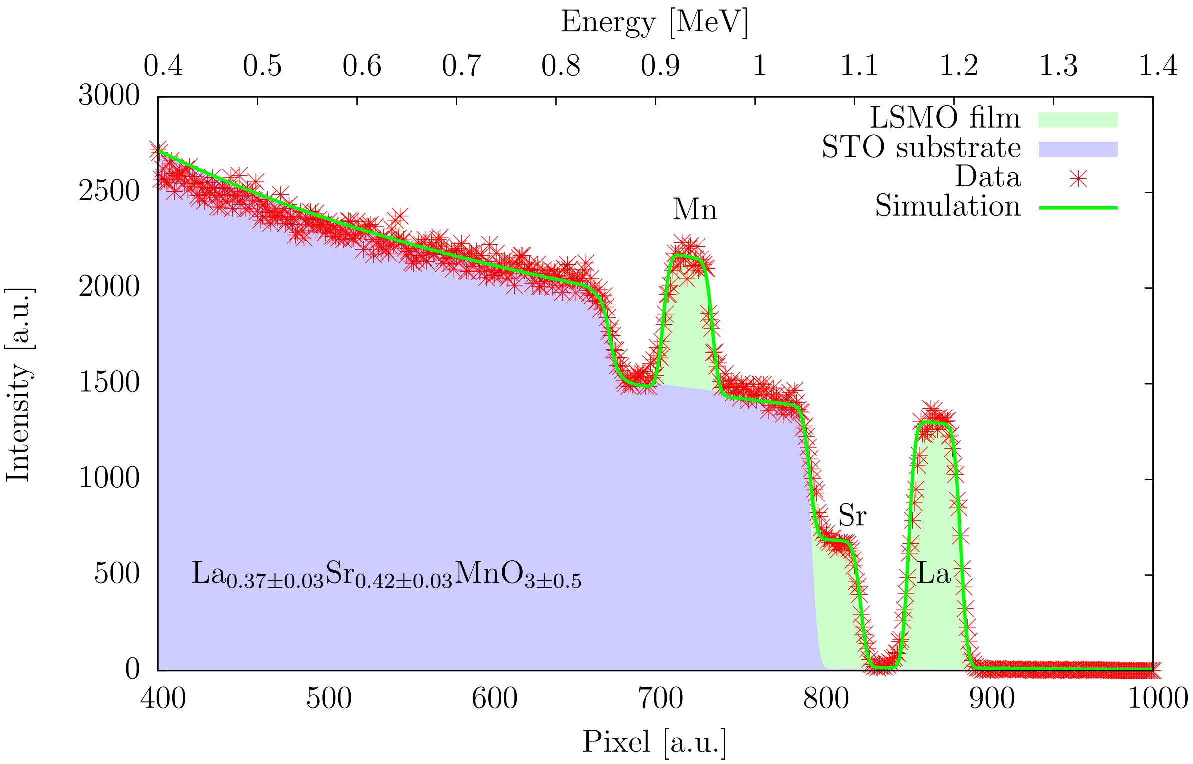

Figure 5.14.: RBS measurement done on a LSMO thin film grown on a STO substrate at 1000°C (Sample: $OMBE_{0248}$), with a simulation in order to derive the stoichiometry.

5.2.2. $La_{0.7}Sr_{0.3}MnO_3$

The LSMO thin films were grown with OMBE and HOPSA in order to compare different growth methods with a desired stoichiometry of $La_{0.7}Sr_{0.3}MnO_3$.

Oxygen Molecular Beam Epitaxy (OMBE)

Normally, film growth parameters, for the OMBE growth, have to be optimized to improve the surface roughness of the growing film and to reduce the full width half maximum (FWHM) of the rocking scans at out-off-plane Bragg reflections. Additionally, the described iterative process of film growth and the RBS measurement has to be done to improve the stoichiometry of the films. As this is a very time-consuming procedure, it could not be carried out to the desired extent. The stoichiometry could only be analyzed afterwards, resulting in a stoichiometry of $La_{0.37\pm0.03}Sr_{0.42\pm0.03}MnO_{3\pm0.5}$ (**figure 5.14**). The LSMO film was grown with the following parameters: oxygen flow of 0.08 sccm, resulting in a pressure in the OMBE system of $\sim 2.5\cdot10^{-6}$ mbar. The substrate temperature during growth was of 1000°C.

The grown LSMO samples have a huge deficiency of La atoms and a slight excess of Sr atoms, but show, nevertheless, a good structural quality (**figure 5.16**) with a surface roughness of 1.7 nm determined with XRR measurements (**figure 5.16**). The

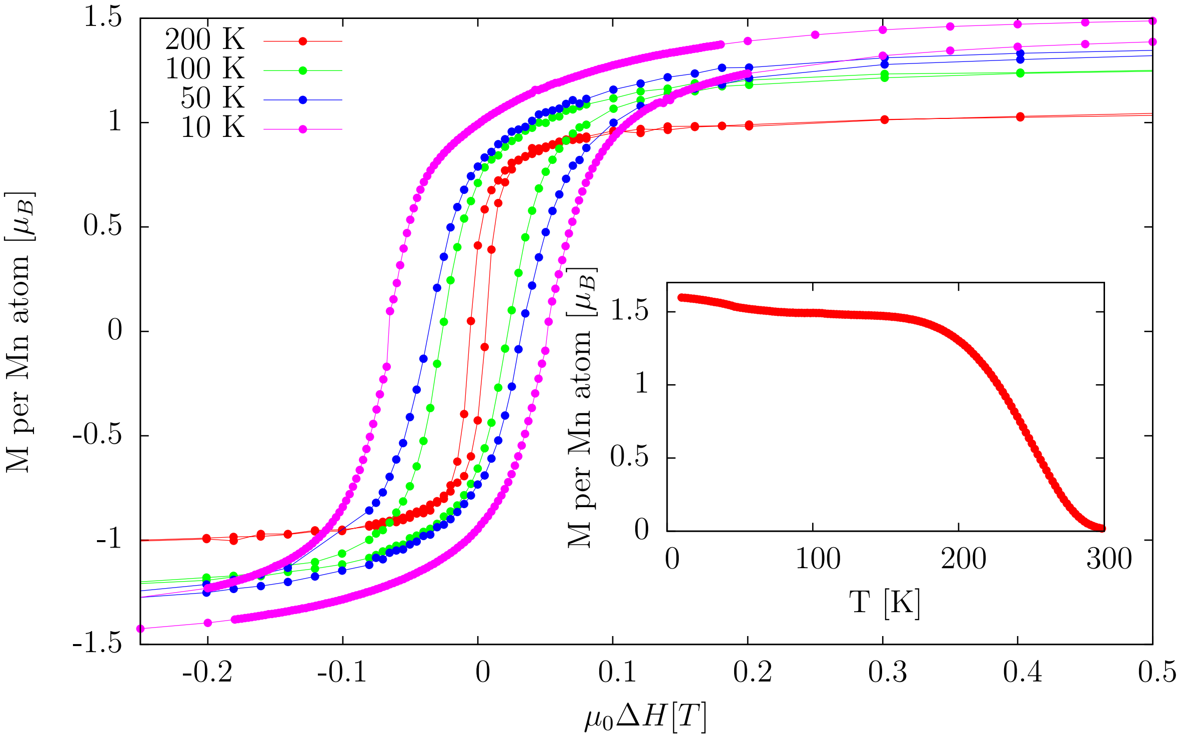

Figure 5.15.: Hysteresis measurements at 10, 50, 100 and 200 K and field-cooled measurement with an applied magnetic field of 100 Oe on LSMO thin film grown on a STO substrate (Sample: OMBE_{0248}).

LSMO film shows a high crystalline quality, visible in the intense Bragg peak in the XRD measurement (**figure 5.16**) and the pronounced thickness oscillations around the (002) Bragg peak. The magnetism of the LSMO layer was assigned to the Mn atoms, by using the following parameters: LSMO layer thickness $d = 407.04\,^{+0.48}_{-0.07}$ Å, the surface area $A = 20.4\ \mathrm{mm}^2 \pm 0.1\ \mathrm{mm}^2$ and the LSMO unit cell density $\rho = 1.71\,^{+0.43}_{-0.37} \cdot 10^{-2}$ Å^{-2}. The LSMO films show normal ferromagnetism with lower Curie temperature ($\mathrm{T_C} \sim 270$ K ± 10 K, **figure 5.15**) compared to a stoichiometric sample ($\mathrm{T_C} \sim 380$ K) as well as a reduced magnetization of less than 2 μ_B compared to 3.7 μ_B. The poorer magnetic properties can be explained with the large off-stoichiometry of the sample. This has a huge effect on the superexchange and double exchange interactions, altering the magnetism inside the LSMO layer.

High Oxygen Pressure Sputtering Automaton (HOPSA)

In order to grow the LSMO films with HOPSA, a target with the desired stoichiometry of $\mathrm{La_{0.7}Sr_{0.3}MnO_3}$, with 2″ diameter and 0.125″ thickness, from Kurt J. Lesker Company [100] was used. The target has a purity of 99.9% and the stoichiometry was checked by analyzing grown LSMO films with RBS measurements (**figure 5.19**).

To determine the growth parameters for the LSMO film, the same procedure was done as for the LCMO film with the same substrate and target preparation before growth.

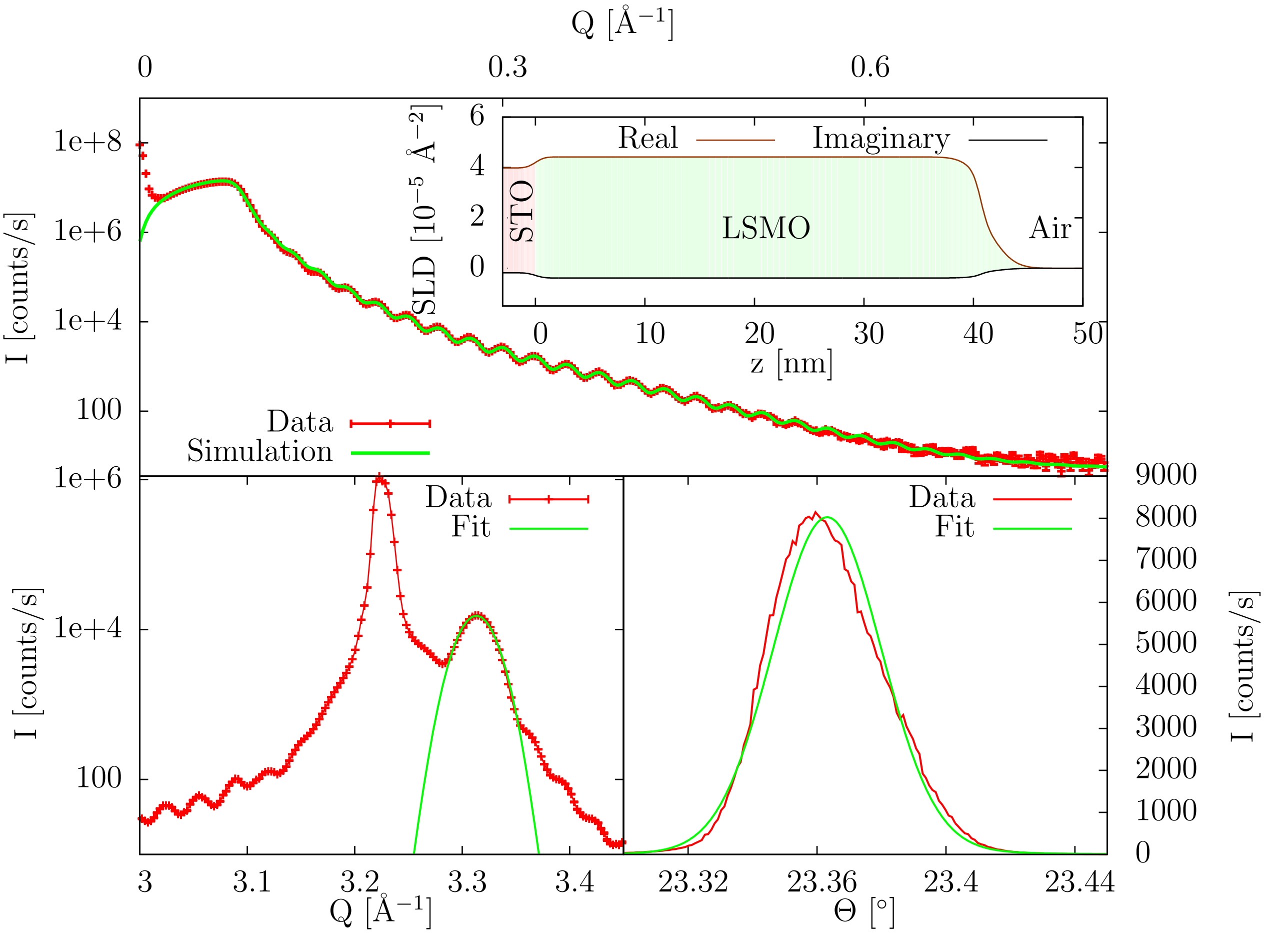

Figure 5.16.: XRR of LSMO film (Sample: OMBE$_{0248}$) grown at 800°C. Inset: XRD measurement of the (002) Bragg reflection in the out-off-plane direction. The out-of-plane lattice parameter of the LSMO film can be derived to 3.79 Å ± 0.02 Å.

The derived parameters from XRR, AFM measurements and rocking scans are given in **table 5.4**. It seems that lower growth temperatures for the LSMO film result in a better film quality, with the best growth temperature at 800°C. The roughness of the LSMO surface is nearly two times larger than the surface roughness of the LCMO film. In contrast to that, the Bragg peak width is slightly smaller than the Bragg peak width of the LCMO film, resulting in a lower surface quality, but a better crystalline quality. The XRR and XRD measurements of the LSMO film, grown at a substrate temperature of 800°C (Sample: SP$_{199}$), are shown in **figure 5.18**, indicating the better structural quality compared to the LCMO films growth with HOPSA (**figure 5.11**).

The better crystalline quality might result from a better stoichiometry, as can be seen in **figure 5.19**. The RBS measurement shows that the LSMO film (Sample: SP$_{207}$) grows in a stoichiometry of: La$_{0.67\pm0.02}$Sr$_{0.22\pm0.03}$MnO$_{2.5\pm0.5}$, with a slightly smaller La and Sr concentration. The reason for the larger surface roughness is unclear.

The field cooled measurement (Sample: SP$_{199}$) at an applied magnetic field of 100 Oe in

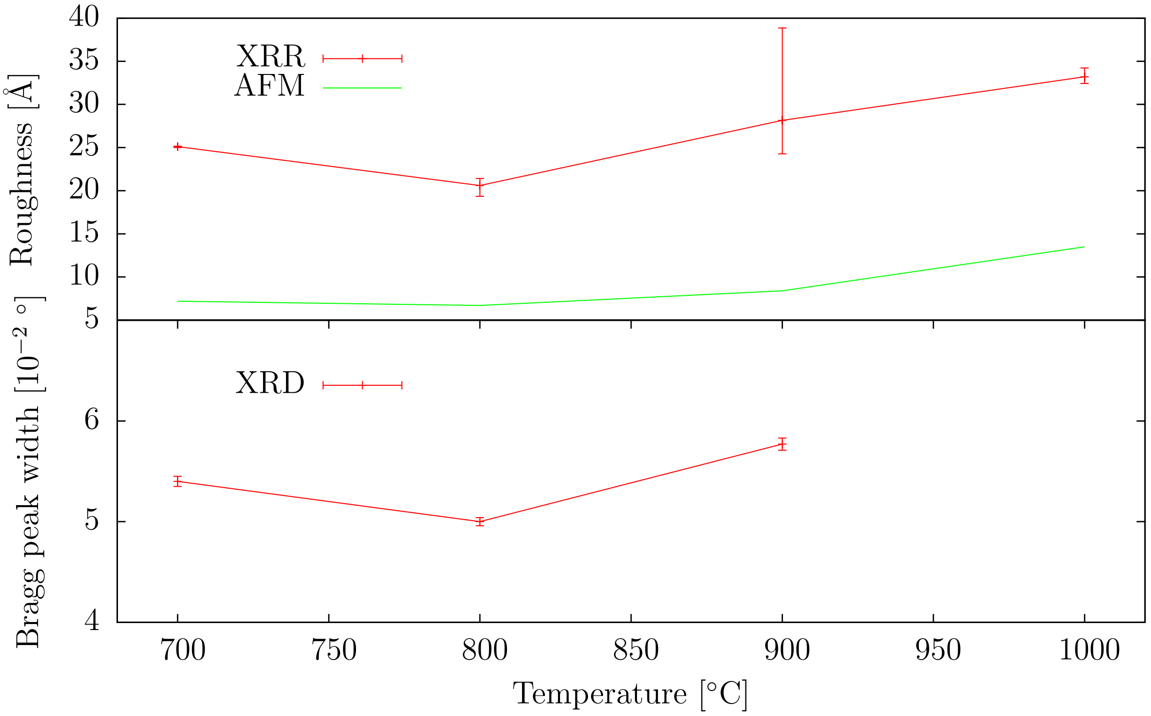

Figure 5.17.: Derived LSMO film parameters from XRR, XRD and AFM measurements. Presented are the film roughness from XRR and AFM measurements as well as (002) Bragg peak width derived from rocking scans.

Temperature [°]C	700 (SP_{203})	800 (SP_{199})	900 (SP_{198})	1000 (SP_{196})
XRR roughness (Top layer) [Å]	$25.11\ ^{+0.04}_{-0.11}$	$20.61\ ^{+0.00}_{-1.25}$	$28.16\ ^{+10.69}_{-3.88}$	$33.21\ ^{+1.01}_{-0.78}$
XRR roughness (LSMO layer) [Å]	$8.90\ ^{+0.04}_{-0.00}$	$3.15\ ^{+0.03}_{-0.13}$	$3.42\ ^{+0.10}_{-0.87}$	$4.00\ ^{+0.03}_{-0.30}$
RO width [10^{-2} °]	5.4 ± 0.05	5.0 ± 0.04	5.77 ± 0.06	-
AFM roughness [Å]	7.25	6.72	8.46	13.51

Table 5.4.: Derived LSMO film parameters from XRR, XRD and AFM measurements. From the XRR measurements the LSMO film roughness is shown. The rocking scan (RO) shows the (002) Bragg peak width. The AFM measurements show the surface roughness from a 5 μm square area.

figure 5.20 shows a typical ferromagnetic behavior with a Curie temperature of around 350 K ± 10 K, which is over 30 K lower then the Curie temperature of bulk LSMO. Additionally, the magnetic moment of Mn is reduced to 3.35 μ_B, from the nominal 3.7 μ_B. The magnetic properties variate only slightly from the bulk LSMO films, compared to the other grown LSMO or LCMO thin films. The following parameters were used for the normalization of the magnetic moment: LSMO layer thickness $d = 202.43\ ^{+1.28}_{-1.27}$ Å, the surface area $A = 25\ \text{mm}^2 \pm 0.1\ \text{mm}^2$ and the LSMO unit cell density $\rho = 1.71\ ^{+0.05}_{-0.02} \cdot 10^{-2}$ Å^{-3}.

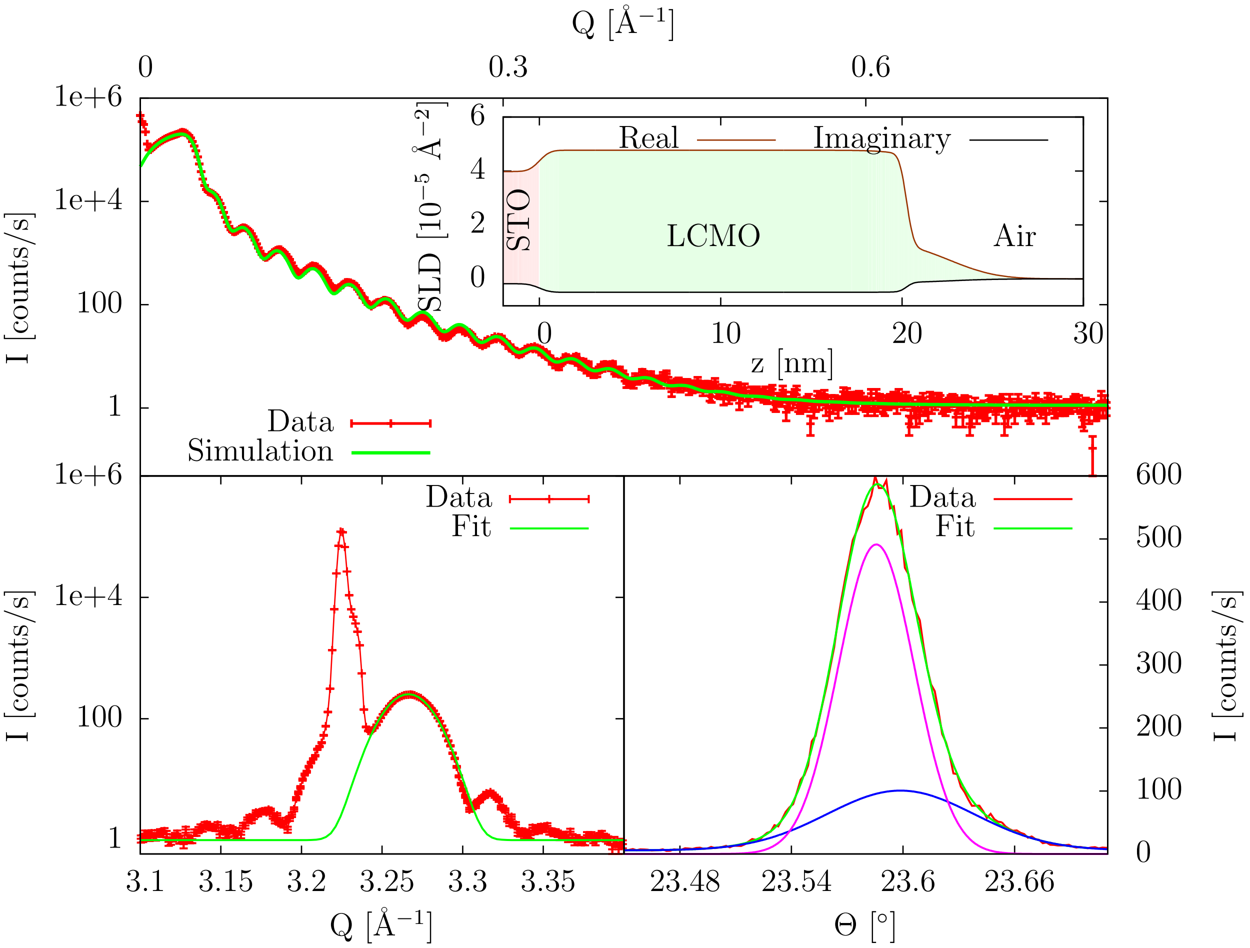

Figure 5.18.: a): XRR of LSMO film (Sample: SP_{199}) grown at 800°C. b) XRD measurement of the (002) Bragg peak in out-off-plane direction. c) Rocking scan of the (002) Bragg peak with Gaussian fit.

5.2.3. Results

The analysis of the temperature-dependence of the LSMO and LCMO film quality indicates that the best growth temperature for LSMO and LCMO films is around 800°C. This temperature is a rough estimation, but around the best growth temperature, the variation of film quality is small. The LSMO and LCMO perovskites are behaving over a large temperature range very well, but the off-stoichiometry limits the film quality.

The magnetic properties of all films are different from the bulk magnetic properties. This might come from off-stoichiometry, strain altered superexchange and double interchange interactions or the known magnetic “dead” layer in transition metal oxide thin films [102].

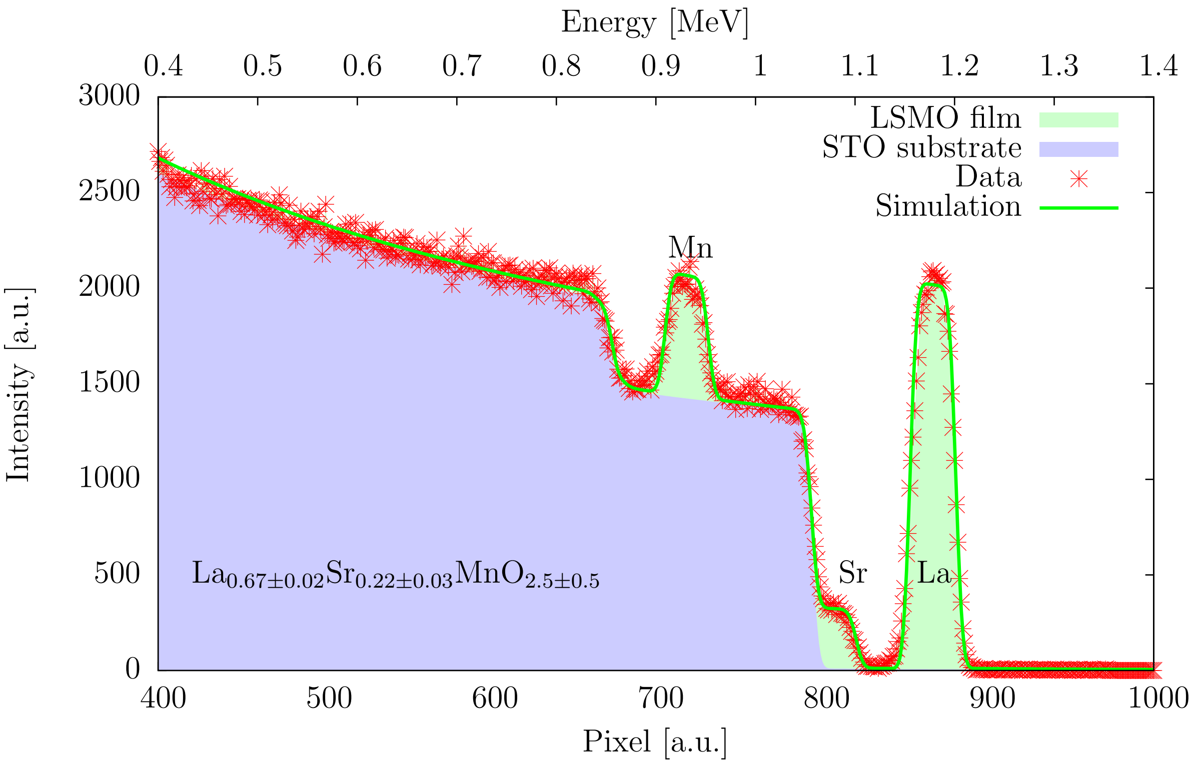

Figure 5.19.: RBS measurement carried out on a LSMO thin film grown on a STO substrate at 800°C (Sample: SP_{207}), with a simulation in order to determine the stoichiometry.

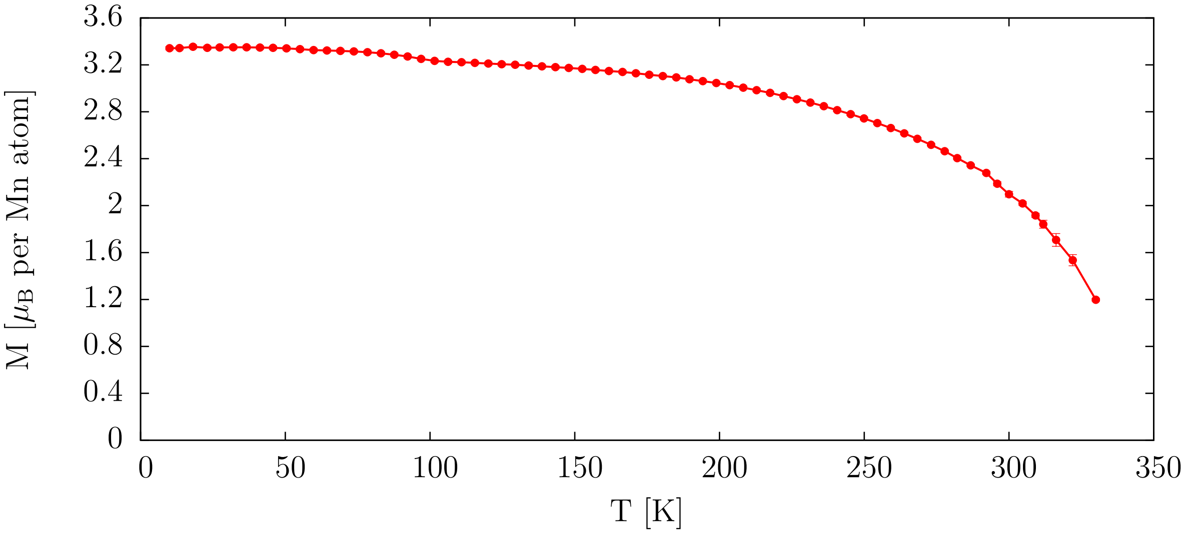

Figure 5.20.: Field cooled measurement of LSMO film grown at 800°C at an applied magnetic field of 100 Oe (Sample: SP_{199}).

5.3. Aging of Transition Metal Oxide Thin Films

Grown transition metal oxide (TMO) thin films are showing aging effects. Repeating the XRR measurements after one year, the XRR measurements show a slightly different behavior, which can be seen in **figure 5.21**. Although the roughness does not change very much, as can be seen in a similar surface roughness in the AFM measurements and in just a slightly higher surface roughness derived from XRR simulations, the XRR measurements show a modulation of the thickness oscillations. The simulation of the XRR measurements indicate a reduced SLD at the surface of the TMO layer (**figure 5.21**). In order to simulate a modulation of the thickness oscillations, the SLD has to be reduced by 25% with a thickness of this reduction of around 2 nm (**table 5.5**). The reduction of the SLD can be explained either with a reduced density of the unit cell or with a stoichiometry change at the TMO layer surface. From heated LSMO thin films in vacuum it is known that oxygen deficiencies can be induced by changing the thermal equilibrium. This can explain the reduced SLD directly at the surface. Due to the small thickness fraction in comparison to the whole film thickness, no change in XRD measurements can be seen.

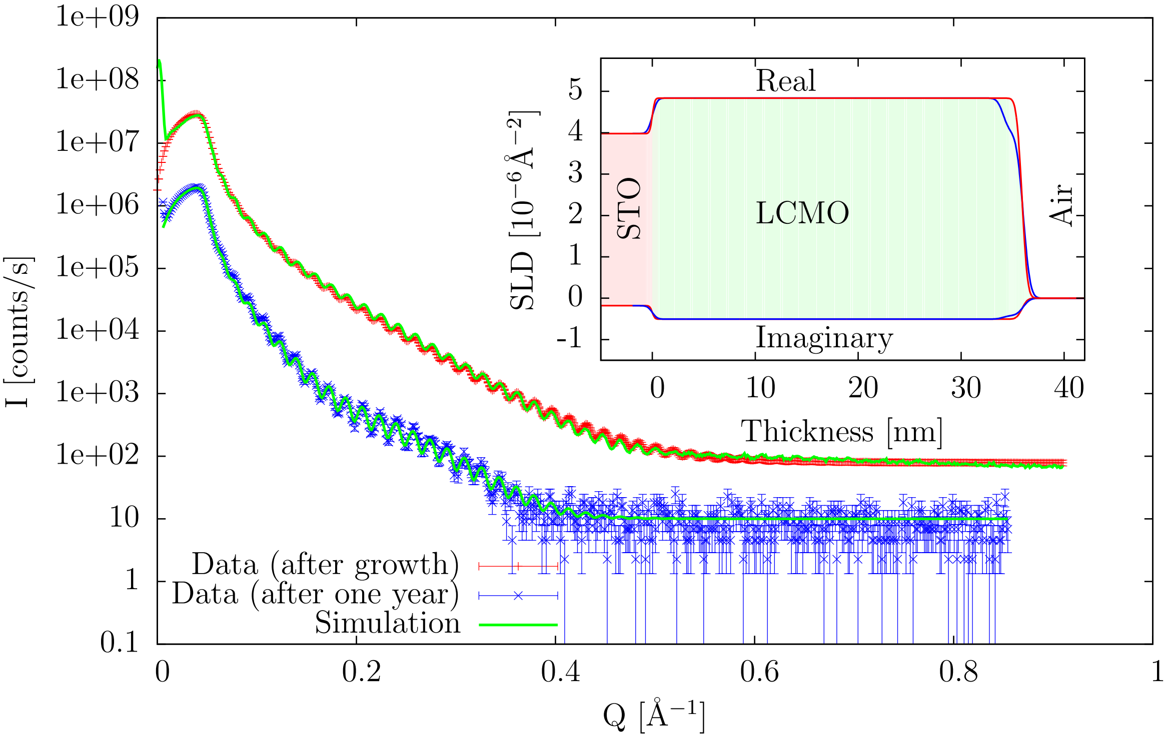

Figure 5.21.: XRR measurement of LCMO thin film grown on STO substrate at 800°C (Sample: OMBE$_{0240}$) directly after growth (red) and one year later (blue). The simulations are shown as a green line. The inset shows the SLD used for both simulations, using the same color code. The negative SLD represents the imaginary part of the SLD.

		d [Å]	σ [Å]	ρ [10^{-2}Å^{-3}]	ρ^{Norm}	**Re** SLD [10^{-5}Å^{-2}]	**Im** SLD
old	STO	-	$3.84^{+0.41}_{-0.74}$	1.68	1.68	3.98	0.18
	LCMO	$340.99^{+1.52}_{-0.40}$	$4.78^{+0.50}_{-0.25}$	$1.73^{+0.02}_{-0.05}$	1.72	$4.58^{+0.07}_{-0.14}$	$0.50^{+0.01}_{-0.02}$
	LCMO_{top}	$19.37^{+0.96}_{-0.90}$	$5.31^{+0.20}_{-0.22}$	$1.44^{+0.02}_{-0.04}$	1.72	$3.81^{+0.04}_{-0.09}$	$0.41^{+0.00}_{-0.01}$
new	STO	-	$1.51^{+0.62}_{-0.02}$	1.68	1.68	3.98	0.18
	LCMO	$359.26^{+0.45}_{-0.04}$	$4.28^{+0.01}_{-0.03}$	$1.73^{+0.04}_{-0.05}$	1.72	$4.49^{+0.12}_{-0.14}$	$0.49^{+0.01}_{-0.02}$

Table 5.5.: Fitting parameters for XRR measurement directly after growth and one year later (Sample: OMBE_{0240}). Presented are: Layer thickness d, roughness σ, density ρ, the real and imaginary part of the scattering length density SLD.

5.4. Growing of Metallic Pd on Oxides

In order to perform PNR measurements, multilayers are desired because of increased intensity and sharper Bragg peaks. For metals or oxides it is mostly possible to grow these multilayers. For a heterostructure of a metal and an oxide film it turned out to be more complicated. Oxides mainly need high temperatures to form the required structure and metals require intermediate temperatures. Additionally, the surface energies of oxides and metals are very different, resulting very likely in Volmer-Weber growth mode. Therefore, the possibility of metal/oxide multilayers is investigated.

As described in the previous section, the investigated LSMO and LCMO films need temperatures around ≈ 800°C. The Pd layer in contrast requires intermediate temperatures around 100°C. When growing the metallic Pd on a LSMO film at room temperature, the film shows a good crystalline quality, with a smooth surface.

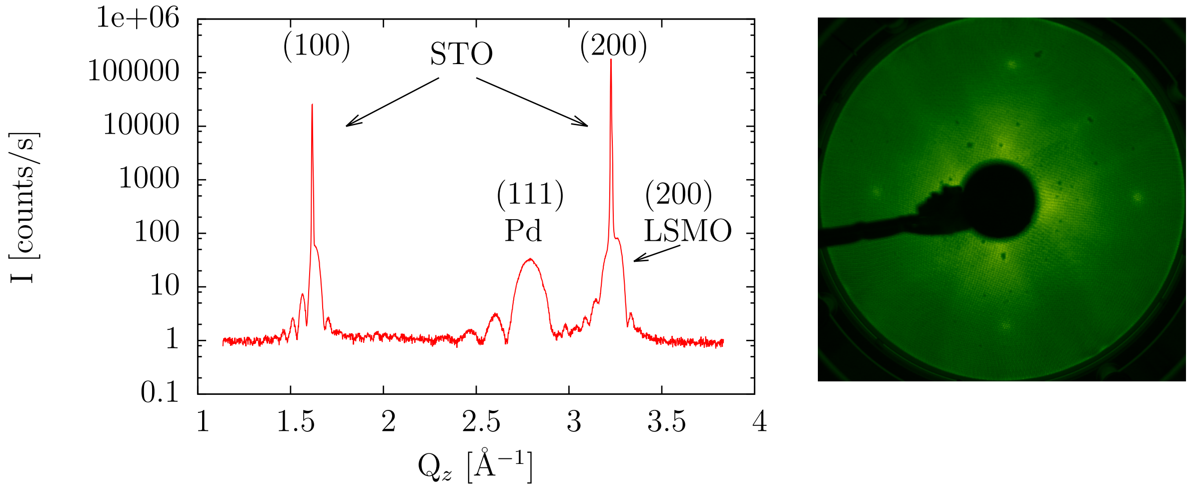

Figure 5.22.: Left: XRD measurement of LSMO/Pd films on a STO substrate in out-of-plane (001) direction. Right: LEED image of the Pd layer directly after growth at 150 eV. (Sample: OMBE_{208})

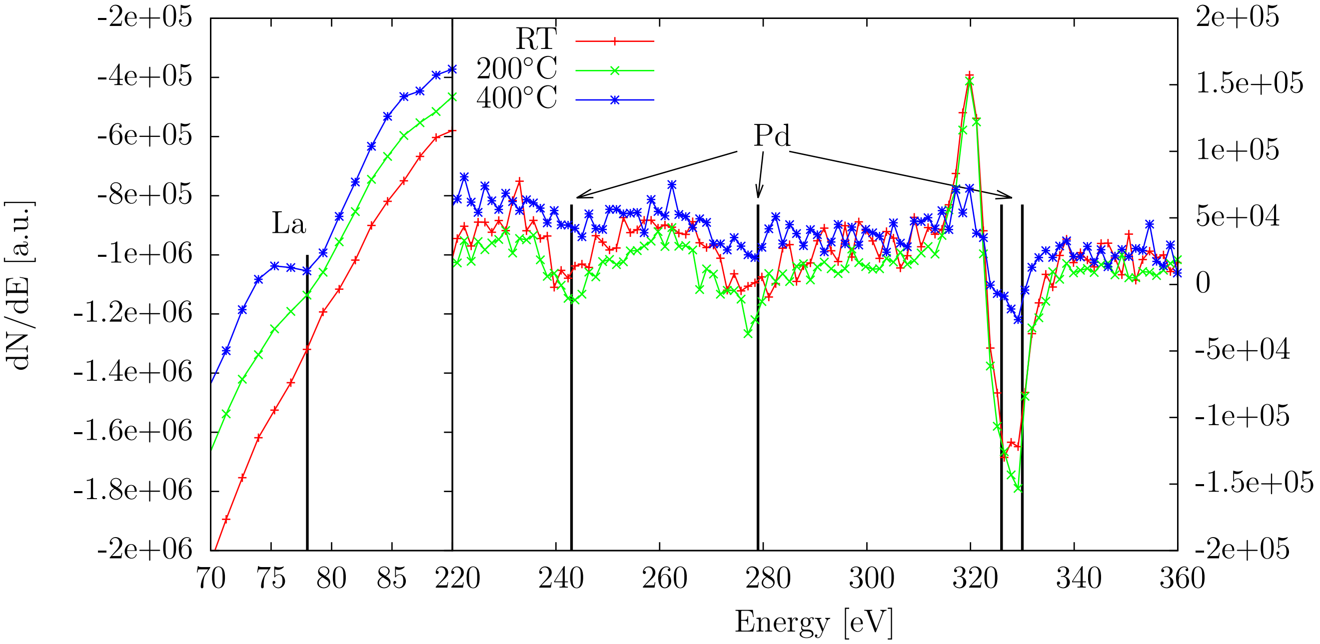

Figure 5.23.: AES measurement of Pd/LCMO film (Sample: OMBE$_{0254}$) directly after growth at RT and after heating the sample at 200 and 400°C.

The out-of-plane line scan in (001) direction of the XRD measurement is shown in **figure 5.22**. The LSMO peaks are located directly at the Bragg peaks of the STO substrate. The additional Bragg peak at 2.79 Å^{-1} has to come from Pd. The Bragg peak position correspond to the (111) Bragg peak of Pd, meaning that Pd grows in (111) direction on the (001) orientated LSMO film. In contrast to this (111) growth direction of Pd, the LEED picture in **figure 5.22** shows a four fold symmetry, which does not fit to the (111) growth direction, but rather to the (001) growth direction. Unfortunately, the (00x) Bragg peaks, with x = 1, 2, 3, 4, are not directly visible in the XRD measurements, as they are overlapping with the corresponding Bragg peaks of LSMO and STO. But the conclusion of the LEED and XRD measurements indicate that Pd does not grow in a single crystalline structure, but in some polycrystalline structure. Nevertheless, the crystalline quality is very good, as can be seen in the intense Pd Bragg peaks.

When heating Pd in order to grow the next LSMO or LCMO layer, the Pd film starts to dewet and to create nanostructures. In **figure 5.23** the AES measurement of a heated Pd layer grown on a LCMO layer is shown. The measurements were carried out after the growth of the Pd layer at room temperature and after heating the sample for 20 min at 200 and 400°C. As can be seen on the right hand side between 230 eV and 340 eV, the peaks in the AES spectrum corresponding to the Pd layer lose in intensity. In contrast to that, the La peak intensity, shown at the left-hand side at an energy of 80 eV, grows in intensity. The Pd film starts to flow together at higher temperatures and creates crystalline nanostructures, reducing the surface energy. This can be seen in the AFM measurement and the height distribution shown in **figure 5.24**, where the nanostructures are clearly visible. As can be seen in the height distribution, the height of the Pd nanostructures

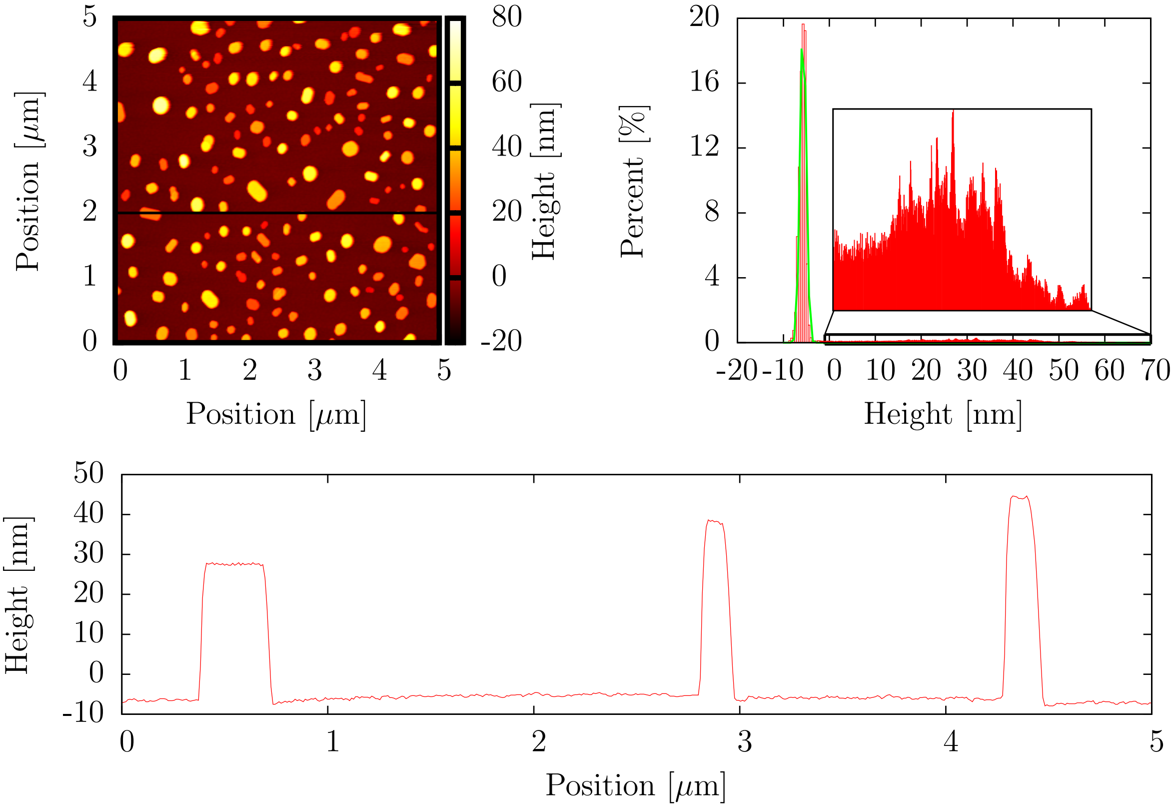

Figure 5.24.: AFM measurement of Pd/LCMO film (Sample: OMBE$_{0254}$) with topography (top left), height distribution with Gaussian fit to peak at -5 nm (top right) and line profile (bottom). The line profile is indicated in the topography image.

is nearly uniformly distributed between 0 nm and 70 nm, whereas the LCMO film has nearly the same surface roughness, as the the single LCMO film (see **section 5.2.1**). The roughness of the LCMO films is around 0.62 nm ± 0.02 nm, when fitting a Gaussian function to the peak in the height distribution. Due to the formation of the Pd nanostructures, when heating the samples to growth temperatures of the LSMO and LCMO films, multilayered samples are not possible.

6. Data Treatment

State of the art polarized neutron reflectometry (PNR) and X-ray magnetic circular dichroism (XMCD) experiments are very complex, when small effects are investigated. Additionally, the data treatment can become very complicated due to e.g. an area detector. Therefore, the data treatment of PNR and XMCD experiments will be discussed in the following, beginning with PNR experiments.

6.1. Data Treatment of PNR Experiments

Investigation of interface effects with PNR measurements requires proper data treatment due to small effects on the measured signal. An additional complication is the overlapping of the interface effects with effects from imperfect interfaces and instrument inaccuracies.

Therefore, different aspects of PNR measurements with an area detector will be discussed in the following subsection. It starts with the handling of off-specular scattering, followed by the description of the sensitivity variations of a ^{3}He detector. The third section covers the corrections for a misalignment of the sample, followed by resolution considerations, especially with a asymmetric wavelength distribution. The last section is about modeling of the sample and the simulation thereof.

6.1.1. Background Subtraction and Off-Specular Contribution

Nowadays, polarized neutron reflectometry measurements mainly use a two dimensional ^{3}He detector. Two dimensional detectors have the advantage to directly measure the background coming from the scattering of the sample holder, the air and from other surrounding neutron experiments. The contributions have different effects on the measured background. The background coming from other neutron experiments is mostly angle-independent and can be either subtracted from the reduced data or just simulated. Air scattering, scattering from the sample holder or off-specular scattering can be, in the worst case, angle-dependent, making the data treatment complicated. In this case every detector image has to treated separately and the background has to be subtracted individually.

Detector Image

Figure 6.1 shows the scattering geometry at the MARIA reflectometer at the MLZ. The measured sample is in a magnetic field of 1 T, which is in the plane of the sample surface and parallel to the polarization direction of the neutron beam. The scattering vector $\vec{Q}$ lies perpendicular to the sample surface. The detector, moving in the horizontal plane,

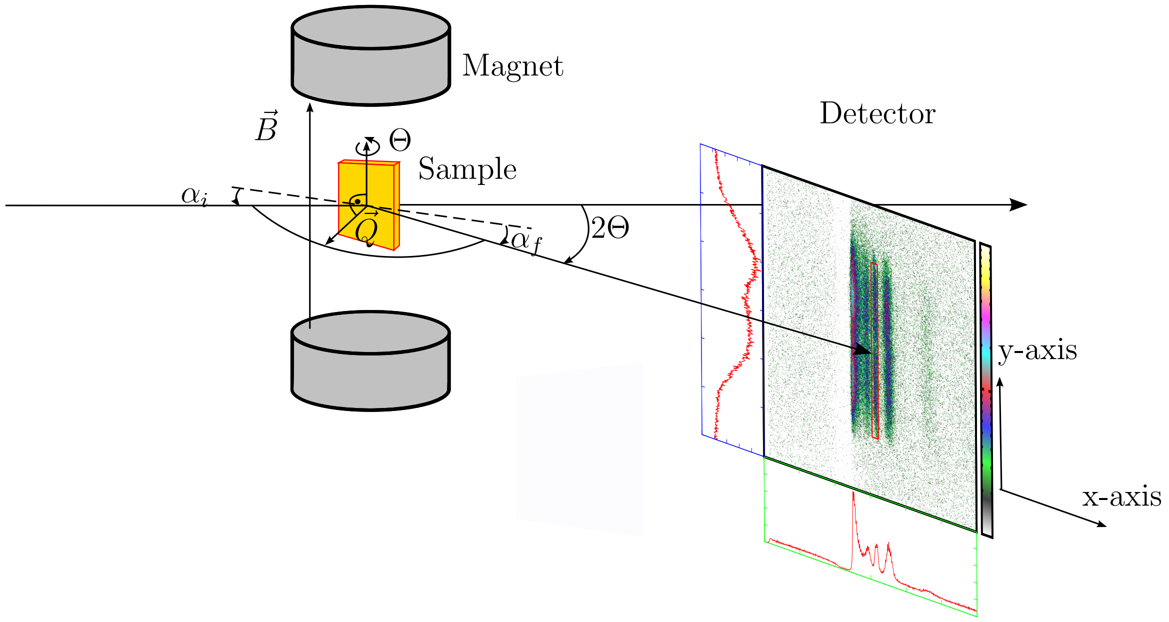

Figure 6.1.: Scattering geometry at the MARIA reflectometer with a two dimensional ^{3}He detector.

covers an area of 400 × 400 mm^2 with a pixel size of 0.019° in 2Θ, in a distance of 1910 mm from the sample.

A typical detector image of a Pd/Fe multilayer is shown in **figure 6.2** which has been measured at MARIA at a wavelength of 6 Å and $\alpha_i = 0.75°$. The sample consists of ten repetitions of 10 Å Fe/155 Å Pd bi-layers with a 155 Å Pd cover layer grown on a 10x10 mm^2 GaAs substrate with a 5 Å Fe seed layer and a 1500 Å Ag buffer layer. On the left-hand side the integration along the x-axis of the detector image is seen and on the bottom the integration along the y-axis. The beamstop at ① blocks the direct beam, but on the right-hand side of the beamstop at ② the tail from the direct beam is visible. The specular reflectivity is determined by integrating over the red boundary box at ③, which is the region of interest and was chosen to be smallest to minimize the background, but also to collect the whole scattered intensity. Between the tail of the direct beam and the reflected beam at ⑤ an additional peak can be found, coming from the surface scattering directly at the critical angle, called Yoneda peak. The other peaks at ④ or ⑥ are off-specular scattering (Bragg sheets) from the sample, due to correlated roughness throughout the different layers.

PNR Intensity Maps

The measured intensity in typical reflectometry experiments is the specular reflectivity, where the incident angle α_i is equal to the outgoing angle α_f of the neutron beam with respect to the sample surface. The roughness of real films reduces the intensity of the specular reflectivity and creates off-specular scattering (see **section 3.1**, specially **equation 3.14**). This off-specular scattering is randomly distributed in the case of uncorrelated

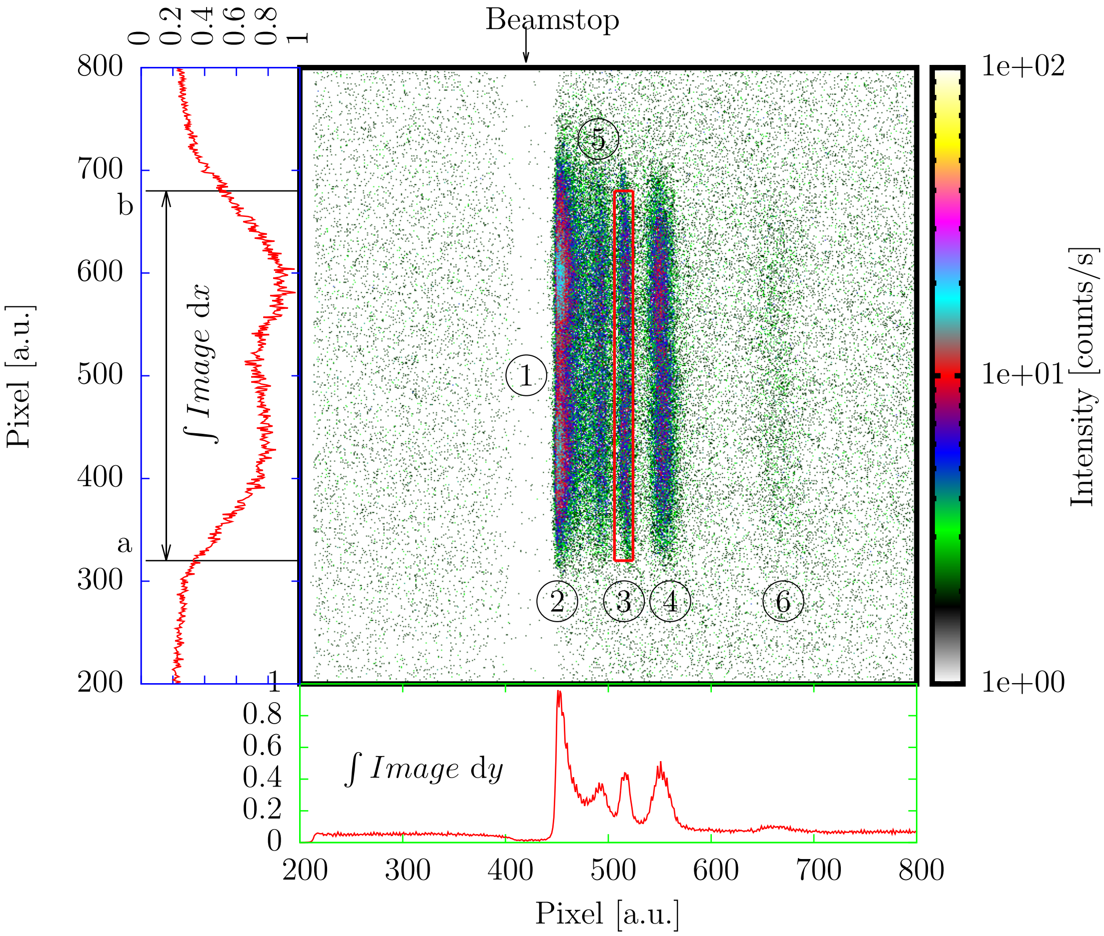

Figure 6.2.: The detector image from a neutron reflectometry measurement performed at MARIA on Pd/Fe multilayers with projections on the x- and y-axis.

roughnesses between different layers and can just be subtracted from the specular reflectivity. But in the case of correlated roughnesses between different layers, the off-specular scattering forms Bragg sheets and proper handling is necessary. In order to correct this off-specular scattering, each detector image is integrated along the y-axis and plotted as an α_i vs. α_f-map (**figure 6.3** left). The α_f is calculated from the detector position and the position of the considered pixel on the detector image by the equation,

$$\alpha_f = \alpha_0 + d_p \cdot x, \tag{6.1}$$

where $\alpha_0 = \alpha_i$ is the nominal position of the detector, $d_p = 0.0085°$ is the pixel size and x is the pixel position with respect to the center pixel, namely 512.5 (pixel at $\alpha_i = \alpha_f$). The finite sample size can be ignored, because it just broadens the peak of the specular reflectivity. The integration along the y-axis are plotted against the incident angle α_i and, as can be seen in **figure 6.3** on the left-hand side, are vertical lines in these kind of maps. The Bragg sheets have an angle α' to the integrated intensity along the y-axis of the detector images. This is the reason that the background subtraction cannot be done while working with each detector image individually. Therefore, the α_i vs. α_f-map

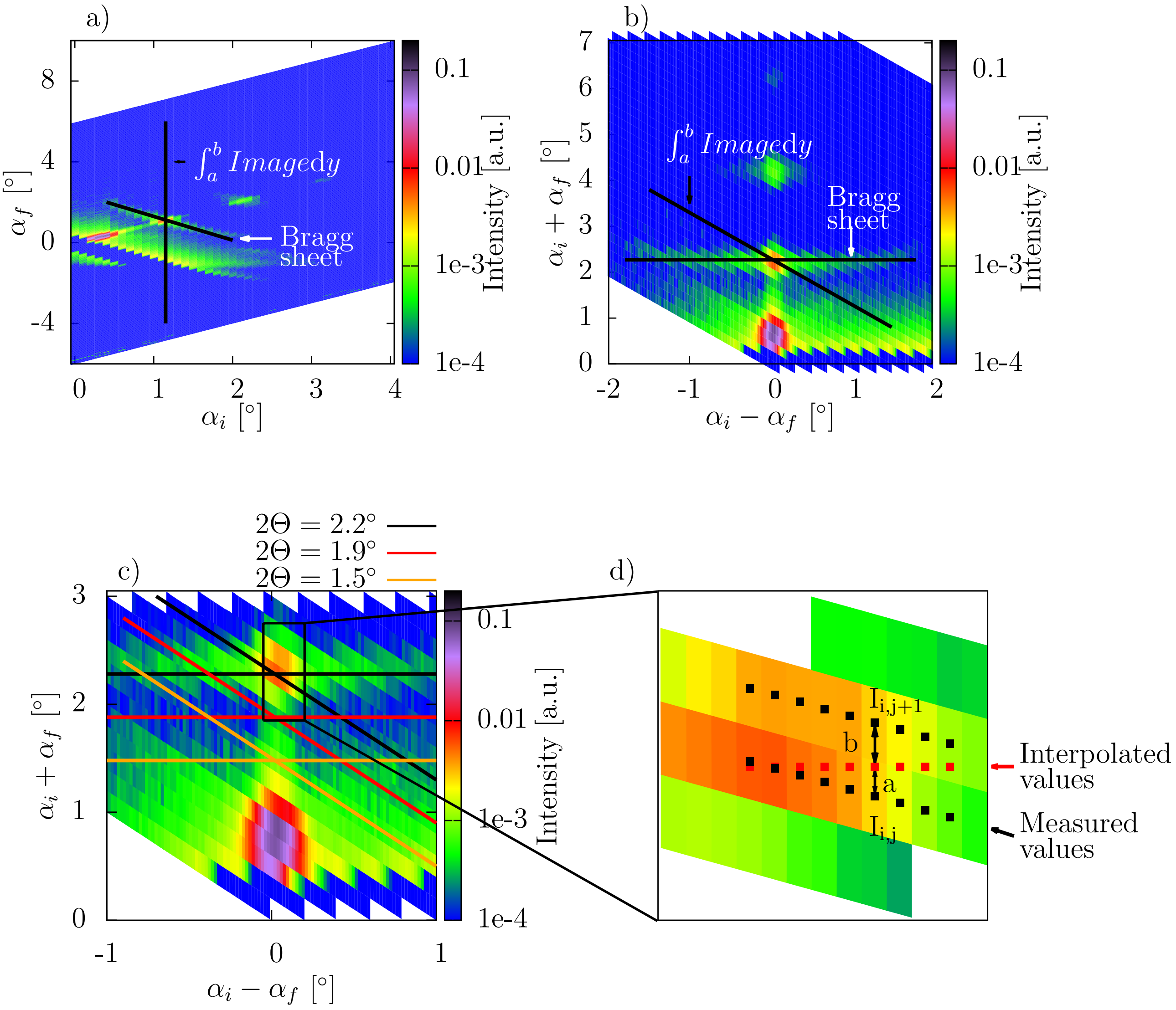

Figure 6.3.: a) α_i vs. α_f-map of Pd/Fe multilayer (Sample: MBE$_{05}$) measured at MARIA at MLZ. The integrated intensity of the detector images are vertical lines and the specular reflectivity is at $\alpha_i = \alpha_f$. The Bragg sheets and the specular reflectivity have an angle of 90°. b) The same intensity map as in *a* transformed into the $\alpha_i - \alpha_f$ vs. $\alpha_i + \alpha_f$-map. The vertical line at $\alpha_i - \alpha_f = 0$ is the specular reflectivity and the Bragg sheets are horizontal lines. c) An enlarged section of the intensity map shown in *b*. The orange, red and black lines are cuts discussed further in **figure 6.4** at different 2θ values.

has to be transformed into an $\alpha_i - \alpha_f$ vs. $\alpha_i + \alpha_f$-map in order to get the true specular reflectivity. The advantage of the $\alpha_i - \alpha_f$ vs. $\alpha_i + \alpha_f$-map is the clear position of the

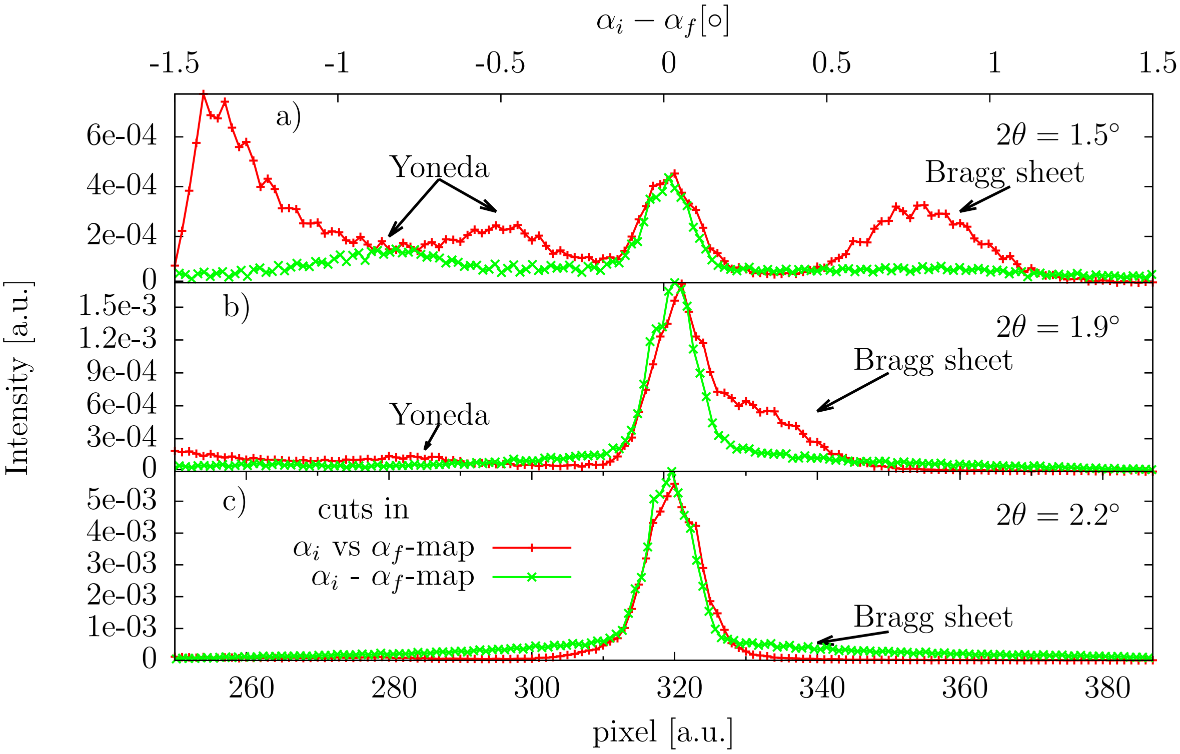

Figure 6.4.: Comparison between cuts in the α_i vs. α_f-map (red) and the $\alpha_i - \alpha_f$ vs. $\alpha_i + \alpha_f$-map (green) at 2θ angles of 1.5°, 1.9°, 2.2° (see **figure 6.3**) c). The 2θ values are at the pixel position of the specular path.

Bragg sheets, which are horizontal lines perpendicular to the vertical specular path.

By taking horizontal cuts for each measured 2θ angle of the detector position, the background of the Bragg sheets and the specular scattering can be distinguished. The intensities of the $\alpha_i - \alpha_f$ vs. $\alpha_i + \alpha_f$-map are interpolated to a regular grid (**figure 6.3** d). The x-values for this interpolated map are the same as in the original $\alpha_i - \alpha_f$ vs. $\alpha_i + \alpha_f$-map but the 2θ values are set to the 2θ values of the specular path. The intensities interpolated to the regular grid $I'_{i,j}$ can be calculated with

$$I'_{i,j} = \frac{b \cdot I_{i,j} + a \cdot I_{i,j+1}}{a + b}, \tag{6.2}$$

where $I_{i,j}$ are the intensities of the original measurement and a, b are the distances between the new pixel position and adjacent old pixel positions in vertical direction. In **figure 6.4** the difference of the cuts in α_i vs. α_f-map (red) and cuts in $\alpha_i - \alpha_f$ vs. $\alpha_i + \alpha_f$-map with 2θ values of 1.5°, 1.9° and 2.2° can be seen.

In **figure 6.4** a) all peaks are clearly separated making nearly no difference when integrating about the specular peak between pixel 310 and 330. At a 2θ value of 1.9° the Bragg sheet of the red curve migrates left, resulting in an overlap with the specular peak. Either the background is underestimated, when taking the background of the left flank, or overestimated when including the Bragg sheet. In **figure 6.4** c) the Bragg sheet overlaps with the specular peak, so the background will be underestimated, when using the integration along the y-axis of the detector images. Transforming the coordinate system to the $\alpha_i - \alpha_f$ vs. $\alpha_i + \alpha_f$-map, the off-specular scattering can be clearly distinguished from the specular one. Therefore, it is necessary to determine the specular reflectivity and the background by transforming into the $\alpha_i - \alpha_f$ vs. $\alpha_i + \alpha_f$-map, when off-specular scattering is present or small effects are investigated. This procedure was carried out for all multilayer samples, because of the pronounced and angle-dependent off-specular scattering. Though, the normally procedure is an ignoring if this problem.

6.1.2. ^{3}He Detector for Neutron Detection

The collected data from an area detector used for PNR measurements has to be corrected for inaccuracies. The correction is, normally, achieved through the usage of a sensitivity map, but can also be achieved using a model of the detector.

The neutron detector at MARIA is a position sensitive ^{3}He detector, which uses a multi-wire concept to determine the position of the scattering event [103]. The detector consists of three wire planes with an anode wire layer sandwiched between two cathode wire layers, filled with a ^{3}He, Ar and CO_2 gas mixture. The neutron detection takes place, using the charged-particle reaction,

$$^3He + n \to ^3H + p + 0.764\ \mathrm{MeV}, \tag{6.3}$$

and detecting the gas-discharge. The wire planes are used to detect the position of the gas ionization due to the proton charge. Because of a low stopping power of ^{3}He (proton range in ^{3}He alone is ~ 7.9 mm), an additional quenching gas is necessary to achieve a good spatial resolution. A mixture of Ar and CO_2 will have enough stopping power to increase the spatial resolution to ~ 2.3 mm. The resolution increases with increasing gas pressure. The gas pressure has to be adjusted to the wire distances in order to maximize the resolution. The problem with such multi-wire ^{3}He detectors might be the oscillating sensitivity with respect to the position on the detector, due to the huge quenching of the charge ionization. The normal approach to correct such insensitivities is to measure a sensitivity map, but this cannot correct the detector insensitivities properly, as will be described in the following subsection.

Sensitivity Map of ^{3}He Detectors

Normally, the ^{3}He detector can be corrected with a sensitivity map, describing the detector sensitivity position-dependent. In order to measure such a sensitivity map of the ^{3}He detector, the scattering of an incoherent scatterer has to be measured (scattering uniformly into 4π). At MARIA at MLZ the sensitivity map was determined by moving the detector to a high angle of 60° and measuring a PVC sample containing hydrogen. At this position no direct beam is visible and air scattering is negligible. Measuring one hour creates a sensitivity map, which can be seen in **figure 6.5**. The sensitivity map shows the stripe-like structure, which can be attributed to the equidistant wire position in the ^{3}He detector.

The detector images are usually corrected with this sensitivity map, by scaling the

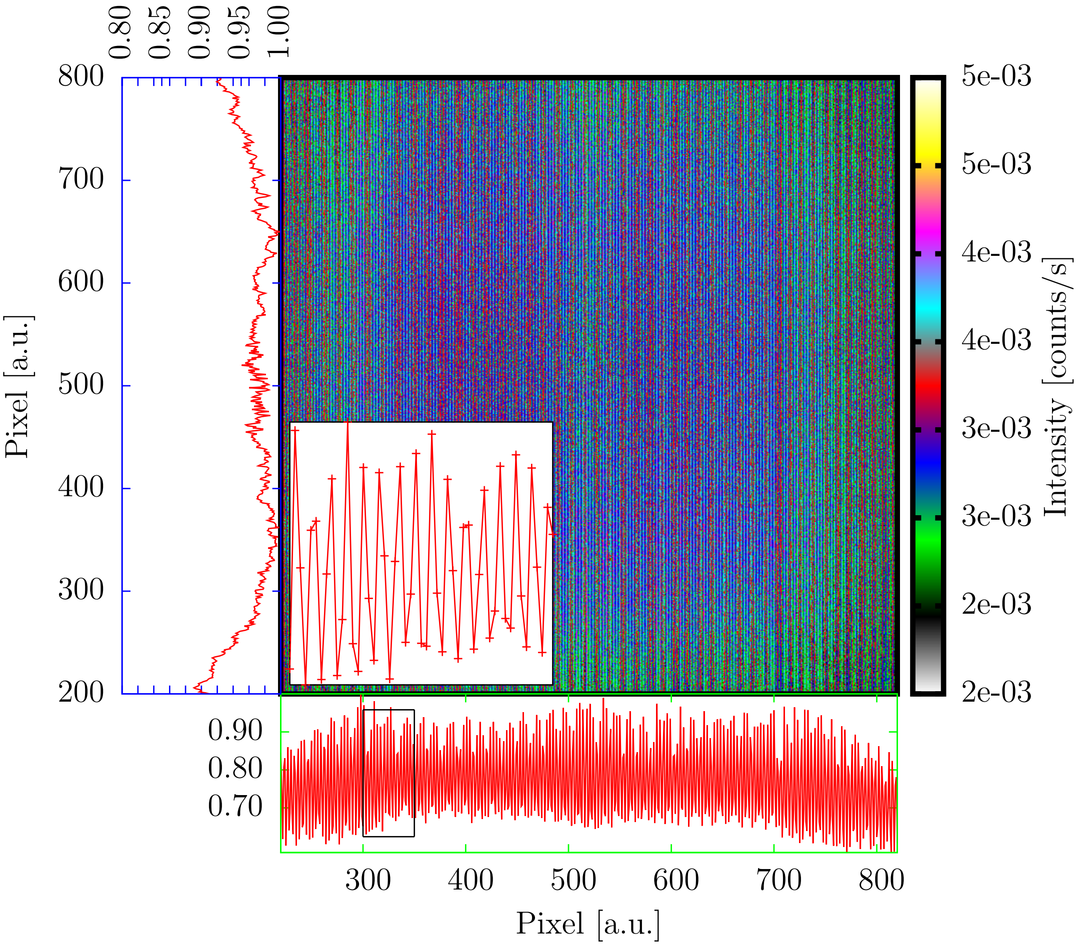

Figure 6.5.: Sensitivity maps of the MARIA detector measured with an incoherent scatterer.

measured intensities accordingly. But it turned out that this approach cannot correct the spatial inhomogeneous sensitivity of the detector correctly.

Problem of ^{3}He Detectors

In order to investigate the influence of the anode and cathode wires on the measured intensity, a specular reflex was scanned over the detector (Sample: SP$_{113}$) with a beam size of 0.5 mm. The sample angle was set to $\alpha_i = 0.3°$ at the plateau of total reflexion and the detector was scanned from 0.55° to 0.65° in steps of 0.005°. In **figure 6.6** some of the integrations along the y-axis of the detector image are shown. Due to the fixed α_i value, only the position of the reflected peak should change with different detector positions, but not the shape of the peak. At pixel positions 510.5 and 513.5, the measured intensity is reduced to half of the normal intensity, showing the insensitivities of the multi-wire detector. This large effect is not visible in the sensitivity maps, as it shows changes in the measured intensity of about 20%.

This effect can be clearly seen in the oscillating behavior of the integrated peak intensity. Integrating over the peaks from pixel position 500 to 525 for all 2θ values shows

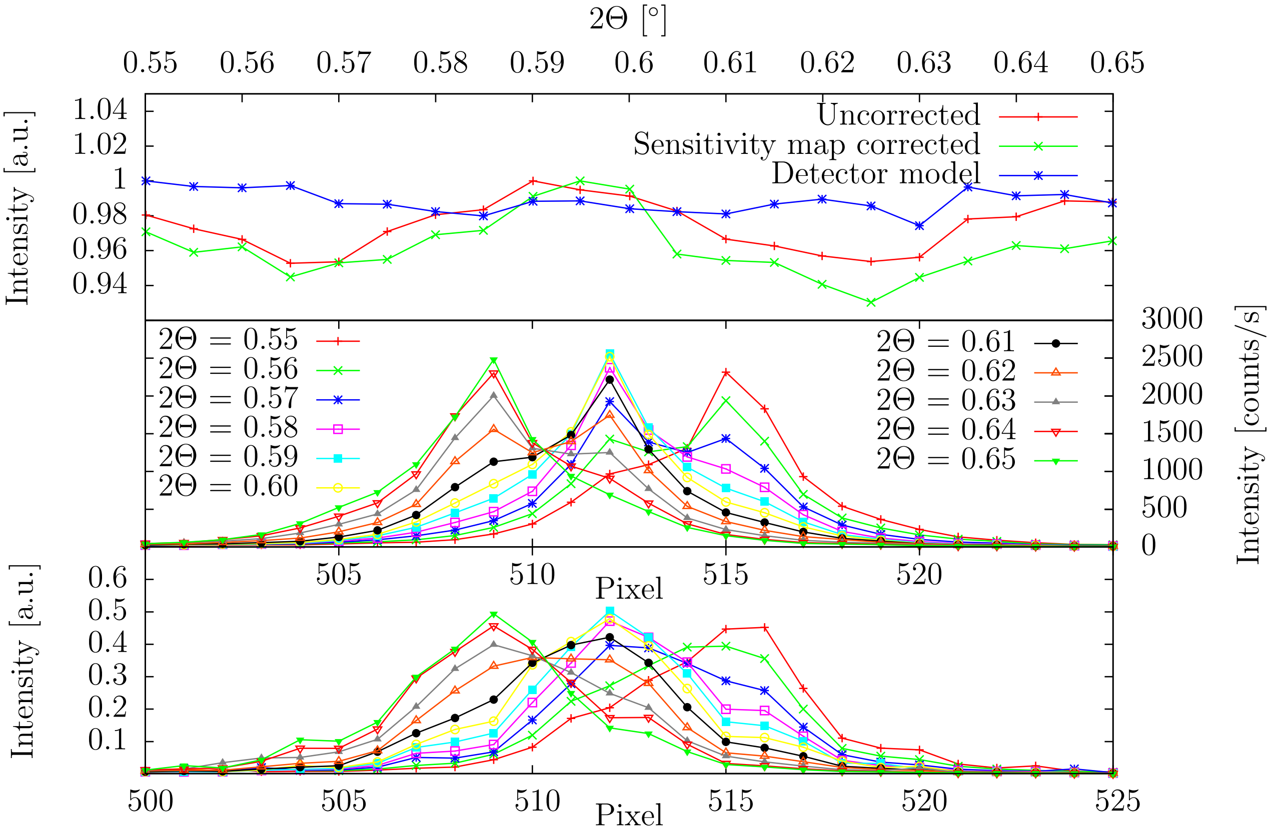

Figure 6.6.: Top: Integrated intensities of the specular reflectivity at different 2Θ values with and without correction of the sensitivity map, as well as with the model described here. The intensity is normalized to 1. Middle: Projections of the detector images on the x-axis at different 2Θ values. Bottom: Projections of the detector images on the x-axis at different 2Θ values after the correction with the sensitivity map.

an oscillating behavior, depending on the detector position with an amplitude of 5% (**figure 6.6** a). Correcting the detector images with the sensitivity map, obtained from the measurement of an incoherent scatterer, deforms the peak but not correctly. Furthermore, the amplitude of the oscillation in the integrated peak intensity increases to 7%. The behavior of the multi-wire detector is complicated and cannot be described by a sensitivity map alone.

^{3}He Detector Model

A simple model for such a multi-wire ^{3}He detector is to assume a different neutron detection efficiency for pixels in proximity to wire positions and between wires. This alone could be corrected with a normal sensitivity map. Additionally, it is necessary to assume a probability that the measured intensity is distributed between pixels in close proximity, because of the spatial expansion of the electron cloud. This probability σ_i^{lr} might be different for pixel positions i near wires and between them. Due to equidistant wire positions, an oscillating behavior of the sensitivity and the σ^{lr}, can be assumed. This can

	min	max
ρ [%]	0.3149	1
σ^{lr} [%]	0.444	0.445
l [pixel]	3.282	

Table 6.1.: Parameters derived from fitting the detector model to the swipe of the neutron beam over the detector and the sensitivity map. ρ is the sensitivity of the detector position, σ^{lr} is the part of the detected intensity allocated to adjacent pixels and l is the wire distance, describing the periodicity of the assumed sinus function.

be well described by a sinus function with a periodicity equal to the wire distance l:

$$\rho_i = \frac{\rho_{\max} + \rho_{\min}}{2} + \frac{\rho_{\max} - \rho_{\min}}{2} \sin(i + l) \tag{6.4}$$

$$\sigma^{lr} = \frac{\sigma_{\max} + \sigma_{\min}}{2} + \frac{\sigma_{\max} - \sigma_{\min}}{2} \sin(i + l). \tag{6.5}$$

Assuming an incoming neutron beam with a given shape e.g. Gaussian, the detected intensity can be simulated. In the initial step, the measured intensity for all pixels is set to zero and the number of ^{3}He reactions is set to the neutron beam intensity ϕ_i^n multiplied by the sensitivity ρ_i of the pixel. The ϕ_i^s are the detection events and $\phi_i^{\prime m}$ is the measured intensity at pixel position i. Thus the ϕ_i^s and $\phi_i^{\prime m}$ can be initialized with:

$$\phi_i^s = \rho_i \cdot \phi_i^n, \tag{6.6}$$

$$\phi_i^{\prime m} = 0. \tag{6.7}$$

Due to the spatial extension of the $^3He{+}n$ reaction, only $1-\sigma_i^{lr}$ of the registered detection events is assigned to pixel i. Other σ_i^{lr} events are assigned to pixels $i-1$ and $i+1$. The following assignment rule has to be applied iteratively for all pixel positions:

$$\phi_i^{\prime m} = \phi_i^m + \phi_i^s \cdot (1 - \sigma_i^{lr}), \tag{6.8}$$

$$\phi_{i+1}^{\prime m} = \phi_{i+1}^m + \phi_i^s \cdot \sigma_i^{lr}/2, \tag{6.9}$$

$$\phi_{i-1}^{\prime m} = \phi_{i-1}^m + \phi_i^s \cdot \sigma_i^{lr}/2, \tag{6.10}$$

$$\phi_i^s = 0, \tag{6.11}$$

With this model, the sensitivity map, as well as the sweep of the reflected neutron beam across the detector, can be simulated by assuming a neutron beam with a Gaussian spatial distribution and applying **equation 6.6-6.11**. The simulated sensitivity map and the sweep of the reflected neutron beam can be seen in **figure 6.7**. The differences between simulated intensity and measured intensity come from the inaccuracies in the pixel sensitivity at different positions. The assumed model of a sinusoidal sensitivity is too simple to describe the behavior of the detector correctly. It would be necessary to tune the sensitivities of the pixels individually, but with this the number of free parameters would increase significantly and such a model would not be well interpretable.

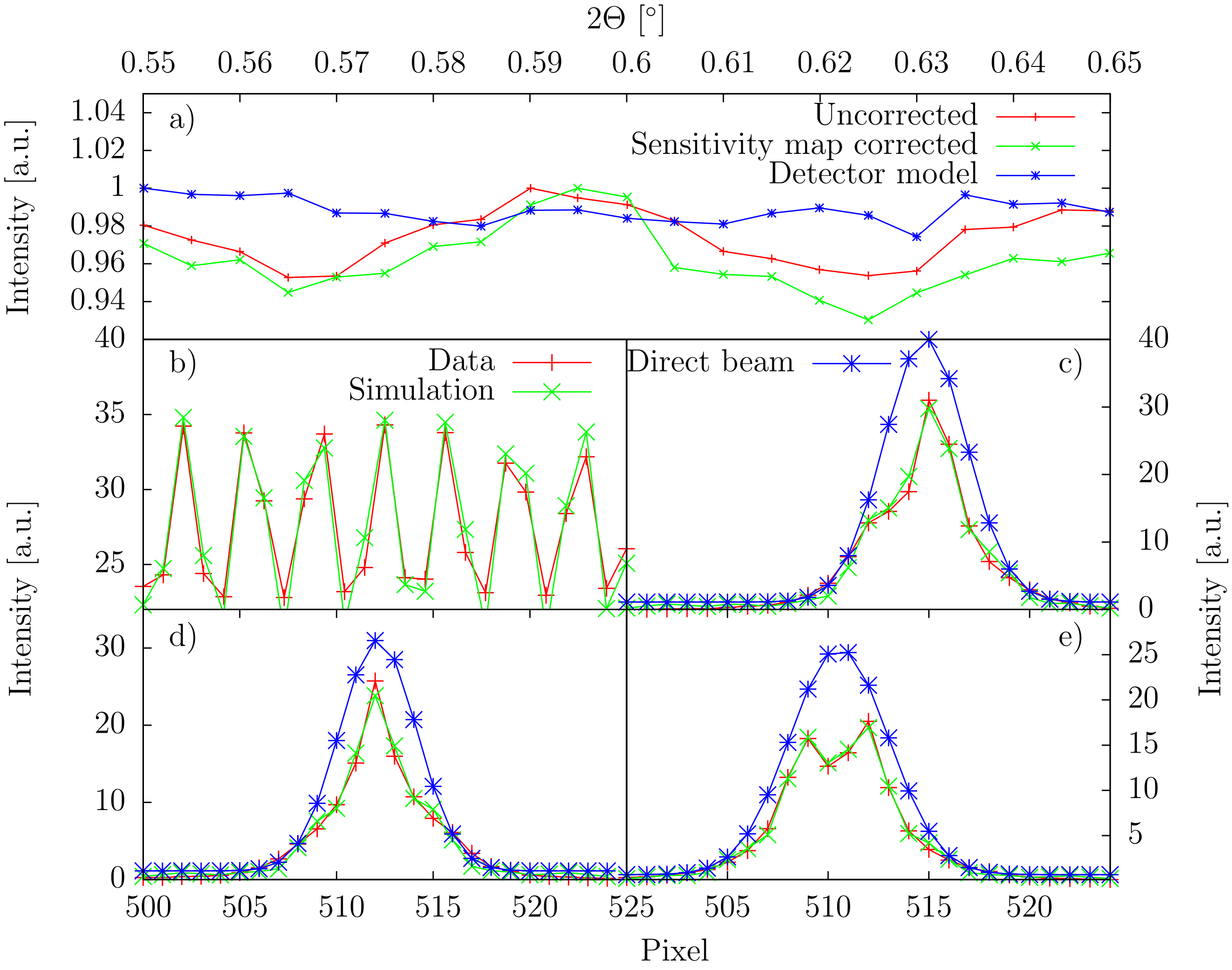

Figure 6.7.: a) Integrated peak intensity using the detector model. b)-e) Data and simulations of sensitivity map and the sweep of reflected beam across detector.

The measured specular peaks can be fitted with an incoming neutron beam using this model. Fitting only the parameters for a Gaussian shape of the neutron beam and leaving the detector parameters fixed, integrated intensities, with a smaller error, can be obtained. **Figure 6.7** a) shows the resulting integrated intensities normalized to the maximum value. The maximum error of the integrated intensities is reduced by half. Furthermore, a random distribution of the integrated intensities is obtained.

Conclusion

The behavior of a multi-wire neutron detector is complicated and could be at least simulated accurately enough for this dataset. In order to use this approach for correction of the detector insensitivities, in a real reflectometry experiment, additional test would be needed to exclude e.g. systematic errors. Due to the fact that no confirmation measurement could be performed, neither a correction with the sensitivity map nor a simulation of the detector behavior, was carried out for measurements at the MARIA reflectometer.

6.1.3. Corrections of Alignment Inaccuracies

Before starting a neutron reflectometry experiment, the sample angle has to be adjusted with respect to the detector angle 2θ. The sample angle α_i has to be $2\theta/2$ when measuring the specular reflex. Measuring temperature-dependent reflectometry, this adjustment has to be done for all temperatures, due to thermal expansion of the sample holder. Because of the deformed specular reflex, due to insensitivities between wire positions, this adjustment is not precise enough and a misalignment of one pixel is normal.

The estimation of the possible errors on significant fitting parameters, like the scattering length density (SLD), can be done by considering the dependence of the critical angle Θ_C on the SLD. The measurements at MARIA were carried out at a wavelength of $\lambda = 6$ Å, with a pixel size of 0.66 mm, corresponding to an 2θ angle of 0.019° at a sample detector distance of $l = 1910$ mm. Assuming a misalignment of one pixel and a critical angle of around 0.35°, the difference in the SLD, between a misaligned sample and a perfect aligned sample, can be calculated with the formulas

$$\Theta_C = \lambda\sqrt{\frac{SLD}{\pi}}, \Longleftrightarrow \Theta_C^2 = \lambda^2 \frac{SLD}{\pi}, \tag{6.12}$$

$$\Rightarrow \frac{SLD_\mathrm{aligned}}{SLD_\mathrm{misaligned}} = \frac{0.35^2}{(0.35 + 0.019/2)^2} \sim 0.948. \tag{6.13}$$

A misalignment of one pixel leads to a difference in scattering length density of around 5.2%. To correct the misalignment after the experiments have been carried out, the peak positions at the total reflexion plateau are averaged and all detector images are shifted with respect to this value.

In **figure 6.8** the position of the specular reflex, determined by a Gaussian fit, is plotted against the incident angle of the neutron beam in PNR experiment, at MARIA, on the LSMO/LCMO multilayer (Sample: SP_{113}) at 10 K. The average of the peak positions, below the critical angle, is determined to be 511.53 pixel. The difference to the reference position of 512.5 pixel is around one pixel. Therefore, the angles of the detector images have to be corrected by shifting with $(0.019/2)^\circ$. The differences of the peak position, at different incident angles, are due to a divergent neutron beam. The reflected intensity scales as $\sin^{-4}(\alpha_i)$ with incident angle α_i. Therefore, the intensity of neutrons with a smaller incident angle is bigger than the intensity of neutrons with a higher incident angle of the same neutron beam. This leads to a shift of the reflected peak to lower pixel positions, which can be seen in **figure 6.8**. At a Bragg peak this behavior is inverted due to an increase of reflected intensity at the Bragg peak position. Because of this, the peak positions at the plateau of total reflexion, not showing this behavior, has to be used for the correction. The shifting of the peak position cannot be explained with the increased divergence of the neutron beam with increasing incident angle. On the one hand, the divergence of the neutron beam does only change from $\Delta\alpha = 6.0 \cdot 10^{-4}$ to $\Delta\alpha = 7.4 \cdot 10^{-4}$,

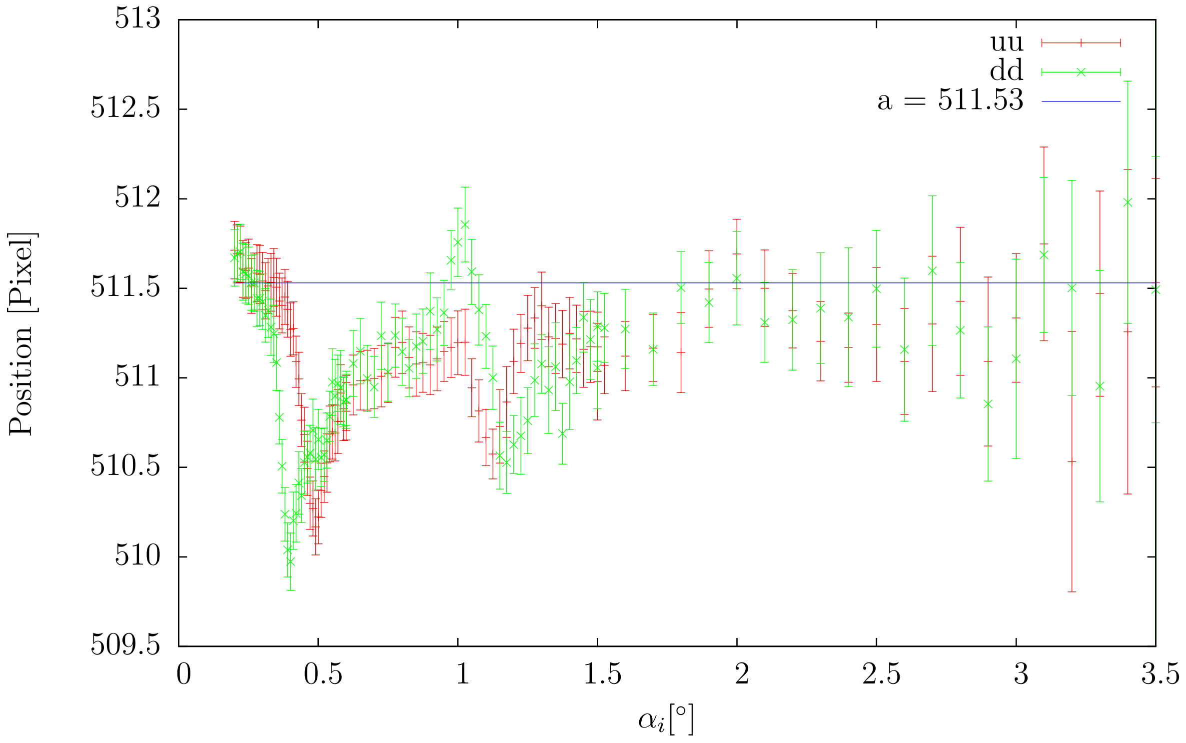

Figure 6.8.: Position of the specular reflex on the detector for different incident angles and both polarization states for the PNR experiment at MARIA on the LSMO/LCMO multilayer (Sample: SP_{113}) at 10 K. The peak position was determined by fitting a Gaussian function to the integration along the y-axis of the detector images (**section 6.1.1**).

and on the other hand, an increase of the divergence only broadens the peak.

Without an automatic alignment, following this procedure, the data has to be corrected afterwards for all measurements. Otherwise a small misalignment would have a large effect on the reflectometry data and the simulation thereof.

6.1.4. Resolution and Wavelength Distribution

Resolution

The resolution in reflectometry or diffractometry measurements depends on the wavelength spread $\Delta\lambda$ and the divergence $\Delta\alpha$ of the beam. In oder to simulate the measured intensity in scattering experiments, the resolution has to be taken into account. The measured intensity is a “convolution of the resolution function R and the scattering function S” [104] defined by:

$$I(Q_0,\omega_0) = \int R(Q-Q_0,\omega-\omega_0)S(Q,\omega)dQdw \xrightarrow{elastic} I(Q_0) = \int R(Q-Q_0)S(Q)dQ, \tag{6.14}$$

where Q is the momentum transfer and ω is energy transfer. With no energy transfer, the resolution solely depends on Q. A Gaussian function is mainly used as a resolution function, because the angular and spatial distributions are described very well with a Gaussian function. The resolution $\Delta Q_{\mathrm{x,y,z}}$ is then defined as the FWHM of this Gaussian function for the directions x, y, z. In reflectometry experiments only the Q_{z} resolution component is important, which is perpendicular to the sample surface. Assuming incident and out-going angles to be equal, which is the case when measuring reflectometry, then the resolution in z-direction can be determined to

$$R(Q-Q_0) = \frac{1}{\Delta Q\sqrt{2\pi}} e^{-\frac{1}{2}\left(\frac{Q-Q_0}{\Delta Q}\right)^2} \text{ with} \tag{6.15}$$

$$\Delta Q_{\mathrm{z}} = \sqrt{\left(\frac{4\pi}{\lambda^2} sin(\alpha) \cdot \Delta\lambda\right)^2 + \left(\frac{4\pi}{\lambda} cos(\alpha) \cdot \Delta\alpha\right)^2}, \tag{6.16}$$

$$\text{leading to} \quad \frac{\Delta Q_{\mathrm{z}}}{Q} = \sqrt{\left(\cot^2\alpha \frac{\Delta\alpha}{\alpha}\right)^2 + \left(\frac{\Delta\lambda}{\lambda}\right)^2} \approx \sqrt{\left(\frac{\Delta\alpha}{\alpha}\right)^2 + \left(\frac{\Delta\lambda}{\lambda}\right)^2}, \tag{6.17}$$

where Q is the momentum transfer, α is the incident angle, λ is the wavelength and $\Delta\alpha$, $\Delta\lambda$ the spreads thereof. This equation holds for X-ray reflectometry and neutron reflectometry, but with different contributions of the summands. For X-rays, the wavelength resolution can be neglected and for neutrons both have to be taken into account.

Neutron Beam Divergence

The simplest way to take the divergence $\Delta\alpha$ of the neutron beam into account is to assume a point like sample. Drawing the beam paths from the edges of the first slit S_1 to the sample will result in an opening of the neutron beam, which can be calculated to

$$\tan(\Delta\alpha/2) = \frac{d_{\mathrm{S1}}/2}{L}, \tag{6.18}$$

where d_{S1} is the width of the first slit and L is the distance between the first slit and the sample. This will result in a constant divergence at all α_i values, which is easy to handle but cannot describe a real reflectometry experiment. The assumption of a point like sample holds true for $\alpha_i = 0°$. For $\alpha_i \neq 0$ the sample acts as an additional slit and the width of this slit increases with increasing α_i, given by the formula $d\sin(\alpha_i)$, where d is the sample length. This will result in a variable resolution and has to be taken into account.

The equation to describe this variable resolution can be derived from the beam paths shown in **figure 6.9**. The beam paths are restricted by the first slit S_1, the second slit S_2 and the sample. The widths of these slits are given by d_{S_1}, d_{S_2} and $d_{S_{\mathrm{Sample}}}$. The sample has a distance of L from the first slit and is rotated around α_i resulting in $d_{S_{\mathrm{Sample}}} = d\sin(\alpha_i)$. In the performed PNR experiments the second slit was used for background reduction and can be neglected for the derivation of the divergence. The red beam paths from the top/bottom edge of S_1 to the bottom/top edge of the sample have the largest divergence.

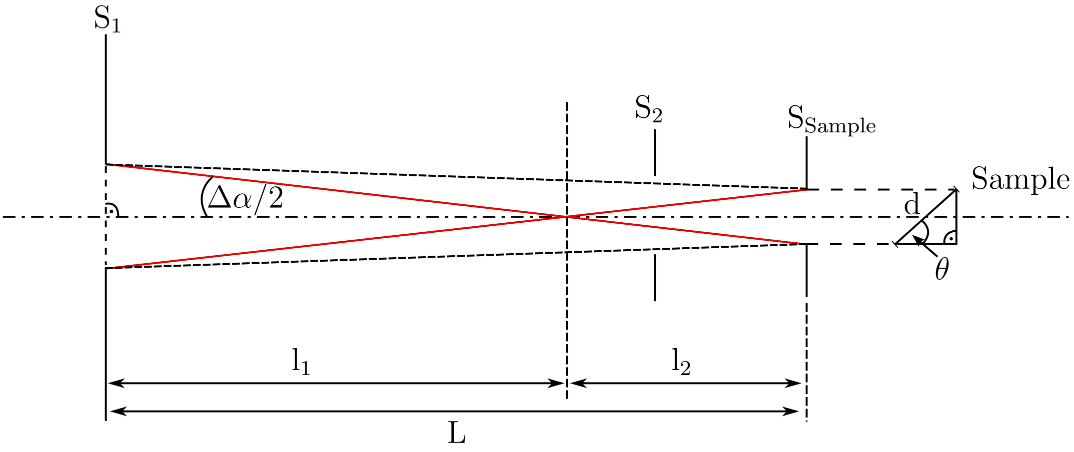

Figure 6.9.: Geometrical sketch to derive the divergence of the beam. The beam path is restricted by the slits S$_1$ and S$_2$. The sample acts as an additional slit, changing the width with the α_i value. The beam paths with the biggest divergence are drawn in red.

The intersection point of these red paths divide the distance L into the distances l_1 and l_2. With the intercept theorem, these distances can be calculated with

$$l_1 = L \cdot \frac{d_{S_1}}{d_{S_1} + d_{S_{\text{Sample}}}} \quad \text{and} \tag{6.19}$$

$$l_2 = L \cdot \frac{d_{S_{\text{Sample}}}}{d_{S_1} + d_{S_{\text{Sample}}}}. \tag{6.20}$$

The divergence of the beam can be determined by:

$$\tan(\Delta\alpha/2) = \frac{d_{S_1}/2}{l_1} = \frac{d_{S_1}}{2L \cdot \frac{d_{S_1}}{d_{S_1}+d_{S_{\text{Sample}}}}} = \frac{d_{S_1} + d \cdot \sin(\alpha_i)}{2L}. \tag{6.21}$$

Because of a small divergence in reflectometry experiments $\Delta\alpha \ll 1$ this equation can be simplified to:

$$\Delta\alpha/2 = \frac{d_{S_1} + d \cdot \alpha_i}{2L} \Rightarrow \Delta\alpha = \frac{d_{S_1} + d \cdot \alpha_i}{L}. \tag{6.22}$$

As can be seen in **equation 6.22**, the divergence increases linearly with α_i for small α_i values. Although this approach overestimates the divergence, this change in the divergence has to be implemented in the simulations by a variable resolution, which can be done in the “GenX” program [89].

Wavelength Resolution and D17 Neutron Reflectometer

In most programs for the simulation of reflectometry data, the resolution is described by a Gaussian function, which is in most cases good enough. The wavelength contribution

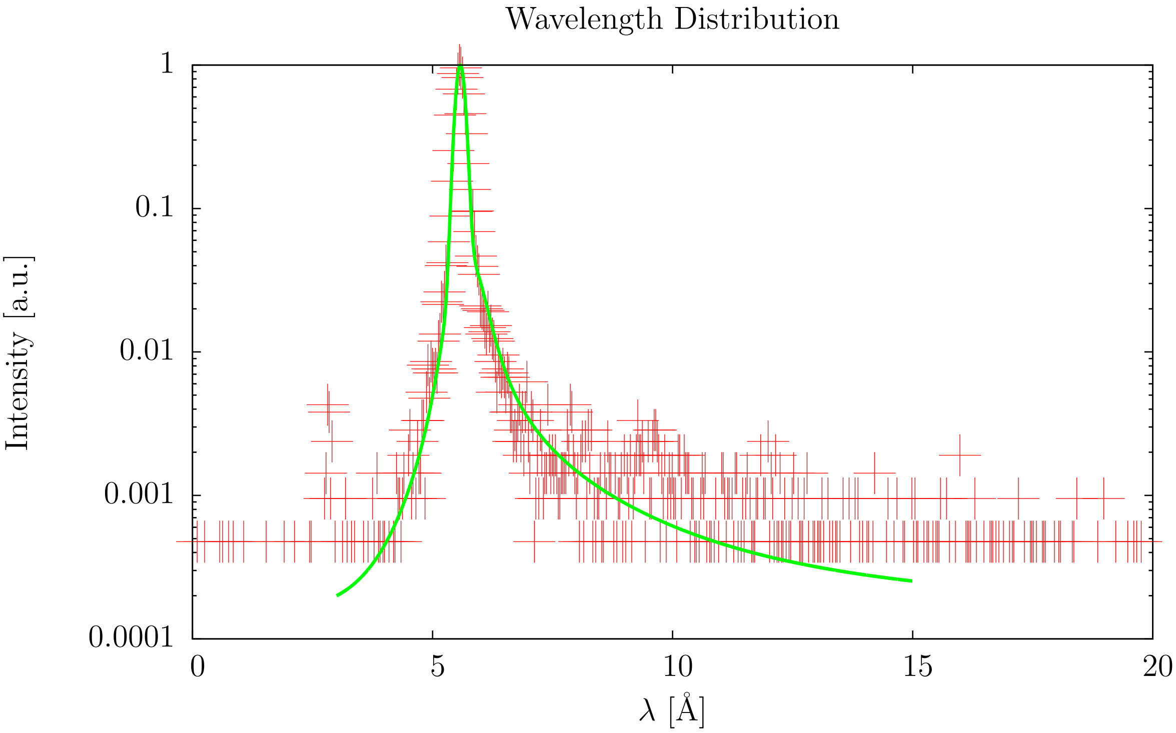

Figure 6.10.: Wavelength distribution at D17 reflectometer, with approximation of the wavelength distribution.

is then just a constant value $\Delta\lambda$ given as the FWHM of the Gaussian function.

Problems emerge, when the resolution is not Gaussian. At the D17 reflectometer the wavelength spreed is 0.04%, but has a tail to higher wavelengths, which cannot be neglected. The wavelength distribution for this instrument, measured by Andrew Wildes, is shown in **figure 6.10**. The wavelength distribution was fitted with three Gaussians in order to approximate the shape and to create a continuous and analytical function. To be able to cumulate the results accordingly, one has to set the wavelength distribution in the simulation to zero and then convoluting the simulation with the wavelength distribution.

PNR measurements and simulations of the LSMO/Pd films (Sample: OMBE$_{208}$) with and without wavelength distribution are shown in **figure 6.11**. It is evident that the wavelength distribution has to be considered. Without this distribution the resolution is too high. A change in resolution cannot be achieved by simply increasing $\Delta\lambda/\lambda$ from 0.04 to higher values in the normal Gaussian resolution function. Simply increasing $\Delta\lambda/\lambda$ would mean a bad overall resolution, especially at the plateau of total reflection, where a good resolution is present in the measurements.

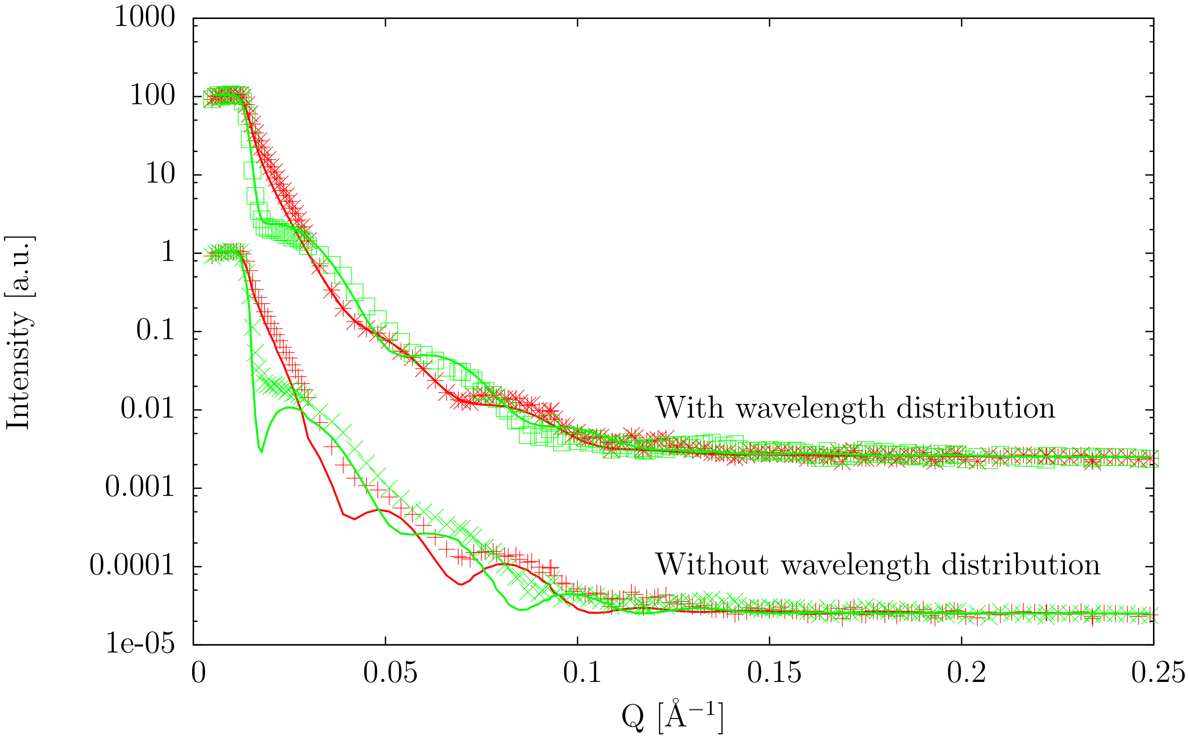

Figure 6.11.: Measurement of LSMO/Pd film (Sample: OMBE$_{208}$) done at D17 and simulation with accounting for asymmetric wavelength distribution (top) and Gaussian wavelength distribution (bottom). The divergence was kept the same for both simulations.

6.2. Simulations of XRR and PNR Measurements

The XRR and PNR measurements are analyzed by simulating the reflectometry data with the Parratt formalism used in the "GenX" program [89]. The different layers are described by their magnetic and nuclear scattering length, their density, their roughness and their layer thickness. By slicing the layers into smaller ones, it is possible to separate the magnetic scattering length density (SLD) from the nuclear SLD. This allows to concentrate only on the magnetic SLD and to define arbitrary magnetic profiles, allowing the simulation of magnetic interface effects. The simulations can then be compared by the figure of merit (FOM) defined below.

6.2.1. Magnetic and Nuclear SLD Profiles

The magnetic and nuclear SLD's are separated by defining two different layered samples, with one sample representation without magnetism and the other sample consisting of layers with a nuclear scattering length of zero and a well defined magnetism (see **figure 6.12**). The magnetism can then be defined by analytical functions that are independent of the nuclear roughness and the interface position.

In order to simulate the reflectometry measurements, the magnetic and nuclear SLD

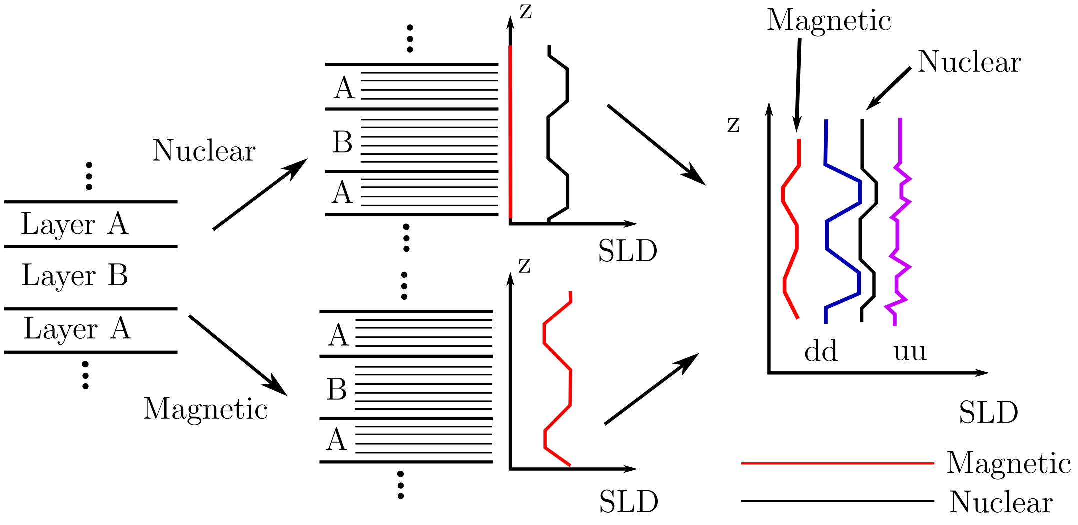

Figure 6.12.: Procedure for the reflectometry simulation of a layered sample with a magnetic contribution. The sample is separated into two samples, from which one has a nuclear contribution and the other one a magnetic contribution. The nuclear and magnetic SLD's are then combined to a SLD for the whole sample.

have to be combined to two SLD profiles for the ++ channel and the - - channel. This is done by slicing all layers to a predefined number of sublayers and then adding and subtracting the magnetic SLD from the nuclear SLD for the ++ channel and the - - channel, respectively. The resulting SLD for the ++ channel and the – channel is then used to simulate the reflectometry measurements.

6.2.2. Figure of Merit (FOM) and Fitting

In order to compare the quality of different simulations a quantitative measure is necessary. The χ^2 test is one possible quantitative measure, which overestimates the differences at the plateau of total reflexion due to the high intensity. This would impede the fitting of the reflectometry data. Therefore, another figure of merit (FOM) is needed, which considers the specific shape of the reflectometry curve with the Q^{-4} decay. The used FOM in the fitting and analysis of the reflectometry data, with Y_i as the y-values of the measured data and S_i as the simulation thereof, is

$$FOM_{\log} = \frac{1}{N-1} \sum_i |\log Y_i - \log S_i|. \tag{6.23}$$

This FOM increases the sensitivity of the fitting for higher Q and facilitates the fitting. The error estimation of the parameters, used for the simulations, is possible with such a definition of the FOM. The error $\sigma_\pm$ of an parameter is defined as the difference of the parameter value for the best FOM and a 5% worse FOM. This procedure gives two different errors, as the FOM does not change symmetrically with a change of the parameters.

6.3. XAS Normalization and XMCD Calculation

The X-ray magnetic circular dichroism (XMCD) signal is the difference of the X-ray absorption spectroscopy (XAS) spectrum, in this work measured in fluorescence mode, for left and right circular polarized light. In order to apply the sum rules, the XAS spectrum has to be normalized and corrected for instrument artifacts or optical issues.

XMCD Signal

XMCD measurements can be carried out twofold, either the direction of the magnetic field can be flipped or the polarization of the X-ray beam can be changed from left σ^- to right σ^+. Both procedures should yield equivalent results, as long as the magnetization follows the flip of the magnetic field completely. To ensure that the XMCD measurements do not obtain any artifacts, the XMCD signal was measured both ways.

Defining $\mathrm{XMCD}_{\mathrm{H+/H-}}$ as the difference in the absorption coefficient between left and right circular polarized light at an applied magnetic field parallel H+ and anti-parallel H- to the X-ray beam, the true XMCD measurement is given by

$$XMCD = (XMCD_{\mathrm{H+}} - XMCD_{\mathrm{H-}})/2. \tag{6.24}$$

The XAS spectrum has to be normalized before the calculation of the XMCD signal in order to get absolute values for the sample magnetization. The normalization of the XAS spectrum will be therefore discussed for the L_2 (3.330 keV) and L_3 (3.173 keV) edges of Pd [105] in the following subsection.

XMCD Normalization

Due to the large energy difference ($\sim$ 160 eV) of the L_2 and L_3 edges, it was not possible to measure the absorption spectrum over the whole energy region from the L_3 edge to the L_2 edge at the 4-ID-D beamline at the APS. The monochromator has to be aligned for each edge individually, which makes the analysis of the XMCD more complicated.

In the first step the background has to be subtracted, which can be determined by fitting a linear function to the pre-edges and then subtracting the linear function from the whole XAS curve, setting the pre-edge region to zero. Afterwards, the post-edges have to be normalized, depending on the branching ratio of the $L_{2,3}$ edges. Sham [106] investigated the edge-jumps of the $L_{2,3}$ edges and showed that the ratio of these edge-jumps is approximately two. Therefore, the post-edges of the L_2 and L_3 edges can be normalized to 0.5 and 1, respectively. The XMCD signal is than just the difference between left and right circular polarized light corrected by dividing through $P_{\mathrm{L2,L3}}/\cos\theta$, where $P_{\mathrm{L2}} = 0.6$ and $P_{\mathrm{L3}} = 0.56$ are the polarization efficiencies at the $L_{2,3}$ edges and $\cos(\theta)$ is the angle between the applied magnetic field and the propagation vector of the X-rays.

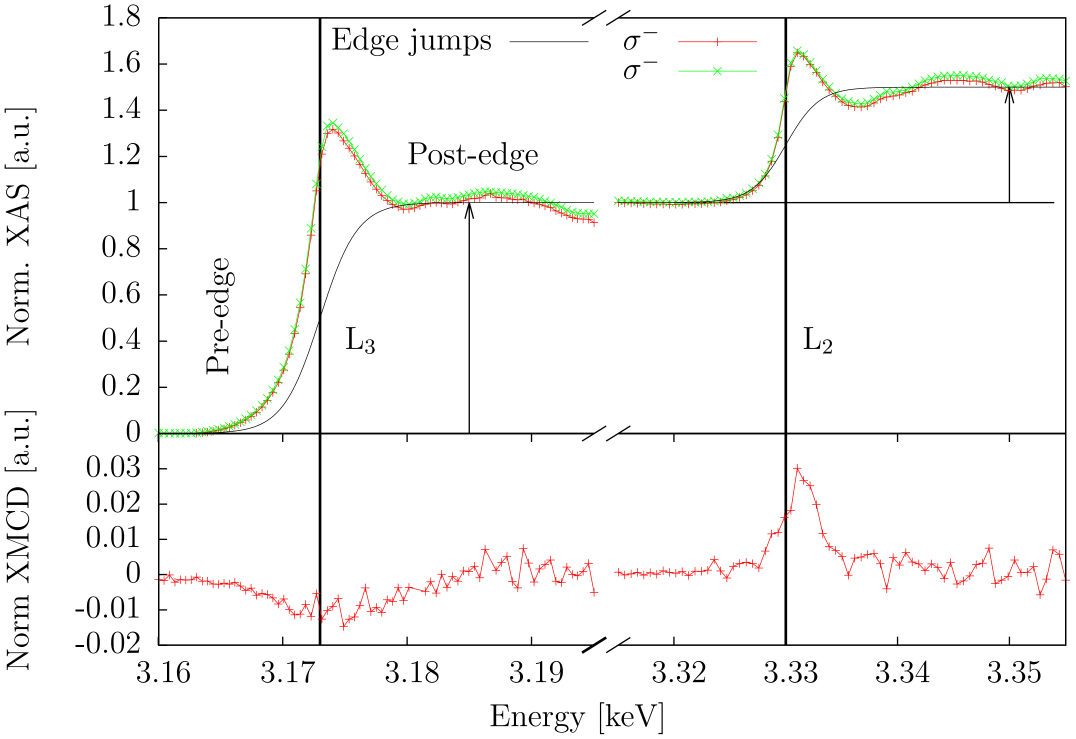

Figure 6.13.: Top: Normalized XAS spectrum of Pd L_2 (3.330 keV) and L_3 (3.173 keV) edges [105] measured in fluorescence mode with a step-like function to approximate the edge jump. The pre-edge region was set to zero and the post-edge region was set to 1 or 0.5 for the L_3 or L_2 edges, respectively, to normalize the curves. Bottom: Normalized XMCD spectrum for both edges, which is the difference of both XAS measurements corrected for polarization efficiencies and an angle between applied magnetic field and X-ray propagation vector.

Edge-Jump

In order to determine the S_z and L_z expectation values from the XMCD curves, the integral over the difference between left and right circular polarized light has to be divided by the integral over the sum with subtracted $L_{2,3}$ edge jumps. These edge jumps can be approximated by a step-like function (**figure 6.13**), which is a convolution of a Voigt function with step functions [75] or a Boltzmann function resulting in

$$\mu_{\text{step}} = \frac{3}{2}\left(1 - \frac{2}{3}\frac{1}{1+e^{(E-E_{\text{L3}})/\delta}} - \frac{1}{3}\frac{1}{1+e^{(E-E_{\text{L2}})/\delta}}\right), \tag{6.25}$$

with δ as the step width of the $L_{2,3}$ edges, which was set to $\delta = 0.002$ keV, but does not influence the calculation very much, and $E_{\text{L2,L3}}$ as the energy positions of the edge jumps, corresponding to the edge positions. Due to the uncertainties in the edge-jump approximation, with the step-like function, the absolute values of the L_z and S_z expectation values are quite inaccurate. Nevertheless, it gives a first approximation of magnetism in Pd.

7. Results

In the following section, the three different systems are investigated concerning their magnetic interface effects. It begins with the metal/metal interface, Pd/Fe, as a reference system, where the induced magnetism is well known. The second system is the metal/oxide interface, Pd/LSMO and Pd/LCMO, where two types of magnetic interface effects could be possible, either with the superexchange and double exchange interaction, or due to hybridization. The last part covers the oxide/oxide interface system, LSMO/LCMO, where the magnetism comes alone from double exchange and superexchange interactions.

7.1. Pd/Fe Multilayer

The Pd/Fe multilayer system was part of my Diploma thesis, which focused on the investigation of the growth parameters for smooth surfaces. The Pd/Fe multilayers, grown on a GaAs substrate, presented here, were deposited in the same way. They were grown with a MBE system, by electron beam physical vapor deposition at a base pressure of 10^{-9} mbar. The GaAs substrate was cleaned from adatoms with ultrasonic cleaning in isopropyl alcohol and heated for one hour at 650°C in ultra high vacuum (UHV). A 1 nm Fe seed layer was deposited on the GaAs substrate, to ensure the preferred (001) growth direction [107] of the 150 nm Ag buffer layer deposited afterwards. The roughness of the Ag layer decreases, when tempered at 300°C [108] for approximately one hour after the growth. On the Ag buffer layer the Pd/Fe multilayer was grown with desired thicknesses of 5 nm for Pd and 1 nm for Fe. The deposition temperatures of the Pd and Fe layers were 100°C and 130°C, respectively. Growing at these temperatures prevents interdiffusion and produces smooth surfaces [109].

Before analyzing the magnetic properties, especially at the interface, the samples are investigated for the structural quality with XRR, XRD and AFM. In **subsection 7.1.2**, the magnetic properties are investigated with SQUID, PNR and XMCD measurements.

7.1.1. Structural Characterization

XRR, XRD and AFM measurements were performed to investigate the structural quality of the Pd/Fe multilayer. The XRD measurement shows (**figure 7.1**) a high crystalline quality of the Pd layers. The position of the Fe layers cannot be determined because of the low intensity of the Bragg peaks due to the thin Fe layers. The XRR measurement can be seen in **figure 7.1**, after the data was corrected for off-specular scattering, which is present in Pd/Fe multilayer samples.

In **figure 7.1** a broadening of the Bragg peaks is visible, which can be explained through a variation in the layer thicknesses. Therefore, a linear change Δd of the layer thickness

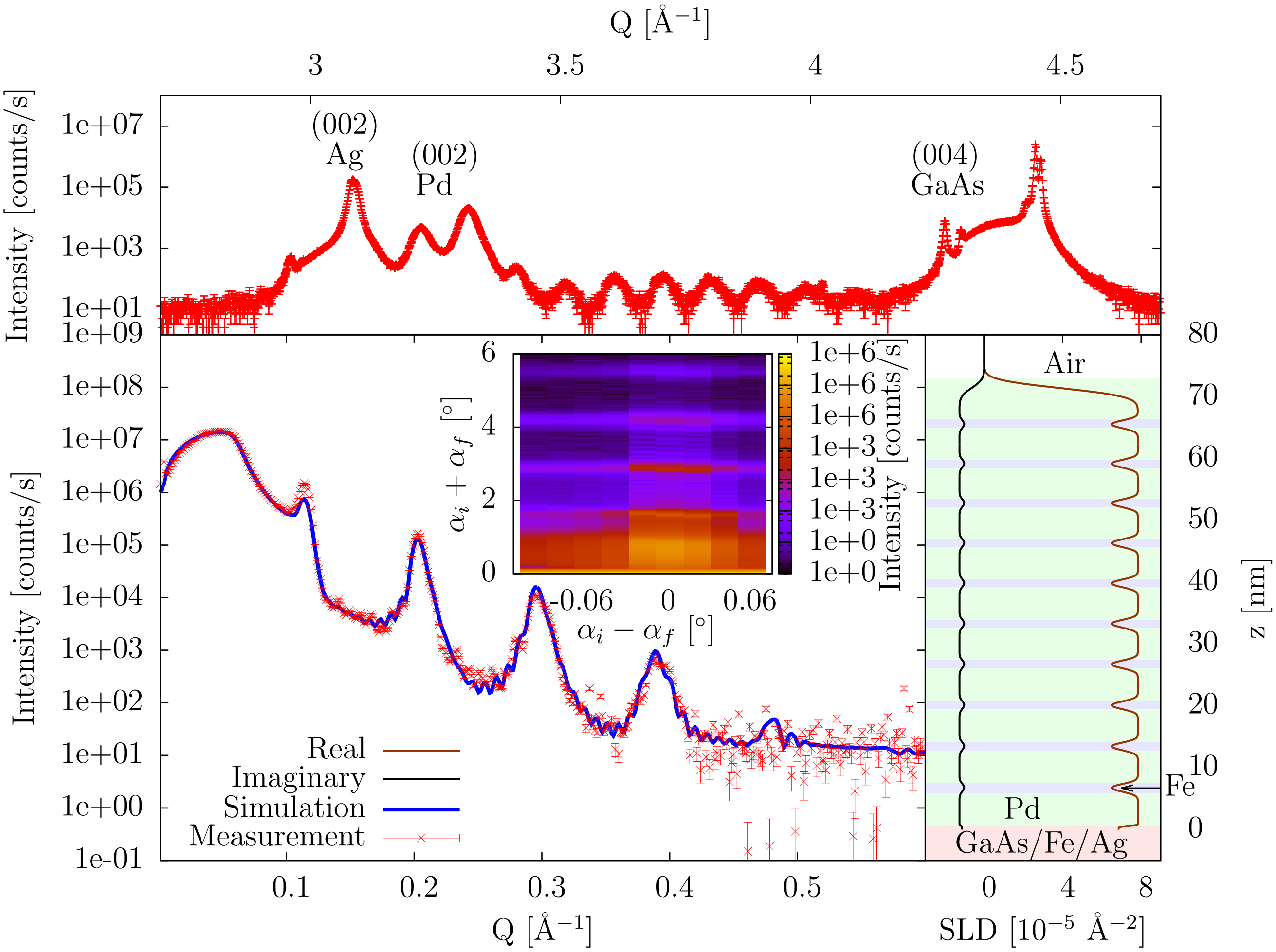

Figure 7.1.: Top: XRD measurement in out-of-plane direction. Left: XRR measurement of Pd/Fe multilayer after the correction for off-specular scattering with simulation thereof. Right: Used SLD for the simulation of the Pd/Fe multilayer. Inset: $\alpha_i - \alpha_f$ vs. $\alpha_i + \alpha_f$ map used for the data reduction and the correction of the off-specular scattering.

was used in the simulation thereof. The best simulation (FOM of $2.14 \cdot 10^{-1}$) with this method is shown in **figure 7.1** (green line) and the SLD for this simulation is shown on the right-hand side. Making the layer independent, the fit might be improved, but on the cost of an significant increase of the number of parameters. However, for a better understanding, a model with only few fitting parameters is more helpful. Additionally, a top Pd layer was assumed, where the roughness and the density were fitted separately from other Pd layers, because of possible oxidization and, thus, an increased roughness and a decreased density. All parameters used for the simulation are shown in **table 7.1**.

The change of the layer thickness of 0.5 Å from one layer to the other does not seem to be large, but this means that the change from the first to the last Pd layer is higher than 5 Å, which is ten percent of the layer thickness. Nevertheless, the Pd and Fe layers have

Layers	$\mathrm{Pd}_{\mathrm{top}}$	11*Pd	10*Fe	Ag on GaAs
d [Å]	$1.03\ ^{+1.19}_{-0.47}$	$53.89\ ^{+0.19}_{-0.13}$	$11.4\ ^{+0.17}_{-0.12}$	Substrate
Δd [Å]	-	$-0.45\ ^{+0.05}_{-0.19}$	$-0.03\ ^{+0.16}_{-0.011}$	-
σ [Å]	$11.1\ ^{+0.12}_{-0.21}$	$5.08\ ^{+0.7}_{-0.6}$	$4.77\ ^{+0.04}_{-0.1}$	$1.16\ ^{+0.03}_{-0.03}$
ρ [10^{-2} Å^{-3}]	$6.95\ ^{+0.02}_{-0.01}$	$6.95\ ^{+0.02}_{-0.01}$	$8.27\ ^{+0.07}_{-0.01}$	5.87
ρ_{Norm} [10^{-2} Å^{-3}]	6.80	6.80	8.30	5.87
f_1 [e/atom]	39.98	39.98	26.02	41.46
f_2 [e/atom]	3.985	3.985	3.209	4.265
Re SLD [10^{-5} Å^{-2}]	$7.84\ ^{+0.02}_{-0.01}$	$7.84\ ^{+0.02}_{-0.01}$	$6.07\ ^{+0.05}_{-0.01}$	6.86
Im SLD [10^{-5} Å^{-2}]	$0.78\ ^{+0.01}_{-0.001}$	$0.78\ ^{+0.01}_{-0.01}$	$0.75\ ^{+0.01}_{-0.01}$	0.7
$\mathrm{SLD}_{\mathrm{Norm}}$ [10^{-5} Å^{-2}]	7.67	7.67	6.09	6.86

Table 7.1.: Summary of all parameters used for the simulation of the XRR measurement. The following parameters are shown: Thickness d, thickness variation Δd, roughness σ, density of the unit cell ρ, atomic scattering factors f_1 and f_2 and scattering length density SLD. Simulations with these parameters result in a FOM of 0.2138.

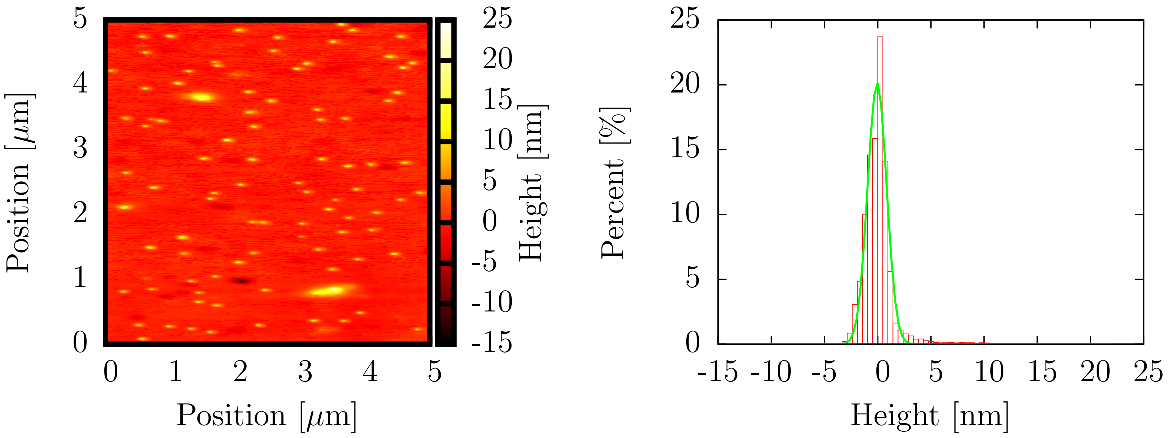

Figure 7.2.: On the left hand side the topography of the AFM measurement is presented and on the right hand side the height distribution thereof. A Gaussian profile is fitted to the height distribution, with a roughness or 8.87 Å.

smooth surfaces in the order of 5 Å, as can be seen in the SLD profile and in **table 7.1**. The roughnesses at the Pd/Fe interface might indicate that these layers interdiffuse in the range of one to two unit cells, but considering the pronounced off-specular scattering (inset in **figure 7.1**), these interfaces are well defined. On the other hand, the roughness of the top Pd layer is increased in comparison to the other layers. As mentioned, this comes most likely from oxidization of the Pd surface. The AFM measurement (**figure 7.2**) shows similar results as the XRR measurements, with a slightly lower roughness of around 9 Å.

7.1.2. Magnetic Characterization

The magnetic properties were investigated macroscopically with a SQUID magnetometer. But with this technique the contributions of the individual layers cannot be distinguished. Therefore, the Pd/Fe multilayers were investigated microscopically for their magnetic properties with PNR and XMCD measurements. The PNR measurements show a possible magnetization of the Pd interface, which could then be verified with XMCD measurements.

Macroscopic (SQUID)

The Pd/Fe multilayer was measured in a SQUID magnetometer using the RSO option for a better resolution. The magnetic field was applied in-plane in the direction of the easy axis of Fe. Field cooled measurements at 100 Oe and hysteresis measurement at 10 K, 50 K, 100 K, 200 K and 300 K were performed. The measurements are normalized to the number of Fe atoms inside the Pd/Fe multilayer assigning the whole magnetization to the Fe atoms. The number of atoms was calculated from the layer thicknesses determined with XRR measurements ($\mathrm{d_{Fe}} = 11.4 \ {}^{+0.17}_{-0.12}$ Å, $\mathrm{d_{Pd}} = 53.89 \ {}^{+0.19}_{-0.13}$ Å), the surface area of the sample ($A = (6 \pm 0.06)\ \mathrm{mm}^2$) and the unit cell densities ($\rho_{\mathrm{Pd}} = 6.95 \ {}^{+0.02}_{-0.01} \cdot 10^{-2}$ Å^{-3}, $\rho_{\mathrm{Fe}} = 8.27 \ {}^{+0.07}_{-0.01} \cdot 10^{-2}$ Å^{-3}). The normalized measurements are shown in **figure 7.3**.

The significant drop of the magnetization in the field cooled measurement from 10 K to 330 K indicates a lower Curie temperature than the nominal 1041 K. But a reduced Curie temperature in thin magnetic layers is normal [110]. An indication of an induced magnetization in the Pd layer is the increased magnetization of Fe, when assigning the magnetization to the Fe layers. The large increase of the Fe moment from $m = 2.2\ \mu_{\mathrm{B}}$ to around $m = 3\ \mu_{\mathrm{B}}$ is a clear evidence for an induced magnetization in the Pd layer. Subtracting the nominal magnetic moment of Fe from the field cooled data, the average magnetic moment of Pd can be derived. It varies from $0.17\ \mu_{\mathrm{B}} \pm 0.01\ \mu_{\mathrm{B}}$ at 10 K to $0.064\ \mu_{\mathrm{B}} \pm\ 0.01\ \mu_{\mathrm{B}}$ at 330 K. The hysteresis measurements (inset of **figure 7.3**) show typical ferromagnetic hysteresis loops. In oder to clear all doubts, additional PNR and XMCD measurements were performed.

Polarized neutron reflectometry (PNR)

Polarized neutron reflectometry (PNR) measurements were performed at the MARIA reflectometer of JCNS at MLZ. The sample was mounted in a cryostat inside a 1 T electromagnet. During the measurements, the magnetic moments in the sample were saturated by applying a magnetic field in-plane and perpendicular to the propagation vector of the neutrons. The spin-up and spin-down channels with the simulation thereof are shown in **figure 7.5** at a temperature of 10 K.

The measurement was corrected for off-specular scattering, as described in **section 6.1.1** and for alignment inaccuracies. The model used for the nuclear scattering of this PNR measurement is the same model as for the XRR measurement. Only the magnetic contribution was fitted afterwards with an induced magnetization in the Pd layer. A Gaussian magnetic profile of the Pd magnetization, at the interface to Fe, was assumed. Using p_{Fe_i}

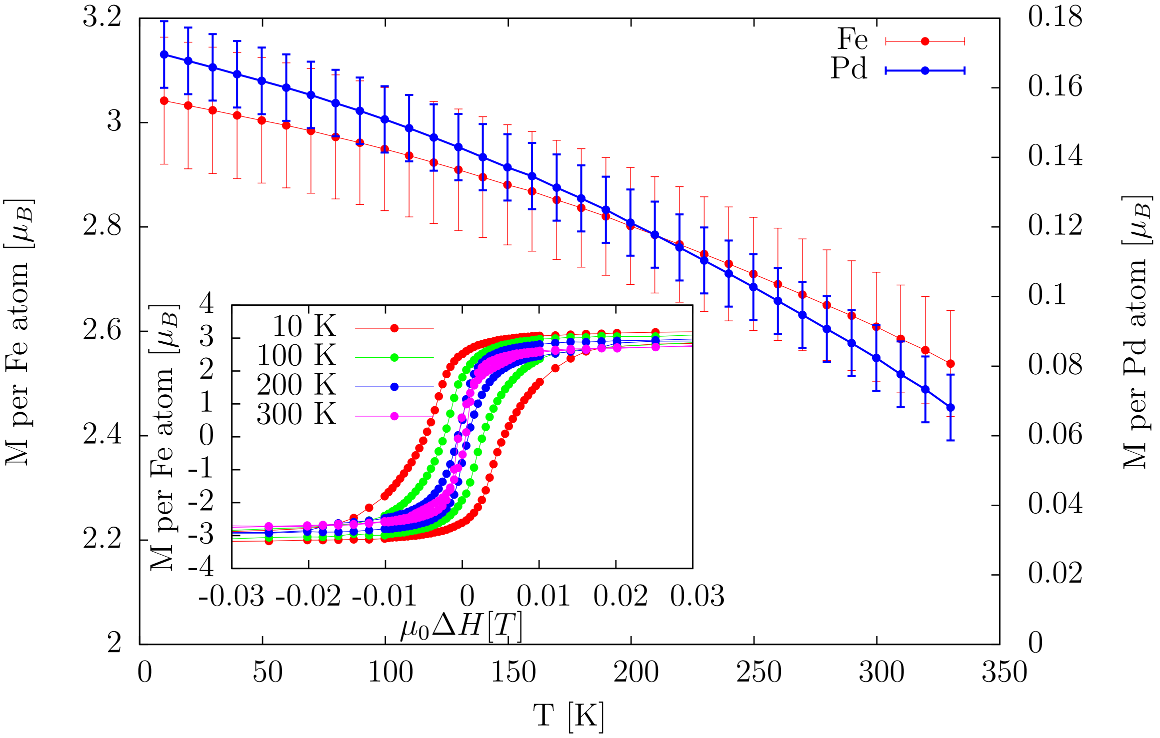

Figure 7.3.: Field cooled measurement of Pd/Fe multilayer (Sample: MBE$_{113}$) at an applied magnetic field of 100 Oe. Inset: Hysteresis measurements done at 10 K, 100 K, 200 K and 300 K which were corrected for paramagnetism by fitting a line to the saturation region and subtracting this line from the hysteresis. The red curve shows the magnetic moment of Fe, with zero Pd magnetization. The blue curve shows the magnetization of Pd, when assuming a Fe magnetization of 2.2 μ_B.

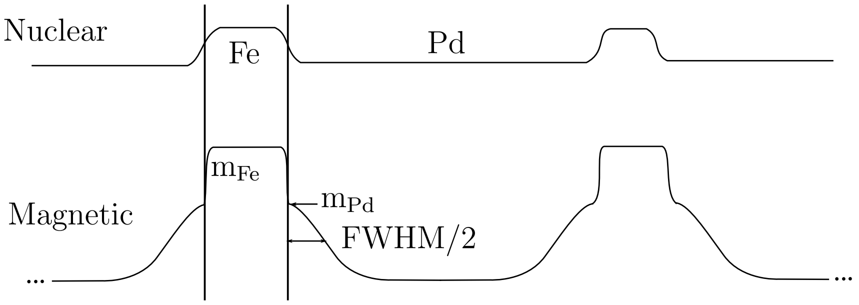

Figure 7.4.: Shows the SLD model for the Pd/Fe multilayer. The model for the nuclear SLD is the same as for the model for the XRR measurements.

as the position of the i-th Fe layer, p_{Pd_i} as the position of the i-th Pd layer and σ_{Pd}^{mag} as the standard deviation width of the induced Pd magnetization, the model for the magnetic

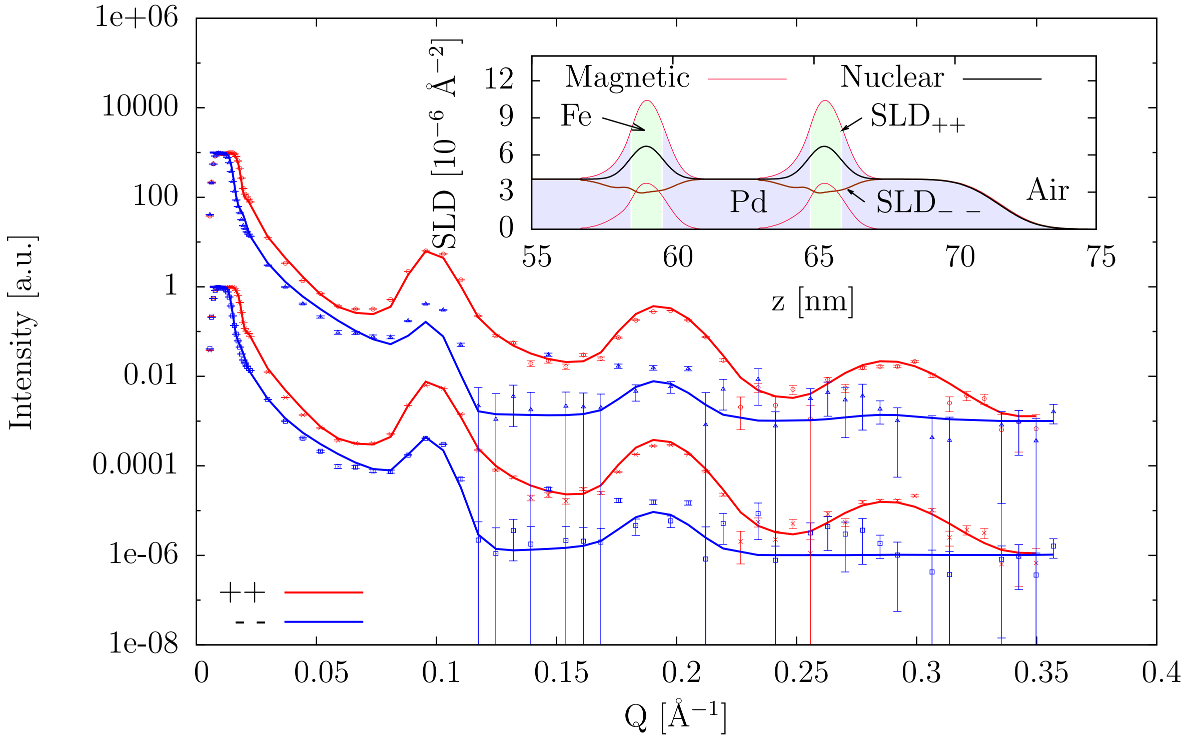

Figure 7.5.: PNR measurement of Pd/Fe multilayer done at MARIA at MLZ. Shown are the up-up (blue) and down-down (red) channels together with simulations with (bottom curves) and without (top curves) magnetically polarized Pd layer (shifted by a factor of 10^3 for better visibility). The SLD for the case of magnetically polarized Pd layer is shown in the inset.

profile in the Pd/Fe multilayer can be expressed with

$$\sum_{i=1}^{10} \Theta\left(x - p_{Fe_i}\right) m_{\mathrm{Fe}} \Theta\left(p_{Fe_{i+1}} - x\right) + \qquad \text{“Fe magnetism“} \tag{7.1}$$

$$\sum_{i=1}^{10} \Theta\left(x - p_{Pd_i}\right) exp\left(-\frac{1}{2}\left(\frac{x - p_{Pd_i}}{\sigma_{Pd}^{mag}}\right)^2\right) m_{\mathrm{Pd}} + \qquad \text{“Pd magnetism with Gaussian profile on left side of Fe“} \tag{7.2}$$

$$\sum_{i=2}^{11} \Theta\left(p_{Pd_i} - x\right) exp\left(-\frac{1}{2}\left(\frac{x - p_{Pd_i}}{\sigma_{Pd}^{mag}}\right)^2\right) m_{\mathrm{Pd}}, \qquad \text{“Pd magnetism with Gaussian profile on right side of Fe“} \tag{7.3}$$

where m_{Pd} is the maximum magnetic moment of Pd and $m_{\mathrm{Fe}} = 2.2\ \mu_{\mathrm{B}}$ is the magnetic moment of Fe. At the interfaces between Pd and Fe, the magnetic profile is smeared out (using the ”GenX“ program [89]) with the error function

$$erf(p_i - x) = \frac{2}{\sqrt{\pi}} \int_0^{\frac{x}{\sqrt{2}\sigma_i}} e^{-t2} dt, \tag{7.4}$$

where p_i is the position of the layer interface and σ is the interface roughness. In order to achieve a resolution suitable to the sharp plateau of total reflexion and the broad features at high Q_z values, a variable resolution (see **section 6.1.4**) has to be assume for the simulations.

Best simulations for models, with and without Pd magnetization, (parameters are listed in **table 7.2**) are shown in **figure 7.5**, where it is clearly visible that the model with induced magnetization in the Pd layer is more suitable (FOM with Pd magnetization: 0.176, FOM without Pd magnetization: 0.202). Especially, the intensity at the first Bragg peak cannot be simulated very well without a magnetic Pd interface. Only by increasing the moment of Fe to 2.7 μ_B, the simulation is as good as the simulation with a magnetic Pd. Thus, a magnetized Pd interface is the most plausible. The inset in **figure 7.5** shows a zoom of the SLD for the model with induced magnetization in the Pd layer. The magnetization of Pd, at the interface to Fe, is 0.54 μ_B $^{+0.04}_{-0.02}$ μ_B, having a standard deviation width of the magnetization of 4.91 Å $^{+0.4}_{-0.06}$ Å. This corresponds to an average magnetic moment of Pd of 0.13 μ_B. The width of the induced magnetization $\sigma_\mathrm{M} = 4.91$ Å is in the same order as the roughness $\sigma = 4.77$ Å, $\sigma = 5.08$ Å at the Pd/Fe interface. This roughness, creates an additional magnetization in the Pd layer, which is handled with the error function and the smearing out of the Fe magnetization. With the model described above, the induced magnetization in the Pd layer is a real additional magnetic moment.

A magnetization of 0.54 μ_B for the Pd layer and a width of the induced magnetization of 4.91 Å does fit to the values determined by Vogel et al. [9]. In order to explicitly show that the Pd layer is magnetically polarized, element specific XMCD measurement at the $L_{2,3}$ edges of Pd were performed.

X-ray magnetic circular dichroism (XMCD)

X-ray magnetic circular dichroism (XMCD) measurements at 4-ID-D at Advanced Photon Source (APS) were performed to verify the induced magnetization of Pd at the interface to Fe. The left and right polarized light was created by a diamond plate and the XMCD signal was measured with a fluorescence detector. These measurements were performed at room temperature and a magnetic field of 300 Oe was applied in-plane and in the direction of the X-ray beam.

Due to a change in intensity, when changing the helicity of the X-rays, the data was treated as described in **section 6.3**. The XMCD signal was determined from XAS measurements in fluorescence mode, measured by changing the helicity of the X-rays and by changing the direction of the magnetic field. For the normalization, the pre-edge region was set to zero and the post-edge region was set to 1 and 1.5 for the L_3 and L_2 edge, respectively. This results in edge-jumps of 1 and 0.5 for the L_3 and L_2 edge, respectively. The resulting XAS spectrum and the XMCD signal are shown in **figure 7.6**, having a

Layers	$\mathrm{Pd_{top}}$	11*Pd	10*Fe	Ag on GaAs	Instrument	
d [Å]	$1.03^{+1.19}_{-0.47}$	$53.89^{+0.19}_{-0.13}$	$11.4^{+0.17}_{-0.12}$	Substrate	$\Delta\lambda/\lambda$	0.1
Δd [Å]	-	$-0.45^{+0.05}_{-0.19}$	$-0.03^{+0.16}_{-0.011}$	-	d_{S_1-Sam} [mm]	4500
σ [Å]	$11.1^{+0.12}_{-0.21}$	$5.08^{+0.7}_{-0.6}$	$4.77^{+0.04}_{-0.1}$	$1.16^{+0.03}_{-0.03}$		
ρ [10^{-2} Å^{-3}]	$6.95^{+0.02}_{-0.01}$	$6.95^{+0.02}_{-0.01}$	$8.27^{+0.07}_{-0.01}$	5.87	$\mathrm{S_1}$ [mm]	2.0
μ_M [μ_B]	-	$0.54^{+0.04}_{-0.02}$	2.2	-	FOM	
σ_M [Å]	-	$4.91^{+0.4}_{-0.06}$	$4.77^{+0.04}_{-0.1}$	-	mag	0.176
$\mathrm{SL_N}$ [10^{-5} Å]	5.91	5.91	9.45	5.92	non-mag	0.202
$\mathrm{SLD_N}$ [10^{-6} Å^{-2}]	$4.11^{+0.01}_{-0.01}$	$4.11^{+0.01}_{-0.01}$	$7.82^{+0.07}_{-0.01}$	3.47		
$\mathrm{SLD_N^{Norm}}$ [10^{-6} Å^{-2}]	4.02	4.02	7.83	3.47		
$\mathrm{SLD_M}$ [10^{-6} Å^{-2}]	-	$0.99^{+0.07}_{-0.04}$	$4.81^{+0.04}_{-0.01}$	-		

Table 7.2.: Summary of the parameters used for the simulation of the PNR measurement. The following parameters are shown: Layer thickness d, thickness variation Δd, density ρ, magnetic moment μ_M, roughness of magnetization σ_M, nuclear scattering length $\mathrm{SL_N}$, nuclear scattering length density $\mathrm{SLD_N}$, magnetic scattering length density $\mathrm{SLD_M}$. With these parameters, FOM accounts for 0.176 (with Pd magnetization) and 0.202 (without Pd magnetization).

S_z	-0.137 ± 0.005	$\mathrm{A_2 + A_3}$	$560 \cdot 10^{-5} \pm 1.65 \cdot 10^{-5}$
L_z	0.014 ± 0.003	$\Delta\mathrm{A_2}$	$-13.7 \cdot 10^{-5} \pm 0.5 \cdot 10^{-5}$
$S_\mathrm{z}/L_\mathrm{z}$	-9.88 ± 2.3	$\Delta\mathrm{A_3}$	$10.8 \cdot 10^{-5} \pm 0.5 \cdot 10^{-5}$

Table 7.3.: Presented are the following parameters derived from the XMCD experiment: Spin moment expectation value $\mathrm{S_z}$, orbital moment expectation value $\mathrm{L_z}$, integration over both edges $\mathrm{A_2 + A_3}$, integration over the XMCD signal at the $\mathrm{L_2}$ and $\mathrm{L_3}$ edge $\Delta\mathrm{A_2}$ and $\Delta\mathrm{A_3}$, respectively.

clear XMCD signal. The $\mathrm{L_3}$ edge shows a negative XMCD signal and the $\mathrm{L_2}$ edge a positive one. Furthermore this XMCD signal changes sign, when changing the helicity of the X-rays or the direction of the applied magnetic field. Thus, artifacts can be excluded.

Applying the sum rules to these XMCD signals will result in the expectation values for the spin and orbital angular moment operator as shown in **table 7.3**. Because of different signs of the XMCD signal at both edges, the L_z expectation value is nearly zero and the ratio between the S_z and L_z expectation values is quite large. The induced magnetism in the Pd layer mainly originates from the spin magnetic moment, which is in agreement with the references [9, 7]. The spin magnetic moment is $\mu_S = g_\mathrm{e} \langle S_\mathrm{z} \rangle = 0.274\ \mu_\mathrm{B}$, with the electron g-factor $g_e \approx 2$. The orbital magnetic moment is $\mu_L = \langle L_\mathrm{z} \rangle = 0.014\ \mu_\mathrm{B}$, resulting in a total magnetic moment of $\mu_\mathrm{z} = \mu_\mathrm{S} + \mu_\mathrm{L} = 0.288\ \mu_\mathrm{B} \pm 0.01\ \mu_\mathrm{B}$. These values are the

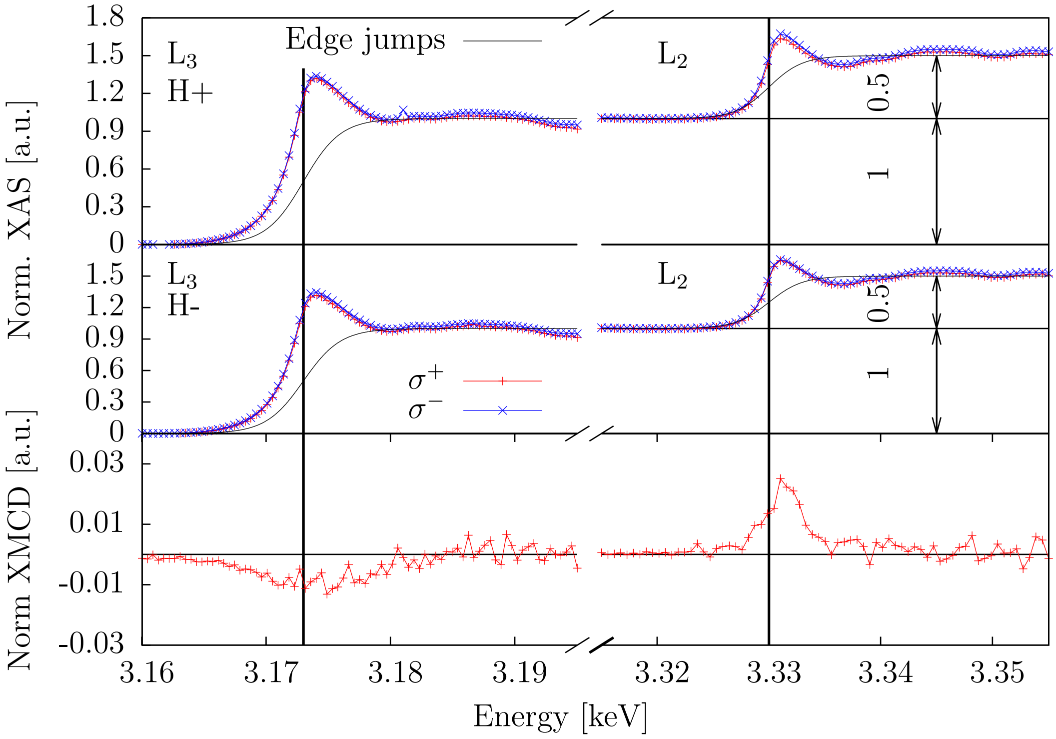

Figure 7.6.: Top: XAS measurement in fluorescence mode at L_3 (3.173 keV) and L_2 edges (3.33 keV) of Pd for left and right circular polarized light with an applied magnetic field of $H = 300$ Oe. Middle: Same fluorescence measurement at an applied magnetic field of $H = -300$ Oe. Bottom: XMCD signal derived thereof.

average of all Pd magnetic moments in the Pd/Fe multilayer. Assuming that only at the interface the Pd layer is magnetically polarized, as can be seen from PNR measurements, and taking a Gaussian magnetic profile for the magnetic moment in the Pd sample, a constrain can be derived for the maximum magnetic moment and the width of the decay.

$$\mu = \frac{\int \mu_{\max} e^{-\frac{1}{2}(x/\sigma)^2}}{d} = \frac{\mu_{\max} \cdot \sigma\sqrt{2\pi}}{d} \rightarrow \mu_{\max} = \frac{\mu \cdot d}{\sigma \cdot \sqrt{2\pi}}, \tag{7.5}$$

with μ the average magnetic moment determined by XMCD, $\mu_{\max}$ the maximum magnetic moment in the Pd layer, directly at the interface, and σ the standard deviation width of the magnetic distribution. Taking the thickness of the Pd layers from XRR measurements ($d = 53.89$ Å) and inserting the width of the magnetic Pd layer $\sigma_M = 4.91$ Å derived from PNR measurements, will result in a maximum magnetic moment in the Pd layer of $\mu_{\max} = 1.26\ \mu_B$, which is larger then the value determined by PNR measurements. With a varying layer thickness and layer roughness in the range of the induced magnetization width, it is difficult to exactly separate the magnetic contributions at the interface in PNR experiments. Considering the SQUID, PNR and XMCD measurements all together, it is clear that Pd is magnetically polarized at the interface to Fe.

7.1.3. Conclusion

SQUID, PNR and XMCD are different measurements, which fit nicely together, although their values for the Pd magnetization are slightly different. Pd is, at the interface to ferromagnetic Fe, definitely magnetically polarized. From SQUID measurements the average magnetic moment of Pd can be determined and it varies from 0.17 $\mu_\mathrm{B} \pm$ 0.01 μ_B at 10 K to 0.065 $\mu_\mathrm{B} \pm$ 0.01 μ_B at 330 K. The PNR measurement confirms this result and shows, that Pd is magnetically polarized at the interface to Fe. The magnetic moment of Pd at the interface is 0.54 μ_B $^{+0.04}_{-0.02}$ μ_B and has a standard deviation width of 4.91 Å $^{+0.4}_{-0.06}$ nm, resulting in an average magnetic moment of 0.13 μ_B. The XMCD measurement proves that the increased magnetization at the interface between Fe and Pd originates from Pd. The averaged magnetic moment of Pd, derived from XMCD measurements, is 0.288 μ_B.

7.2. Oxide/Pd

The LSMO/Pd (Sample: OMBE_{0208}) and LCMO/Pd (Sample: OMBE_{0293}) thin films were grown with OMBE (**section 5.2**). The growth parameters for the 15 nm LSMO and LCMO layers were the same as described in **section 2.1**, where the stoichiometry of the LSMO film was $\mathrm{La_{0.37}Sr_{0.42}MnO_3}$ and the stoichiometry of the LCMO film was $\mathrm{La_{0.72}Ca_{0.3}MnO_3}$. After the growth of the LSMO or LCMO film, a 5 nm Pd layer was deposited at least eight hours after the growth of the oxide layer to minimize oxidization of the Pd film. The Pd film was grown at room temperature to obtain a flat and homogeneous surface, as described in **section 5.4**.

7.2.1. LSMO/Pd

7.2.1.1. Structural Characterization

XRR, XRD, LEED, RHEED and AFM measurements were performed to characterize the structural quality. The LEED and RHEED images indicate the good structural quality

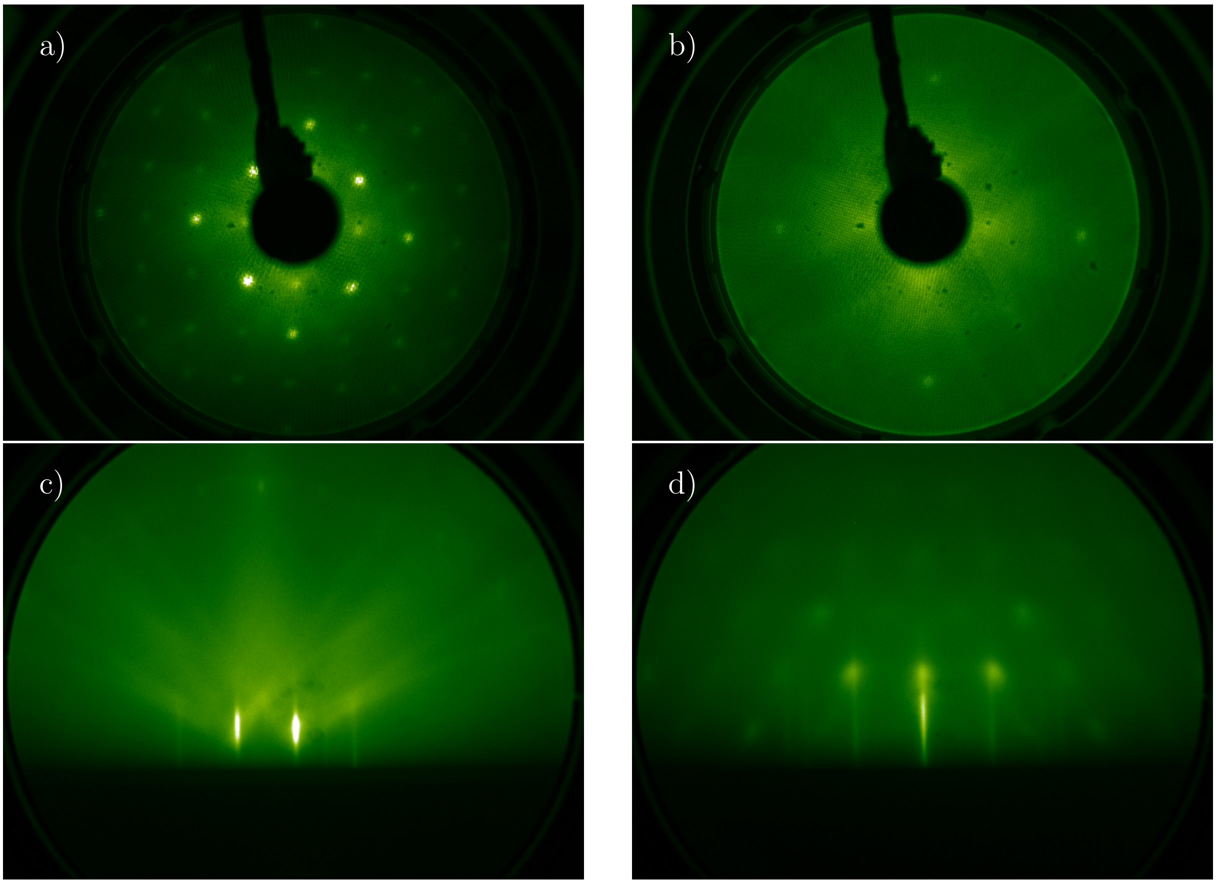

Figure 7.7.: a) LEED image of LSMO film at 150 eV. b) LEED image of Pd film at 150 eV. c) RHEED image of LSMO film after growth. d) RHEED image of Pd film after growth.

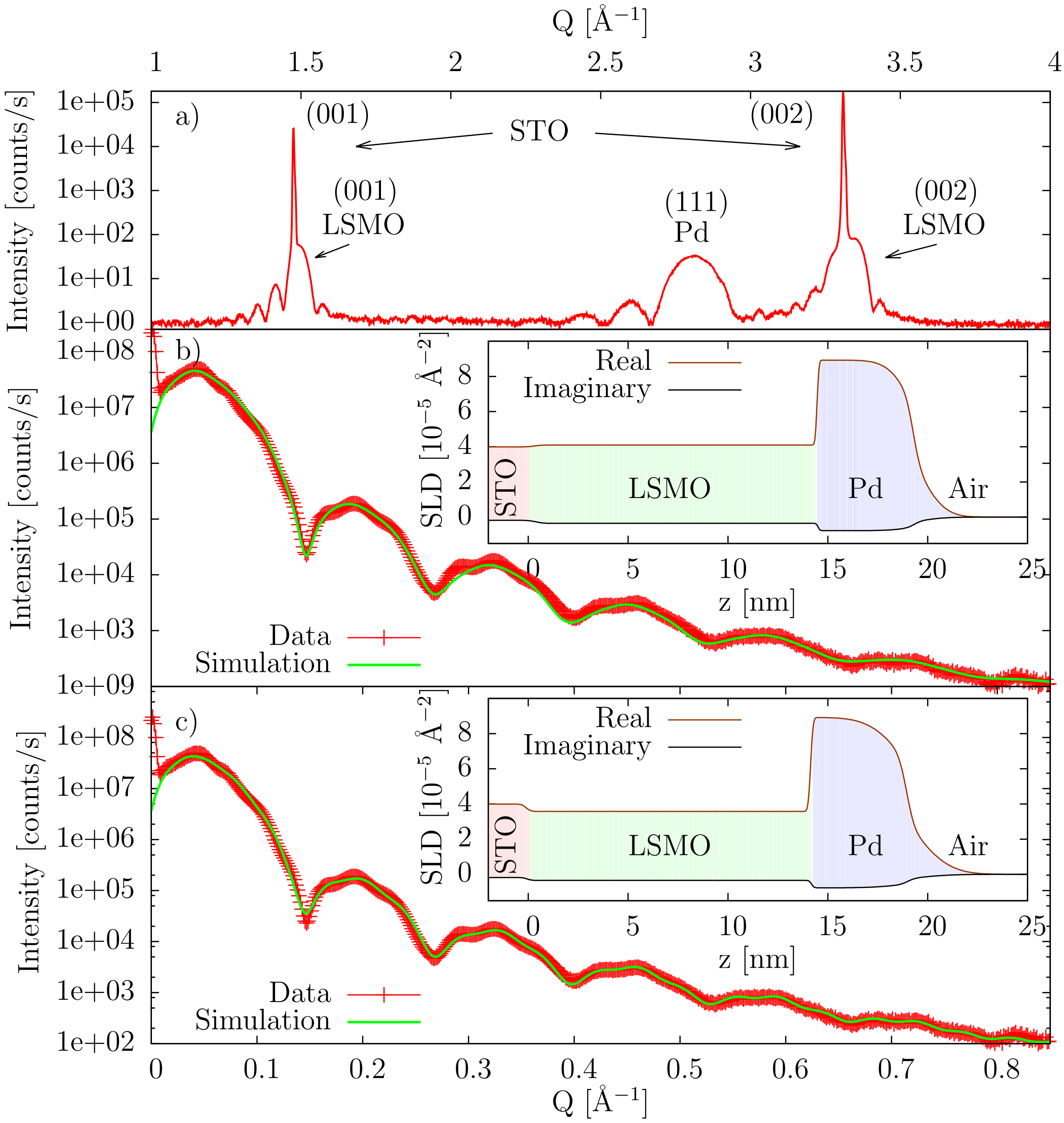

Figure 7.8.: a) XRD measurement in out-of-plane direction. b) XRR measurement and simulation with fixed stoichiometry. The inset shows the SLD, which was used for the simulations. c) XRR measurement and simulation with free stoichiometry. The inset shows the SLD, which was used for the simulations.

(**figure 7.7**) of the LSMO and Pd layer. The sharp and intense Bragg peaks show the high crystalline quality of the LSMO layer, which can also be seen in the RHEED image, in the form of the Laue circle. The Bragg peaks of the Pd layer in the LEED image are less pronounced, but it indicates a crystalline structure with a four fold symmetry. The Bragg peak pattern of the RHEED image fits to a polycrystalline structure, which is in agreement with the visible (111) growth direction in the XRD measurement (**figure 7.8**).

The XRR measurements are shown in **figure 7.8**, where the large pronounced oscillations originate from the 5 nm thick Pd layer and the smaller oscillations from the 15 nm thick LSMO layer. The contrast between the LSMO layer and the STO substrate is negligible with the stoichiometry $La_{0.37}Sr_{0.42}MnO_3$ derived from RBS measurements and the density of LSMO given in the literature $\rho = 1.71 \cdot 10^{-2}$ Å^{-2} [31]. The smaller oscillations in the XRR measurement cannot be simulated with these values. Relaxing the stoichiometry to $La_{0.58}Sr_{0.29}Mn_{0.42}O_{3.03}$ and the density of the LSMO layer to $\rho = 1.62 \cdot 10^{-2}$ Å^{-2}, an increase in the contrast between the LSMO layer and the STO substrate can be achieved, resulting in a better simulation of the smaller oscillations. Mn has a negative neutron scattering length of -3.73 $\cdot 10^{-5}$ Å and influences the scattering length density for X-rays and neutrons differently. The density, as well as the stoichiometry of the LSMO film have to be varied together for the X-ray reflectometry measurement and the polarized neutron reflectometry measurement. Because of the difficulty to measure the stoichiometry in such thin layers, the data will be discussed with fixed and free stoichiometry.

The simulations with fixed (FOM = 4.637) and free (FOM = 4.468) stoichiometry are shown in **figure 7.8** and the parameters for the simulations are presented in **table 7.4** (element parameters taken from literature are shown in **appendix F**). Except the stoichiometry and the SLD of the LSMO layer, the other parameters for fixed and free stoichiometry are very similar. The large difference in the stoichiometry of the LSMO layer, determined by fitting the X-ray reflectometry curve and from the RBS measurement, cannot be explained with the uncertainties of both methods. The Mn rate, during the growth of the LSMO layer, has to be different. This might come from a near empty Mn crucible and, thus, a drop of the Mn rate during growth.

The simulations with fixed and free stoichiometry show a very sharp interface between the LSMO and Pd layer, which is important to measure interface effects and not effects from interdiffusion. In contrast to the sharp LSMO layer, the metallic Pd layer shows a rather smeared out interface to air, which might be a result of the oxidization of the Pd layer.

The oxidized Pd surface might be the only explanation taking the flat surface with a roughness of $\sigma_{\mathrm{AFM}} = 3.39$ Å, visible in the AFM measurements (**figure 7.9**), into account. With a oxygen gradient at the Pd surface, the scattering length density will show a similar profile as with a higher surface roughness.

7.2.1.2. Magnetic Characterization

The magnetic properties are investigated macroscopically with SQUID measurements and then the microscopic properties are investigated with PNR and XMCD measurements.

SQUID magnetometry measurements

The macroscopic magnetometry measurements were performed at the SQUID magnetometer, using the RSO option to get a better resolution. The measured magnetic moments were assigned to the Mn atoms. The XRR results, for the LSMO layer thickness $d = 142.41\ ^{+0.32}_{-0.20}$ Å and the density $\rho = 1.62\ ^{+0.02}_{-0.01} \cdot 10^{-2}$Å^{-2}, are used to calculate the

	d [Å]	σ [Å]	ρ [10^{-2}Å^{-3}]	ρ^{Norm}	**Re** SLD [10^{-5}Å^{-2}]	**Im** SLD
$\mathrm{STO}_{\mathrm{free}}$	-	$1.79^{+0.03}_{-0.08}$	1.68	1.68	3.98	0.18
$\mathrm{STO}_{\mathrm{fix}}$	-	$3.05^{+0.21}_{-0.16}$				
$\mathrm{LSMO}_{\mathrm{free}}$	$142.41^{+0.32}_{-0.20}$	$0.99^{+0.03}_{-0.03}$	$1.62^{+0.02}_{-0.01}$	1.71	$3.58^{+0.07}_{-0.06}$	$0.34^{+0.01}_{-0.01}$
$\mathrm{LSMO}_{\mathrm{fix}}$	$141.34^{+1.19}_{-0.94}$	$0.72^{+0.06}_{-0.07}$	1.71		4.10	0.35
$\mathrm{Pd}_{\mathrm{free}}$	$48.05^{+0.09}_{-0.05}$	$3.05^{+0.06}_{-0.10}$	$6.89^{+0.02}_{-0.02}$	6.85	$8.97^{+0.03}_{-0.03}$	$0.77^{+0.00}_{-0.00}$
$\mathrm{Pd}_{\mathrm{fix}}$	$48.15^{+0.25}_{-0.18}$	$2.91^{+0.07}_{-0.11}$	$6.87^{+0.02}_{-0.03}$		$8.94^{+0.03}_{-0.04}$	$0.77^{+0.00}_{-0.00}$
$\mathrm{Pd}^{\mathrm{top}}_{\mathrm{free}}$	$1.58^{+0.08}_{-0.08}$	$14.84^{+0.18}_{-0.35}$	$5.25^{+0.04}_{-0.01}$	6.85	$5.64^{+0.05}_{-0.01}$	$0.47^{+0.00}_{-0.00}$
$\mathrm{Pd}^{\mathrm{top}}_{\mathrm{fix}}$	$1.62^{+0.20}_{-0.18}$	$10.59^{+0.94}_{-0.69}$	$6.69^{+0.04}_{-0.07}$		$5.85^{+0.05}_{-0.09}$	$0.46^{+0.00}_{-0.01}$

	La	Sr	Mn	O	FOM
$\mathrm{LSMO}_{\mathrm{free}}$	$0.58^{+0.01}_{-0.01}$	$0.29^{+0.01}_{-0.01}$	$0.42^{+0.01}_{-0.01}$	$3.03^{+0.02}_{-0.02}$	4.468
$\mathrm{LSMO}_{\mathrm{fix}}$	0.37	0.42	1.00	3.00	4.637

Table 7.4.: Parameters derived from analysis of XRR measurement of LSMO/Pd thin films with the fixed and free stoichiometry for the LSMO layer. The following parameters are presented: Thickness d, roughness σ, unit cell density ρ and the scattering length density SLD.

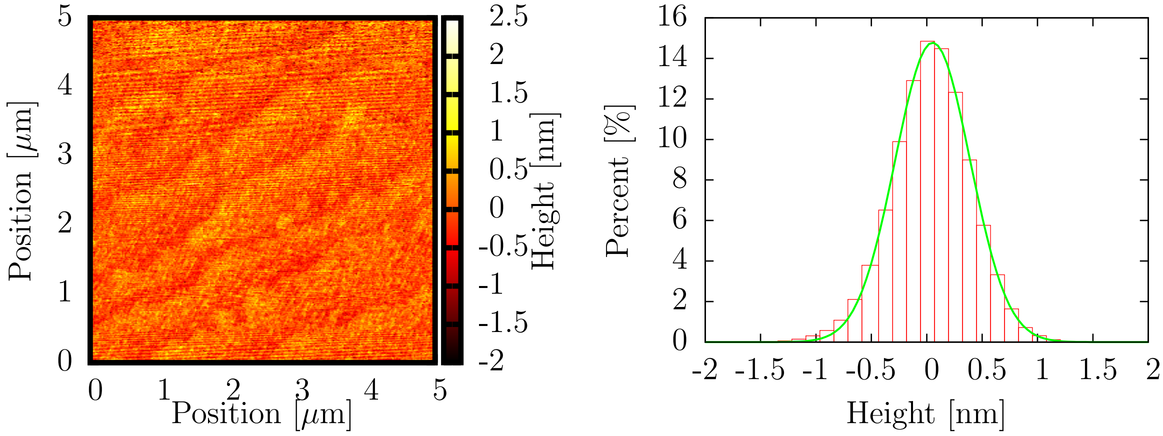

Figure 7.9.: On the left-hand side the topography of the AFM measurement is presented and on the right-hand side the height distribution thereof. Gaussian profile is fitted to the height distribution, with a roughness of 3.39 Å. The lower roughness of this AFM measurement, compared to the large Pd layer roughness of the XRR measurement, might indicate an oxidized Pd surface.

number of Mn atoms in the LSMO layer (surface area of the sample: 21.55 ± 0.4 mm^2). The field cooled measurement is shown in **figure 7.10**, where the STO transition at 105 K [111] is clearly visible. Around this transition the STO a lattice parameter changes

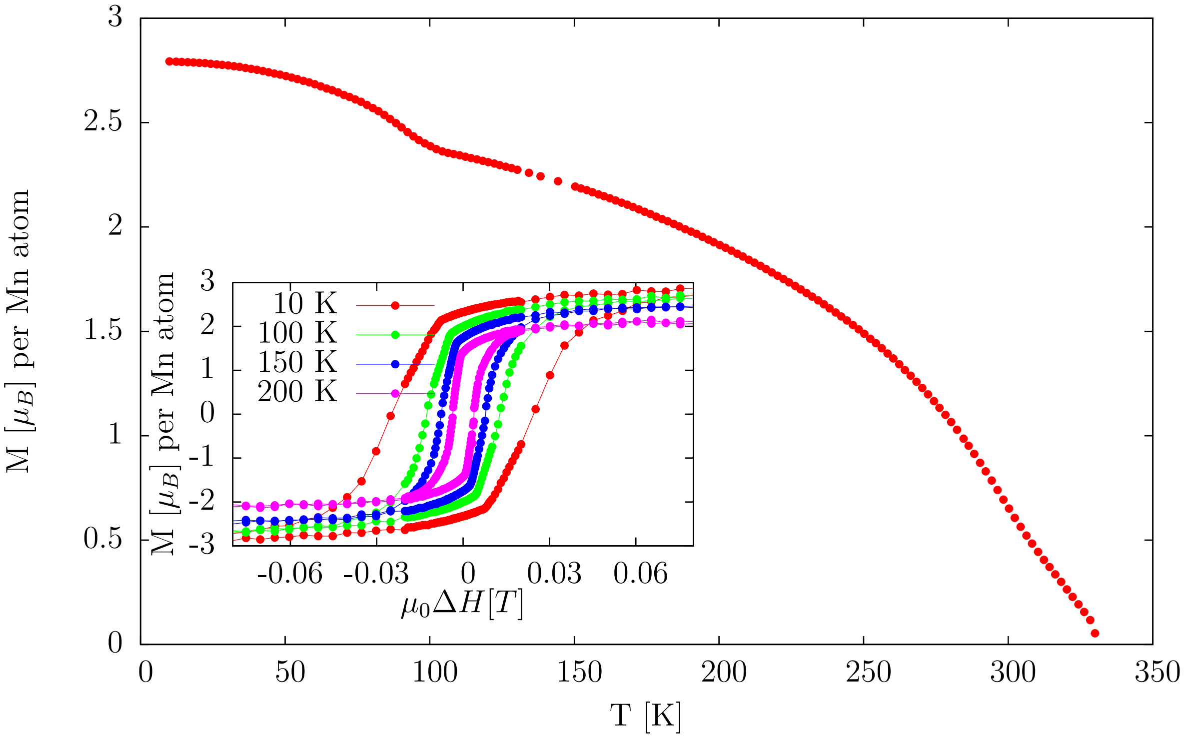

Figure 7.10.: Field cooled measurement of LSMO/Pd thin films (Sample: OMBE_{0208}) at an applied magnetic field of 100 Oe. Inset shows hysteresis measurements performed at 10 K, 100 K, 150 K, 200 K, which were corrected for diamagnetism and paramagnetism by fitting a line to the saturation region and subtracting this line from the hysteresis curves. The Curie temperature is reduced to 325 K ± 5 K from 380 K.

from 3.8984 Å to 3.8974 and the c lattice parameter to 3.8987 [112], which results in different bonding lengths and bonding angles and, therefore, altered superexchange and double exchange interactions. The high T_C temperature 325 K ± 5 K indicates a high crystalline quality sample, although it is reduced from bulk Curie temperature of 380 K. A small kink might occur at 300 K, which may indicate a second magnetic contribution (induced magnetic moment in the Pd layer). In the field cooled measurement and the hysteresis measurement a reduced magnetization in comparison to the nominal magnetization of $m = 3.7\ \mu_\mathrm{B}$ is visible. This might arise from the off-stoichiometry of the LSMO film, the aging of the sample or just due to the cutting procedure of the sample. The explanation, due to the cutting or the aging, is most plausible if the results from the PNR measurement (see next section) are taken into account.

The hysteresis measurements are corrected for diamagnetism and paramagnetism by fitting a line to the saturation region and subtracting this line from the measurements. The hysteresis measurements show the typical increase of the coercive field with a decreasing temperature. A slight misalignment of the samples easy axis might be present because of the rounded shape of the hysteresis loops. From macroscopic magnetometry measurements no clear evidence of an induced magnetization in the Pd layer can be de-

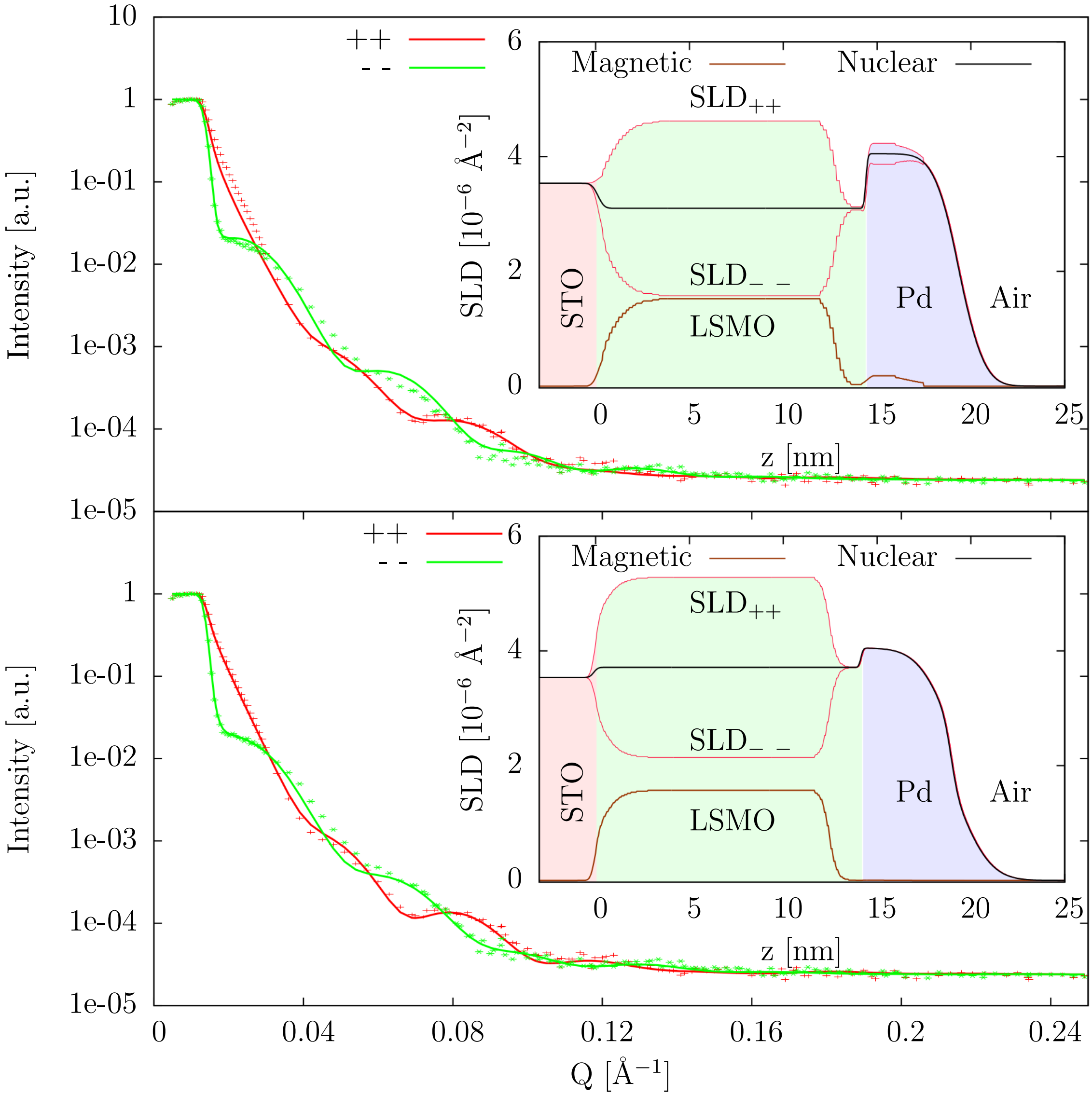

Figure 7.11.: PNR measurement of LSMO/Pd sample at D17 at ILL. The up-up and down-down channels are shown with the simulations thereof. The points are the measured data and the solid lines are the simulations. The inset shows the SLD, which was used for the simulations. Top: Fixed stoichiometry. Bottom: Free stoichiometry.

rived. Due to this, other methods like PNR measurements or XMCD measurements were applied.

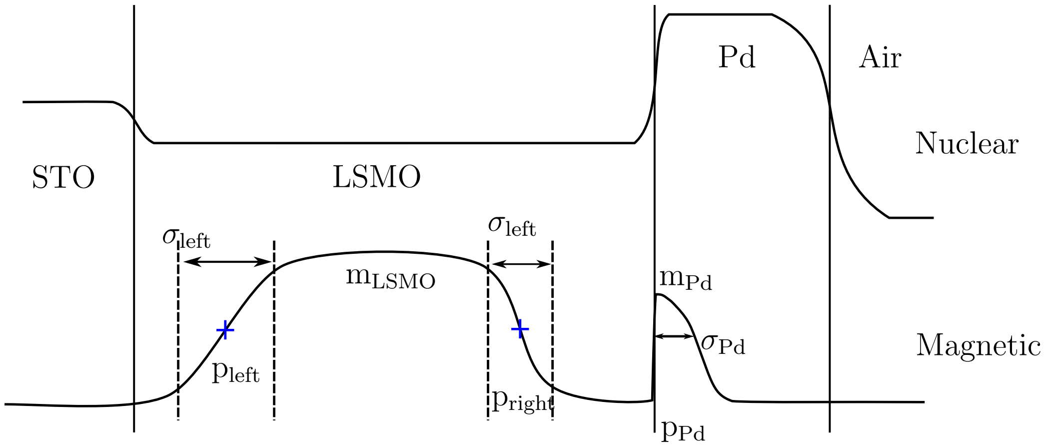

Figure 7.12.: SLD model for the LSMO/Pd sample. The model for the nuclear SLD is the same as for the model for the XRR measurements.

Polarized Neutron Reflectometry Measurements (PNR)

Polarized neutron reflectometry (PNR) measurements were performed at the D17 reflectometer at ILL. A magnetic field of 1 T was applied in-plane and perpendicular to the incident neutron beam. The width of the second slit was adjusted at each angle position of the sample to fully illuminate the sample, but also to reduce the background by cutting off the edges of the neutron beam. The PNR measurement is shown in **figure 7.11**, where both channels (++, - -) are presented with simulations thereof.

The simulations of these PNR measurements were carried out together with the XRR measurements to obtain one model. As described in **section 6.1.4**, it was necessary to take a non Gaussian profile of the wavelength distribution into account. Otherwise the resolution of the simulations would not fit the resolution of the measurement. Additionally, a variable resolution was used. The stoichiometry was taken from RBS measurements (**section 5.2.2**) as well as fitted together with the density. In order to simulate an induced magnetization in the Pd layer, as well as a reduced magnetization of the LSMO layer at the interfaces [102], the nuclear SLD profile was separated from the magnetic SLD profile. The model for the nuclear SLD profile consists of the LSMO and Pd layers without magnetization. The model for the magnetic contribution are the individual LSMO and Pd layers, but sliced into smaller layers. The edges of the magnetization in the LSMO layer were simulated with two Fermi-Dirac distributions, with variable positions (p_{left}, p_{right}) and magnetic roughnesses (σ_{left}, σ_{right}). The magnetism of the Pd interface was simulated with a Gaussian function, at position p_{Pd} and standard deviation σ_{Pd} multiplied with a Heaviside function $\Theta(x)$. The magnetism in these layers was, thus, set according to the model shown in **figure 7.12** and the formula

$$M = \frac{m_{\text{LSMO}}}{\left(1 + e^{-(x-p_{\text{left}})/\sigma_{\text{left}}}\right) \cdot \left(1 + e^{+(x-p_{\text{right}})/\sigma_{\text{right}}}\right)} + m_{\text{Pd}} \cdot \Theta(p_{Pd}) \cdot e^{\frac{(x-p_{Pd})^2}{2\sigma_{\text{Pd}}}}. \tag{7.6}$$

With a fixed stoichiometry and density of the LSMO layer, the shape of the curve in

	d [Å]	σ [Å]	ρ [10^{-2}Å^{-3}]	ρ^{Norm} [10^{-2}Å^{-3}]	SL [10^{-5} Å]	SLD [10^{-6}Å^{-2}]
$\mathrm{STO_{free}}$	-	$1.79\ ^{+0.03}_{-0.08}$	1.68	1.68	20.99	3.53
$\mathrm{STO_{fix}}$	-	$3.05\ ^{+0.21}_{-0.16}$				
$\mathrm{LSMO_{free}}$	$142.41\ ^{+0.32}_{-0.20}$	$0.99\ ^{+0.03}_{-0.03}$	$1.62\ ^{+0.02}_{-0.01}$	1.71	$22.88\ ^{+0.23}_{-0.18}$	$3.71\ ^{+0.04}_{-0.03}$
$\mathrm{LSMO_{fix}}$	$141.34\ ^{+1.19}_{-0.94}$	$0.72\ ^{+0.06}_{-0.07}$	1.71		19.68	3.36
$\mathrm{Pd_{free}}$	$48.05\ ^{+0.09}_{-0.05}$	$3.05\ ^{+0.06}_{-0.10}$	$6.89\ ^{+0.02}_{-0.02}$	6.85	5.91	$4.07\ ^{+0.01}_{-0.01}$
$\mathrm{Pd_{fix}}$	$48.15\ ^{+0.25}_{-0.18}$	$2.91\ ^{+0.07}_{-0.11}$	$6.87\ ^{+0.02}_{-0.03}$			$4.06\ ^{+0.01}_{-0.02}$
$\mathrm{Pd^{top}_{free}}$	$1.58\ ^{+0.08}_{-0.08}$	$14.84\ ^{+0.18}_{-0.35}$	$5.25\ ^{+0.04}_{-0.01}$	6.85	5.91	$3.09\ ^{+0.02}_{-0.01}$
$\mathrm{Pd^{top}_{fix}}$	$1.62\ ^{+0.20}_{-0.18}$	$10.59\ ^{+0.94}_{-0.69}$	$6.69\ ^{+0.04}_{-0.07}$			$3.93\ ^{+0.02}_{-0.04}$

	μ_{M} [μ_{B}]	σ_{M} [Å]	$\mathrm{p_M}$ [Å]	$\mathrm{SLD_M}$ [10^{-6}Å^{-2}]	Instrument	
$\mathrm{LSMO_{free}}$	$3.66\ ^{+0.11}_{-0.03}$	$10.99\ ^{+0.33}_{-0.72}$	$0.16\ ^{+9.23}_{-0.06}$	$1.57\ ^{+0.06}_{-0.01}$	$\Delta\lambda/\lambda$	Real
		$12.39\ ^{+0.43}_{-0.34}$	$124.77\ ^{+0.74}_{-0.74}$		d_{S_1-Sam} [mm]	3605
$\mathrm{LSMO_{fix}}$	$3.67\ ^{+0.12}_{-0.03}$	$10.17\ ^{+0.24}_{-0.54}$	$0.65\ ^{+2.56}_{-0.39}$	$1.66\ ^{+0.05}_{-0.01}$	$\mathrm{S_1}$ [mm]	1.8
		$12.24\ ^{+1.35}_{-0.99}$	$124.64\ ^{+2.10}_{-6.75}$			
$\mathrm{Pd_{free}}$	$0.00\ ^{+0.26}_{-0.00}$	$11.27\ ^{+1.17}_{-0.56}$	Interface	$0.00\ ^{+0.47}_{-0.00}$	$\mathrm{FOM_{free}}$	3.53
$\mathrm{Pd_{fix}}$	$0.11\ ^{+0.16}_{-0.09}$	$17.16\ ^{+0.09}_{-0.22}$	Interface	$0.05\ ^{+0.30}_{-0.16}$	$\mathrm{FOM_{fix}}$	3.87

Table 7.5.: Parameters derived from the analysis of the PNR measurement of LSMO/Pd thin film. The parameters are: Thickness d, roughness σ, density ρ, neutron scattering length SL, scattering length density SLD, magnetic moment μ_{B}, magnetic roughness σ_{M}, position of the beginning and end of the magnetization p_{M}, magnetic scattering length density SLD_{M} as well as the instrument parameters.

the ++ channel, after the plateau of total reflexion, cannot be simulated (**figure 7.11**). The scattering length density of the LSMO layer has to be increased, which can be achieved by reducing the Mn concentration. Mn has a negative neutron scattering length $SL = -3.73 \cdot 10^{-5}$ Å and influences the SLD for neutrons and X-rays differently. By relaxing the stoichiometry to $\mathrm{La_{0.58}Sr_{0.29}Mn_{0.42}O_{3.03}}$ and the density of the LSMO layer to $\rho = 1.62$ Å^{-3} the simulation can be improved (**figure 7.11**). The quality of both simulations is $FOM_{\mathrm{fix}} = 3.87$ and $FOM_{\mathrm{free}} = 3.53$, which differs around 10%. Otherwise, the shape of the curve is fitted pretty well with this model, although small deviations between simulation and measurement are present in both channels, especially at $Q = 0.05$ Å^{-1} in the - - channel.

As can be seen in the SLD profile or in **table 7.5**, a reduced magnetization in the LSMO

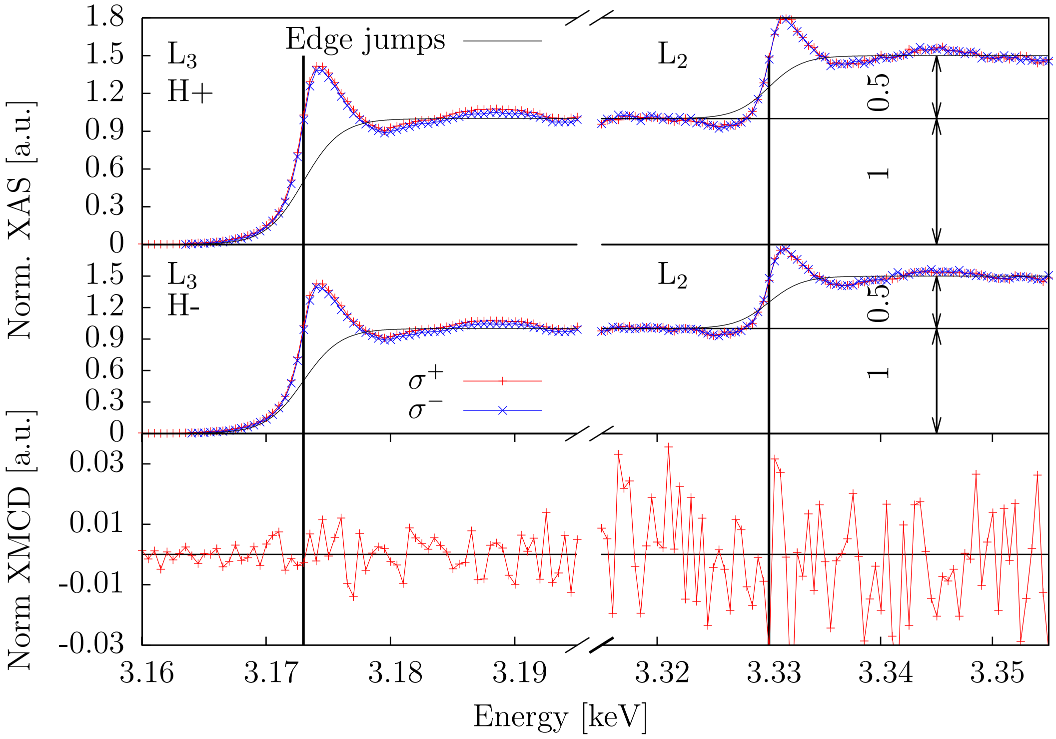

Figure 7.13.: Top: XAS measurement in fluorescence mode at L_3 (3.173 keV) and L_2 edges (3.33 keV) of Pd for left and right circular polarized light with an applied magnetic field of $H = 300$ *Oe*. Middle: Same fluorescence measurement at an applied magnetic field of $H = -300$ *Oe*. Bottom: XMCD signal derived thereof.

layer has to be assumed. The width of the LSMO magnetization is 124.61 Å (123.99 Å), in contrast to the LSMO layer thickness of 142.41 Å (141.34 Å) for free (fixed) stoichiometry. Pd has only a small magnetization of 0.00 μ_B (0.11 μ_B) with a roughness of the magnetization of 11.27 Å (17.16 Å). The larger Pd magnetization, for the fixed stoichiometry, can be attributed to the differences between the simulation and the data after the plateau of total reflexion, which can be slightly reduced by inducing a magnetization inside the Pd layer. Considering the better simulation with free stoichiometry and negligible induced magnetization inside the Pd layer and the suppressed magnetization of the LSMO layer at the interface to Pd, the most plausible result of the PNR measurement is that Pd can only have a negligible or no induced magnetization at the interface to LSMO.

The effects of the induced magnetization overlap with resolution problems and the uncertainty of the LSMO magnetization. XMCD measurement will give a further understanding of a possible induced Pd magnetization.

XMCD measurements

X-ray magnetic circular dichroism (XMCD) measurement of the LSMO/Pd sample was performed at the 4-ID-D beamline at APS at 10 K and the $L_{2,3}$ edges of Pd. The magnetic

S_z [$\hbar$]	0.06 ± 0.05	A1	$467 \cdot 10^{-5} \pm 1.66 \cdot 10^{-5}$
L_z [$\hbar$]	-0.04 ± 0.04	A2	$-6.87 \cdot 10^{-5} \pm 5.84 \cdot 10^{-5}$
S_z/L_z [$\hbar$]	-1.47 ± 1.82	A3	$-0.01 \cdot 10^{-5} \pm 1.96 \cdot 10^{-5}$

Table 7.6.: Presented are the following parameters derived from the XMCD experiment: Spin moment expectation value S_z, orbital moment expectation value L_z, integration over both edges $A_2 + A_3$, integration over the XMCD signal at the L_2 and L_3 edge ΔA_2 and ΔA_3, respectively.

field of 300 Oe was applied in-plain and in direction of the X-ray beam. The XMCD signal was measured twofold, by changing the helicity of the X-ray beam with a phase retarder and by rotating the direction of the applied magnetic field. In this way any artifact can be excluded.

As described in **section 6.3**, the XAS measurements were normalized by setting the pre-edge region to zero for both edges and then the edge jumps were scaled to 1 or 0.5 for the L_3 or L_2 edges, respectively [106]. The resulting XAS and XMCD measurements are shown in **figure 7.13**. The L_3 edge was measured longer than the L_2 edge, because it seemed that a XMCD signal was present at the L_3 edge. Due to the shorter measuring time, the bigger noise at the L_2 edge is clearly visible. Applying the XMCD sum rules to the XMCD signals results in the expectation values for the spin and orbital moments, as shown in **table 7.6**.

Although, the sum rules show a spin and orbital moment, it is clearly visible from **figure 7.13** and from the derived errors that these values originate from the large noise at the L_2 edge and the statistical error thereof. The integral over the XMCD signal at the L_3 edge is nearly two orders below the integral over the XMCD signal at the L_2 edge. According to **equation 3.24**, the ratio between spin and orbital operator is nearly 3/2. The total average magnetic moment of Pd can be calculated to $\mu_z = g_e \langle S_z \rangle + \langle L_z \rangle = \frac{5 \cdot A3 - 4 \cdot A2}{A1} n_h = 0.08\ \mu_B \pm 0.07\ \mu_B$, with $n_h = 1.34$.

The PNR measurements show a magnetically "dead" layer inside LSMO and a negligible Pd magnetization. The XMCD measurement could not prove that Pd is magnetically polarized. The deduced magnetic moment is small and has a large error. Considering both results together indicates that Pd carries no magnetization at the interface to LSMO.

7.2.2. LCMO/Pd

Although the LSMO/Pd layered sample shows no induced magnetization at the Pd interface, it is worth to investigate the second system. The double exchange and superexchange will be different for LSMO and LCMO, changing any interface effects.

7.2.2.1. Structural Characterization

The structure of the LCMO/Pd layered sample was investigated with XRR, XRD, LEED and RHEED measurements. The LEED and RHEED measurements indicate a good

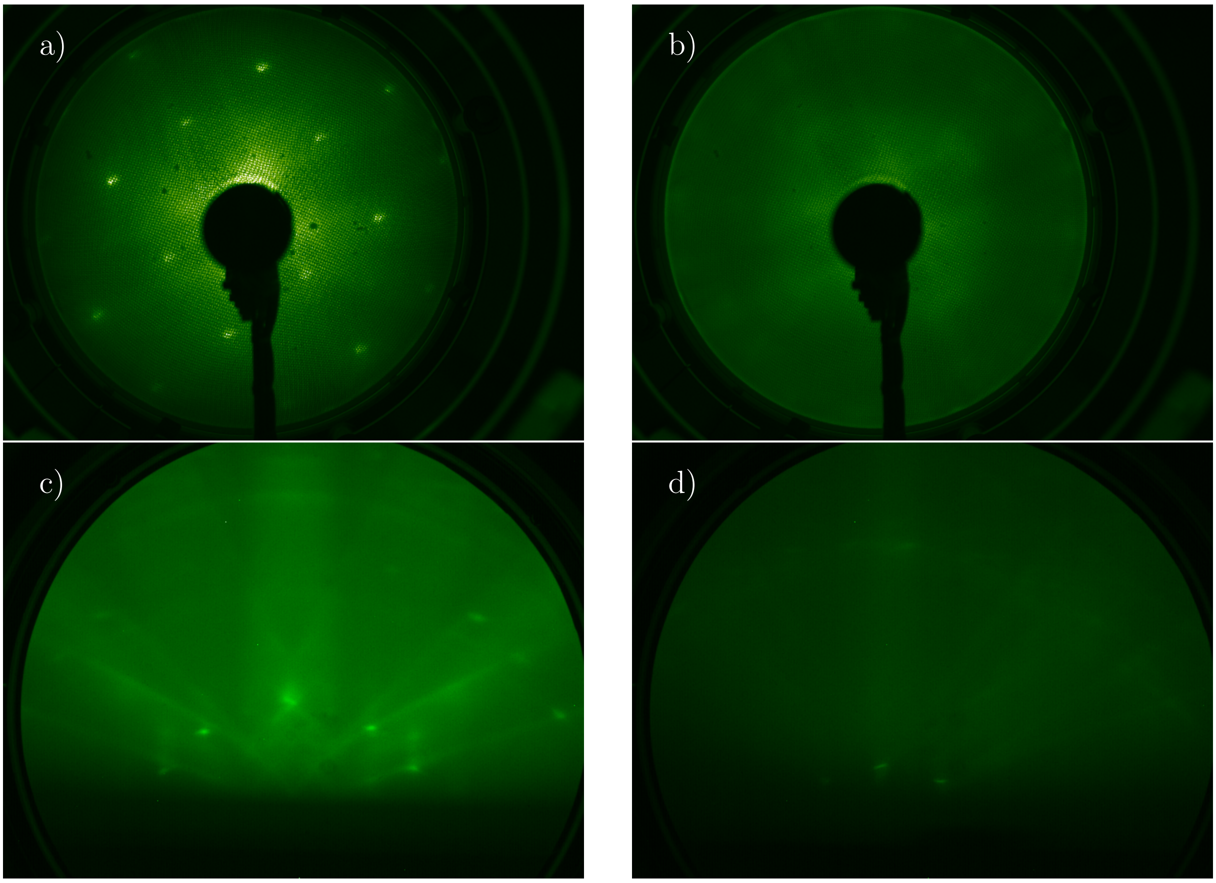

Figure 7.14.: a) LEED image of LCMO film at 100 eV. b) LEED image of Pd film at 100 eV. c) RHEED image of LCMO film after growth. d) RHEED image of Pd film after growth.

	d	σ	ρ	ρ^{Norm}	**Re** SLD	**Im** SLD
	[Å]	[Å]	[10^{-2}Å^{-3}]	[10^{-2}Å^{-3}]	[10^{-5}Å^{-2}]	
STO	-	$4.61^{+0.21}_{-0.85}$	1.68	1.68	3.98	0.18
LCMO	$171.57^{+0.46}_{-0.67}$	$2.36^{+0.18}_{-0.16}$	$1.67^{+0.03}_{-0.02}$	1.71	$4.47^{+0.07}_{-0.05}$	$0.49^{+0.01}_{-0.01}$
Pd	$58.79^{+0.11}_{-0.20}$	$1.00^{+0.02}_{-0.00}$	$6.88^{+0.02}_{-0.04}$	6.85	$8.96^{+0.02}_{-0.06}$	$0.77^{+0.00}_{-0.01}$
Pd^{top}	$0.11^{+9.12}_{-0.01}$	$11.47^{+0.41}_{-0.99}$	$5.36^{+0.29}_{-0.08}$	6.85	$2.57^{+0.37}_{-0.11}$	$0.14^{+0.04}_{-0.01}$

Table 7.7.: Parameters for the simulation of the XRR measurements presented in **figure 7.15** of the LCMO/Pd films (Sample: OMBE_{0293}). The following parameters are presented: Thickness d, roughness σ, unit cell density ρ and the scattering length density SLD.

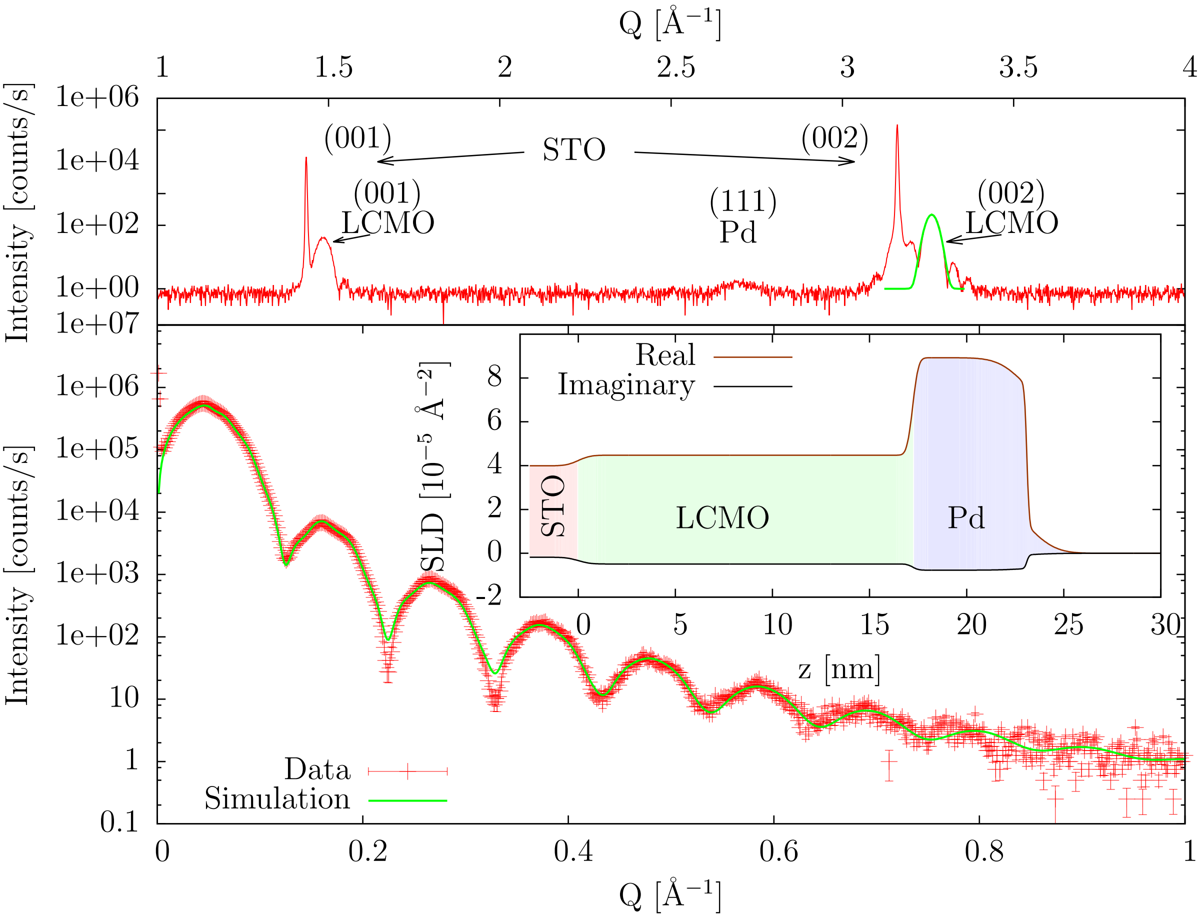

Figure 7.15.: Top: XRD measurement in the out-of-plane direction. Bottom: XRR measurement of the LCMO/Pd films (Sample: OMBE$_{0293}$) with simulation thereof (FOM = $1.03 \cdot 10^{-1}$). The inset side shows the SLD, which was used for the simulations.

structure quality of the LCMO film, which can be confirmed with XRR and XRD measurements (**figure 7.15**). But nearly no structure in the LEED and RHEED images of the Pd layer can be seen. The simulations of the XRR measurement need a Pd top layer with a reduced SLD 2.57 $^{+0.37}_{-0.11} \cdot 10^{-5}$Å^{-2} and an increased roughness 11.47 $^{+0.41}_{-0.99}$ Å in order to simulate the decay appropriately. This can be explained with an oxidized Pd interface, as in the case of the LSMO/Pd sample.

In contrast to the LSMO/Pd sample, the LCMO/Pd sample could be simulated with the stoichiometry $La_{0.72}Ca_{0.3}MnO_3$ determined with RBS measurements on the single LCMO layer described in **section 5.2.1**. But the density of the LCMO layer has to be reduced to 1.67 $^{+0.03}_{-0.02} \cdot 10^{-2}$Å^{-3} from the nominal $1.72 \cdot 10^{-2}$ Å^{-3}. Additional parameters for the stoichiometry of the LCMO film could slightly improve the simulations, but not significantly. The parameters for the simulation of the XRR measurement are presented in **table 7.7**. The roughness of the LCMO layer is in the order of half a unit cell of the LCMO layer, indicating a very smooth interface to the Pd layer. This is necessary to

	d [Å]	σ [Å]	ρ [10^{-2}Å^{-3}]	ρ^{Norm} [10^{-2}Å^{-3}]	SL [10^{-5} Å]	SLD [10^{-6}Å^{-2}]
STO	-	$4.61\ ^{+0.21}_{-0.85}$	1.68	1.68	20.99	3.53
LCMO	$171.57\ ^{+0.46}_{-0.67}$	$2.36\ ^{+0.18}_{-0.16}$	$1.67\ ^{+0.03}_{-0.02}$	1.72	21.02	$3.51\ ^{+0.06}_{0.05}$
Pd	$58.79\ ^{+0.11}_{-0.20}$	$1.00\ ^{+0.02}_{-0.00}$	$6.88\ ^{+0.02}_{-0.04}$	6.85	5.91	$4.07\ ^{+0.01}_{-0.03}$
$\mathrm{Pd^{top}}$	$0.11\ ^{+9.12}_{-0.01}$	$11.47\ ^{+0.41}_{-0.99}$	$5.36\ ^{+0.29}_{-0.08}$	6.85	$5.84\ ^{+0.12}_{-0.05}$	$3.12\ ^{+0.17}_{-0.05}$

	μ_{M} [μ_{B}]	σ_{M} [Å]	$\mathrm{p_M}$ [Å]	$\mathrm{SLD_M}$ [10^{-6}Å^{-2}]	FOM = $4.29{\cdot}10^{-2}$	
					Instrument	
LCMO	$1.12\ ^{+0.26}_{-0.08}$	$16.04\ ^{+2.60}_{-3.37}$	$1.10\ ^{+16.45}_{-0.97}$	$0.49\ ^{+0.12}_{-0.04}$	$\Delta\lambda/\lambda$	0.1
		$4.75\ ^{+0.26}_{-0.30}$	$120.84\ ^{+0.10}_{-0.24}$		d_{S_1-Sam} [mm]	4500
Pd	$0.00\ ^{+0.72}_{-0.00}$	$2.00\ ^{+0.00}_{0.00}$	Interface	$0.00\ ^{+1.31}_{-0.00}$	$\mathrm{S_1}$ [mm]	1.8

Table 7.8.: Parameters derived from the analysis of the PNR measurement of the LCMO/Pd thin films (Sample: $\mathrm{OMBE_{0293}}$). The parameters are: Thickness d, roughness σ, density ρ, neutron scattering length SL, scattering length density SLD, magnetic moment μ_{B}, magnetic roughness σ_{M}, position of magnetization onset and offset p_{M}, magnetic scattering length density SLD_{M} as well as the instrument parameters.

investigate the interface effects and not effects from interdiffusion.

The XRD measurement in **figure 7.15** shows the (002) Bragg peak of the STO substrate and the LCMO layer (3.27 Å^{-1}), with a lattice parameter of 3.80 Å. At 2.8 Å^{-1} an additional peak is visible, although very broad and with very low intensity. The peak position corresponds to the (111) Bragg peak of Pd. In contrast to the LSMO/Pd layer, the intensity of the (111) Bragg peak of Pd is very low indicating an imperfect crystalline quality of the Pd layer, which is in agreement to the LEED and RHEED images.

7.2.2.2. Magnetic Characterization

The magnetic properties at the interface of the LCMO/Pd films were investigated with PNR measurements carried out at MARIA at MLZ. The measurements were performed at 10 K with a magnetic field of 1 T applied in-plane and perpendicular to the scattering vector $\vec{Q}$. The same model as for the LSMO/Pd thin films was used for the simulation of the reflectometry data (**section 7.2.1.2**). The measurements with simulations thereof, as well as the used SLD, are shown in **figure 7.16** and the parameters used for the simulations are shown in **table 7.8**.

The SLD profile shows, as in the case of the LSMO/Pd thin film, a reduced magnetization at interfaces to STO and Pd, but not as pronounced as for the LSMO/Pd films.

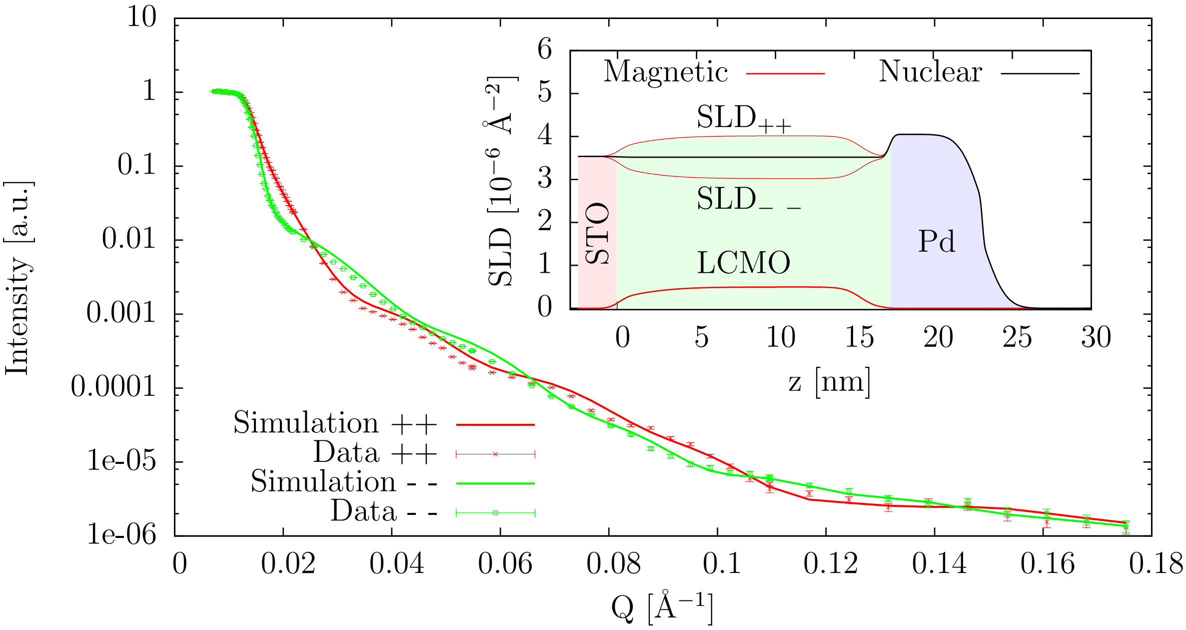

Figure 7.16.: PNR measurement of LCMO/Pd thin film (Sample: OMBE$_{0293}$). The spin-up and spin-down channels are shown with the simulations thereof (FOM = $4.29 \cdot 10^{-2}$). The inset shows the SLD, which was used for the simulations.

Additionally, the overall magnetization of the LCMO layer is drastically reduced to 1.12 $^{+0.26}_{-0.08}$ μ_B from the nominal 3.7 μ_B. The reduced magnetization can be explained through the reduced density of the LCMO layer, indicating an improvable structural quality. The mechanism for the magnetization in LCMO is based on the superexchange and double exchange interactions. The changed structure might hinder these interactions and lead to a reduced magnetization.

The simulations show that the Pd interface carries a negligible magnetic moment of 0.00 $^{+0.72}_{-0.00}$ μ_B. The large error on the Pd magnetization shows the difficulty to measure such small magnetic moments solely present at the interface. This PNR measurement shows that Pd is not magnetically polarized, but in order to prove this result additional XMCD measurements would be necessary.

7.2.3. Conclusion

The magnetization of Pd with an interface to an oxide layer, like LSMO or LCMO, was addressed with different investigation methods. The SQUID measurements cannot distinguish a possible Pd magnetization from the underlying LSMO magnetization. Both microscopic measurements do not detect a magnetization in the Pd layer at the interface to the transition metal oxide outside of the standard deviation of one σ. This suggest that Pd is not magnetically polarized at the interface to an transition metal oxide layer. In contrast, the PNR measurement shows a magnetic “dead” layer extending around 18 Å below the interface of the LSMO layer and less pronounced in the LCMO layer.

7.3. LSMO/LCMO

The LSMO/LCMO multilayer was grown by high oxygen sputtering at an oxygen partial pressure of 3 mbar. Before growth, the substrate was tempered at 1000°C to remove ad-atoms. To minimize thickness variation, due to changing growth rates, the plasma at both targets (LSMO/LCMO) was hold at constant conditions during the whole growth (reflected power at the targets was hold constant). Nonetheless, the rates changed slightly with time. This can be seen in the neutron reflectometry data as a broadening of the Bragg peaks, where the magnetic profiles of the LSMO/LCMO multilayer were investigated (Bulk Curie temperatures: $T_{\mathrm{C}}^{\mathrm{LSMO}} = 380\ K$ and $T_{\mathrm{C}}^{\mathrm{LCMO}} = 260\ K$).

7.3.1. Structural Characterization

The complex oxides LSMO and LCMO have nearly the same X-ray and neutron SLD due to a similar composition. The SLD's of LSMO and LCMO for X-rays and neutrons are given in **appendix F**.

Such similar SLD's lead to a weak contrast between the LSMO and LCMO layers. This makes a determination of the thickness of the individual layers with reflectometry difficult. Additionally, the thickness variations during the growth with HOPSA smear out the Bragg peaks in reflectometry measurements and in the case of LSMO/LCMO multilayers up to the point, where no oscillations are visible, which can be seen in **figure 7.17**. The XRD measurement shows intense LSMO and LCMO Bragg peaks at 3.27 $\mathrm{\AA}^{-1}$, which overlap. The position of the (002) Bragg peak of LSMO and LCMO is at 3.257 $\mathrm{\AA}^{-1}$ and 3.253 $\mathrm{\AA}^{-1}$, corresponding to a lattice parameter of $d = 3.859$ Å and $d = 3.863$ Å, respectively. The assignment to the individual LSMO or LCMO layer is difficult, but due to the higher quality of the LSMO films, the sharper and more intense Bragg peak at 3.257 $\mathrm{\AA}^{-1}$ might come from the LSMO layer.

Assuming that the periodicity of magnetic SLD profile matches the periodicity of the nuclear SLD profile, a hint of the LSMO and LCMO layer thickness can be determined from PNR measurements. From the X-ray reflectometry measurement, the roughness of the top layer can be estimated to 8 Å $^{+0.17}_{-0.08}$ Å, which is smaller than the results from the AFM measurement (roughness is 2.47 Å). The smaller roughness can be attributed to the small measurement area of the AFM measurement in contrast to the X-ray measurement or a density change of the top layer.

7.3.2. Magnetic Characterization

The magnetic properties are investigated macroscopically with SQUID measurements and then microscopically with PNR measurements. The PNR measurements were carried out at the MR reflectometer at the SNS and at the MARIA reflectometer at MLZ.

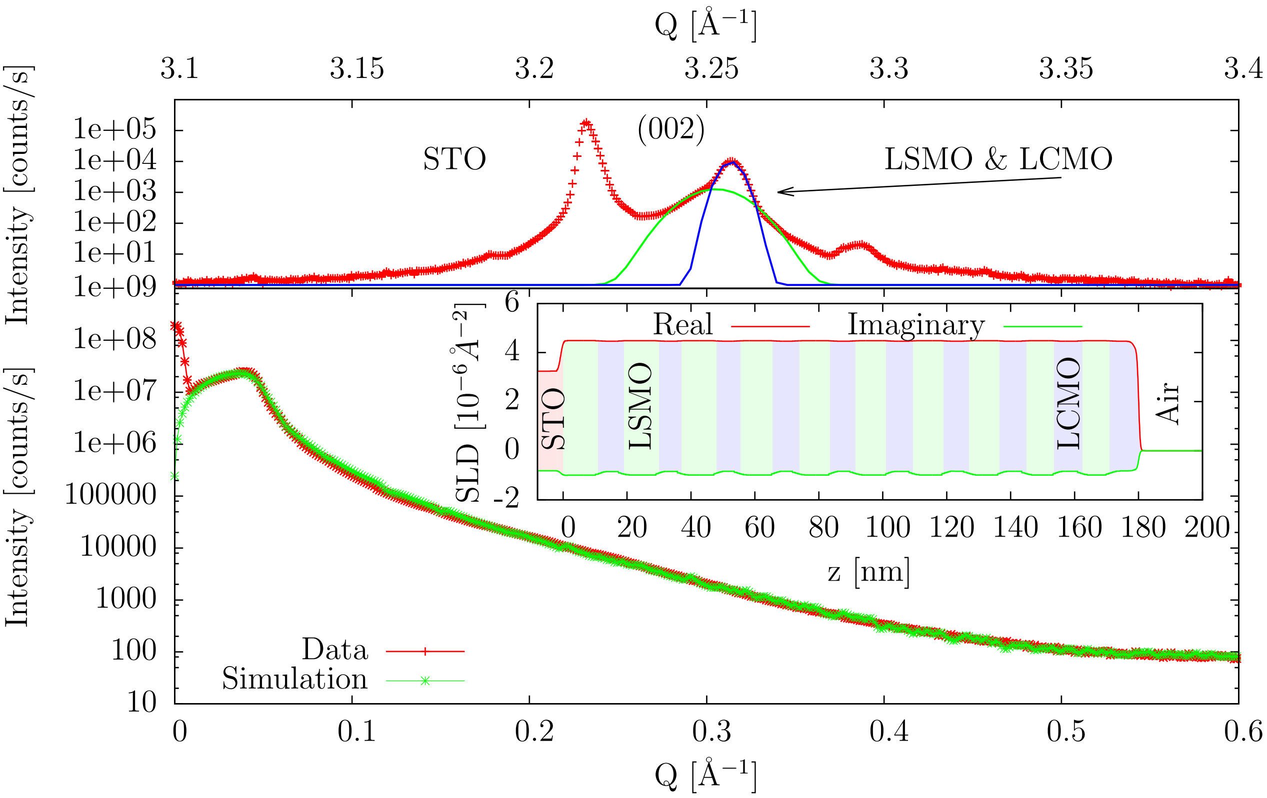

Figure 7.17.: Top: XRD measurement in out-of-plane direction around the (002) Bragg peak. Bottom: X-ray reflectometry measurement of LSMO/LCMO sample with a simulation thereof. The inset shows the SLD used for the simulation.

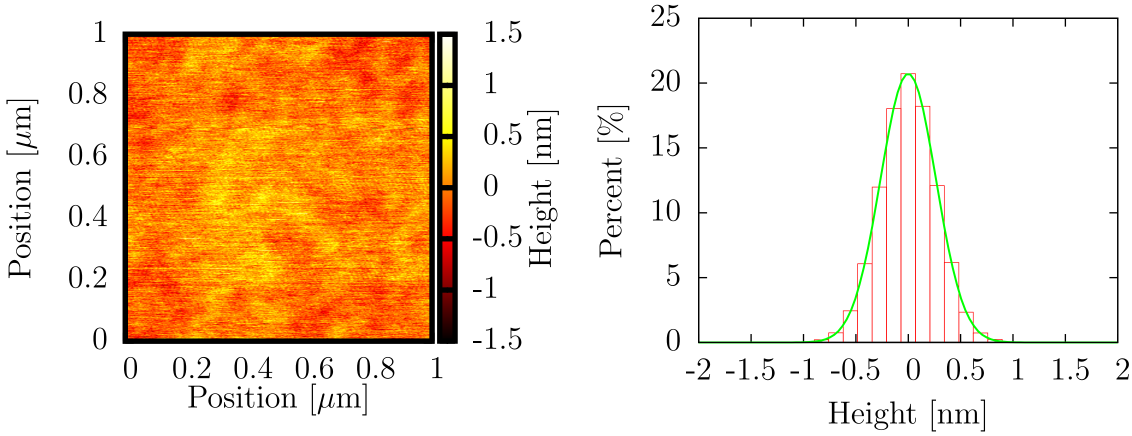

Figure 7.18.: On the left-hand side the topography of the AFM measurement is shown and on the right-hand side the height distribution thereof. Gaussian profile is fitted to the height distribution, with a roughness of 2.47 Å.

Magnetometry Measurements

The macroscopic magnetization of the LSMO/LCMO multilayer can be determined with a SQUID magnetometer, although the magnetization of the independent LSMO and LCMO layers cannot be separated. The field cooled measurement at 100 Oe is shown in **figure 7.20** a, where the magnetization is assigned to the magnetic moment of the Mn atoms, by dividing through the number of Mn atoms in the LSMO/LCMO multilayer. The number of Mn atoms was determined from the surface area ($A = 24.3\ \mathrm{mm}^2 \pm 0.1\ \mathrm{mm}^2$) and from PNR-measurements, where the total thickness ($174\ \mathrm{nm} \pm 5\ \mathrm{nm}$) could be determined (see **section 7.3.2**) and an assumed density of $\rho = (1.7 \pm 0.01) \cdot 10^{-2}\ \text{Å}^{-3}$, which is the average of the LSMO and LCMO unit cell density.

From the field cooled measurement a Curie temperature of 244.5 K ± 2 K can be determined. This is around 100 K lower than the Curie temperature $T_\mathrm{C} = 380$ K [13] of pure $\mathrm{La_{0.7}Sr_{0.3}MnO_3}$. The onset of the LCMO magnetization could be around 140 K, where a kink in the magnetization curve can be observed.

With an electronic configuration of $[Ar]3d^5 4s^2$ of the Mn atoms, the magnetic moment of the Mn atoms for both LSMO and LCMO layers should be $m = 3.7\ \mu_\mathrm{B}$, for a doping of 0.3 Sr/Ca. As can be seen in **figure 7.19** and **7.20**, the magnetic moment is reduced to $2.2\ \mu_\mathrm{B}$. Taking the magnetic moments of the single layers into account (**appendix H**), the reduced magnetization of the LSMO/LCMO multilayer can be attributed to the reduced magnetization of the LCMO layer. This is also consistent with the performed PNR measurements.

The hysteresis measurements were performed for all temperatures for which we could perform PNR measurements and which are presented in **figure 7.19**. The jump at 0 T is an artifact due to the reversing of the applied magnetic field inside the SQUID magnetometer. Between 237.5 K and 187.5 K the hysteresis loop shows a step-like shape. This behavior could arise from exchange bias effects with a strong anisotropy [113]. But this is unlikely because of a small difference of the coercive fields $\Delta \mathrm{H_C} \approx 4$ Oe (**figure 7.20**) for the left and right branches of the hysteresis measurements, which is in the order of the remaining field in the superconducting magnet [114]. The shape of the hysteresis measurements could also be attributed to a different interlayer exchange coupling between magnetic layers with different coercive fields through a non-magnetic layer [115]. Another possibility might be an antiferromagnetic coupling between two neighboring ferromagnetic layers. The hysteresis measurements show the step-like shape exactly, where the bulk LCMO layer becomes ferromagnetic.

Motivated by this effect, hysteresis loops at different angles were measured, where the applied field is in-plane with respect to the LSMO/LCMO films, to determine the anisotropy of the films. Taking the pseudo cubic perovskite structure into account, a four-fold angle dependence can be expected. The anisotropy can be determined by measuring the squareness $m_\mathrm{r}/m_\mathrm{s}$, where m_r is the remanent magnetization and m_s is the saturation magnetization. Another possibility is to determine the magnetizing energy by integrating the hysteresis loops

$$w_m = \int H \mathrm{d}m = 2 \int_0^{m_s} H \mathrm{d}m - 2 \int_{-m_s}^{0} H \mathrm{d}m, \tag{7.7}$$

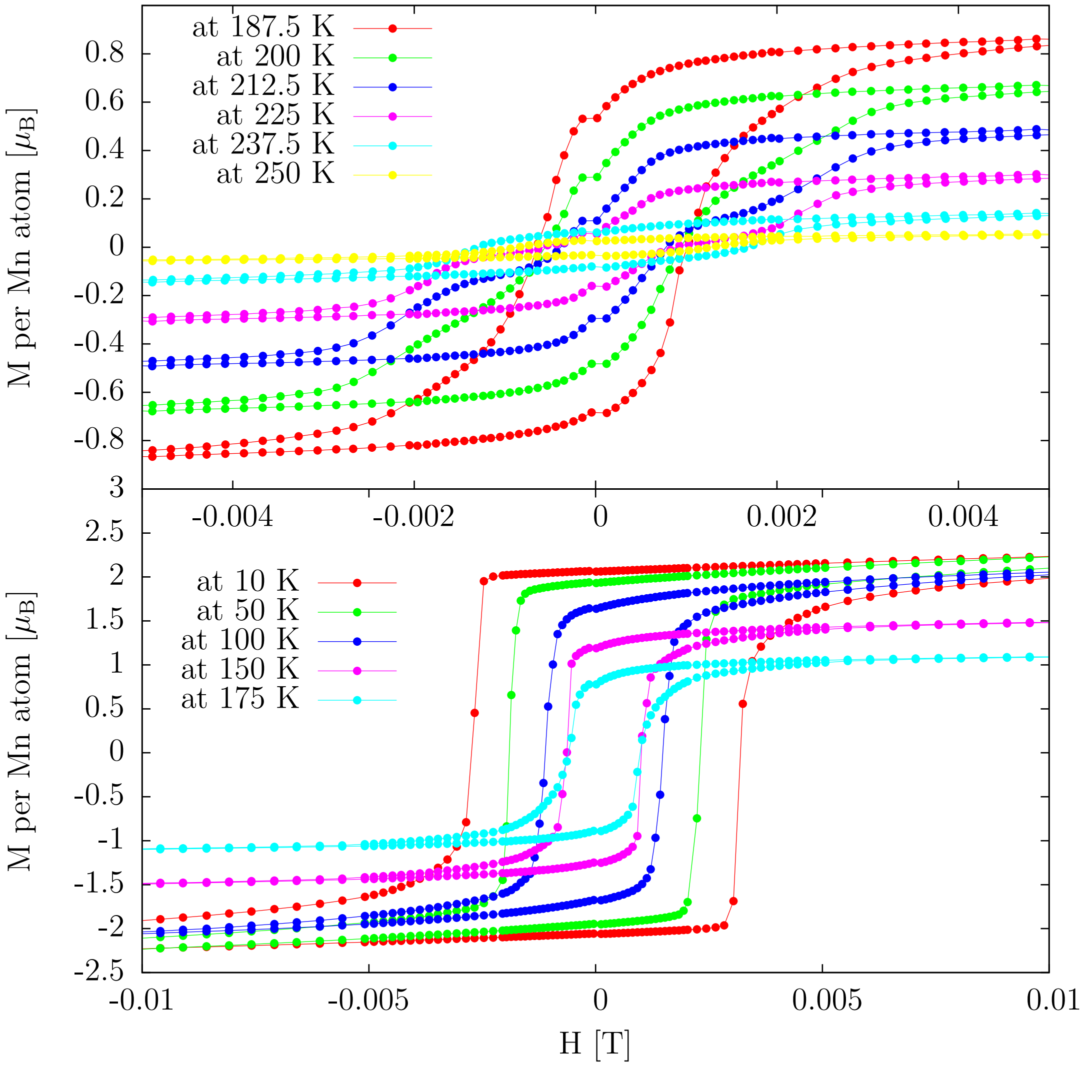

Figure 7.19.: Hysteresis measurements of the LSMO/LCMO multilayer measured at different temperatures from -0.04 T to 0.04 T. The measured magnetizations are normalized to the number of Mn atoms.

where H is the field, swept from negative to positive field. Measuring hysteresis loops, by varying the angle between sample and applied magnetic field, can only be carried out in DC mode. The DC-measurements are considerably more time-consuming than the RSO-measurements and that's why the angular dependence was measured for 180° and only one branch. Additionally, the sensitivity is lower than in the RSO-measurements, resulting in visible noise. To integrate over the hysteresis loops, the curve was approximated with linear functions, as can be seen in **figure 7.21**. Due to the considerable noise at higher fields, the saturation magnetization was set to the highest remanent magnetization.

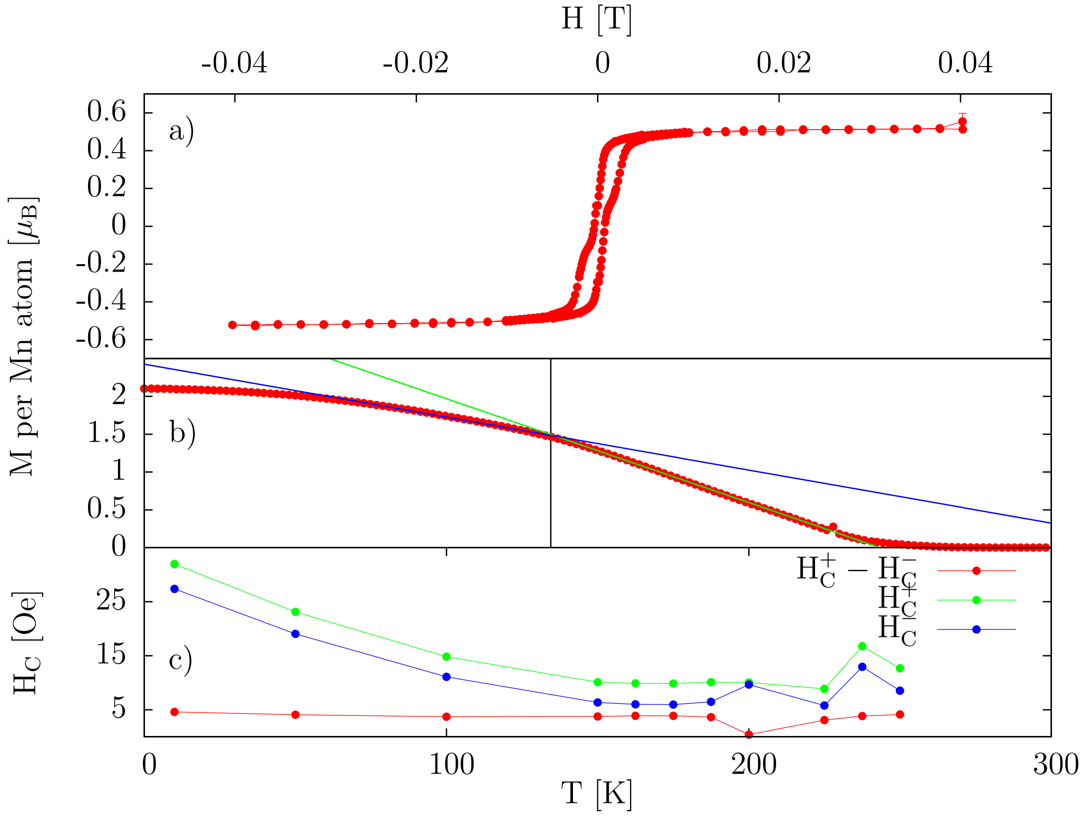

Figure 7.20.: a) Full hysteresis measurements of the LSMO/LCMO multilayer measured at 212.5 K. The measured magnetizations are normalized to the number of Mn atoms. b) Field cooled measurement performed at 100 Oe. The green and blue line are linear fits to the curve. The intersection of these curves indicates a kink, where the LCMO layer might become ferromagnetic. c) Coercive fields H_C of hysteresis measurement at different temperatures.

The resulting energy landscape and the squareness of the hysteresis loops is plotted in **figure 7.21**. A four-fold rotation symmetry can be observed for both methods, where the maxima of the magnetizing energy correspond to the minima of the squareness.

Polarized Neutron Reflectometry Measurements

Polarized neutron reflectometry (PNR) measurements where performed at the MR at SNS and MARIA at MLZ. As described in **section 4.3.1**, the MR reflectometer has a very good resolution and the MARIA reflectometer has a high beam intensity. Therefore, these measurements are complementary to each other. In the first attempt both measurements were analyzed together. But the position of the Bragg peaks shifted slightly, either due to a misalignment of the wavelength or due to a change in the bilayer thickness. A change of the bilayer thickness might come from an altering of the sample with an oxygen desorption, which disturbs the crystal structure. Because of this complication, the measurements were analyzed simultaneously, except for different layer thicknesses.

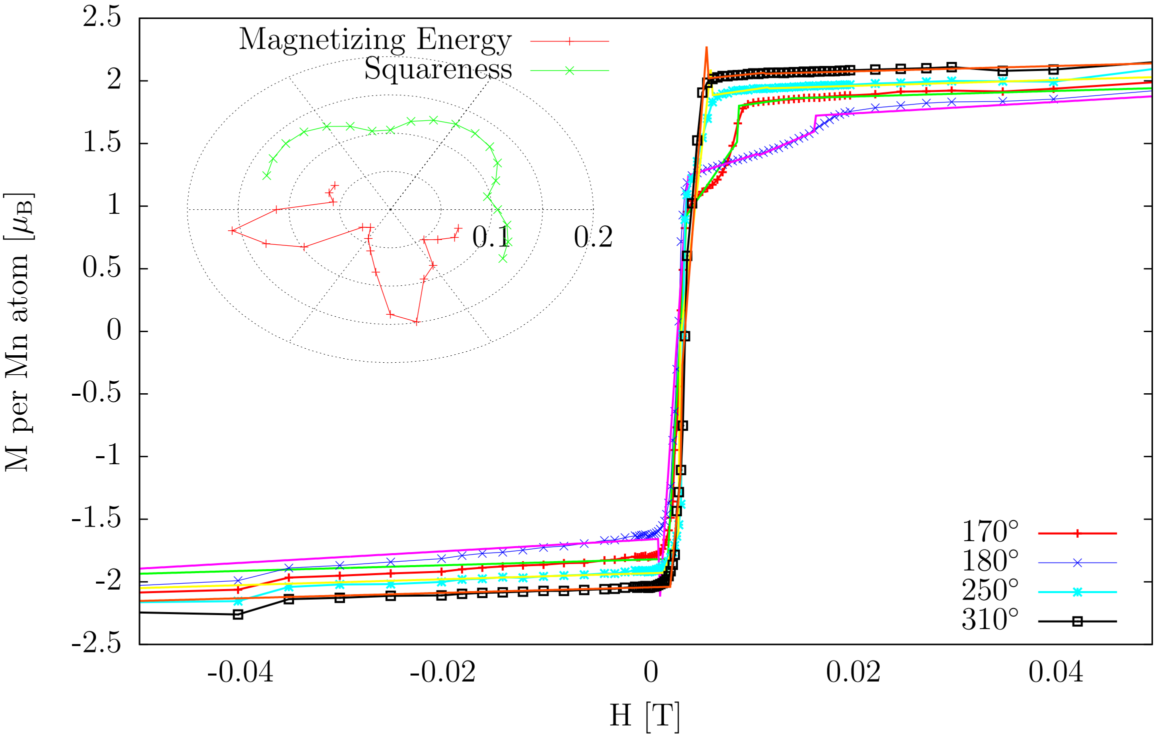

Figure 7.21.: Half hysteresis at different sample angles, which were used to calculate the energy landscape. Inset: Energy landscape and squareness of LSMO/LCMO multilayer shows the in-plane anisotropy.

Magnetism Reflectometer (MR)

At the MR reflectometer the LSMO/LCMO multilayer was measured at a saturation field of 1 T, at seven different temperatures, to determine the temperature-dependent interface effects of the two magnetic layers with different Curie temperatures (Bulk Curie temperatures: $T_C^{\mathrm{LSMO}} = 380$ K and $T_C^{\mathrm{LCMO}} = 260$ K). The temperatures of the measurements were ranging from 150 K to 300 K with 25 K steps. At MR 150 K was chosen as the lowest temperature because of the STO transition at around 105 K. Thus, the sample could be used in the same condition for the beam time at the MARIA reflectometer afterwards. The measurements, which have been carried out at the MR reflectometer, are shown in the upper part of **figure 7.22**. The bottom part of **figure 7.22** shows one selected measurement for a better comparison between data and simulation. At 300 K there is nearly no splitting between the spin-up and spin-down channels, which is expected because of a reduced Curie temperature and the low magnetic moment of the LSMO film in the LSMO/LCMO multilayer (see **section 7.3.2**).

To simulate the temperature-dependent interface effects, like an induced magnetization in the LCMO layer at temperatures above the Curie temperature of the single LCMO layer or an enhancement of the magnetization at the interface between the LSMO and LCMO layers, the nuclear scattering length density and the magnetic scattering length density are separated in the simulations. For the simulation of a possible interface effect, an additional

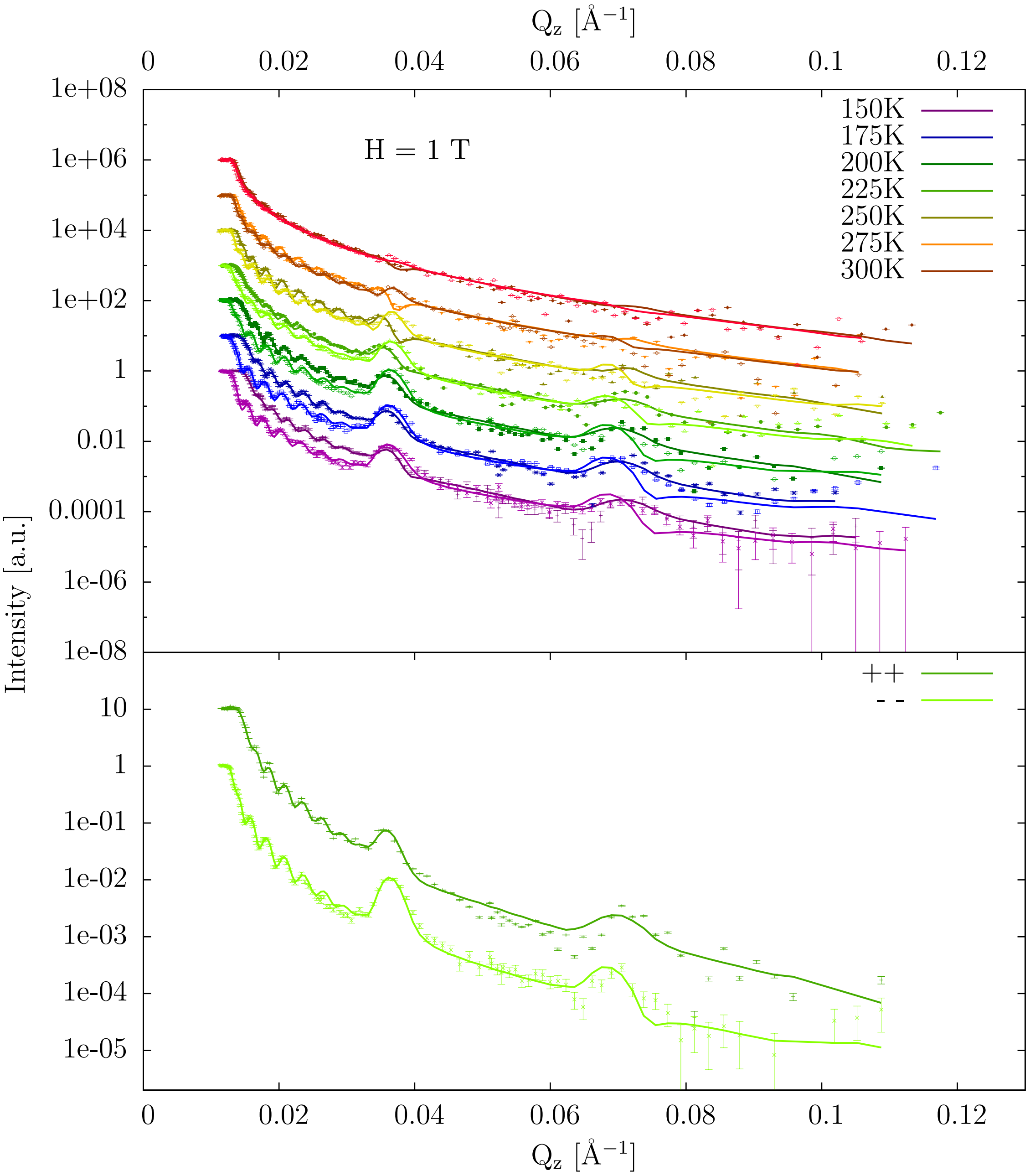

Figure 7.22.: Top: Reflectometry measurement performed at the MR reflectometer at the SNS at an in-plane applied magnetic field of $H = 1$ T at different temperatures. Two polarization channels, for each temperature, are visualized: up-up and down-down. The curves are shifted vertically by a multiple of ten for a better overview. Bottom: One selected measurement is presented for a better visualization.

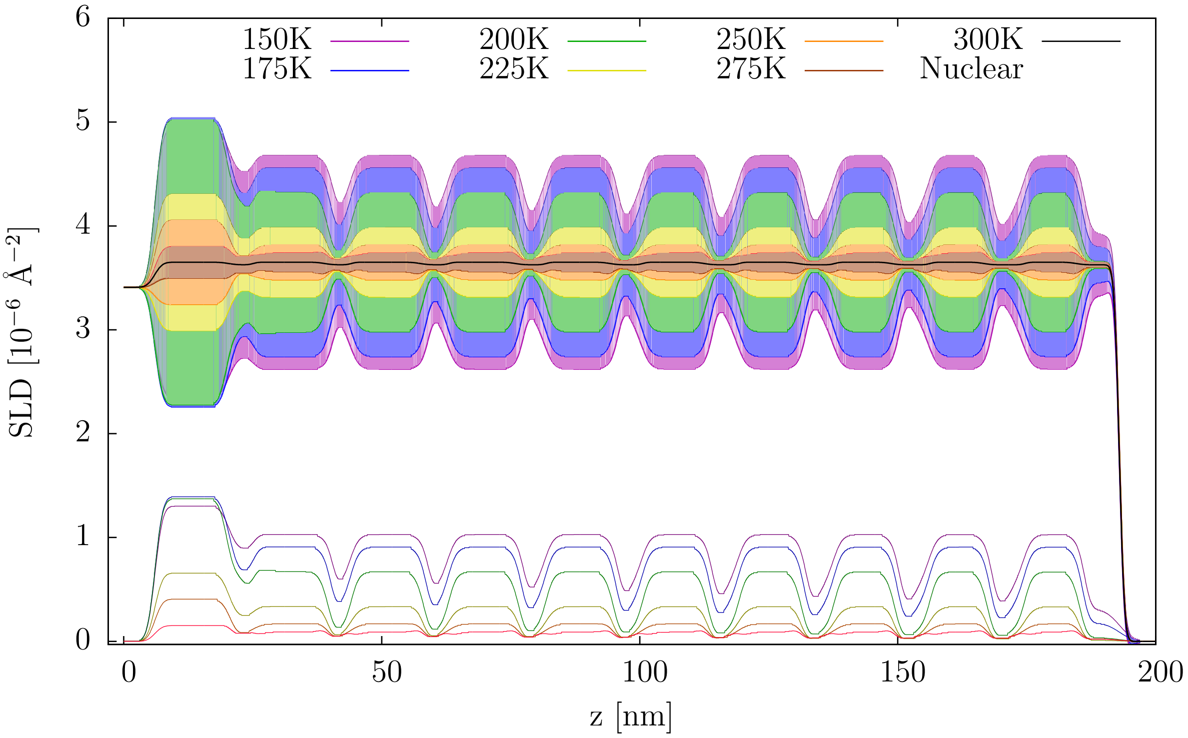

Figure 7.23.: SLD used for the simulation of the reflectivity data shown in **figure 7.22** measurement performed at the MR reflectometer at SNS.

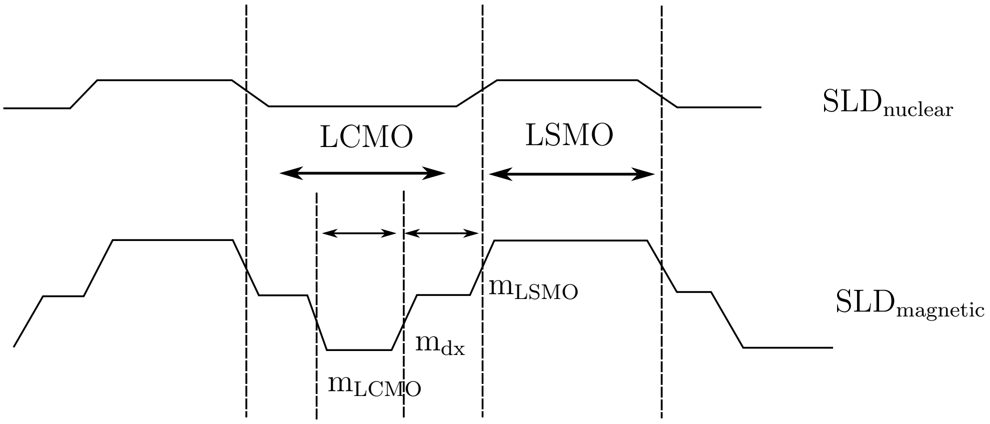

Figure 7.24.: Model for the PNR simulation separating magnetic and nuclear SLD.

variable dx was introduced, describing the width of the interface effect, and the LCMO layer was separated into three layers. Two layers, directly at the interface to LSMO, have the layer thickness dx, and the central LCMO layer has a layer thickness of $d_{\mathrm{LCMO}} - 2dx$. The magnetization of the LCMO layers at the interface was fitted independently from the magnetization in the central LCMO layer (see **figure 7.24**). Because of varying layer

Layers	LSMO	LCMO	Interface
d [Å]	$93.32\ ^{+1.78}_{-1.47}$	$81.42\ ^{+1.83}_{1.64}$	-
Δd [Å]	$4.54\ ^{+0.23}_{-0.46}$	$0.99\ ^{+0.05}_{-0.09}$	-
σ [Å]	$13.47\ ^{+1.09}_{-1.39}$	$7.92\ ^{+0.07}_{-0.07}$	$13.84\ ^{+0.10}_{-0.21}$
$\mathrm{SL_N}$ [10^{-5} Å]	$21.55\ ^{+0.05}_{-0.03}$	$21.61\ ^{+0.08}_{-0.16}$	$21.61\ ^{+0.08}_{-0.16}$
ρ [10^{-2}Å^{-3}]	$1.70\ ^{+0.01}_{-0.01}$	$1.69\ ^{+0.01}_{-0.01}$	$1.69\ ^{+0.01}_{-0.01}$
$\mathrm{SLD_N}$ [10^{-6} Å^{-2}]	$3.66\ ^{+0.01}_{-0.00}$	$3.65\ ^{+0.01}_{-0.03}$	$3.65\ ^{+0.01}_{-0.03}$
$\mathrm{SLD_N^{Norm}}$ [10^{-6} Å^{-2}]	3.69	3.59	3.59

	$\mathrm{d_{Interface}}$ [Å]	$\mu_\mathrm{B}^\mathrm{LSMO}$ [μ_B]	$\mu_\mathrm{B}^\mathrm{LCMO}$ [μ_B]	$\mu_\mathrm{B}^\mathrm{Interface}$ [μ_B]	$\mathrm{SLD_M^{LSMO}}$ [10^{-6} Å^{-2}]	$\mathrm{SLD_M^{LCMO}}$ [10^{-6} Å^{-2}]	$\mathrm{SLD_M^{Interface}}$ [10^{-6} Å^{-2}]
150 K	$16.46\ ^{+0.05}_{-0.05}$	$2.38\ ^{+0.00}_{-0.01}$	$0.69\ ^{+0.00}_{-0.02}$	$1.97\ ^{+0.08}_{-0.04}$	$1.07\ ^{+0.01}_{-0.01}$	$0.31\ ^{+0.00}_{-0.01}$	$0.88\ ^{+0.03}_{-0.02}$
175 K	$13.19\ ^{+0.02}_{-0.02}$	$2.03\ ^{+0.11}_{-0.11}$	$0.40\ ^{+0.00}_{-0.00}$	$1.57\ ^{+0.02}_{-0.01}$	$0.91\ ^{+0.05}_{-0.05}$	$0.18\ ^{+0.00}_{-0.00}$	$0.70\ ^{+0.01}_{-0.00}$
200 K	$9.28\ ^{+0.03}_{-0.02}$	$1.60\ ^{+0.06}_{-0.14}$	$0.08\ ^{+0.01}_{-0.00}$	$0.79\ ^{+0.05}_{-0.06}$	$0.72\ ^{+0.03}_{-0.06}$	$0.03\ ^{+0.00}_{-0.00}$	$0.35\ ^{+0.02}_{-0.03}$
225 K	$8.02\ ^{+0.21}_{-0.12}$	$1.15\ ^{+0.07}_{-0.18}$	$0.16\ ^{+0.09}_{-0.05}$	$0.87\ ^{+0.08}_{-0.13}$	$0.52\ ^{+0.03}_{-0.08}$	$0.07\ ^{+0.04}_{-0.02}$	$0.39\ ^{+0.03}_{-0.06}$
250 K	$6.63\ ^{+0.02}_{-0.03}$	$0.60\ ^{+0.01}_{-0.01}$	$0.01\ ^{+0.01}_{-0.01}$	$0.57\ ^{+0.00}_{-0.00}$	$0.27\ ^{+0.00}_{-0.01}$	$0.00\ ^{+0.00}_{-0.00}$	$0.25\ ^{+0.00}_{-0.00}$
275 K	$6.31\ ^{+0.07}_{-0.09}$	$0.28\ ^{+0.10}_{-0.09}$	$0.12\ ^{+0.00}_{-0.00}$	$0.34\ ^{+0.02}_{-0.01}$	$0.12\ ^{+0.04}_{-0.04}$	$0.06\ ^{+0.00}_{-0.00}$	$0.15\ ^{+0.01}_{-0.01}$
300 K	$5.88\ ^{+0.08}_{-0.07}$	$0.23\ ^{+0.02}_{-0.01}$	$0.05\ ^{+0.00}_{-0.00}$	$0.38\ ^{+0.01}_{-0.01}$	$0.10\ ^{+0.01}_{-0.01}$	$0.02\ ^{+0.00}_{-0.00}$	$0.17\ ^{+0.00}_{-0.00}$

Table 7.9.: Summary of the parameters used for the simulation of the PNR measurement. The following parameters are listed: Thickness d, thickness variation Δd, density ρ, magnetic moment μ_B, roughness σ, nuclear scattering length $\mathrm{SL_N}$, nuclear scattering length density $\mathrm{SLD_N}$, magnetic scattering length density $\mathrm{SLD_M}$.

thicknesses, due to the sample growth with HOPSA, a linear change of the LSMO and the LCMO layer thickness was simulated. Only with the change of the layer thicknesses, the shape of the first and second Bragg-peak could be fitted sufficiently enough. Additionally, the magnetization of the first two LSMO and LCMO layers, directly at the STO substrate, were fitted independently. Only with this increased magnetization in the first two layers, the Kissieg fringes between the plateau of total reflection and the first Bragg peak could be fitted.

The XRR measurement could not distinguish between the LSMO and LCMO layers, due to the very similar SLD's, resulting in very sensitive PNR measurements for the magnetic SLD profile. In order to grasp the layer thicknesses, it is assumed that the periodicity of the nuclear SLD profile corresponds to the magnetic SLD profile. Because of a large magnetic SLD contrast, the bilayer thickness can be fitted with a better precision and

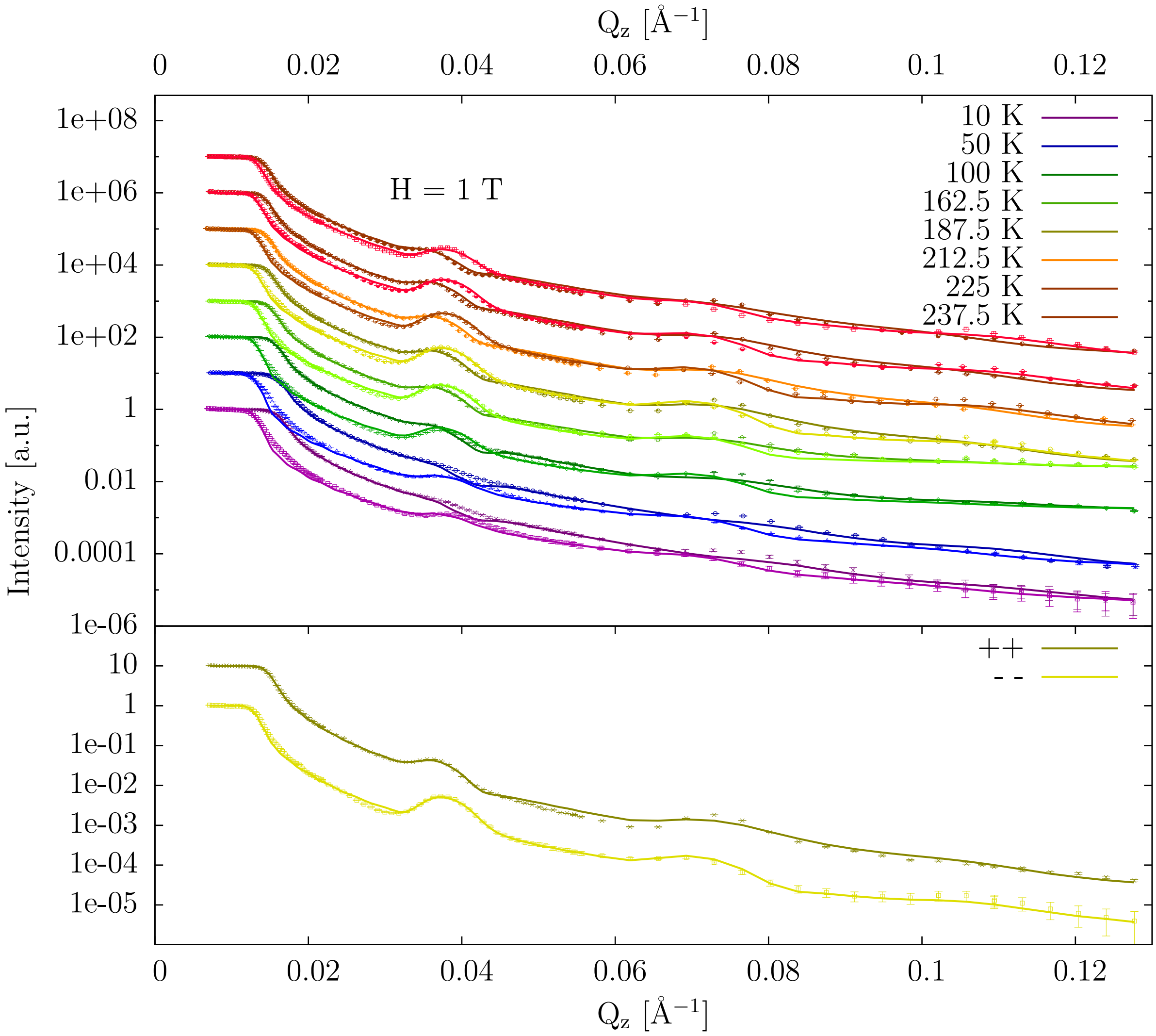

Figure 7.25.: TOP: Reflectometry measurement performed at the MARIA reflectometer at the MLZ at an applied magnetic field of H = 1 T. The polarization channels up-up and down-down are presented. The curves are shifted by a multiple of ten to ensure the best clarity. Bottom: One selected measurement is presented for a better visualization.

can be determined to $d_{\text{LSMO+LCMO}} = 182.67$ Å $^{+0.65}_{-0.69}$ Å. The individual layer thicknesses are still vague, especially because of the introduction of the interface layer.

Figure 7.22 shows the simulations of all measurements (FOM of $9.02 \cdot 10^{-2}$). The best FOM for a simulation without interface effects is $9.17 \cdot 10^{-2}$. Although better results can be obtained by introducing more variables, like fitting the layer thicknesses of all layers independently or with no constraints to the magnetization of the layers, less variables make the simulations more plausible. The SLD for the simulations are shown in **figure 7.23** and all parameters are presented in **table 7.9**. The step-like magnetic SLD profile, as described in the model, is not clearly visible, because of the large magnetic roughness of around 13.84 Å. Nevertheless, it is evident that the interface layer thickness changes with temperature.

Magnetic Reflectometer with high Incident Angle (MARIA)

At the MARIA reflectometer similar measurements were performed, but at lower temperatures, down to 10 K. As MARIA has a higher beam flux, measurements up to the third Bragg peak are possible, as can be seen in **figure 7.25** at 0.11 Å^{-1}. One selected measurement is presented at the bottom of **figure 7.25** to better compare the simulation to the data.

The measurements were corrected for the inaccuracy of the alignment as described in **section 6.1.3** and for the off-specular scattering (**section 6.1.1**). Although, in the case of the LSMO/LCMO multilayer, almost non off-specular scattering could be observed. No corrections for the sensitivity map were performed, which is due to the issues described in **section 6.1.2**. The variable resolution, as described in **section 6.2.1**, was used for all measurements.

Directly behind the sample a movable beamstop was mounted. The beamstop should move with the horizon of the sample surface and block the refracted and the direct beam. Unfortunately, sometimes the beamstop stopped moving increasing the background at higher Q values, as can be seen in the measurements performed at 100 K and 162.5 K. Thus, the background had to be changed for these two temperatures.

As already mentioned, the bilayer thickness might have changed in the period between the measurements performed at the MR reflectometer and the measurements at the MARIA reflectometer. This might come from a misalignment of the wavelength, but

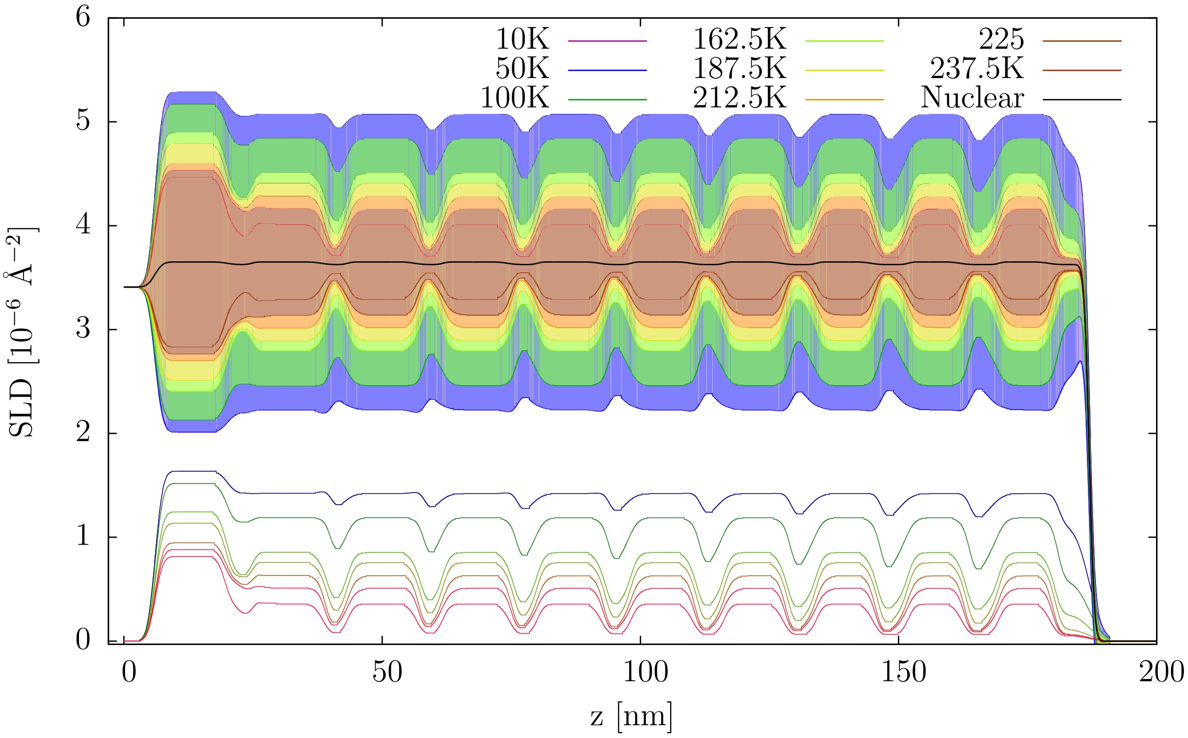

Figure 7.26.: Shown is the SLD used for the simulation of the reflectivity data presented in **figure 7.25**.

Layers	LSMO	LCMO	Interface	Instrument	
d [Å]	$93.32\ ^{+1.78}_{-1.47}$	$81.42\ ^{+1.83}_{1.64}$	-		
Δd [Å]	$4.93\ ^{+0.06}_{-0.25}$	$1.16\ ^{+0.02}_{-0.02}$	-		
σ [Å]	$13.84\ ^{+0.10}_{-0.21}$	$21.53\ ^{+0.15}_{-0.08}$	$13.84\ ^{+0.10}_{-0.21}$	$\Delta\lambda/\lambda$	0.1
$\mathrm{SL_N}$ [10^{-5} Å]	$21.55\ ^{+0.05}_{-0.03}$	$21.61\ ^{+0.08}_{-0.16}$	$21.61\ ^{+0.08}_{-0.16}$	d_{S_1-Sam} [mm]	4500
ρ [Å^{-3}]	$1.70\ ^{+0.01}_{-0.01}$	$1.69\ ^{+0.01}_{-0.01}$	$1.69\ ^{+0.01}_{-0.01}$	$\mathrm{S_1}$ [mm]	2
$\mathrm{SLD_N}$ [10^{-6} Å^{-2}]	$3.66\ ^{+0.01}_{-0.00}$	$3.65\ ^{+0.01}_{-0.03}$	$3.65\ ^{+0.01}_{-0.03}$		
$\mathrm{SLD_N^{Norm}}$ [10^{-6} Å^{-2}]	3.69	3.59	3.59		

	$\mathrm{d_{Interface}}$ [Å]	$\mu_\mathrm{B}^\mathrm{LSMO}$ [μ_B]	$\mu_\mathrm{B}^\mathrm{LCMO}$ [μ_B]	$\mu_\mathrm{B}^\mathrm{Interface}$ [μ_B]	$\mathrm{SLD_M^{LSMO}}$ [10^{-6} Å^{-2}]	$\mathrm{SLD_M^{LCMO}}$ [10^{-6} Å^{-2}]	$\mathrm{SLD_M^{Interface}}$ [10^{-6} Å^{-2}]
10 K	$21.62\ ^{+0.38}_{-0.10}$	$3.20\ ^{+0.21}_{-0.11}$	$2.54\ ^{+0.02}_{-0.01}$	$3.19\ ^{+0.01}_{-0.02}$	$1.44\ ^{+0.10}_{-0.05}$	$1.14\ ^{+0.01}_{-0.01}$	$1.43\ ^{+0.01}_{-0.01}$
50 K	$28.41\ ^{+0.59}_{-0.35}$	$3.33\ ^{+0.03}_{-0.03}$	$2.32\ ^{+0.04}_{-0.06}$	$3.22\ ^{+0.03}_{-0.02}$	$1.50\ ^{+0.02}_{-0.02}$	$1.04\ ^{+0.02}_{-0.03}$	$1.44\ ^{+0.01}_{-0.01}$
100 K	$18.56\ ^{+0.13}_{-0.15}$	$2.66\ ^{+0.05}_{-0.02}$	$1.32\ ^{+0.05}_{-0.27}$	$2.48\ ^{+0.08}_{-0.03}$	$1.19\ ^{+0.02}_{-0.01}$	$0.59\ ^{+0.02}_{-0.12}$	$1.11\ ^{+0.03}_{-0.02}$
150 K	$16.46\ ^{+0.05}_{-0.05}$	$2.38\ ^{+0.00}_{-0.01}$	$0.69\ ^{+0.00}_{-0.02}$	$1.97\ ^{+0.08}_{-0.04}$	$1.07\ ^{+0.01}_{-0.01}$	$0.31\ ^{+0.00}_{-0.01}$	$0.88\ ^{+0.03}_{-0.02}$
162.5 K	$14.64\ ^{+0.27}_{-0.29}$	$1.91\ ^{+0.08}_{-0.04}$	$0.60\ ^{+0.05}_{-0.02}$	$1.32\ ^{+0.01}_{-0.01}$	$0.86\ ^{+0.04}_{-0.02}$	$0.27\ ^{+0.02}_{-0.01}$	$0.59\ ^{+0.01}_{-0.00}$
187.5 K	$14.94\ ^{+0.02}_{-0.19}$	$1.69\ ^{+0.04}_{-0.06}$	$0.26\ ^{+0.14}_{-0.27}$	$1.11\ ^{+0.01}_{-0.02}$	$0.76\ ^{+0.02}_{-0.03}$	$0.12\ ^{+0.06}_{-0.12}$	$0.50\ ^{+0.00}_{-0.01}$
212.5 K	$12.04\ ^{+0.08}_{-0.26}$	$1.42\ ^{+0.02}_{-0.01}$	$0.22\ ^{+0.05}_{-0.03}$	$1.01\ ^{+0.00}_{-0.00}$	$0.64\ ^{+0.01}_{-0.01}$	$0.10\ ^{+0.02}_{-0.01}$	$0.45\ ^{+0.00}_{-0.00}$
225 K	$8.02\ ^{+0.21}_{-0.12}$	$1.15\ ^{+0.07}_{-0.18}$	$0.16\ ^{+0.09}_{-0.05}$	$0.87\ ^{+0.08}_{-0.13}$	$0.52\ ^{+0.03}_{-0.08}$	$0.52\ ^{+0.03}_{-0.08}$	$0.39\ ^{+0.03}_{-0.06}$
237.5 K	$10.85\ ^{+0.28}_{-0.91}$	$0.76\ ^{+0.01}_{-0.01}$	$0.10\ ^{+0.08}_{-0.08}$	$0.27\ ^{+0.28}_{-0.23}$	$0.34\ ^{+0.00}_{-0.01}$	$0.34\ ^{+0.00}_{-0.01}$	$0.12\ ^{+0.13}_{-0.10}$

Table 7.10.: Summary of the parameters used for the simulation of the PNR measurement. The Following parameters are listed: Thickness d, density ρ, magnetic moment μ_B, roughness σ, nuclear scattering length $\mathrm{SL_N}$, nuclear scattering length density $\mathrm{SLD_N}$, magnetic scattering length density $\mathrm{SLD_M}$, wavelength spread $\Delta\lambda/\lambda$, sample to first slit distance d_{S_1-Sam} and width of first slit S_1.

it is not very plausible, due to the matching of the plateau of total reflexion. Therefore, all parameters, except for the layer thicknesses, the thickness variation and the resolution, were kept fixed and all measurements were fitted together. The parameters are presented in **table 7.10** and the SLD used for the simulations are shown in **figure 7.26**. The FOM for the best fit for the simulations of the MARIA measurements is $4.11 \cdot 10^{-2}$. The best simulation without interface effect has a FOM of $4.71 \cdot 10^{-2}$, which is around 15% larger than the FOM for the simulations with interface effects.

The bilayer thickness, used for the simulations of the MARIA measurements, was

$d_{\text{Bilayer}} = 174.75$ Å $^{+0.45}_{-0.72}$ Åcompared to $d = 182.67$ Å $^{+0.65}_{-0.69}$ Åfor the MR measurement, which is a change of around 5%. The data presented in **table 7.10** indicates an existing interface effect, where the magnetization at the interface in the LCMO layer is between the magnetization of the LSMO layer and the LCMO layer. Additionally, the width of the interface effect increases with decreasing temperature. The temperature-dependent magnetization and the interface width for both measurements are shown in **figure 7.27**.

7.3.3. Conclusion

All relevant parameters for the magnetic interface effect, obtained from both measurements at the MARIA and at the MR reflectometer, are summarized in **figure 7.27**. The magnetic moment of the LSMO, LCMO and the interface layer in combination with the interface thickness are presented. As is expected from ferromagnetic materials, the magnetization increases with decreasing temperature. The magnetic moment of the interface layer is between the magnetic moments of the LCMO and LSMO layer. The increase of the LCMO magnetic moment, at the interface, can be explained either through intermixing of the LSMO and LCMO layers or due to altered superexchange and double exchange interactions. But the increase of the magnetic interface thickness dx, with decreasing

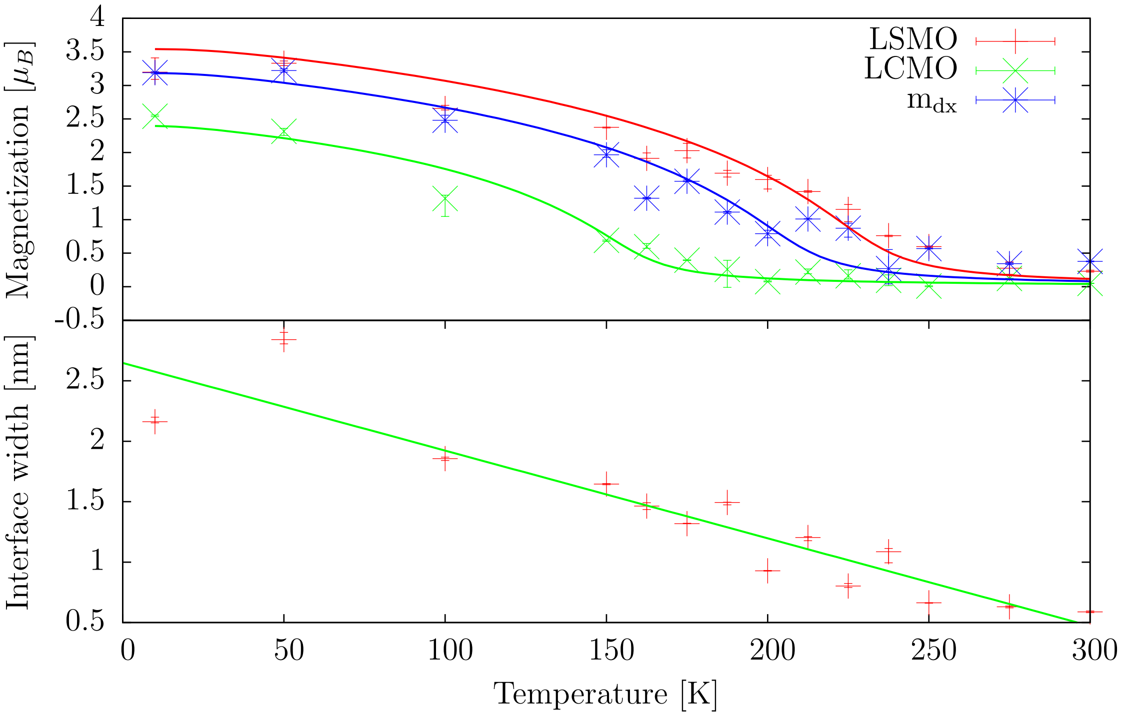

Figure 7.27.: The relevant parameters derived from PNR measurements carried out at the MARIA and the MR reflectometer. Shown are the magnetization of the Mn atoms inside the LSMO and LCMO layer with a fit of the magnetization using the mean field theory. Additionally, the difference in magnetic and nuclear layer thickness is shown with a linear fit.

	LSMO	LCMO	Interface
M_s	3.07	2.13	2.78
J	1.10	1.12	1.12
g_J	2.00	2.00	2.00
γ	82.52	81.44	81.37
T_C [K]	238.81	164.67	215.16

Table 7.11.: Parameters used for the fit of the temperature-dependence of the magnetization in the LSMO layer, the LCMO layer and at the interface.

temperature, indicates a change of magnetic interaction with temperature and, thus, a real interface effect.

The mean field theory can be used to describe the ferromagnetism in these materials, where in addition to the external magnetic field $\vec{B}_{ext}$ an internal magnetic field $\vec{B}_{in}$ is present. This internal magnetic field is caused by the magnetism $\vec{M}$ in these materials $\vec{B}_{in} = \gamma\vec{M}$, where γ is the molecular field constant. This approach reduces the complexity of the interactions of all atoms to the behavior of one atom in the mean field. The magnetism in the mean field theory can be described with

$$M = M_s B_J(y) \quad \text{with} \quad y = \frac{g_J \mu_B J (B_{ext} + \gamma M)}{k_B T}, \tag{7.8}$$

where M_s is the saturation magnetization, $B_J(y)$ is the Brillouin function, g_J is the Landé g-factor, J is the total angular momentum quantum number, μ_B is the Bohr magneton and k_B is the Boltzmann constant. The Brillouin function is given by:

$$B_J(y) = \frac{2J+1}{2J} \coth\left(\frac{2J+1}{2J} y\right) - \coth\left(\frac{1}{2J} y\right) \tag{7.9}$$

Equation 7.8 can be solved numerically for the temperature-dependent magnetization of the LSMO layer, the LCMO layer and the interface (**figure 7.27**). The parameters for the fits are summarized in **table 7.11**, without considering error evaluation. The errors of the fit parameters are largely overestimated due to the large covariance. The total angular momentum quantum number of Mn should be 5/2 and, thus, a value around 1 is too small. The small value might originate from the strong covariance with the γ parameter. Additionally, this model is not designed for strongly localized magnetic moments, where the magnetism originates from the superexchange and double exchange interactions.

Nevertheless, the Curie temperature of the different layers can be estimated from the fit parameters by

$$T_{\mathrm{C}} = g_{\mathrm{J}}\mu_{\mathrm{B}}(J+1)\gamma M_{\mathrm{s}}/3k_{\mathrm{B}}. \tag{7.10}$$

The LCMO interface has a Curie temperature ranging between the LCMO layer and the LSMO layer. It is evident that at the interface between different magnetic oxide layers, with similar structures and the same origin for the magnetization, a magnetic interface effect can be observed.

8. Summary, Conclusion and Outlook

As the underlying physic of the three investigated interfaces is different, a comparison of these systems will be given in the following chapter. Afterwards, a conclusion of the underlying physics will be given.

Summary

Pd/Fe

Pd/Fe layered samples were investigated, where magnetic interface effects are well-known [9, 7], but still a matter of ongoing investigations. Especially possible applications in spintronics create a renewed interest [116]. Therefore, this system was investigated to get an entire picture and to ensure that these kinds of interface effects are visible with a combination of SQUID, PNR and XMCD measurements. Additionally, the complementary XMCD and PNR measurements are interesting for this system due to the fact that not many conclusive PNR studies were performed. The interface effect depends also strongly on the sample preparation and sample quality.

The SQUID magnetometry measurements indicate an induced magnetic moment in the Pd layer. An average Pd magnetic moment of $m = 0.17\ \mu_\mathrm{B}$ at 10 K can be determined. XMCD measurements prove that Pd is magnetically polarized, with an average magnetic moment of $m = 0.288\ \mu_\mathrm{B}$, lying slightly above the magnetic moment determined in the

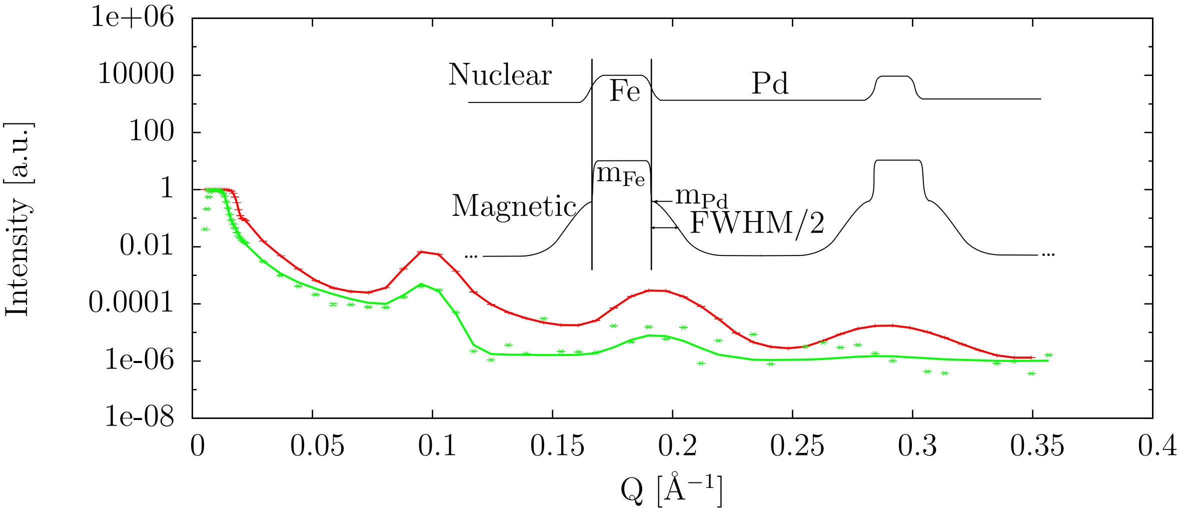

Figure 8.1.: PNR measurement of Pd/Fe multilayer. Inset: Model for the nuclear and magnetic SLD.

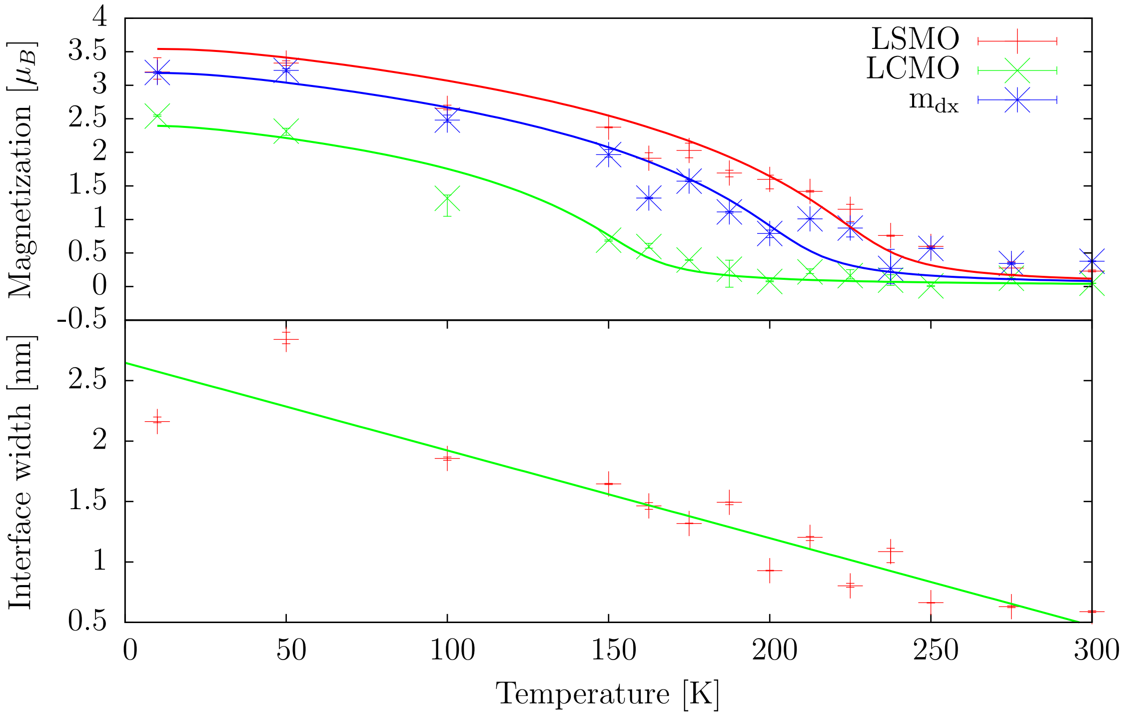

Figure 8.2.: Top: Temperature-dependent magnetic moment of LSMO, LCMO and the interface. Bottom: Temperature-dependent interface width.

SQUID magnetometry measurements. The PNR measurements show that Pd is magnetically polarized at the interface to the Fe layers. The magnetic moment of Pd, directly at the interface to Fe, can be determined to 0.54 μ_B, which decays to the half value after 11.56 Å.

LSMO/LCMO

The LSMO/LCMO multilayer was investigated with SQUID magnetometry measurements and PNR measurements. The SQUID measurements show a reduced magnetic moment and reduced Curie temperature of the whole LSMO/LCMO multilayer. The Curie temperature of the LSMO/LCMO multilayer is reduced to 222 K ± 10 K, although bulk LSMO layers, with same nominal composition of $La_{0.7}Sr_{0.3}MnO_3$, should have a T_C of 380 K. Additionally, the hysteresis measurements shows a step-like shape at intermediate temperatures, where the LCMO layer is expected to become ferromagnetic.

The PNR measurements are very sensitive to the magnetic profile through the whole multilayer, because of nearly similar nuclear scattering length densities of $SLD_{\mathrm{LSMO}} = 3.69\ 10^{-6}\text{Å}^{-2}$ and $SLD_{\mathrm{LCMO}} = 3.59\ 10^{-6}\text{Å}^{-2}$. The LCMO layer shows a higher magnetic moment at the interface to the LSMO layer and the width of this interface effect is increasing with decreasing temperature, indicating an existing interface effect.

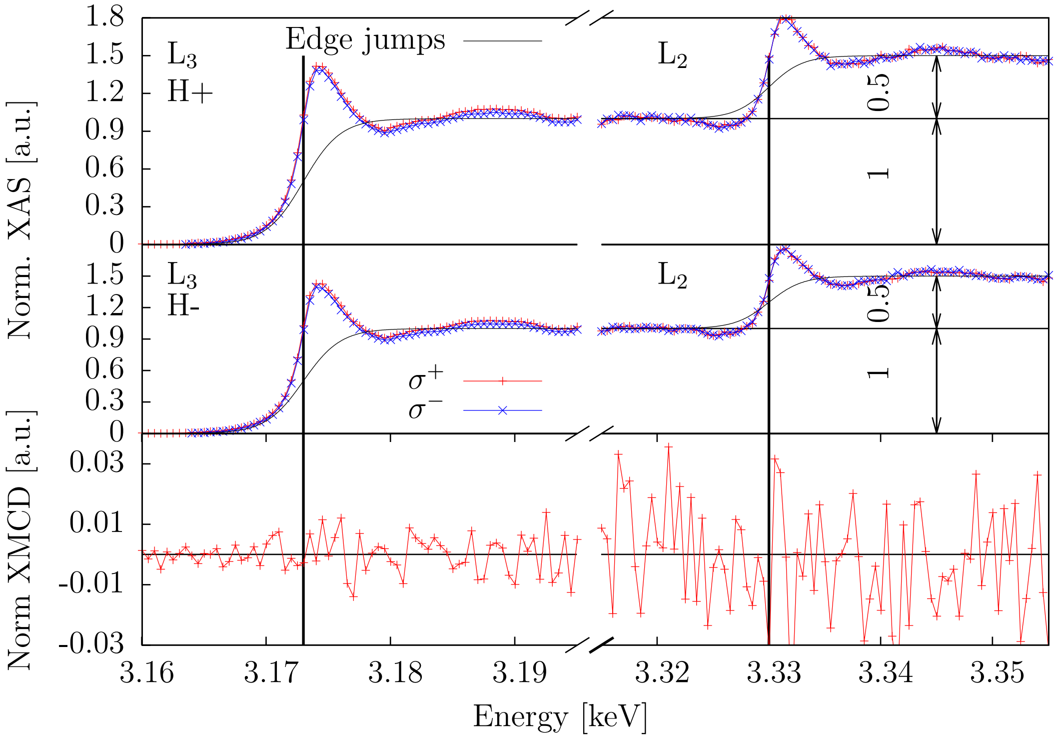

Figure 8.3.: XMCD measurement of LSMO/Pd film.

LSMO/Pd and LCMO/Pd

The LSMO/Pd and LCMO/Pd thin films were investigated with a combination of SQUID, PNR and XMCD measurements, in order to address the question of a possible magnetic interface effect. The SQUID magnetometry measurements show a reduced magnetic moment of the LSMO layer of 3 μ_B, in comparison to the bulk LSMO magnetic moment of 3.7 μ_B [13]. The reduced magnetization might originate from the off-stoichiometry, strain effects and the reduced magnetization at the interfaces of LSMO layers [102]. The off-stoichiometry will lead to a poorer crystalline quality and altered superexchange and double exchange interactions. The SQUID magnetometry and the PNR measurements indicate that Pd has no magnetic moment at the interface to LSMO or LCMO. In order to confirm this result, XMCD measurements were performed. The average magnetic moment of $m = 0.08\ \mu_\mathrm{B} \pm 0.07\ \mu_\mathrm{B}$ in the 4.8 nm thick Pd layer indicates the absence of a significant magnetic moment.

Conclusion

Pd/Fe

The well-known Pd/Fe layered system shows the expected behavior, where Pd is magnetically polarized at the interface to the metallic and ferromagnetic Fe. The induced magnetic moment, as well as the width of the interface effect corresponds to the results

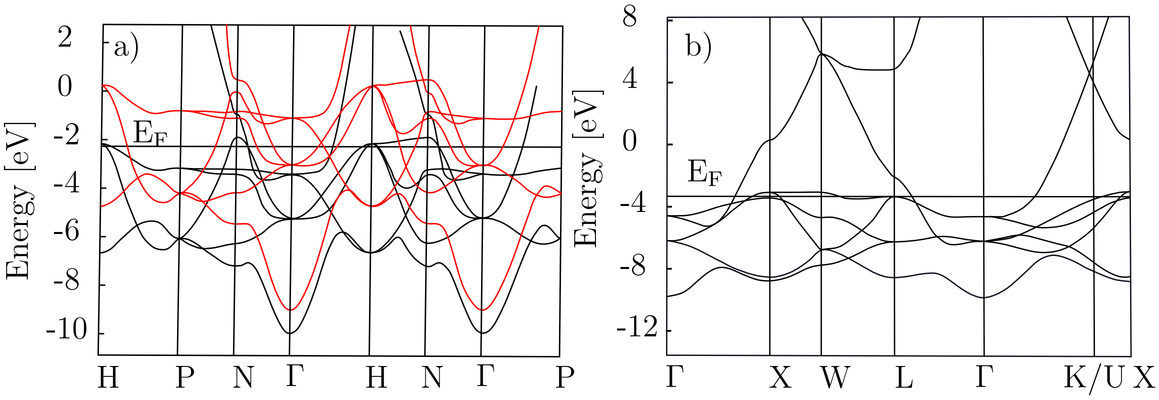

Figure 8.4.: a) The band structure of Fe (based on [117]). b) Pd (based on [118]).

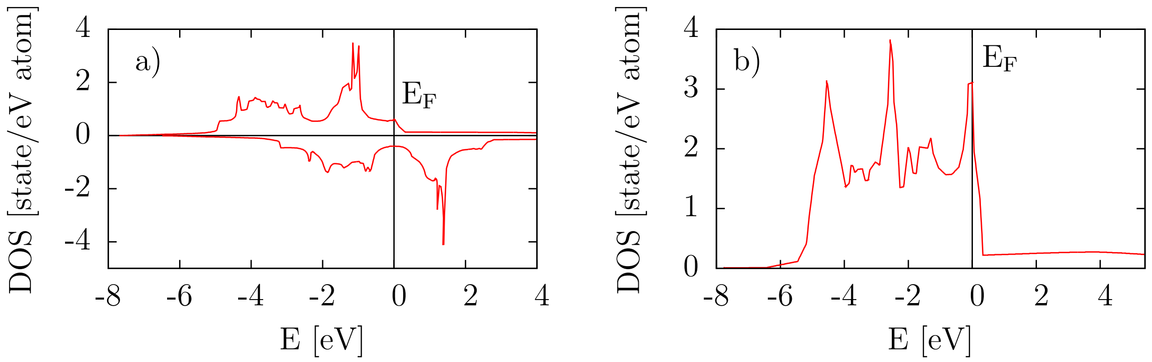

Figure 8.5.: a) Density of states for Fe (based on [117]). b) Pd (based on [118]).

in other publications [9, 7]. Pd nearly fulfills the Stoner criterion for ferromagnetism ($UD(E_\mathrm{F}) = 0.78$) and can, therefore, be magnetically polarized by increasing the density of states at the Fermi level.

The band structure (**figure 8.4** b) of Pd shows very narrow 4d orbitals located directly at the Fermi energy, leading to a large density of states (**figure 8.5** b) with $D(E_\mathrm{F}) = 2.28\ \mathrm{eV}^{-1}$. The spins states in Fe are already split into majority and minority spin states (**figure 8.4** a) due to the fulfillment of the Stoner criterion ($UD(E_\mathrm{F}) = 1.43$). A hybridization of the Pd 4d orbitals with the Fe 3d orbitals [62] increases the density of states of Pd at the Fermi energy. This leads to $UD(E_\mathrm{F}) > 1$ and a splitting of the majority and minority spins (**figure 8.6** c) and to ferromagnetic Pd.

At the interface also the density of states of Fe is altered, due to the hybridization of the 3d and 4d orbitals, which can be seen in **figure 8.6 b**, increasing the magnetism of Fe [62] from 2.2 μ_B to 2.4 μ_B. This effect is difficult to be seen in the PNR measurements, due to the roughness at the interfaces, as well as the additional contribution of the Pd magnetization. But either an increase of the Fe magnetic moment or an induced Pd magnetization is necessary in order to simulate the PNR measurements.

LSMO/LCMO

The magnetism in LSMO and LCMO has to be described with a different model than the itinerant magnetism of Pd/Fe. The electrons of the Mn atoms, carrying the magnetism,

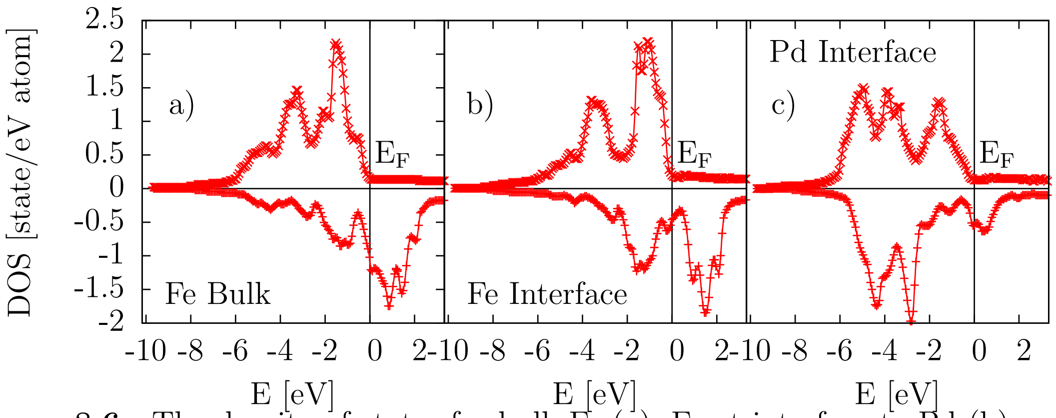

Figure 8.6.: The density of states for bulk Fe (a), Fe at interface to Pd (b) and Pd (c) (based on [62]).

are strongly localized and behave as a highly correlated electron system. The magnetism depends on double exchange and superexchange interactions of localized 3d Mn electrons mediated through an oxygen atom. Due to the same mechanism for ferromagnetism in LSMO and LCMO, the magnetism is altered at the interface. The ionic radii of Ca and Sr are different (Ca has a ionic radius of 1 Å and of Sr of 1.16 Å), resulting in pseudo cubic lattice parameters for bulk LCMO and LSMO of 3.87 Å [32] and 3.88 Å [31], respectively. The lattice distortion, due to different ionic radii and different lattice parameters, changes the bonding lengths and bonding angles, effecting directly the superexchange and double exchange interactions and therefore the ferromagnetism. The results from the SQUID measurements at intermediate temperatures (step-like hysteresis) might be an effect from these altered superexchange and double exchange interactions. The possibility of antiferromagnetic alignment of the ferromagnetic layers can be further investigated with PNR measurement with small applied magnetic fields.

The increased magnetization of LCMO, at the interface to LSMO, might result from the intermixed phase $\mathrm{La_{0.7}Sr_{\mathit{x}}Ca_{0.3-\mathit{x}}MnO_3}$ (LSCMO) with a higher T_C (**table 8.1**) than the single LCMO layer and, thus, a higher magnetic moment at lower temperature than pure LCMO [19, 119]. In [19] the increased $\mathrm{T_C}$ was attributed to a larger $\mathrm{Sr^{2+}}$ ionic radius in comparison to the $\mathrm{Ca^{2+}}$ ionic radius, which strengthens the double exchange interaction and, therefore, the ferromagnetism. The same holds true without intermixing, directly at the interface.

LSMO/Pd and LCMO/Pd

The magnetism in the LSMO and LCMO layers is based on the superexchange and double exchange interaction, but Pd can exhibit a band magnetism. It was shown that Pd can

x	0	0.05	0.1	0.15	0.2	0.25	0.3
$\mathrm{T_C}$ [K]	258.88	280.92	300.83	324.19	330.57	341.14	352.61

Table 8.1.: Curie temperature of $\mathrm{La_{0.7}Sr_xCa_{0.3-x}MnO_3}$ for different x values [19].

become ferromagnetic in dilute Pd(Mn) alloys, but with low T_C [120, 121]. This can be attributed to a hybridization of the Mn 3d and Pd 4d orbitals. Another possibility is the already mentioned (see **section 2.4**) hole-mediated double exchange mechanism in Pd doped CdS [23] or ZnS [122, 123, 22] systems. A strong coupling chain through the Cd-S and Zn-S atoms allows a double exchange interaction and, therefore, ferromagnetic alignment of the Pd atoms. But, as could be shown with PNR and XMCD measurements, either a small magnetic moment or no induced magnetization at the interface can be observed. Especially, Pd has not such a large induced magnetic moment (about 0.6 μ_B) as in the $La_{0.7}Ca_{0.3-x}Sr_xMnO_3$ framework [20], where the induced magnetization was derived from field cooled measurements. Possible reasons for the small or missing magnetic moment will be discussed in the following.

The interactions of Pd and LSMO can be discussed using the Stoner model for ferromagnetism with a direct electron-electron interaction and a possible orbital hybridization. Considering the whole LSMO perovskite structure, the Mn band structure is already altered through the oxygen octahedron and the crystal field. The LSMO band structure and the corresponding DOS is shown in **figure 8.7**, where the splitting in t_{2g} and e_g sub-levels is clearly visible. Because of the quite localized t_{2g} orbitals below the Fermi energy, these orbitals cannot create bonds with possible Pd atoms. Only the delocalized e_g orbitals, which are crossing the Fermi energy can create bonds with Pd atoms. Because of the delocalization and the small DOS of spin-up states at the Fermi energy, these orbitals are not suited to increase the DOS at the Fermi energy of Pd and induce a polarization. Especially considering that the orbitals of Pd suitable for hybridization are located directly below the Fermi energy (**figure 8.4** b), where LSMO has an energy gap between the t_{2g} and the e_g orbitals.

The Pd and LSMO interactions can be discussed in the model of superexchange and double exchange interactions, where Pd interacts directly with the Mn atoms or mediated through an oxygen atom. The lattice parameter of the LSMO perovskite structure is $\sim$ 3.88 Å, resulting in one Mn atom in a 3.88^3 Å^3 volume. Pd has also a lattice parameter of 3.88 Å, but grows in the fcc structure, resulting in four Pd atoms in a 3.88^3 Å^3 volume and approximately a stoichiometry of Pd_4Mn. In a similar stoichiometry, the Pd_3Mn alloy exhibits antiferromagnetic alignment [125, 126], which might also be the case at the Pd/LSMO interface. Additionally, the Mn atoms already form bonds with the oxygen atoms in the perovskite structure, reducing the possibility to create bonds with the Pd atoms.

The superexchange and double exchange interactions might not led to ferromagnetism in Pd, due to the missing bonds between Mn and Pd through oxygen atoms or an competition between ferromagnetic and antiferromagnetic alignments of Pd atoms. Pd has the oxidation states 2+ and 4+, and can form PdO and PdO_2 chemical compounds. At the interface oxygen might form the Pd-O-Pd bond, which should be connected antiferromagnetic after the superexchange interaction rules (see **section 2.1**). Therefore, competition between ferromagnetic superexchange interaction between Mn and Pd atoms and antiferromagnetic superexchange interaction between adjacent Pd atoms might hinder the formation of a ferromagnetic phase in Pd.

Another aspect is the magnetic “dead” layer of LSMO at the interface to Pd, which

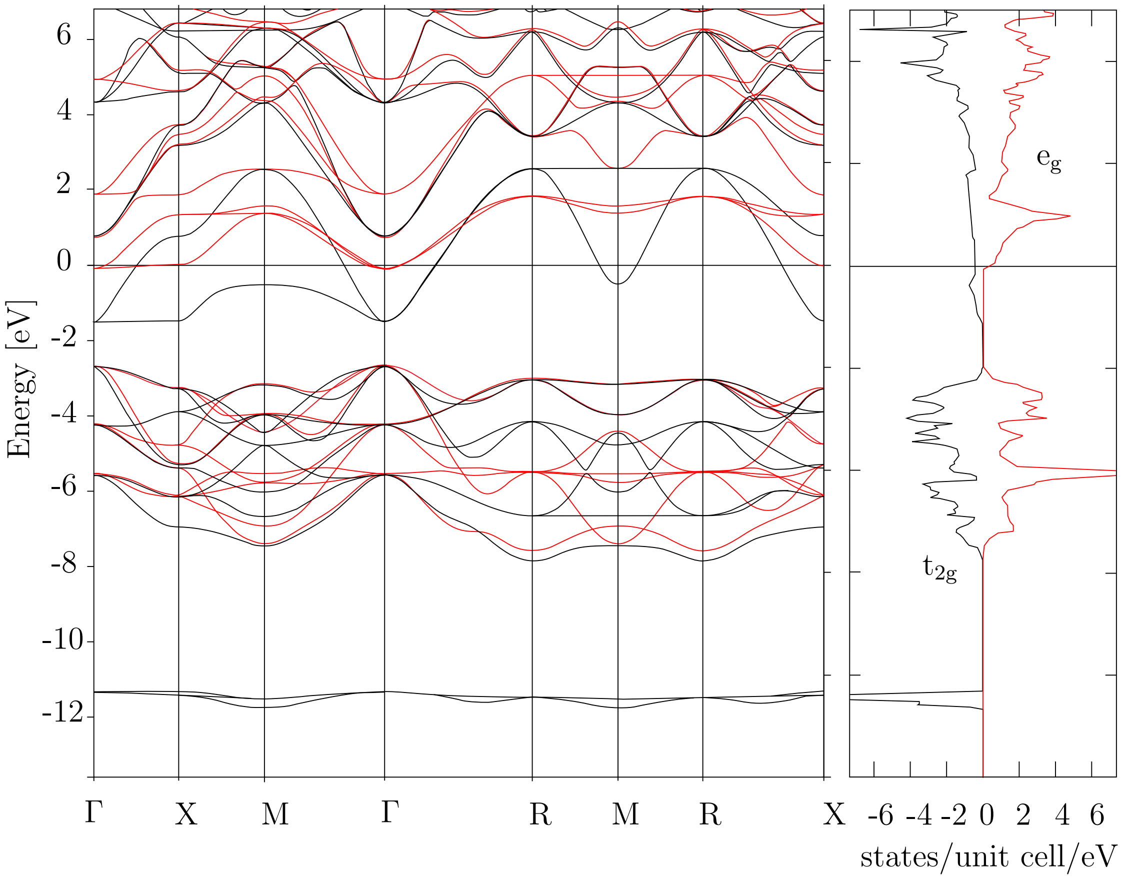

Figure 8.7.: Band structure and DOS of $La_{0.7}Sr_{0.3}MnO_3$ (based on [124]).

might hinder the magnetic polarization of the Pd layer. It is well-known, that LSMO has a reduced magnetization at interfaces [102], but not in the order visible in the performed PNR measurement. One possible explanation of the increased magnetic "dead" layer of LSMO, at the interface to Pd, might be the reason that Pd is a good conductor. This might change the electronic structure of the LSMO interface by creating an electronic depletion layer and hinder the superexchange and double exchange interactions and the magnetic order. Another possibility might be an oxygen deficiency at the LSMO interface caused by an oxidization of the Pd interface. An oxygen deficiency at the LSMO interface will also alter the superexchange and double exchange interactions and might reduce the LSMO magnetization. Both mechanism might led to the significant magnetic "dead" layer in LSMO and prevent a magnetic polarization of Pd.

Outlook

For a further understanding of the interface effects in the oxide/oxide layered samples, the LSMO/LCMO multilayer could be grown with the OMBE system, where smoother interfaces can be created. Another possibility is the usage of a different compound, which has a similar structure, but a larger difference in SLD. It should be possible to grow $La_{1-x}Ba_xMnO_3$/LCMO or $La_{1-x}Ba_xMnO_3$/LSMO multilayers with the OMBE system.

The simulation of the PNR measurements could be further refined with a larger SLD contrast.

In order to increase the understanding of the metal/oxide systems, like LSMO/Pd or LCMO/Pd, it might be helpful to investigate the orbital ordering of the LSMO and LCMO layers at the interface to Pd. Reflectometry measurements with π and σ polarized light performed at the absorption edges of Mn would give a view on the orbital occupation. This would help in the understanding of possible interactions with the Pd atoms. Determining the band structure with photoelectron spectroscopy might give an explanation for the missing hybridization between the LSMO and Pd layer. With X-ray photoelectron spectroscopy this could be done angle-dependent, investigating the band structure at the interfaces between LSMO and Pd. The X-ray photoelectron spectroscopy might explain the reason for the enhanced magnetic “dead” layer of LSMO due to the possibility to measure the band structure depth resolved. Another possibility is the exchange of Pd with Pt, which has a large Stoner parameter ($U = 0.32$ eV). It is known, that Pt can also be magnetically polarized in contact to ferromagnetic Fe [127]. Investigating $Y_3Fe_5O_{12}$/Pt, might further help with the understanding of the oxide/metal interface. Especially due to the reason that the induced magnetism in $Y_3Fe_5O_{12}$/Pt films is still under debate [64, 65, 66].

The experimental results, especially from the metal/oxide system, could be used as test results for ab-initio calculations of interface effects. Interface effects of metal/oxide interfaces are absolutely not trivial and, thus, comparisons between experiments and theory need to be done.

A. List of Figures

B. List of Tables

C. Band Structures

The band structures and the density of states (DOS) of $La_{0.7}Sr_{0.3}MnO_3$, Pd and Fe are presented.

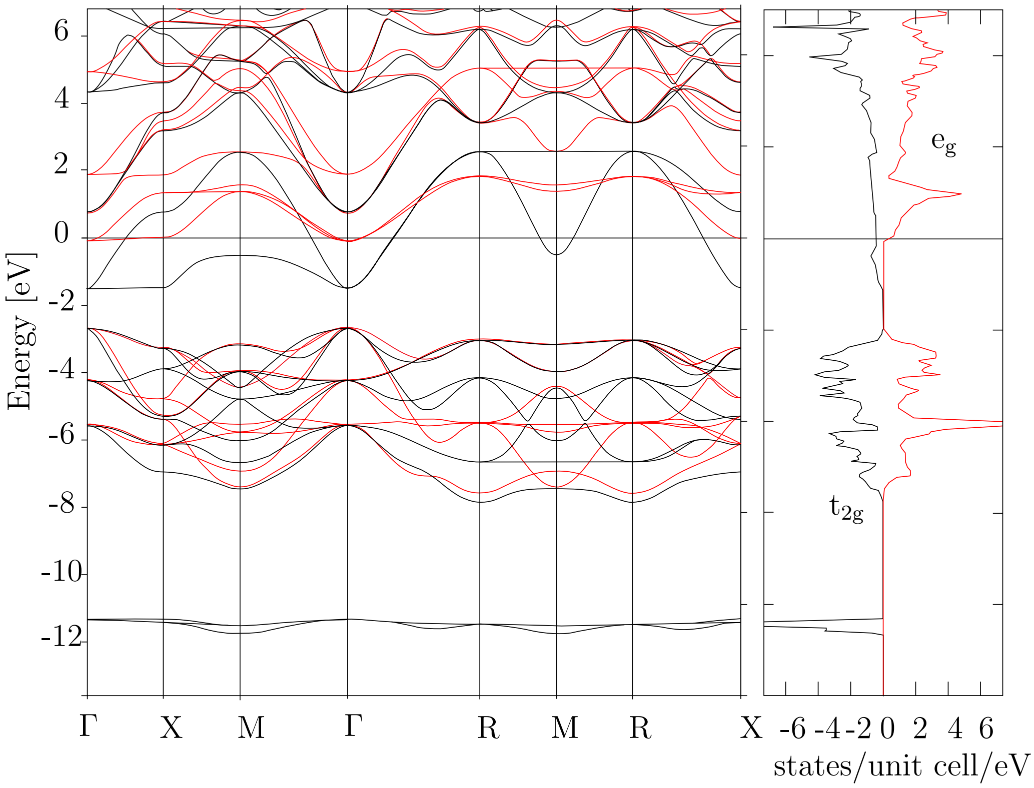

Figure C.1: Band structure and DOS of $La_{0.7}Sr_{0.3}MnO_3$ (based on [124]).

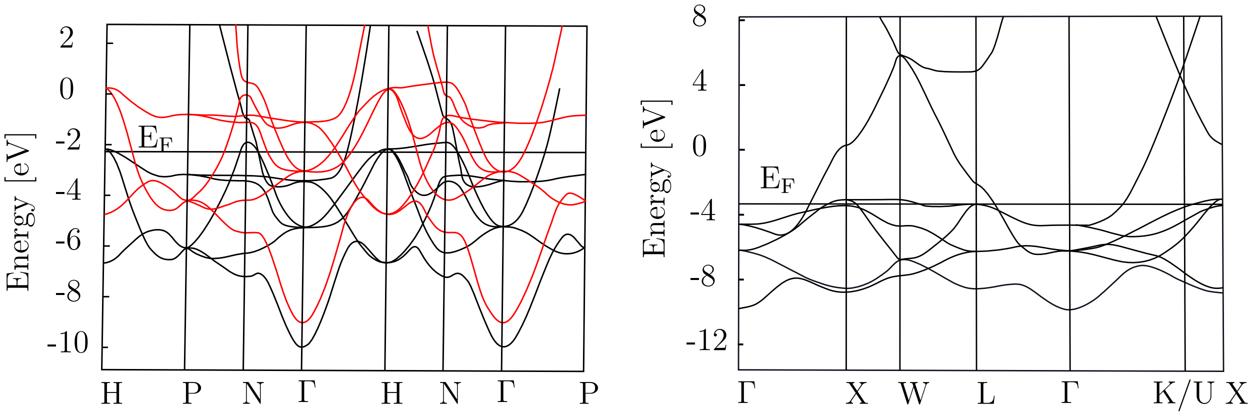

Figure C.2: Band structure of Fe (left) (based on [117]) and Pd (right) (based on [118]).

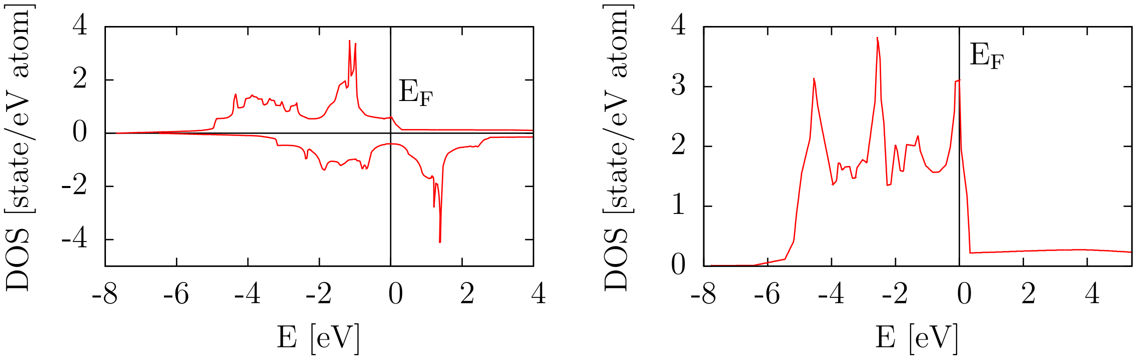

Figure C.3: Density of states for Fe (left) (based on [117]) and for Pd (right) (based on [118]).

D. Receipt for Sample Preparation

In the following a receipt for the film growth with OMBE and HOPSA is presented. Commands are indicated with the ♯ symbol. The growth parameters indicated with “ ” have to be changed to the values given in **appendix E**.

Oxide Molecular Beam Epitaxy (OMBE)

The rates of the elements have to be calibrated to the desired stoichiometry by moving the micro quartz balance to the substrate position and adjusting the frequency changes accordingly (see **section 5.1.2**), which has to be done before the growth process. The receipt can be used after the rate calibration and can be divided into different parts. The first part “Calibrate-Plasma” is for the calibration of the plasma source. The plasma has to be set into high brightness mode and the reflected power has to be minimized (a value lower 5 W). For the growth of metallic films, this part has to be omitted. The second part “Pre-Preparation” is the preparation of the substrate before growth, where the substrate tempered at a high temperature in order to clean the substrate. The third part “Growth” handles the film growth. Depending on the film, this part looks different. For a LSMO or LCMO film, the substrate temperature has to be set to the desired value and the shutters blocking the individual elements have to be opened. Depending on the rate, determined during the rate calibration, the growth time has to be adjusted in order to grow the desired film thickness. For the Pd film, the substrate temperature has to be set to room temperature and the shutter blocking the E-gun has to be opened. The E-gun has a separate micro quartz balance with a feedback loop. Therefore, the growing film thickness can be measured. Is the given thickness achieved, the shutter is closed and the E-gun can be switched off. The last part “Post-Preparation” handles the colling down of the substrate and the turning off of the plasma.

Main Receipt

```
Load Calibrate-Plasma
Load Pre-Preparation
Load Growth
Load Post-Preparation
```

Calibrate-Plasma

```
# Switch on Plasma
Open MFC                                                # Open oxygen valve
Open Oxygen                                             # Open oxygen shutter
Set Oxygen RF-Power "250"                               # Switch on plasma
Set Oxygen Flow "0.15"                                  # Set oxygen flow
# Tune Plasma to high brightness mode and a low reflected power
Set Oxygen Flow "0.08"                                  # Set desired oxygen flow
# Tune Plasma to have a low reflected power
Wait Until User continues
```

Pre-Preparation

```
# Preparation of substrate
Set Manipulator Setpoint "1000.0"                       # Set substrate temperature
Wait Until Manipulator Temperature > "1000.0"           # Wait until temperature reached
Pause 3600.0
```

Growth (LSMO)

```
# Sample Grwoth
Set Manipulator Setpoint "800.0"
Wait Until Manipulator Temperature > "800.0"
Pause "60.0"
Open Sr                                                 # Open shutter growth starts
Open La
Open Mn
Pause "4865"
Close Sr                                                # Close shutter
Close La
Close Mn
```

Growth (LCMO)

```
# Sample Grwoth
Set Manipulator Setpoint "800.0"
Wait Until Manipulator Temperature > "800.0"
Pause "60.0"
Open Ca
Open La
Open Mn
Pause "3865"
Close Ca
Close La
Close Mn
```

Growth (Pd)

```
# Sample Grwoth
Set Manipulator Setpoint "10.0"
Wait Until Manipulator Temperature < "10.0"
Pause "60.0"
Open Multi1                               # Open shutter of E-gun
Reset SQC Thickness                       # Set thickness to zero
Pause 10.0
Wait Until Multi1 Thickness > "0.500"       # Wait until thickness larger 5 nm
Close Multi1                              # Close shutter of E-gun
Set SQC Final Thickness                   # Ramp E-gun down
Wait Until Multi1 Output < 5.0            # Wait until E-gun is at low power
Stop Multi1 Emission                      # Switch E-gun off
```

Post-Preparation

```
# Cool down substrate and switch of plasma
Set Manipulator rate 15.0                        # Set temperature rate
Set Manipulator Setpoint 10.0                    # Set substrate temperature
Wait Until Manipulator Temperature < 50.0
Close Oxygen                                     # Close oxygen shutter
Set Oxygen RF-Power 0                            # Switch off plasma source
Set Oxygen Flow 0.0
Close MFC                                        # Close oxygen valve
```

High Oxygen Pressure Sputtering Automaton (HOPSA)

The receipt for the film growth, with HOPSA, has a similar structure as in the case of the film growth with OMBE. The receipt is separated into different parts: “Preparation”, “Growth” and “Post-Preparation”. The “Preparation” handles the cleaning of the substrate and the target, by setting a high substrate temperature and by turning on the plasma. The tuning of the plasma is done automatically by the RF generator. Solely the desired forward power has to be set. The “Growth” of a single film is done by moving the target over the substrate and waiting a for a certain time period. The growth of a multilayer is done by moving the first target over the substrate and waiting for the growth of the first film and then moving the second target over the substrate and waiting for the growth of the second film. This is repeated until the multilayer is grown. The “Post-Preparation” handles the turning off of the plasma, colling down of the substrate and moving the targets to a holding position.

Receipt for thin film growth

```
#  Preparation:
    Parameters:
      RF-Power=120 W                      # Set forward power of the plasma
      RF-Pon=1                            # Turn on the plasma
      Temp-T_target=900                   # Set the substrate temperature
      Temp-Ramp=10 C/min                  # Set the temperature rate
    Conditions:
          Wait for T to reach 900         # After temperature reached
          Wait for 3600s                  # wait for certain time period

#  Growth (Single Film):
    Parameters:
      Motor-Target="1"                      # Move target 1 over substrate
    Conditions:
      Wait for "14400s"

#  Growth (Multilayer):
    for i in 10:                          # Repeat growth
      Parameters:
        Motor-Target="1  "                  # Move target 1 over substrate
      Conditions:
        Wait for "14400s"
      Parameters:
        Motor-Target="2"                    # Move target 2 over substrate
      Conditions:
        Wait for "5400s"

#  Post-Preparation:
    Parameters:
      Motor-Target=0                      # Move targets to holding position
      Temp-T_target=10                    # Set substrate temperature
      RF-Power=50 W                       # Set low power
      RF-Pon=0                            # Switch of plasma
    Conditions:
      Wait for 60s
```

E. Growth Parameters

The following tables summarize the growth parameters for films grown with HOPSA and OMBE.

High Oxygen Pressure Sputtering Automation (HOPSA)

The presented growth parameters are the substrate temperature and the pressure during growth, the applied power at the target W_{F}, the reflected power W_{R}, the distance from the target to the substrate and the growth time.

Sample/ Size [mm^2]	Layers	Substrate Temperature	Pressure [mbar]	Plasma [W]	Growth Time	Substrate – Target Distance	
SP_{193} 5×5	$La_{0.7}Ca_{0.3}MnO_3$	800	3.0	$W_{\mathrm{F}} = 115$ $W_{\mathrm{R}} = 2$	12000 s	2.5 cm	
SP_{194} 5×5	$La_{0.7}Ca_{0.3}MnO_3$	700	3.0	$W_{\mathrm{F}} = 115$ $W_{\mathrm{R}} = 2$	12000 s	2.5 cm	
SP_{195} 5×5	$La_{0.7}Ca_{0.3}MnO_3$	900	3.0	$W_{\mathrm{F}} = 115$ $W_{\mathrm{R}} = 1$	12000 s	2.5 cm	
SP_{196} 5×5	$La_{0.7}Sr_{0.3}MnO_3$	1000	3.0	$W_{\mathrm{F}} = 120$ $W_{\mathrm{R}} = 3$	6000 s	2.5 cm	
SP_{198} 5×5	$La_{0.7}Sr_{0.3}MnO_3$	900	3.0	$W_{\mathrm{F}} = 120$ $W_{\mathrm{R}} = 1$	6000 s	2.5 cm	
SP_{199} 5×5	$La_{0.7}Sr_{0.3}MnO_3$	800	3.0	$W_{\mathrm{F}} = 120$ $W_{\mathrm{R}} = 2$	6000 s	2.5 cm	
SP_{203} 5×5	$La_{0.7}Sr_{0.3}MnO_3$	700	3.0	$W_{\mathrm{F}} = 120$ $W_{\mathrm{R}} = 3$	6000 s	2.5 cm	
SP_{207} 10×10	$La_{0.7}Sr_{0.3}MnO_3$	800	3.0	$W_{\mathrm{F}} = 120$ $W_{\mathrm{R}} = 1$	10000 s	2.5 cm	
SP_{208} 10×10	$La_{0.7}Ca_{0.3}MnO_3$	800	3.0	$W_{\mathrm{F}} = 120$ $W_{\mathrm{R}} = 2$	30000 s	2.5 cm	
SP_{213} 10×10	$La_{0.7}Sr_{0.3}MnO_3$	800	3.0	$W_{\mathrm{F}} = 120$ $W_{\mathrm{R}} = 3$	2540 s	2.5 cm	×10
	$La_{0.7}Ca_{0.3}MnO_3$	800	3.0	$W_{\mathrm{F}} = 115$ $W_{\mathrm{R}} = 3$	7200 s	2.5 cm	

Oxide Molecular Beam Epitaxy

The presented growth parameters are the frequency change $\Delta f/\Delta t$, the substrate temperature during growth, the pressure in the mean chamber, the oxygen flow, the forward power W_F and the reflected power W_R of the plasma source and the growth time.

Sample/ Size [mm^2]	Layers	Δf/Δt [Hz/s] Rate	Substrate Temp	Pressure [mbar]	Oxygen Flow [sccm]	Plasma Power [W]	Growth Time
OMBE$_{0071}$ 10×10	$La_{0.5}Sr_{0.5}MnO_3$	$\Delta f/\Delta t_{La} = 0.073$ $\Delta f/\Delta t_{Sr} = 0.0489$ $\Delta f/\Delta t_{Mn} = 0.058$	1000°C	$9.33 \cdot 10^{-6}$	0.187	$W_\mathrm{F} = 250$ $W_\mathrm{R} = 4$	182 min
OMBE$_{0113}$ 10×10	$La_{0.5}Bi_{0.5}MnO_3$	$\Delta f/\Delta t_{Bi} = 0.378$ $\Delta f/\Delta t_{Mn} = 0.20$ $\Delta f/\Delta t_{La} = 0.25$	800°C	$5.73 \cdot 10^{-6}$	0.15	$W_\mathrm{F} = 250$ $W_\mathrm{R} = 4$	60 min
OMBE$_{0115}$ 10×10	$La_{0.5}Bi_{0.5}MnO_3$	$\Delta f/\Delta t_{Bi} = 0.378$ $\Delta f/\Delta t_{Mn} = 0.20$ $\Delta f/\Delta t_{La} = 0.25$	700°C	$6.0 \cdot 10^{-6}$	0.15	$W_\mathrm{F} = 250$ $W_\mathrm{R} = 3$	60 min
OMBE$_{0116}$ 10×10	$La_{0.5}Bi_{0.5}MnO_3$	$\Delta f/\Delta t_{Bi} = 0.378$ $\Delta f/\Delta t_{Mn} = 0.201$ $\Delta f/\Delta t_{La} = 0.251$	600°C	$5.73 \cdot 10^{-6}$	0.15	$W_\mathrm{F} = 250$ $W_\mathrm{R} = 5$	60 min
OMBE$_{0118}$ 10×10	$La_{0.5}Bi_{0.5}MnO_3$	$\Delta f/\Delta t_{Bi} = 0.375$ $\Delta f/\Delta t_{Mn} = 0.201$ $\Delta f/\Delta t_{La} = 0.252$	500°C	$3.0 \cdot 10^{-6}$	0.15	$W_\mathrm{F} = 250$ $W_\mathrm{R} = 5$	60 min
OMBE$_{0208}$ 10×10	$La_{0.7}Sr_{0.3}MnO_3$	$\Delta f/\Delta t_{La} = 0.184$ $\Delta f/\Delta t_{Sr} = 0.0499$ $\Delta f/\Delta t_{Mn} = 0.1023$	1000°C	$6.0 \cdot 10^{-6}$	0.15	$W_\mathrm{F} = 250$ $W_\mathrm{R} = 1$	1505 s
	Pd	0.05 Å/s	RT	$3.0 \cdot 10^{-9}$	-	-	1000 s
OMBE$_{0239}$ 10×10	$La_{0.7}Ca_{0.3}MnO_3$	$\Delta f/\Delta t_{La} = 0.2035$ $\Delta f/\Delta t_{Ca} = 0.025$ $\Delta f/\Delta t_{Mn} = 0.116$	900°C	$2.0 \cdot 10^{-6}$	0.08	$W_\mathrm{F} = 300$ $W_\mathrm{R} = 2$	60 min
OMBE$_{0240}$ 10×10	$La_{0.7}Ca_{0.3}MnO_3$	$\Delta f/\Delta t_{La} = 0.199$ $\Delta f/\Delta t_{Ca} = 0.0247$ $\Delta f/\Delta t_{Mn} = 0.111$	800°C	$3.3 \cdot 10^{-6}$	0.08	$W_\mathrm{F} = 300$ $W_\mathrm{R} = 3$	60 min
OMBE$_{0242}$ 10×10	$La_{0.7}Ca_{0.3}MnO_3$	$\Delta f/\Delta t_{La} = 0.209$ $\Delta f/\Delta t_{Ca} = 0.0256$ $\Delta f/\Delta t_{Mn} = 0.118$	700°C	$3.8 \cdot 10^{-6}$	0.08	$W_\mathrm{F} = 300$ $W_\mathrm{R} = 2$	60 min

Sample/ Size [mm^2]	Layers	Δf/Δt [Hz/s] Rate	Substrate Temp	Pressure [mbar]	Oxygen Flow [sccm]	Plasma Power [W]	Growth Time
OMBE$_{0247}$ 10×10	La$_{0.7}$Ca$_{0.3}$MnO$_3$	$\Delta f/\Delta t_{La} = 0.19$ $\Delta f/\Delta t_{Ca} = 0.0223$ $\Delta f/\Delta t_{Mn} = 0.127$	800°C	$2.7 \cdot 10^{-6}$	0.08	$W_{\mathrm{F}} = 300$ $W_{\mathrm{R}} = 2$	60 min
OMBE$_{0248}$ 10×10 5×5	La$_{0.7}$Sr$_{0.3}$MnO$_3$	$\Delta f/\Delta t_{La} = 0.236$ $\Delta f/\Delta t_{Sr} = 0.0626$ $\Delta f/\Delta t_{Mn} = 0.131$	1000°C	$2.5 \cdot 10^{-6}$	0.08	$W_{\mathrm{F}} = 300$ $W_{\mathrm{R}} = 4$	60 min
OMBE$_{0251}$ 10×10 5×5	La$_{0.7}$Ca$_{0.3}$MnO$_3$	$\Delta f/\Delta t_{La} = 0.202$ $\Delta f/\Delta t_{Ca} = 0.0253$ $\Delta f/\Delta t_{Mn} = 0.134$	800°C	$2.6 \cdot 10^{-6}$	0.08	$W_{\mathrm{F}} = 300$ $W_{\mathrm{R}} = 4$	60 min
OMBE$_{0254}$ 10×10	La$_{0.7}$Ca$_{0.3}$MnO$_3$	$\Delta f/\Delta t_{La} = 0.217$ $\Delta f/\Delta t_{Ca} = 0.0268$ $\Delta f/\Delta t_{Mn} = 0.144$	800°C	$2.5 \cdot 10^{-6}$	0.08	$W_{\mathrm{F}} = 300$ $W_{\mathrm{R}} = 2$	20 min
	Pd	0.05 Å/s	RT	$2.8.0 \cdot 10^{-9}$	-	-	1000 s
OMBE$_{0293}$ 10×10	La$_{0.7}$Ca$_{0.3}$MnO$_3$	$\Delta f/\Delta t_{La} = 0.237$ $\Delta f/\Delta t_{Ca} = 0.0299$ $\Delta f/\Delta t_{Mn} = 0.157$	800°C	$3.2 \cdot 10^{-6}$	0.08	$W_{\mathrm{F}} = 300$ $W_{\mathrm{R}} = 2$	20 min
	Pd	0.05 Å/s	RT	$2.2.0 \cdot 10^{-9}$	-	-	1000 s

F. Element Parameters for Scattering

The following table gives an overview about the element parameters necessary for the analysis of the XRR and PNR measurements. The scattering length density (SLD) of $La_{0.7}Sr_{0.3}MnO_3$ (LSMO), $La_{0.7}Ca_{0.3}MnO_3$ (LCMO) and $SrTiO_3$ (STO) was calculated from the values given for the individual elements with the assumed stoichiometry.

	$f_1^{\text{X-ray}}$ [e/atom]	$f_2^{\text{X-ray}}$ [e/atom]	SL^{Neutron} [10^{-5} Å]	ρ [$Å^{-3}$]	**Re** $SLD^{\text{X-ray}}$ [$10^{-5} Å^{-2}$]	**Im** $SLD^{\text{X-ray}}$ [$10^{-5} Å^{-2}$]	SLD^{Neutron} [$10^{-6} Å^{-2}$]
Ti	22.24	1.87	-3.438	-	-	-	-
La	55.68	2.832	8.24	-	-	-	-
Mn	24.46	2.832	-3.73	-	-	-	-
Sr	37.64	1.845	7.02	-	-	-	-
Ca	20.38	1.313	4.70	-	-	-	-
O	8.052	0.03	5.803	-	-	-	-
Ag	47.18	4.265	5.922	0.0586	7.80	0.70	3.47
Fe	24.86	3.209	9.45	0.083	5.83	0.75	7.86
Pd	46.17	3.985	5.91	0.0685	8.92	0.77	4.05
STO	-	-	20.99	0.0168	3.98	0.18	3.53
LSMO	-	-	21.55	0.0171	4.77	0.50	3.69
LCMO	-	-	20.86	0.0172	4.55	0.49	3.59

Presented are the atomic scattering factors f_1 and f_2 of the individual elements for X-ray scattering [128] at an energy of 8048 eV; the scattering lengths (SL) for neutron scattering [129]; the density of LSMO [31] and LCMO [130] and the calculated scattering length densities (SLD).

G. Parameters used for XRR Simulations

The following tables summarize the parameters used for simulations of XRR measurements on samples used for the determination of the best growth temperature (see **section 5.2**). The layers are listed from bottom to top of the sample. The presented errors of the parameters are determined by varying the parameters up to a figure of merit (FOM), which is 5% worse than the best FOM. Parameters without given errors are kept fix. The presented parameters are: Layer thickness d, roughness σ, density ρ, atomic scattering factors f_1 and f_2 and the corresponding scattering length density (SLD).

The films grown with OMBE were measured directly after growth and then approximately one year later (labeled: *old*). An additional top layer, with SLD, has to be assumed in the simulation of the measurements performed one year later.

	Layer	d	σ	ρ	ρ^{Norm}	**Re** SLD	**Im** SLD
		[Å]	[Å]	$[10^{-2}\text{Å}^{-3}]$		$[10^{-5}\text{Å}^{-2}]$	
$\mathrm{OMBE}^{old}_{0239}$	STO	-	$1.04^{+0.20}_{-0.23}$	1.68	1.68	3.98	0.18
	LCMO	$362.15^{+1.60}_{-1.25}$	$4.40^{+0.04}_{-0.05}$	$1.71^{+0.00}_{-0.00}$	1.72	$4.58^{+0.07}_{-0.14}$	$0.50^{+0.01}_{-0.02}$
	$\mathrm{LCMO_{top}}$	$18.83^{+0.22}_{-0.45}$	$5.22^{+0.07}_{-0.05}$	$1.31^{+0.00}_{-0.00}$	1.72	$3.81^{+0.04}_{-0.09}$	$0.41^{+0.00}_{-0.01}$
OMBE_{0239}	STO	-	$1.29^{+0.03}_{-0.04}$	1.68	1.68	3.98	0.18
	LCMO	$382.19^{+1.03}_{-1.00}$	$4.66^{+0.11}_{-0.01}$	$1.69^{+0.02}_{-0.01}$	1.72	$4.47^{+0.05}_{-0.02}$	$0.48^{+0.01}_{-0.00}$
$\mathrm{OMBE}^{old}_{0240}$	STO	-	$3.84^{+0.41}_{-0.74}$	1.68	1.68	3.98	0.18
	LCMO	$340.99^{+1.52}_{-0.40}$	$4.78^{+0.50}_{-0.25}$	$1.73^{+0.02}_{-0.05}$	1.72	$4.58^{+0.07}_{-0.14}$	$0.50^{+0.01}_{-0.02}$
	$\mathrm{LCMO_{top}}$	$19.37^{+0.96}_{-0.90}$	$5.31^{+0.20}_{-0.22}$	$1.44^{+0.02}_{-0.04}$	1.72	$3.81^{+0.04}_{-0.09}$	$0.41^{+0.00}_{-0.01}$
OMBE_{0240}	STO	-	$1.51^{+0.62}_{-0.02}$	1.68	1.68	3.98	0.18
	LCMO	$359.26^{+0.45}_{-0.04}$	$4.28^{+0.01}_{-0.03}$	$1.73^{+0.04}_{-0.05}$	1.72	$4.49^{+0.12}_{-0.14}$	$0.49^{+0.01}_{-0.02}$
$\mathrm{OMBE}^{old}_{0242}$	STO	-	$3.70^{+0.22}_{-0.45}$	1.68	1.68	3.98	0.18
	LCMO	$374.96^{+0.04}_{-1.41}$	$2.87^{+0.33}_{-0.22}$	$1.71^{+0.01}_{-0.01}$	1.72	$4.51^{+0.02}_{-0.04}$	$0.49^{+0.00}_{-0.00}$
	$\mathrm{LCMO_{top}}$	$17.74^{+0.39}_{-0.41}$	$6.36^{+0.12}_{-0.11}$	$1.47^{+0.01}_{-0.01}$	1.72	$3.89^{+0.03}_{-0.01}$	$0.42^{+0.00}_{-0.00}$
OMBE_{0242}	STO	-	$0.54^{+0.26}_{-0.03}$	1.68	1.68	3.98	0.18
	LCMO	$390.79^{+0.90}_{-0.35}$	$5.65^{+0.05}_{-0.03}$	$1.72^{+0.00}_{-0.01}$	1.72	$4.55^{+0.00}_{-0.03}$	$0.49^{+0.00}_{-0.00}$
OMBE_{0248}	STO	-	$5.56^{+0.03}_{-0.05}$	1.68	1.68	3.98	0.18
	LSMO	$407.04^{+0.48}_{-0.07}$	$5.39^{+0.00}_{-0.12}$	$1.71^{+0.43}_{-0.37}$	1.71	$4.78^{+1.20}_{-1.03}$	$0.50^{+0.13}_{-0.11}$
	$\mathrm{LSMO_{top}}$	$9.04^{+0.13}_{-0.48}$	$16.19^{+0.23}_{-0.39}$	$1.04^{+0.03}_{-0.00}$	1.71	$2.91^{+0.08}_{-0.01}$	$0.30^{+0.01}_{-0.00}$
OMBE_{0251}	STO	-	$3.30^{+0.40}_{-0.32}$	1.68	1.68	3.98	0.18
	LCMO	$403.45^{+0.32}_{-0.25}$	$2.11^{+0.01}_{-0.01}$	$1.71^{+0.01}_{-0.01}$	1.72	$4.51^{+0.02}_{-0.02}$	$0.49^{+0.00}_{-0.00}$
	$\mathrm{LCMO_{top}}$	$6.28^{+0.02}_{-0.11}$	$5.56^{+0.14}_{-0.07}$	$1.00^{+0.01}_{-0.00}$	1.72	$2.64^{+0.02}_{-0.00}$	$0.29^{+0.00}_{-0.00}$

	Layer	d	σ	ρ	ρ^{Norm}	**Re** SLD	**Im** SLD
		[Å]	[Å]	$[10^{-2}\,\text{Å}^{-3}]$		$[10^{-5}\,\text{Å}^{-2}]$	
SP_{193}	STO	-	$5.90\ ^{+0.57}_{-0.22}$	1.68	1.68	3.98	0.18
	LCMO	$130.71\ ^{+0.24}_{-0.09}$	$1.59\ ^{+0.06}_{-0.03}$	$1.70\ ^{+0.01}_{-0.00}$	1.72	$4.50\ ^{+0.03}_{-0.00}$	$0.49\ ^{+0.00}_{-0.00}$
	$LCMO_{top}$	$8.77\ ^{+0.21}_{-0.13}$	$6.56\ ^{+0.33}_{-0.14}$	$1.01\ ^{+0.03}_{-0.00}$	1.72	$2.68\ ^{+0.07}_{-0.00}$	$0.29\ ^{+0.01}_{-0.00}$
SP_{194}	STO	-	$9.26\ ^{+0.74}_{-0.41}$	1.68	1.68	3.98	0.18
	LCMO	$113.96\ ^{+2.66}_{-6.33}$	$3.95\ ^{+0.25}_{-0.24}$	$1.71\ ^{+0.00}_{-0.02}$	1.72	$4.52\ ^{+0.01}_{-0.06}$	$0.49\ ^{+0.00}_{-0.01}$
	$LCMO_{top}$	$1.01\ ^{+9.34}_{-0.01}$	$16.03\ ^{+1.10}_{-1.23}$	$1.08\ ^{+0.03}_{-0.02}$	1.72	$2.86\ ^{+0.07}_{-0.06}$	$0.31\ ^{+0.01}_{-0.01}$
SP_{195}	STO	-	$15.00\ ^{+0.00}_{-7.65}$	1.68	1.68	3.98	0.18
	LCMO	$156.38\ ^{+32.01}_{-30.45}$	$4.00\ ^{+0.23}_{-0.25}$	$1.70\ ^{+0.01}_{-0.00}$	1.72	$4.50\ ^{+0.02}_{-0.00}$	$0.49\ ^{+0.00}_{-0.00}$
	$LCMO_{top}$	$17.03\ ^{+12.38}_{-16.47}$	$48.08\ ^{+6.98}_{-2.73}$	$0.83\ ^{+0.06}_{-0.06}$	1.72	$2.18\ ^{+0.17}_{-0.16}$	$0.24\ ^{+0.02}_{-0.02}$
SP_{196}	STO	-	$10.95\ ^{+2.63}_{-0.45}$	1.68	1.68	3.98	0.18
	LSMO	$201.58\ ^{+7.75}_{-10.09}$	$4.00\ ^{+0.03}_{-0.30}$	$1.71\ ^{+0.00}_{-0.00}$	1.71	$4.76\ ^{+0.01}_{-0.01}$	$0.50\ ^{+0.00}_{-0.00}$
	$LSMO_{top}$	$2.53\ ^{+26.69}_{-1.45}$	$33.21\ ^{+1.01}_{-0.78}$	$0.61\ ^{+0.10}_{-0.01}$	1.71	$1.69\ ^{+0.29}_{-0.04}$	$0.18\ ^{+0.03}_{-0.00}$
SP_{198}	STO	-	$9.06\ ^{+0.48}_{-1.47}$	1.68	1.68	3.98	0.18
	LSMO	$191.47\ ^{+7.20}_{-8.32}$	$3.42\ ^{+0.10}_{-0.87}$	$1.72\ ^{+0.00}_{-0.02}$	1.71	$4.79\ ^{+0.00}_{-0.05}$	$0.50\ ^{+0.00}_{-0.00}$
	$LSMO_{top}$	$3.27\ ^{+4.26}_{-2.12}$	$28.16\ ^{+10.69}_{-3.88}$	$1.08\ ^{+0.09}_{-0.02}$	1.71	$3.02\ ^{+0.26}_{-0.06}$	$0.32\ ^{+0.03}_{-0.01}$
SP_{199}	STO	-	$4.66\ ^{+0.73}_{-0.80}$	1.68	1.68	3.98	0.18
	LSMO	$202.43\ ^{+1.28}_{-1.27}$	$3.15\ ^{+0.03}_{-0.13}$	$1.71\ ^{+0.05}_{-0.02}$	1.71	$4.77\ ^{+0.14}_{-0.06}$	$0.50\ ^{+0.05}_{-0.03}$
	$LSMO_{top}$	$23.67\ ^{+0.39}_{-5.08}$	$20.61\ ^{+0.00}_{-1.25}$	$0.50\ ^{+0.04}_{-0.00}$	1.71	$1.39\ ^{+0.10}_{-0.00}$	$0.15\ ^{+0.01}_{-0.00}$
SP_{203}	STO	-	$0.26\ ^{+0.26}_{-0.00}$	1.68	1.68	3.98	0.18
	LSMO	$195.04\ ^{+0.07}_{-0.25}$	$8.90\ ^{+0.04}_{-0.00}$	$1.71\ ^{+0.02}_{-0.04}$	1.71	$4.77\ ^{+0.06}_{-0.11}$	$0.50\ ^{+0.01}_{-0.03}$
	$LSMO_{top}$	$32.22\ ^{+0.27}_{-0.18}$	$25.11\ ^{+0.04}_{-0.11}$	$0.62\ ^{+0.04}_{-0.04}$	1.71	$1.74\ ^{+0.11}_{-0.13}$	$0.18\ ^{+0.01}_{-0.01}$

H. Temperature Variation for Film Growth

Temperature Variation for LCMO film by HOPSA

Presented are the measurements for growth parameter optimization of LCMO thin films grown by HOPSA.

SP$_{0193}$

LCMO thin films grown on STO (001) substrates at a temperature of 800°C and 3 mbar oxygen partial pressure.

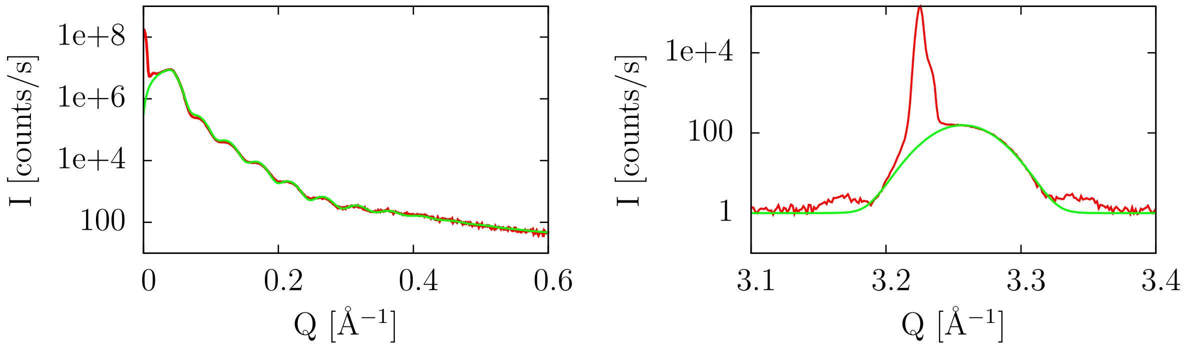

Figure H.1.: Left: X-ray reflectometry measurement with simulation thereof. Right: X-ray diffraction of the (002) Bragg peak.

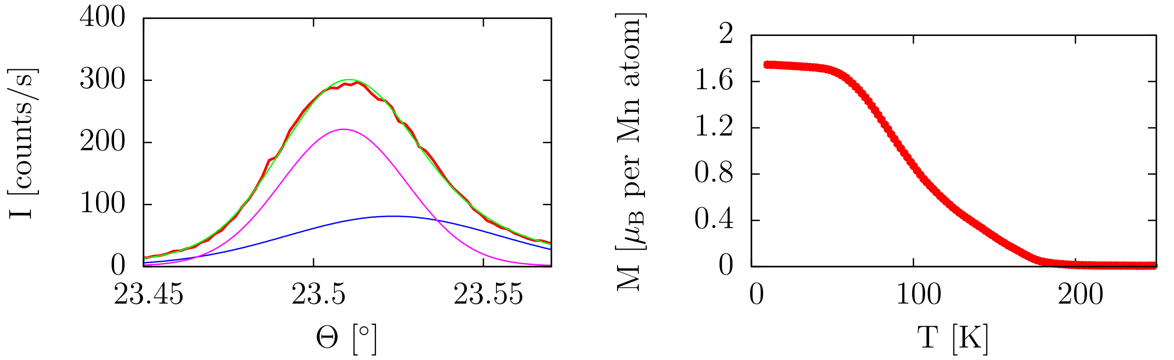

Figure H.2.: Left: Rocking scan of the (002) Bragg peak with Gaussian fit. The FWHM is $5.24° \cdot 10^{-2} \pm 0.01° \cdot 10^{-2}$. Right: Field cooled measurement at 100 Oe.

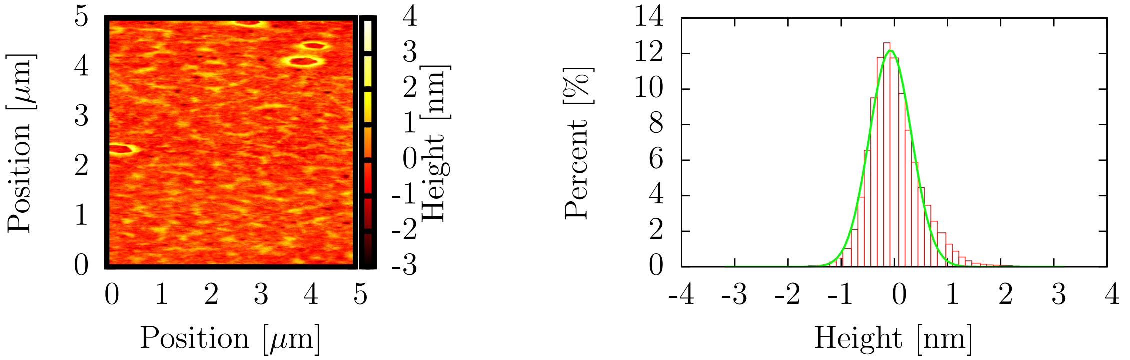

Figure H.3.: Left: Topography of AFM measurement, the roughness is 0.49 nm. Right: Height distribution of AFM measurement with Gaussian fit, resulting in roughness of 0.40 nm.

SP$_{0194}$

LCMO thin films grown on STO (001) substrates at a temperature of 700°C and 3 mbar oxygen partial pressure.

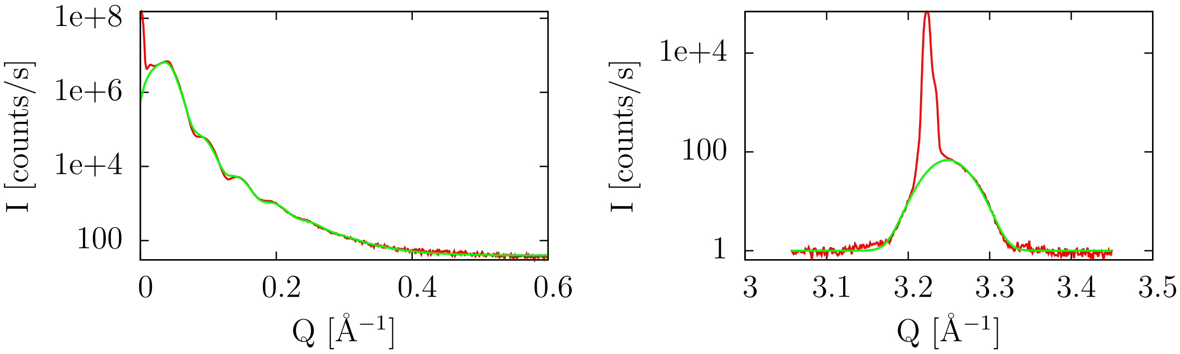

Figure H.4.: Left: X-ray reflectometry measurement with simulation thereof. Right: X-ray diffraction of the (002) Bragg peak.

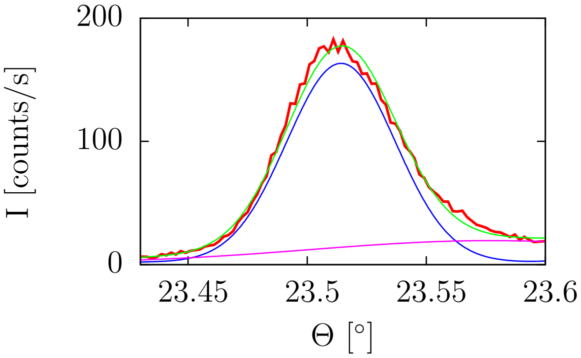

Figure H.5.: Rocking scan of the (002) Bragg peak with Gaussian fit. The FWHM is $5.77° \cdot 10^{-2} \pm 0.02° \cdot 10^{-2}$.

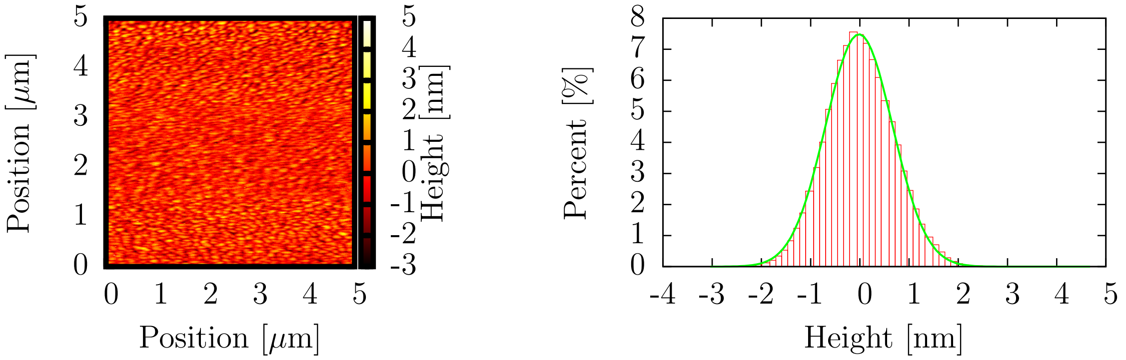

Figure H.6.: Left: Topography of AFM measurement, the roughness is 0.68 nm. Right: Height distribution of AFM measurement with Gaussian fit, resulting in roughness of 0.69 nm.

SP$_{0195}$

LCMO thin films grown on STO (001) substrates at a temperature of 900°C and 3 mbar oxygen partial pressure.

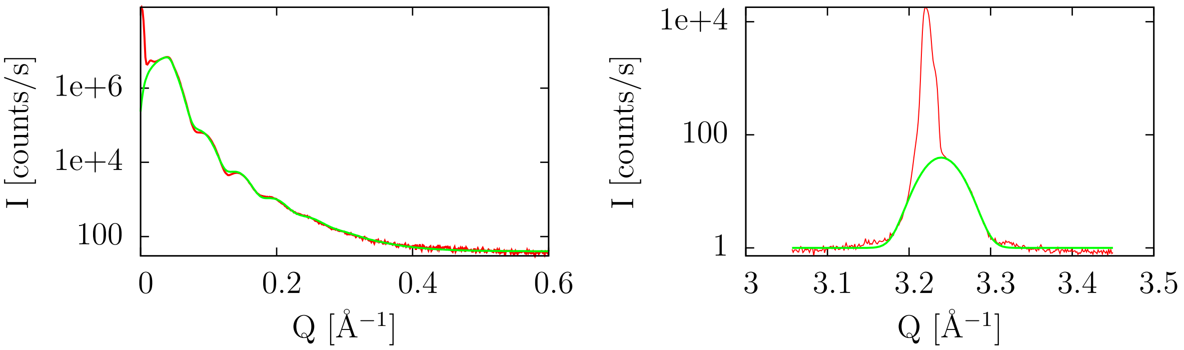

Figure H.7.: Left: X-ray reflectometry measurement with simulation thereof. Right: X-ray diffraction of the (002) Bragg peak.

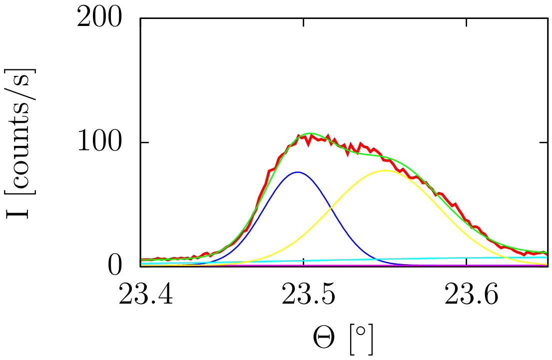

Figure H.8.: Rocking scan of the (002) Bragg peak with Gaussian fit. The FWHM is $11.99° \cdot 10^{-2} \pm 0.03° \cdot 10^{-2}$.

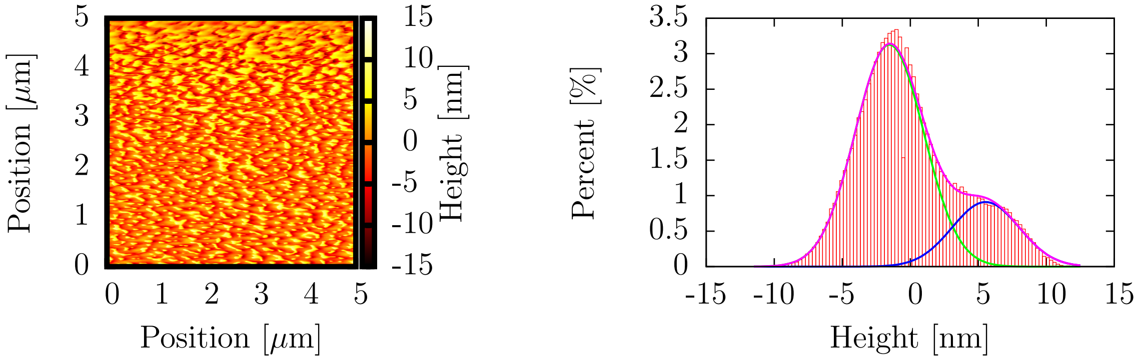

Figure H.9.: Left: Topography of AFM measurement, the roughness is 3.79 nm. Right: Height distribution of AFM measurement with Gaussian fit.

Temperature Variation for LSMO film by HOPSA

All prepared LSMO thin films grown by OMBE, for the optimization of growth parameters, are shown including all relevant measurements: AFM, XRR and XRD.

$\mathbf{SP}_{0196}$

LSMO thin films grown on STO (001) substrates at a temperature of 1000°C and 3 mbar oxygen partial pressure.

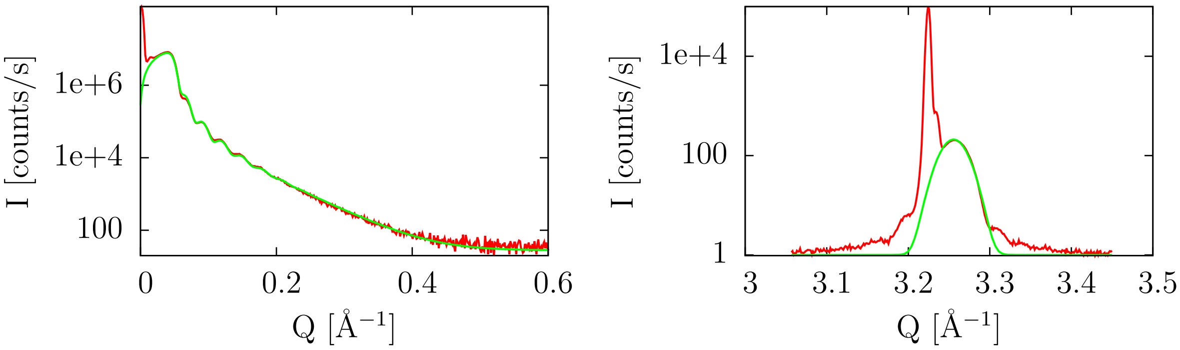

Figure H.10.: Left: X-ray reflectometry measurement with simulation thereof. Right: X-ray diffraction of the (002) Bragg peak.

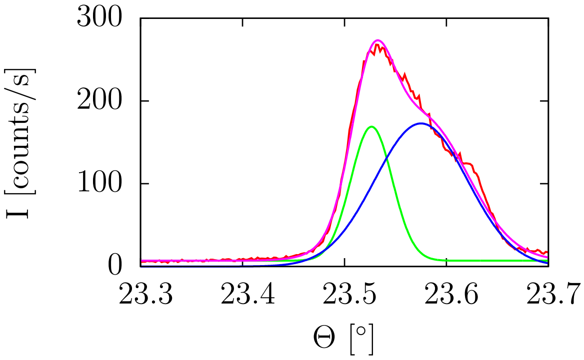

Figure H.11.: Rocking scan of the (002) Bragg peak with Gaussian fit.

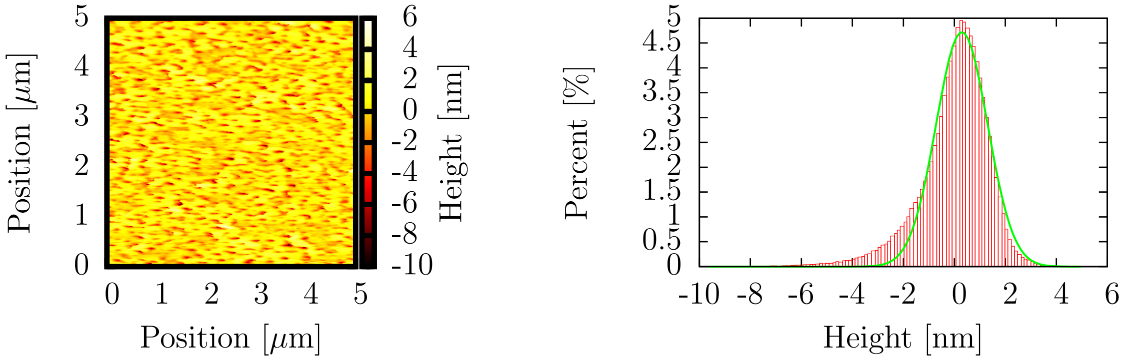

Figure H.12.: Left: Topography of AFM measurement, the roughness is 1.35 nm. Right: Height distribution of AFM measurement with Gaussian fit, resulting in roughness of 1.01 nm.

SP$_{0198}$

LSMO thin films grown on STO (001) substrates at temperature 900°C and 3 mbar oxygen partial pressure.

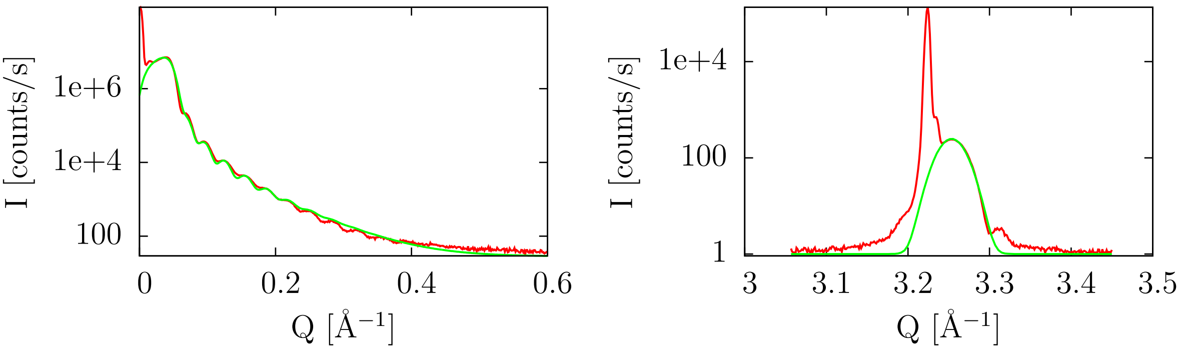

Figure H.13.: Left: X-ray reflectometry measurement with simulation thereof. Right: X-ray diffraction of the (002) Bragg peak.

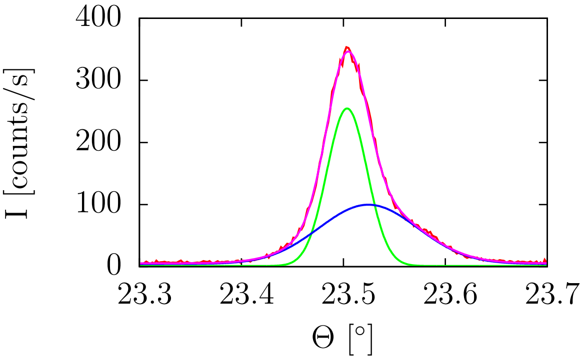

Figure H.14.: Rocking scan of the (002) Bragg peak with Gaussian fit. The FWHM is 5.77° ± 0.61°.

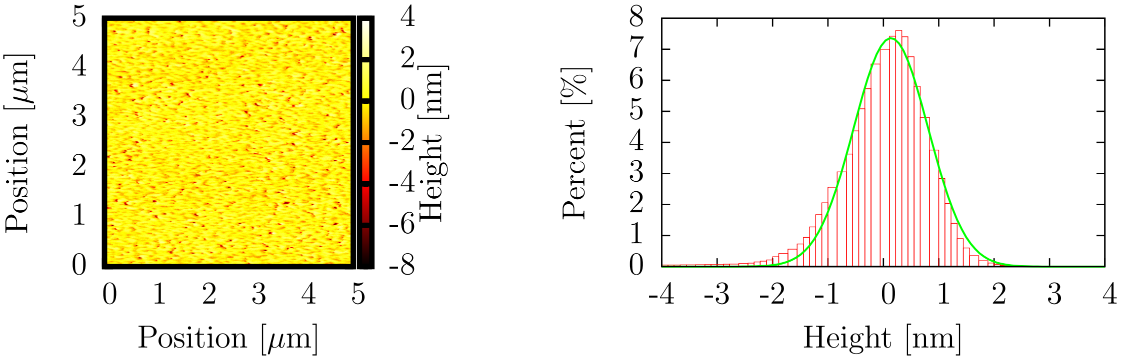

Figure H.15.: Left: Topography of AFM measurement, the roughness is 0.84 nm. Right: Height distribution of AFM measurement with Gaussian fit, resulting in roughness of 0.67 nm.

SP$_{0199}$

LSMO thin films grown on STO (001) substrates at a temperature of 800°C and 3 mbar oxygen partial pressure.

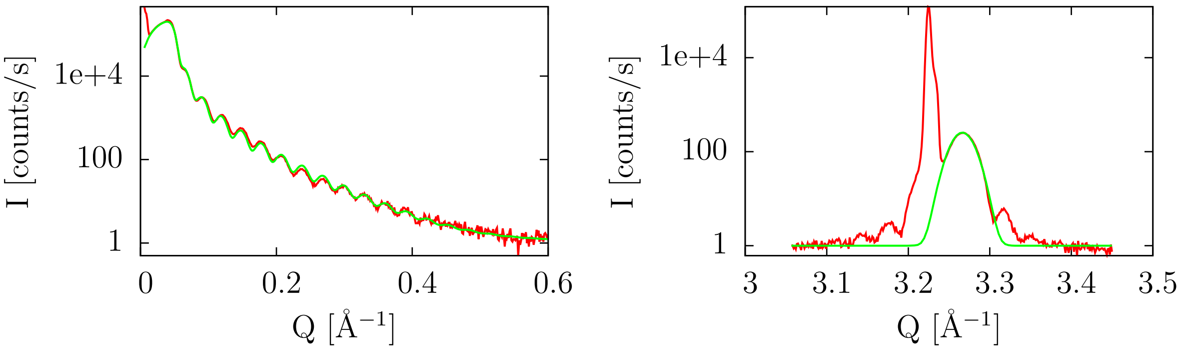

Figure H.16.: Left: X-ray reflectometry measurement with simulation thereof. Right: X-ray diffraction of the (002) Bragg peak.

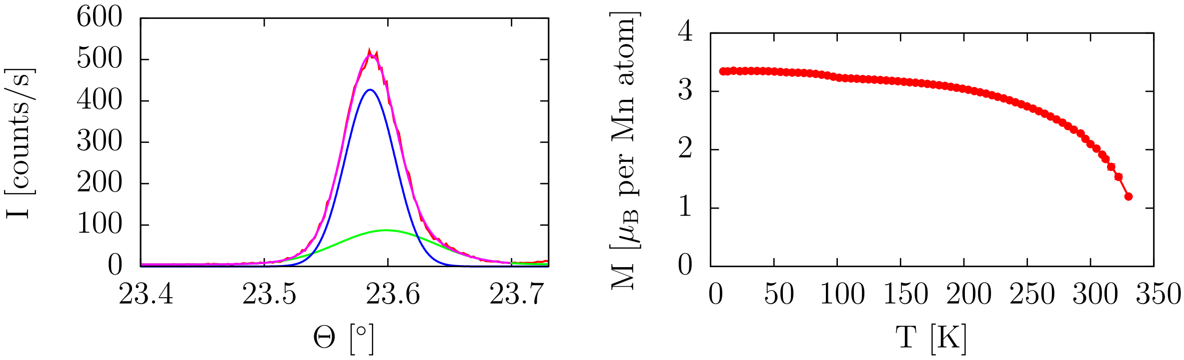

Figure H.17.: Left: Rocking scan of the (002) Bragg peak with Gaussian fit. The FWHM is 5.0 ° ± 0.04°. Right: Field cooled measurement with applied magnetic field of 100 Oe.

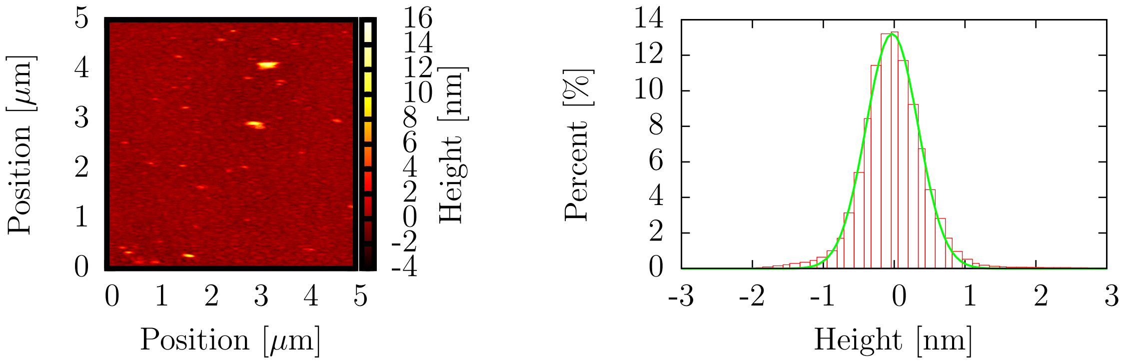

Figure H.18.: Left: Topography of AFM measurement, the roughness is 0.67 nm. Right: Height distribution of AFM measurement with Gaussian fit, resulting in roughness of 0.37 nm.

SP$_{203}$

LSMO thin films grown on STO (001) substrates at a temperature of 700°C and 3 mbar oxygen partial pressure.

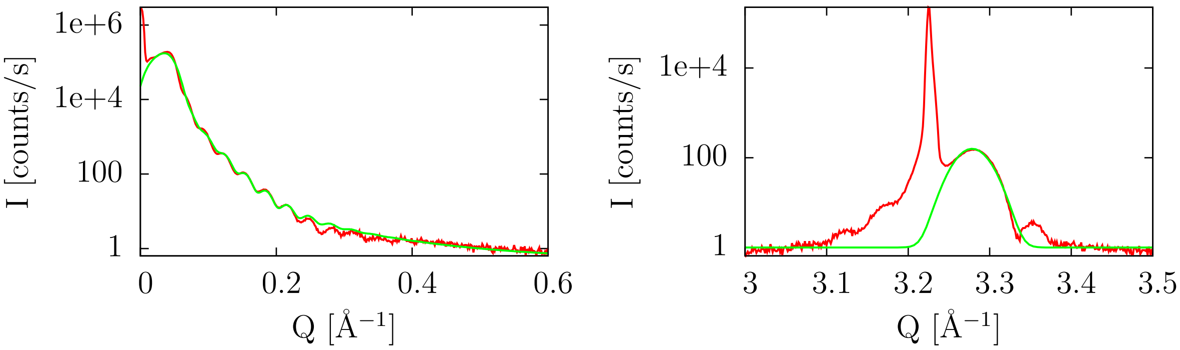

Figure H.19.: Left: X-ray reflectometry measurement with simulation thereof. Right: X-ray diffraction of the (002) Bragg peak.

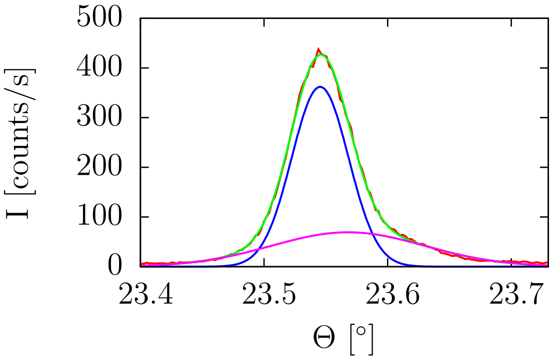

Figure H.20.: Rocking scan of the (002) Bragg peak with Gaussian fit. The FWHM is 5.4 ° ± 0.05°.

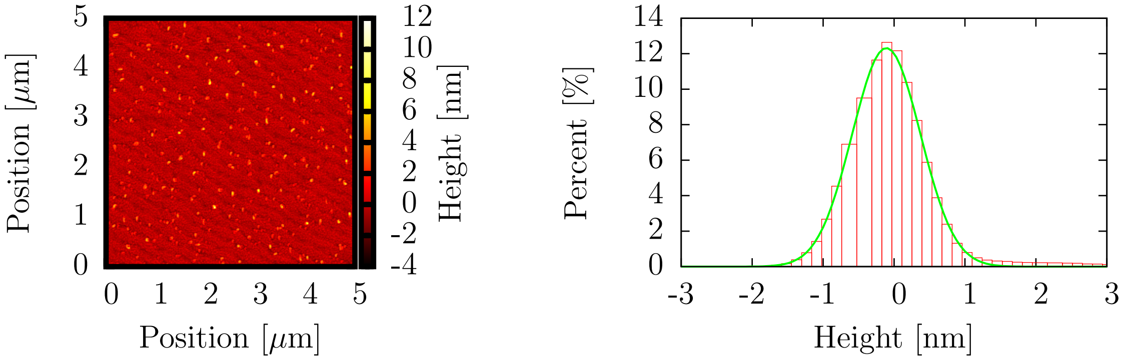

Figure H.21.: Left: Topography of AFM measurement, the roughness is 0.72 nm. Right: Height distribution of AFM measurement with Gaussian fit, resulting in roughness of 0.48 nm.

Temperature Variation for LCMO film by OMBE

All prepared LCMO thin films grown by OMBE, for the optimization of growth parameters, are shown including all relevant measurements: LEED, RHEED, AFM, XRR and XRD.

OMBE$_{0242}$

LCMO thin films grown on STO (001) substrates at a temperature of 700°C.

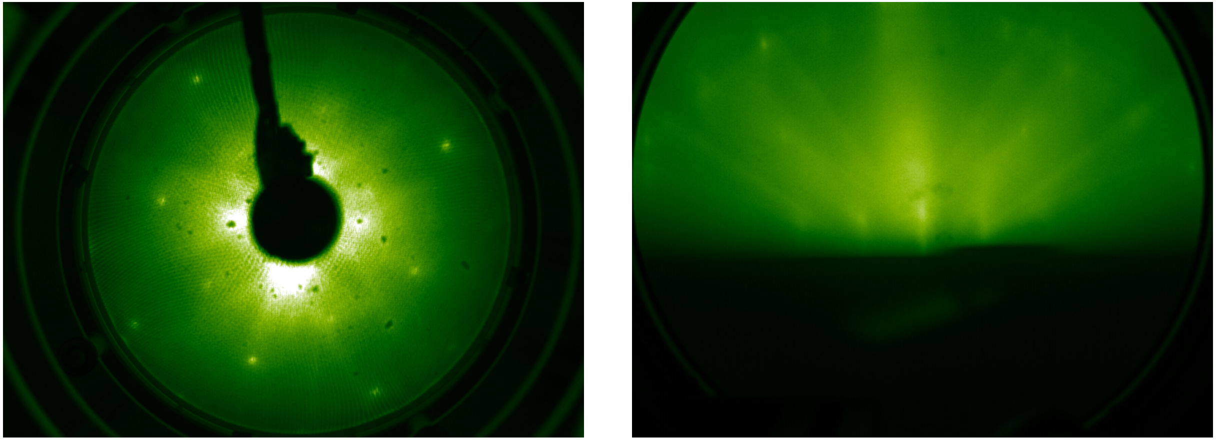

Figure H.22.: Left: LEED image at 100 eV. Right: RHEED image.

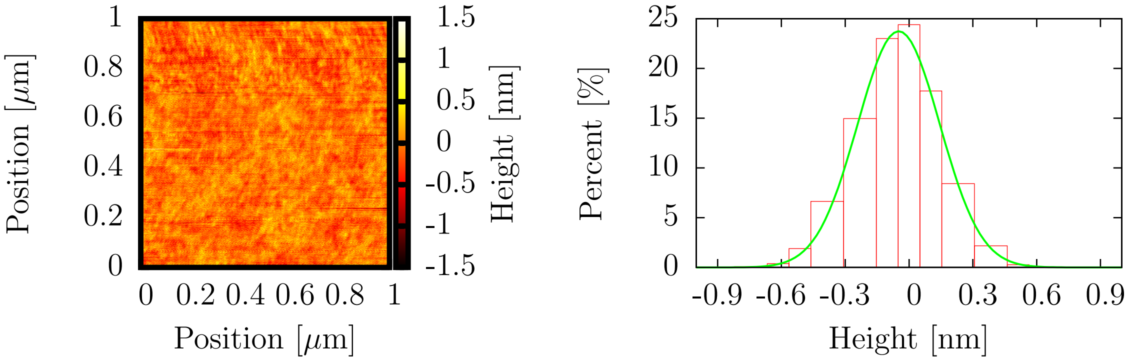

Figure H.23.: Left: AFM measurement with surface roughness of 0.2 nm. Right: Height distribution with Gaussian fit, result in RMS of 0.19 nm.

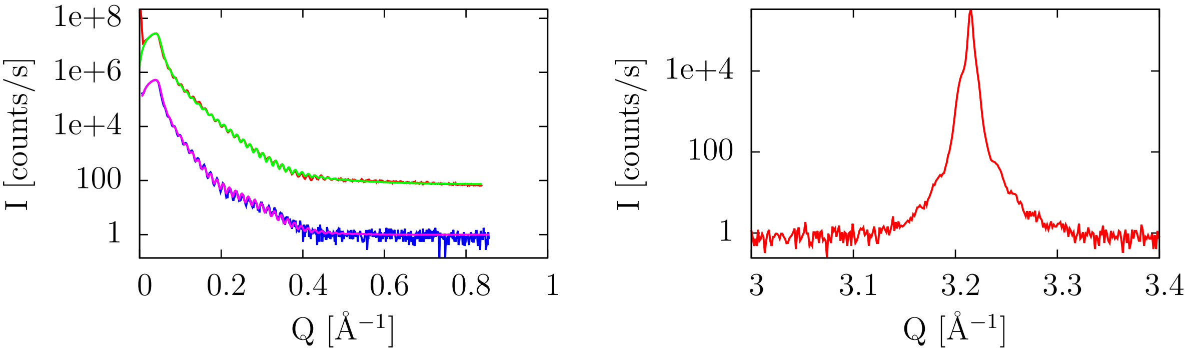

Figure H.24.: Left: X-ray reflectometry measurement with simulation thereof. Right: X-ray diffraction of the (002) Bragg peak.

OMBE$_{0240}$

LCMO thin films grown on STO (001) substrates at a temperature of 800°C.

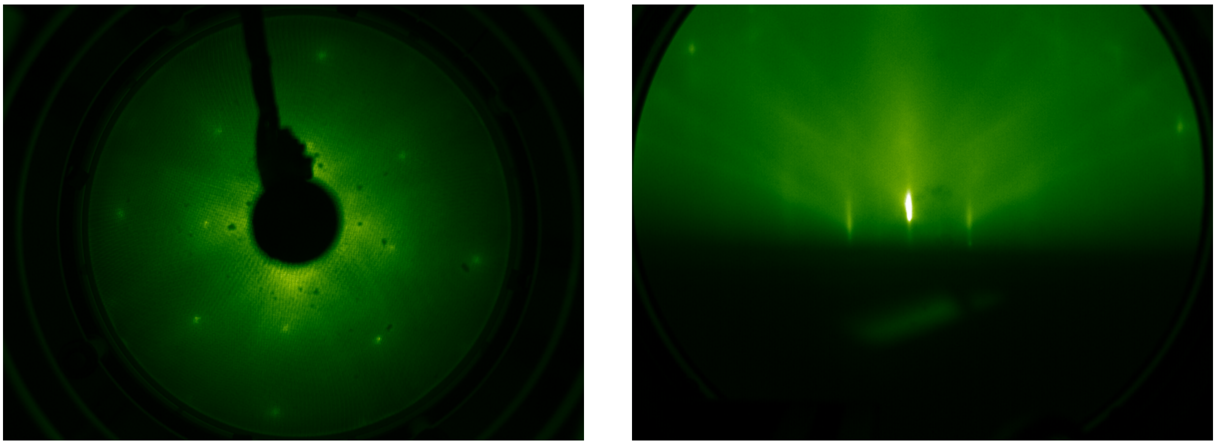

Figure H.25.: Left: LEED image at 100 eV. Right: RHEED image.

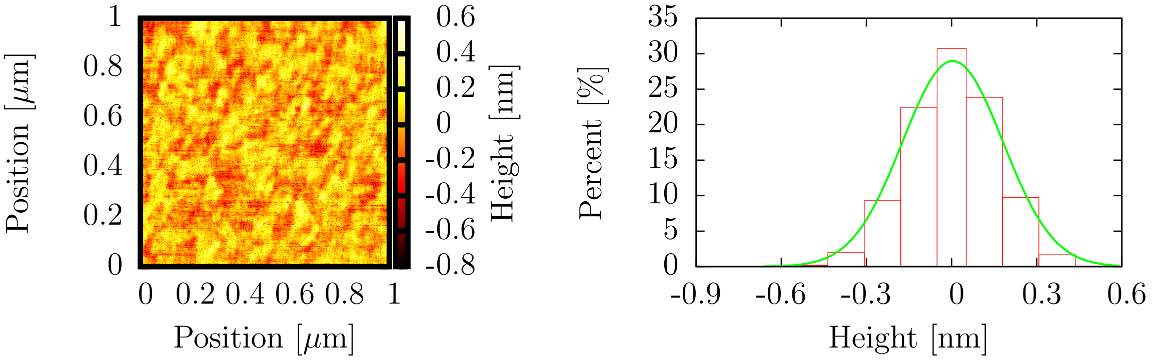

Figure H.26.: Left: AFM measurement with a surface roughness of 0.16 nm. Height distribution with Gaussian fit, result in RMS of 0.16 nm.

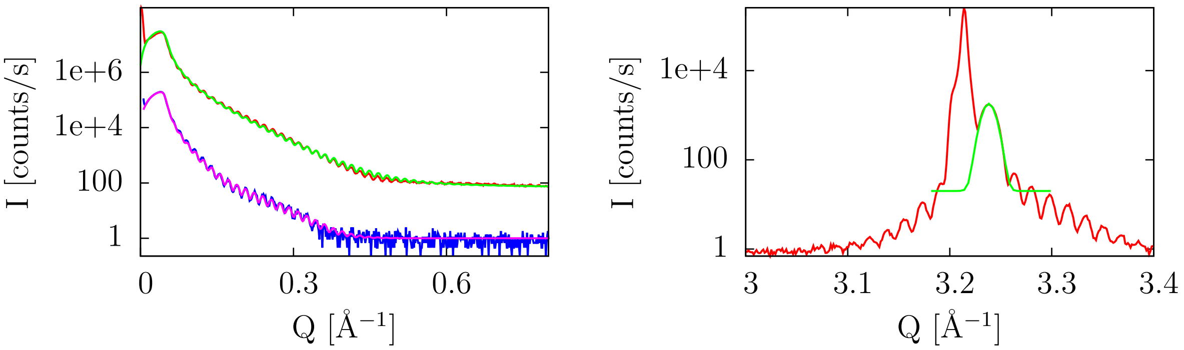

Figure H.27.: Left: X-ray reflectometry measurement with simulation thereof. Right: X-ray diffraction of the (002) Bragg peak.

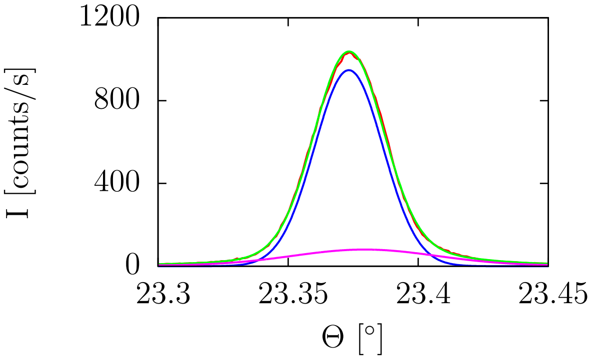

Figure H.28.: Left: Rocking scan of the (002) Bragg peak with Gaussian fit. The FWHM is $3.57° \cdot 10^{-2} \pm 0.04° \cdot 10^{-2}$.

OMBE$_{0239}$

LCMO thin films grown on STO (001) substrates at a temperature of 900°C.

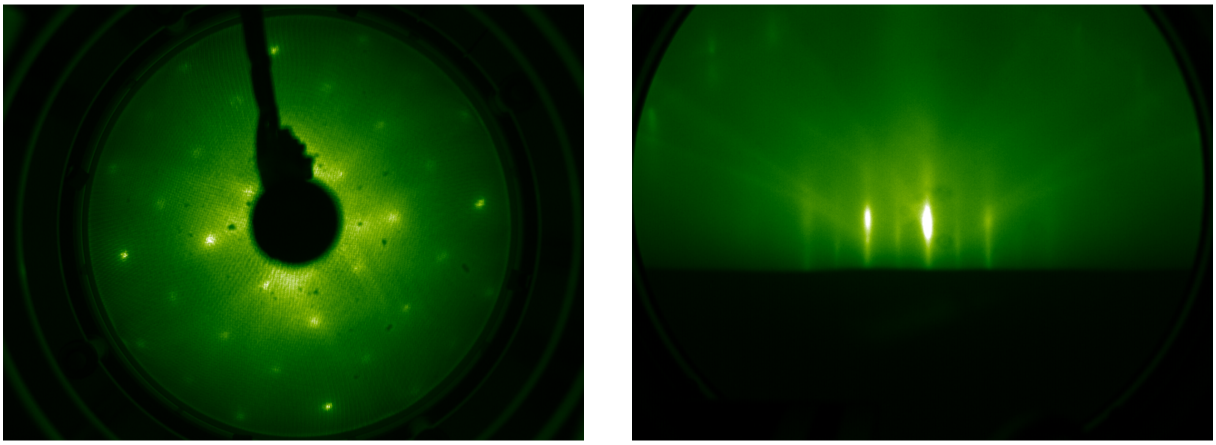

Figure H.29.: Left: LEED image at 100 eV. Right: RHEED image.

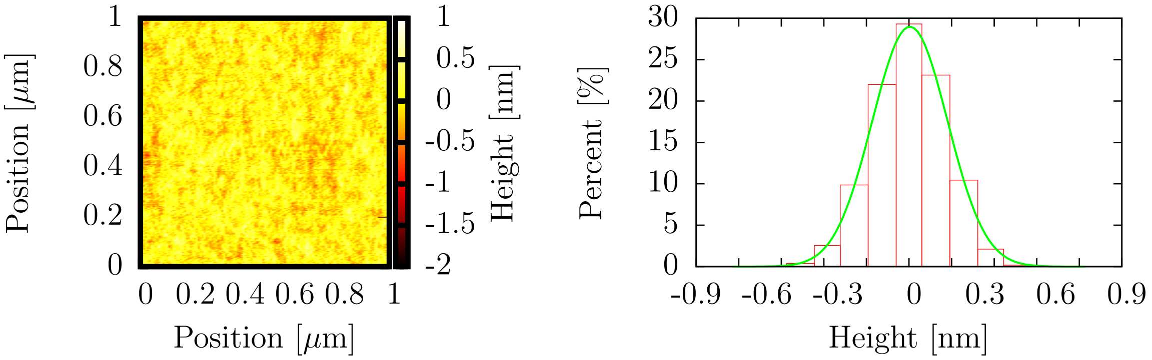

Figure H.30.: Left: AFM measurement with surface roughness of 0.2 nm. Height distribution with Gaussian fit, result in RMS of 0.18 nm.

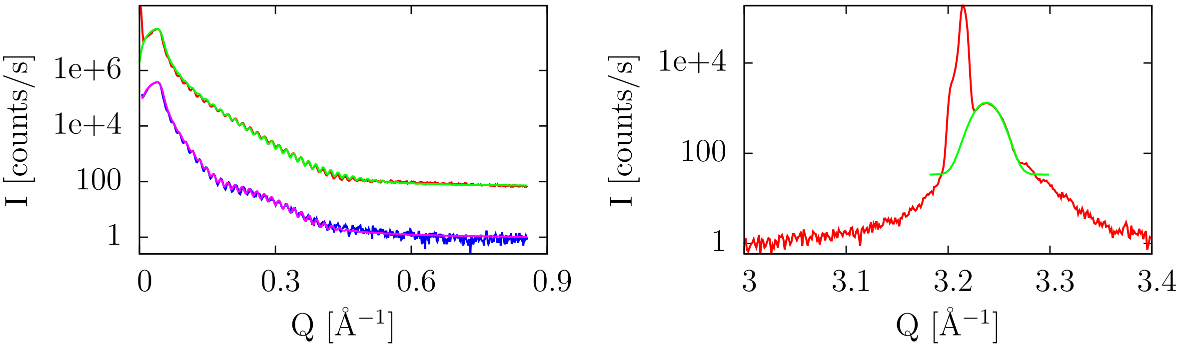

Figure H.31.: Left: X-ray reflectometry measurement with simulation thereof. Right: X-ray diffraction of the (002) Bragg peak.

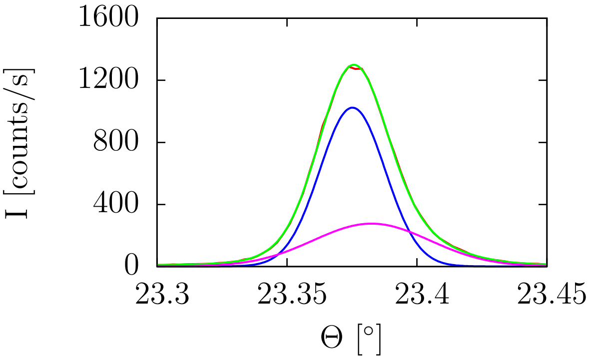

Figure H.32.: Left: Rocking scan of the (002) Bragg peak with Gaussian fit. The FWHM is $3.79^\circ \cdot 10^{-2} \pm 0.07^\circ \cdot 10^{-2}$.

I. Abbreviations

AES	Auger-electron spectroscopy	27
AFM	Atomic force microscopy	27
APS	Advanced Photon Source	91
DC	Direct current	34
DOS	Density of states	10
FOM	Figure of merit	80
FWHM	Full width half maximum	55
HOPSA	High oxygen pressure sputtering automaton	27
JCNS	Jülich Centre for Neutron Science	37
LBMO	$La_xBi_{1-x}MnO_3$	43
LCMO	$La_xCa_{1-x}MnO_3$	1
LEED	Low-energy electron diffraction	27
LSCMO	$La_{0.7}Sr_xCa_{0.3-x}MnO_3$	129
LSMO	$La_xSr_{1-x}MnO_3$	1
MFC	Mass flow controller	28
MPMS	Magnetic property measurement system	33
OMBE	Oxide molecular beam epitaxy	27
PLD	Pulsed laser deposition	30
PNR	Polarized neutron reflectometry	13
QMB	Quartz micro balance	43
RBS	Rutherford backscattering	27
RHEED	Reflection high energy electron diffraction	27
RSO	Reciprocating sample option	34

SLD	Scattering length density	80
SQUID	Superconducting quantum interference device	27
STO	$SrTiO_3$	5
TMO	Transition metal oxide	5
TOF	Time-of-flight	38
UHV	Ultra high vacuum	42
XAS	X-ray absorption spectroscopy	82
XMCD	X-ray magnetic circular dichroism	21
XRD	X-ray diffraction	27
XRR	X-ray reflectometry	13

Bibliography

[1] D. G. Schlom, L.-Q. Chen, X. Pan, A. Schmehl, and M. A. Zurbuchen. “A Thin Film Approach to Engineering Functionality into Oxides”. In: *Journal of the American Ceramic Society* 91 (2008), pp. 2429–2454.

[2] J. Coey, Ariando, and W. Pickett. “Magnetism at the edge: New phenomena at oxide interfaces”. In: *MRS Bulletin* 38 (2013), pp. 1040–1047.

[3] C. Adamo, X. Ke, P. Schiffer, A. Soukiassian, M. Warusawithana, L. Maritato, and D. G. Schlom. “Electrical and magnetic properties of $(\mathrm{SrMnO_3})_n/(\mathrm{LaMnO_3})_{2n}$ superlattices”. In: *Applied Physics Letters* 92 (2008), p. 112508.

[4] H. Boschker, J. Kautz, E. P. Houwman, W. Siemons, D. H. A. Blank, M. Huijben, G. Koster, A. Vailionis, and G. Rijnders. “High-Temperature Magnetic Insulating Phase in Ultrathin $\mathrm{La_{0.67}Sr_{0.33}MnO_3}$ Films”. In: *Physical Review Letters* 109 (2012), p. 157207.

[5] A. Sadoc, B. Mercey, C. Simon, D. Grebille, W. Prellier, and M.-B. Lepetit. “Large Increase of the Curie Temperature by Orbital Ordering Control”. In: *Physical Review Letters* 104 (2010), p. 046804.

[6] D. A. Dikin, M. Mehta, C. W. Bark, C. M. Folkman, C. B. Eom, and V. Chandrasekhar. “Coexistence of Superconductivity and Ferromagnetism in Two Dimensions”. In: *Physical Review Letters* 107 (2011), p. 056802.

[7] S. Blügel, B. Drittler, R. Zeller, and P. Dederichs. “Magnetic properties of 3d transition metal monolayers on metal substrates”. In: *Applied Physics A* 49 (1989), pp. 547–562.

[8] A. Oswald, R. Zeller, and P. H. Dederichs. “Giant Moments in Palladium”. In: *Physical Review Letters* 56 (1986), pp. 1419–1422.

[9] J. Vogel, A. Fontaine, V. Cros, F. Petroff, J.-P. Kappler, G. Krill, A. Rogalev, and J. Goulon. “Palladium magnetism in Pd/Fe multilayers studied by XMCD at the $\mathrm{PdL_{2,3}}$ edges”. In: *Journal of Magnetism and Magnetic Materials* 165 (1997), pp. 96 –99.

[10] L Fritsche, J Noffke, and H Eckardt. “A relativistic treatment of interacting spin-aligned electron systems: application to ferromagnetic iron, nickel and palladium metal”. In: *Journal of Physics F: Metal Physics* 17 (1987), p. 943.

[11] J. C. Ododo. “The onset of ferromagnetism in PdFe and PdNi alloys”. In: *Solid State Communications* 25 (1978), pp. 25–29.

[12] K. Kobayashi, H. Maruyama, T. Iwazumi, N. Kawamura, and H. Yamazaki. “Magnetic circular x-ray dichroism at Pd $\mathrm{L_{2,3}}$-edges in Fe-Pd alloys”. In: *Solid State Communications* 97 (1996), pp. 491–496.

[13] J. Hemberger, A. Krimmel, T. Kurz, H.-A. Krug von Nidda, V. Y. Ivanov, A. A. Mukhin, A. M. Balbashov, and A. Loidl. “Structural, magnetic, and electrical properties of single-crystalline $La_{1-x}Sr_xMnO_3$ $(0.4 \leq x \leq 0.85)$”. In: *Physical Review B* 66 (2002), p. 094410.

[14] P. Schiffer, A. P. Ramirez, W. Bao, and S.-W. Cheong. “Low Temperature Magnetoresistance and the Magnetic Phase Diagram of $La_{1-x}Ca_xMnO_3$”. In: *Physical Review Letters* 75 (1995), pp. 3336–3339.

[15] J. B. Goodenough. “Theory of the Role of Covalence in the Perovskite-Type Manganites [La, M(II)]MnO_3”. In: *Physical Review* 100 (1955), pp. 564–573.

[16] J. B. Goodenough. “An interpretation of the magnetic properties of the perovskite-type mixed crystals $La_{1-x}Sr_xCoO_{3-\lambda}$”. In: *Journal of Physics and Chemistry of Solids* 6 (1958), pp. 287 –297.

[17] J. Kanamori. “Superexchange interaction and symmetry properties of electron orbitals”. In: *Journal of Physics and Chemistry of Solids* 10 (1959), pp. 87 –98.

[18] C. A. F. Vaz, J. A. Moyer, D. A. Arena, C. H. Ahn, and V. E. Henrich. “Magnetic and electronic structure of ultrathin $La_{1-x}Sr_xMnO_3$ films at half doping”. In: *Physical Review B* 90 (2014), p. 024414.

[19] T. Thanh, L. Nguyen, D. Manh, N. Chien, P. Phong, N. Khiem, L. Hong, and N. Phuc. “Structural, magnetic and magnetotransport behavior of $La_{0.7}Sr_xCa_{0.3-x}MnO_3$ compounds”. In: *Physica B: Condensed Matter* 407 (2012), pp. 145 –152.

[20] Y. N. Kim, E. K. Lee, Y. B. Lee, H. Shim, N. H. Hur, and W. S. Kim. “Direct Evidence for Ferromagnetism of Nanometer-Scale Palladium by Contact with Perovskite Manganite”. In: *Journal of the American Chemical Society* 126 (2004), pp. 8672–8673.

[21] A. Delin, E. Tosatti, and R. Weht. “Magnetism in Atomic-Size Palladium Contacts and Nanowires”. In: *Physical Review Letters* 92 (2004), p. 057201.

[22] X. Dong, Q. Li, and M. Xu. “Magnetic properties in Pd doped ZnS from ab initio calculations”. In: *The European Physical Journal B* 86, 465 (2013).

[23] M. Ren, C. Zhang, P. Li, Z. Song, and X. Liu. “The origin of ferromagnetism in Pd-doped CdS”. In: *Journal of Magnetism and Magnetic Materials* 324 (2012), pp. 2039 –2042.

[24] Y. Tokura, Y. Tomioka, H. Kuwahara, A. Asamitsu, Y. Moritomo, and M. Kasai. “Origins of colossal magnetoresistance in perovskite type manganese oxides (invited)”. In: *Journal of Applied Physics* 79 (1996), pp. 5288–5291.

[25] A. P. Ramirez. “Colossal magnetoresistance”. In: *Journal of Physics: Condensed Matter* 9 (1997), p. 8171.

[26] J. Wang, J. B. Neaton, H. Zheng, V. Nagarajan, S. B. Ogale, B. Liu, D. Viehland, V. Vaithyanathan, D. G. Schlom, U. V. Waghmare, N. A. Spaldin, K. M. Rabe, M. Wuttig, and R. Ramesh. “Epitaxial $BiFeO_3$ Multiferroic Thin Film Heterostructures”. In: *Science* 299 (2003), pp. 1719–1722.

[27] S.-W. Cheong and M. Mostovoy. “Multiferroics: a magnetic twist for ferroelectricity”. In: *Nature Materials* 6 (2007), pp. 13–20.

[28] N. Chau, P. Q. Niem, H. N. Nhat, N. H. Luong, and N. D. Tho. “Influence of Cu substitution for Mn on the structure, magnetic, magnetocaloric and magnetoresistance properties of $La_{0.7}Sr_{0.3}MnO_3$ perovskites”. In: *Physica B: Condensed Matter* 327 (2003), pp. 214 –217.

[29] M.-H. Phan, T.-L. Phan, S.-C. Yu, N. D. Tho, and N. Chau. “Large magnetocaloric effect in $La_{0.845}Sr_{0.155}Mn_{1-x}M_xO_3$ (M = Mn, Cu, Co) perovskites”. In: *Physica Status Solidi (B)* 241 (2004), pp. 1744–1747.

[30] R. D. Shannon and C. T. Prewitt. “Effective ionic radii in oxides and fluorides”. In: *Acta Crystallographica Section B* 25 (1969), pp. 925–946.

[31] P. G. Radaelli, G. Iannone, M. Marezio, H. Y. Hwang, S.-W. Cheong, J. D. Jorgensen, and D. N. Argyriou. “Structural effects on the magnetic and transport properties of perovskite $A_{1-x}A'_x\mathrm{MnO_3}$ ($x = 0.25, 0.30$)”. In: *Physical Review B* 56 (1997), pp. 8265–8276.

[32] P. Lisboa-Filho, A. Mombrú, H Pardo, W. Ortiz, and E. Leite. “Influence of processing conditions on the crystal structure and magnetic behavior of $La_{0.7}Ca_{0.3}MnO_{3\,\pm\,\delta}$ samples”. In: *Journal of Physics and Chemistry of Solids* 64 (2003), pp. 583 –591.

[33] Y. A. Abramov, V. G. Tsirelson, V. E. Zavodnik, S. A. Ivanov, and B. I. D. “The chemical bond and atomic displacements in $SrTiO_3$ from X-ray diffraction analysis”. In: *Acta Crystallographica Section B* 51 (1995), pp. 942–951.

[34] P. W. Anderson. “Antiferromagnetism. Theory of Superexchange Interaction”. In: *Physical Review* 79 (1950), pp. 350–356.

[35] A. J. Millis. “Orbital ordering and superexchange in manganite oxides”. In: *Physical Review B* 55 (1997), pp. 6405–6408.

[36] E. Pavarini and E. Koch. “Origin of Jahn-Teller Distortion and Orbital Order in $LaMnO_3$”. In: *Physical Review Letters* 104 (2010), p. 086402.

[37] Lekcure Notes of Dr. Opel at Bayerische Akademie der Wissenschaften. URL: `www.wmi.badw.de/teaching/Lecturenotes/magnetismus/Kapitel-6.pdf`.

[38] C. Zener. “Interaction Between the d Shells in the Transition Metals”. In: *Physical Review* 81 (1951), pp. 440–444.

[39] V. Skumryev, F. Ott, J. Coey, A. Anane, J.-P. Renard, L. Pinsard-Gaudart, and A. Revcolevschi. “Weak ferromagnetism in $LaMnO_3$”. In: *The European Physical Journal B - Condensed Matter and Complex Systems* 11 (1999), pp. 401–406.

[40] M. C. Guidi, G. Allodi, R. D. Renzi, G. Guidi, M. Hennion, L. Pinsard, and A. Amato. “Staggered magnetization, critical behavior, and weak ferromagnetic properties of $LaMnO_3$ by muon spin rotation”. In: *Physical Review B* 64 (2001), p. 064414.

[41] M Paraskevopoulos, F Mayr, J Hemberger, A Loidl, R Heichele, D Maurer, V Müller, A. A. Mukhin, and A. M. Balbashov. “Magnetic properties and the phase diagram of $\mathrm{La_{1-x}Sr_xMnO_3}$ for $\mathrm{x} \leq 0.2$”. In: *Journal of Physics: Condensed Matter* 12 (2000), p. 3993.

[42] R. Laiho, E. Lähderanta, J. Salminen, K. G. Lisunov, and V. S. Zakhvalinskii. “Spin dynamics and magnetic phase diagram of $\mathrm{La}_{1-x}\mathrm{Ca}_x\mathrm{MnO}_3$ $(0 \leq x \leq 0.15)$”. In: *Physical Review B* 63 (2001), p. 094405.

[43] S. Blundell. *Magnetism in Condensed Matter.* Oxford Master Series in Condensed Matter Physics. OUP Oxford, 2001.

[44] R. Gross and A. Marx. *Festkörperphysik.* Oldenbourg Wissenschaftsverlag, 2012.

[45] J. F. Janak. “Uniform susceptibilities of metallic elements”. In: *Physical Review B* 16 (1977), pp. 255–262.

[46] O. Gunnarsson. “Band model for magnetism of transition metals in the spin-density-functional formalism”. In: *Journal of Physics F: Metal Physics* 6 (1976), p. 587.

[47] J. A. Venables, G. D. T. Spiller, and M Hanbucken. “Nucleation and growth of thin films”. In: *Reports on Progress in Physics* 47 (1984), p. 399.

[48] J. A. Venables. “Atomic processes in crystal growth”. In: *Surface Science* 299-300 (1994), pp. 798 –817.

[49] P. Dobson, B. Joyce, J. Neave, and J. Zhang. “Current understanding and applications of the RHEED intensity oscillation technique”. In: *Journal of Crystal Growth* 81 (1987), pp. 1 –8.

[50] L. Zhang, R. Persaud, and T. E. Madey. “Ultrathin metal films on a metal oxide surface: Growth of Au on $\mathrm{TiO_2}$ (110)”. In: *Physical Review B* 56 (1997), pp. 10549–10557.

[51] G. Haas, A. Menck, H. Brune, J. V. Barth, J. A. Venables, and K. Kern. “Nucleation and growth of supported clusters at defect sites: Pd/MgO(001)”. In: *Physical Review B* 61 (2000), pp. 11105–11108.

[52] F. M. Granozio, G. Koster, and G. Rijnders. “Functional oxide interfaces”. In: *MRS Bulletin* 38 (2013), pp. 1017–1023.

[53] A. Ohtomo and H. Y. Hwang. “A high-mobility electron gas at the LaAlO3/SrTiO3 heterointerface”. In: *Nature* 427 (2004), pp. 423–426.

[54] S. J. May, A. B. Shah, S. G. E. te Velthuis, M. R. Fitzsimmons, J. M. Zuo, X. Zhai, J. N. Eckstein, S. D. Bader, and A. Bhattacharya. “Magnetically asymmetric interfaces in a $\mathrm{LaMnO_3/SrMnO_3}$ superlattice due to structural asymmetries”. In: *Physical Review B* 77 (2008), p. 174409.

[55] O. Diéguez, K. M. Rabe, and D. Vanderbilt. “First-principles study of epitaxial strain in perovskites”. In: *Physical Review B* 72 (2005), p. 144101.

[56] A. Vailionis, H. Boschker, W. Siemons, E. P. Houwman, D. H. A. Blank, G. Rijnders, and G. Koster. “Misfit strain accommodation in epitaxial $AB\mathrm{O}_3$ perovskites: Lattice rotations and lattice modulations”. In: *Physical Review B* 83 (2011), p. 064101.

[57] F. He, B. O. Wells, and S. M. Shapiro. “Strain Phase Diagram and Domain Orientation in $SrTiO_3$ Thin Films”. In: *Physical Review Letters* 94 (2005), p. 176101.

[58] F. Tsui, M. C. Smoak, T. K. Nath, and C. B. Eom. “Strain-dependent magnetic phase diagram of epitaxial $La_{0.67}Sr_{0.33}MnO_3$ thin films”. In: *Applied Physics Letters* 76 (2000), pp. 2421–2423.

[59] R. A. Rao, D. Lavric, T. K. Nath, C. B. Eom, L. Wu, and F. Tsui. “Effects of film thickness and lattice mismatch on strain states and magnetic properties of $La_{0.8}Ca_{0.2}MnO_3$ thin films”. In: *Journal of Applied Physics* 85 (1999), pp. 4794–4796.

[60] D. Gutiérrez, G. Radaelli, F. Sánchez, R. Bertacco, and J. Fontcuberta. “Bandwidth-limited control of orbital and magnetic orders in half-doped manganites by epitaxial strain”. In: *Physical Review B* 89 (2014), p. 075107.

[61] J. H. Haeni, P. Irvin, W. Chang, R. Uecker, P. Reiche, Y. L. Li, S. Choudhury, W. Tian, M. E. Hawley, B. Craigo, A. K. Tagantsev, X. Q. Pan, S. K. Streiffer, L. Q. Chen, S. W. Kirchoefer, J. Levy, and D. G. Schlom. “Room-temperature ferroelectricity in strained $SrTiO_3$”. In: *Nature* 430 (2004), pp. 758–761.

[62] D. Stoeffler, K. Ounadjela, J. Sticht, and F. Gautier. “Magnetic polarization of the Pd spacer and interlayer magnetic couplings in Fe/Pd (001) superlattices: First principles calculations”. In: *Physical Review B* 49 (1994), pp. 299–309.

[63] H. Lu, T. A. George, Y. Wang, I. Ketsman, J. D. Burton, C.-W. Bark, S. Ryu, D. J. Kim, J. Wang, C. Binek, P. A. Dowben, A. Sokolov, C.-B. Eom, E. Y. Tsymbal, and A. Gruverman. “Electric modulation of magnetization at the $BaTiO_3/La_{0.67}Sr_{0.33}MnO_3$ interfaces”. In: *Applied Physics Letters* 100 (2012), p. 232904.

[64] Y. Lu, Y. Choi, C. Ortega, X. Cheng, J. Cai, S. Huang, L. Sun, and C. Chien. “Pt Magnetic Polarization on $Y_3Fe_5O_{12}$ and Magnetotransport Characteristics”. In: *Physical Review Letters* 110 (2013), p. 147207.

[65] S. Geprägs, S. Meyer, S. Altmannshofer, M. Opel, F. Wilhelm, A. Rogalev, R. Gross, and S. T. B. Goennenwein. “Investigation of induced Pt magnetic polarization in Pt/Y3Fe5O12 bilayers”. In: *Applied Physics Letters* 101, 262407 (2012), pp. –.

[66] S. Geprägs, S. T. B. Goennenwein, M. Schneider, F. Wilhelm, K. Ollefs, A. Rogalev, M. Opel, and R. Gross. “Comment on ”Pt magnetic polarization on Y3Fe5O12 and magnetotransport characteristics””. In: *ArXiv e-prints* (2013). arXiv:`1307.4869`.

[67] G. Thomas Brückel. *Neutron Scattering Lectures of the JCNS Laborator Course held at Forschungszentrum Jülich and the research reactor FRM II of TU Munich In cooperation with RWTH Aachen and University of Münster.* Schriften des Forschungszentrums Jülich: Reihe Schlüsseltechnologien. Forschungszentrum Jülich, 2012.

[68] L. G. Parratt. “Surface Studies of Solids by Total Reflection of X-Rays”. In: *Physical Review* 95 (1954), pp. 359–369.

[69] S. K. Sinha, E. B. Sirota, S. Garoff, and H. B. Stanley. “X-ray and neutron scattering from rough surfaces”. In: *Physical Review B* 38 (1988), pp. 2297–2311.

[70] J. Stöhr. “X-ray magnetic circular dichroism spectroscopy of transition metal thin films”. In: *Journal of Electron Spectroscopy and Related Phenomena* 75 (1995), pp. 253 – 272.

[71] U. Fano. “Spin Orientation of Photoelectrons Ejected by Circularly Polarized Light”. In: *Physical Review* 178 (1969), pp. 131–136.

[72] J. Stöhr. “Exploring the microscopic origin of magnetic anisotropies with X-ray magnetic circular dichroism (XMCD) spectroscopy”. In: *Journal of Magnetism and Magnetic Materials* 200 (1999), pp. 470 –497.

[73] B. T. Thole, P. Carra, F. Sette, and G. van der Laan. “X-ray circular dichroism as a probe of orbital magnetization”. In: *Physical Review Letters* 68 (1992), pp. 1943–1946.

[74] P. Carra, B. T. Thole, M. Altarelli, and X. Wang. “X-ray circular dichroism and local magnetic fields”. In: *Physical Review Letters* 70 (1993), pp. 694–697.

[75] C. T. Chen, Y. U. Idzerda, H.-J. Lin, N. V. Smith, G. Meigs, E. Chaban, G. H. Ho, E. Pellegrin, and F. Sette. “Experimental Confirmation of the X-Ray Magnetic Circular Dichroism Sum Rules for Iron and Cobalt”. In: *Physical Review Letters* 75 (1995), pp. 152–155.

[76] M. M. Schwickert, G. Y. Guo, M. A. Tomaz, W. L. O’Brien, and G. R. Harp. “X-ray magnetic linear dichroism in absorption at the L edge of metallic Co, Fe, Cr, and V”. In: *Physical Review B* 58 (1998), R4289–R4292.

[77] J. Heydenreich. “M. A. Van Hove, W. H. Weinberg, C.-M. Chan. Low-energy electron diffraction. Springer-verlag berlin heidelberg, 1986, 603 pages, 220 figs., 20 tables. DM 124.00 ISBN 3-540-16262-3”. In: *Crystal Research and Technology* 23 (1988), pp. 178–178.

[78] H. Lüth. “Scattering from Surfaces and Thin Films”. In: *Solid Surfaces, Interfaces and Thin Films*. Graduate Texts in Physics. Springer Berlin Heidelberg, 2010, pp. 133–213.

[79] W. Braun. “Applied RHEED”. In: *Springer Tracts in Modern Physics* 154 (1999).

[80] J. C. Riviere. “Auger Electron Spectroscopy”. In: *Contemporary Physics* 14 (1973), p. 513.

[81] C. C. Chang. “Auger electron spectroscopy”. In: *Surface Science* 25 (1971), pp. 53 –79.

[82] T. Alford, L. Feldman, and J. Mayer. *Fundamentals of Nanoscale Film Analysis*. Springer Science & Business Media. Springer, 2007.

[83] P. Palmberg and P. E. Industries. *Handbook of Auger Electron Spectroscopy: A Reference Book of Standard Data for Identification and Interpretation of Auger Electron Spectroscopy Data*. Physical Electronics Industries, 1972.

[84] B. Josephson. “Possible new effects in superconductive tunnelling”. In: *Physics Letters* 1 (1962), pp. 251 –253.

---

[85] B. D. Josephson. "The discovery of tunnelling supercurrents". In: *Reviews of Modern Physics* 46 (1974), pp. 251–254.

[86] J. F. Ziegler, U Littmark, J. P. Biersack, and H. H. Andersen. *The stopping and ranges of ions in matter.* New York, NY: Pergamon, 1977.

[87] L. R. Doolittle. "Algorithms for the rapid simulation of Rutherford backscattering spectra". In: *Nuclear Instruments and Methods in Physics Research Section B: Beam Interactions with Materials and Atoms* 9 (1985), pp. 344 –351.

[88] A. Glavic. *Multiferroicity in oxide thin films and heterostructures.* Vol. 45. Schriften des Forschungszentrums Jülich : Schlüsseltechnologien / Key Technologies. Jülich: Forschungszentrum Jülich, Zentralbibliothek, 2012.

[89] M. Björck and G. Andersson. "*GenX*: an extensible X-ray reflectivity refinement program utilizing differential evolution". In: *Journal of Applied Crystallography* 40 (2007), pp. 1174–1178.

[90] J. Neuhaus, I. Lommatzsch, and A. Voit, eds. *Experimental facilities.* Forschungs-Neutronenquelle Heinz Maier-Leibnitz (FRM II) Technische Universität München, 2013.

[91] R. Cubitt and G. Fragneto. "D17: the new reflectometer at the ILL". English. In: *Applied Physics A* 74 (2002), pp. 329–331.

[92] *D17 LAMP Book.* URL: `http://www.ill.eu/instruments-support/instruments-groups/instruments/d17/more/documentation/d17-lamp-book/`.

[93] H. Ambaye, R. Goyette, A. Parizzi, and F. Klose. "SNS Magnetism Reflectometer". In: *Neutron News* 19 (2008), pp. 11–13.

[94] *QuickNXS User Manual.* URL: `https://neutrons.ornl.gov/sites/default/files/Magnetism-Reflectometer-Data-Reduction-Manual.pdf`.

[95] *Argonne Advanced Photon Source.* URL: `http://www.aps.anl.gov/Sectors/Sector4/4idd/beamline/`.

[96] J. Haeni, C. Theis, and D. Schlom. "RHEED Intensity Oscillations for the Stoichiometric Growth of $SrTiO_3$ Thin Films by Reactive Molecular Beam Epitaxy". In: *Journal of Electroceramics* 4 (2000), pp. 385–391.

[97] T. Kawamura and P. Maksym. "RHEED from stepped surfaces and its relation to RHEED intensity oscillations observed during MBE". In: *Surface Science* 161 (1985), pp. 12 –24.

[98] M. Waschk. personal communication. 2013.

[99] *MaTecK.* URL: `http://www.mateck.de/`.

[100] *Kurt J. Lesker Company.* URL: `http://www.lesker.com/newweb/index.cfm`.

[101] A. Stefan. personal communication. 2013.

[102] R. P. Borges, W. Guichard, J. G. Lunney, J. M. D. Coey, and F. Ott. "Magnetic and electric "dead" layers in $(La_{0.7}Sr_{0.3})MnO_3$ thin films". In: *Journal of Applied Physics* 89 (2001), pp. 3868–3873.

[103] J. Alberi, J. Fischer, V. Radeka, L. Rogers, and B. Schoenborn. “A two-dimensional position-sensitive detector for thermal neutrons”. In: *Nuclear Instruments and Methods* 127 (1975), pp. 507 –523.

[104] B. Dorner and A. R. Wildes. “Some Considerations on Resolution and Coherence Length in Reflectrometry”. In: *Langmuir* 19 (2003), pp. 7823–7828.

[105] M. O. Krause. “Atomic radiative and radiationless yields for K and L shells”. In: *Journal of Physical and Chemical Reference Data* 8 (1979), pp. 307–327.

[106] T. K. Sham. “L-edge x-ray-absorption systematics of the noble metals Rh, Pd, and Ag and the main-group metals In and Sn: A study of the unoccupied density of states in 4d elements”. In: *Physical Review B* 31 (1985), pp. 1888–1902.

[107] P. Etienne, J. Massies, F. Nguyen-Van-Dau, A. Barthélémy, and A. Fert. “Critical steps in the molecular beam epitaxy of high quality Ag/Fe superlattices on (001) GaAs”. In: *Applied Physics Letters* 55 (1989), pp. 2239–2241.

[108] D. Bürgler, C. Schmidt, J. Wolf, T. Schaub, and H.-J. Güntherodt. “Ag films on FeGaAs(001): from clean surfaces to atomic Ga structures”. In: *Surface Science* 366 (1996), pp. 295 –305.

[109] P. Zakalek. “Magnetische Grenzflächenphänomene in Eisen-Palladium-Vielfachschicht-systemen”. MA thesis. RWTH Aachen, 2010.

[110] C. Schneider, P. Bressler, P. Schuster, J. Kirschner, J. de Miguel, and R. Miranda. “Curie temperature of ultrathin films of fcc-cobalt epitaxially grown on atomically flat Cu(100) surfaces”. In: *Physical Review Letters* 64 (1990), pp. 1059–1062.

[111] S. A. Hayward and E. K. H. Salje. “Cubic-tetragonal phase transition in $SrTiO_3$ revisited: Landau theory and transition mechanism”. In: *Phase Transitions* 68 (1999), pp. 501–522.

[112] M. Sato, Y. Soejima, N. Ohama, A. Okazaki, H. J. Scheel, and K. A. Müller. “The lattice constant vs. temperature relation around the 105 K transition of a flux-grown $SrTiO_3$ crystal”. In: *Phase Transitions* 5 (1985), pp. 207–218.

[113] J Wang, Y Liu, Z Xie, and Q. M. Ma. “The step effect of hysteresis loop in FM/AFM mixed magnetic system”. In: *Journal of Physics: Conference Series* 29 (2006), p. 65.

[114] *Magnetic Property Measurement System MPMS MultiVu Application User’s Manual Part Number 1014-110C.*

[115] H.-C. Wu, O. N. Mryasov, M. Abid, K. Radican, and I. V. Shvets. “Magnetization States of All-Oxide Spin Valves Controlled by Charge-orbital Ordering of Coupled Ferromagnets”. In: *Scientific Reports* 3 (2013).

[116] C. S. Chang, M. Kostylev, and E. Ivanov. “Metallic spintronic thin film as a hydrogen sensor”. In: *Applied Physics Letters* 102 (2013),

[117] R. A. Tawil and J. Callaway. “Energy Bands in Ferromagnetic Iron”. In: *Physical Review B* 7 (1973), pp. 4242–4252.

[118] H. Chen, N. E. Brener, and J. Callaway. “Electronic structure, optical and magnetic properties of fcc palladium”. In: *Physical Review B* 40 (1989), pp. 1443–1449.

[119] Z. Mohamed, E. Tka, J. Dhahri, and E. Hlil. “Short-range ferromagnetic order in $La_{0.67}Sr_{0.16}Ca_{0.17}MnO_3$ perovskite manganite”. In: *Journal of Alloys and Compounds* 619 (2015), pp. 520 –526.

[120] W. M. Star, S. Foner, and E. J. McNiff. “Giant moment and ferromagnetism in dilute Pd(Mn) alloys”. In: *Physical Review B* 12 (1975), pp. 2690–2709.

[121] B. R. Coles, H Jamieson, R. H. Taylor, and A Tari. “Limited ferromagnetism and other magnetic properties of Pd-Mn alloys”. In: *Journal of Physics F: Metal Physics* 5 (1975), p. 565.

[122] J.-P. Tang, L.-L. Wang, W.-Z. Xiao, and X.-F. Li. “First principles study on magnetic properties in ZnS doped with palladium”. In: *The European Physical Journal B* 86 (2013), p. 362.

[123] Z. Tan, W. Xiao, L. Wang, and Y. Yang. “Magnetic properties of ZnS doped with noble metals (X= Ru, Rh, Pd, and Ag)”. In: *Journal of Applied Physics* 112 (2012), p. 123920.

[124] H Zenia, G. A. Gehring, and W. M. Temmerman. “Magnetic order and valency at $La_{0.7}Sr_{0.3}MnO_3$ /$SrTiO_3$ interfaces”. In: *New Journal of Physics* 9 (2007), p. 105.

[125] F. Delbecq and P. Sautet. “Density functional periodic study of CO adsorption on the $Pd_3Mn(100)$ alloy surface: Comparison with Pd(100)”. In: *Physical Review B* 59 (1999), pp. 5142–5153.

[126] J. W. Cable, E. O. Wollan, W. C. Koehler, and H. R. Child. “Antiferromagnetism of the Antiphase Domain Structure of Pd_3Mn”. In: *Physical Review* 128 (1962), pp. 2118–2120.

[127] J. Crangle and W. R. Scott. “Dilute Ferromagnetic Alloys”. In: *Journal of Applied Physics* 36 (1965), pp. 921–928.

[128] B. Henke, E. Gullikson, and J. Davis. “X-Ray Interactions: Photoabsorption, Scattering, Transmission, and Reflection at E = 50-30,000 eV, Z = 1-92”. In: *Atomic Data and Nuclear Data Tables* 54 (1993), pp. 181 –342.

[129] V. Sears. “Neutron scattering lengths and cross sections”. In: *Neutron News* 3 (1992), pp. 29–37.

[130] S. J. Hibble, S. P. Cooper, A. C. Hannon, I. D. Fawcett, and M Greenblatt. “Local distortions in the colossal magnetoresistive manganates La 0.70 Ca 0.30 MnO 3 , La 0.80 Ca 0.20 MnO 3 and La 0.70 Sr 0.30 MnO 3 revealed by total neutron diffraction”. In: *Journal of Physics: Condensed Matter* 11 (1999), p. 9221.

Acknowledgements

This dissertation can be seen as a milestone in my life. Nevertheless, without the help and encouragement of many people, this work would still be in progress. Thus, my special appreciation and tanks goes to:

- The first person I am most grateful is **Prof. Dr. Thomas Brückel**. He gave me the opportunity to work as the first PhD student with the new OMBE system and supported me throughout the whole time.
- I am very grateful to **Prof. Dr. Larissa Juschkin** to be the second reviewer.
- Special thanks goes to **Dr. Alexander Weber** for his great support during the last 4 years. I will always remember the interesting discussions at work and in leisure time, e.g. by a beer.
- I thank **Dr. Stefan Mattauch** for the support at the MARIA reflectometer.
- **Dr. Artur Glavic** for the great help at the MR reflectometer and the possibility to work together on the LSMO/LCMO system. He could always help with programming issues and the problems during the analysis of the PNR data.
- I thank **Dr. Andrew Wildes** for his support at the D17 reflectometer. He was always there for help and that at anytime.
- **Dr. Yongseong Choi** for the support at the XMCD beamline and the help in understanding XMCD.
- Many thanks to **Dr. Bernd Holländer** for performing the RBS measurements.
- Special thanks to **Dr. Jürgen Schubert** for the preparation of PLD samples and the help with the LSMO/LCMO system.
- I thank **Markus Waschk** a lot for the help at the XMCD beamtime and for sharing some of his beamtime at the D17 reflectometer with me.
- I am very thankful, that I could work together with great people at the Oxdie-MBE, namely: **Markus Schmitz, Markus Waschk and Dr. Alexander Weber**. Everyone helped each other the occurring problems. Although it was hard work, it was also an enjoyable time.
- Special thanks to the whole **Oxide-Club**, where I could discuss and learn a lot about oxides. Any problem could be addressed and many discussions gave fruitful results.
- I would like to thank the whole **Institute for Scattering Methods**. It was fun to work with great people. I will always remember the wonderful coffee beaks.

Zum Schluss möchte ich meiner Familie danken, die mich über die ganze Zeit unterstützt, als auch ertragen hat, besonders am Ende als es stressig wurde. Meiner Frau Canan gebührt mein größter Dank. Sie war immer an meiner Seite und hat mir Kraft gegeben diese Arbeit zu Ende zu machen. Ohne Sie wäre ich nicht hier wo ich jetzt bin.